

Durham E-Theses

Climate-ice sheet-ocean interactions in the Gulf of Alaska through the Pliocene and Pleistocene

SANCHEZ-MONTES, MARIA,LUISA

How to cite:

SANCHEZ-MONTES, MARIA,LUISA (2018) *Climate-ice sheet-ocean interactions in the Gulf of Alaska through the Pliocene and Pleistocene*, Durham theses, Durham University. Available at Durham E-Theses Online: <http://etheses.dur.ac.uk/12634/>

Use policy

The full-text may be used and/or reproduced, and given to third parties in any format or medium, without prior permission or charge, for personal research or study, educational, or not-for-profit purposes provided that:

- a full bibliographic reference is made to the original source
- a [link](#) is made to the metadata record in Durham E-Theses
- the full-text is not changed in any way

The full-text must not be sold in any format or medium without the formal permission of the copyright holders.

Please consult the [full Durham E-Theses policy](#) for further details.

Climate-ice sheet-ocean interactions in the Gulf of Alaska through the Pliocene and Pleistocene

Maria Luisa Sánchez Montes

**A thesis submitted in fulfilment of the requirements for
the degree of Doctor of Philosophy**

2018

Geography Department

Durham University

United Kingdom



Maria Luisa Sánchez Montes

Climate-ice sheet-ocean interactions in the Gulf of Alaska through the Pliocene and Pleistocene

Global climate is characterised by a long term cooling trend since the Pliocene. However, we lack climate records from the North Pacific to confirm this. The proximity of the GOA to the Mount St. Elias, the highest mountain in the world uplifted during the Plio-Pleistocene, makes the location a target to study the Pacific climate evolution towards present climate, the influence over the growth of large ice sheets over North America as well as the tectonic-ice sheet-climate interactions. This is important as the mid-Pliocene and MIS 5e have been identified as potential analogues for current climate. This thesis focuses on the Pliocene and Pleistocene study of Site U1417 (~700km away from the coast) and U1418 (~150km away from the coast) from the Gulf of Alaska, recovered during IODP Expedition 341. Biomarker extraction and analyses are used for sea surface temperature (SSTs from $U^{K_{37}}$ and $U^{K_{37}'}$ indices), sea surface salinity ($C_{37:4}$), terrestrial and aquatic organic carbon inputs (long, short chain n-alkanes, TAR index, TOC, TON, $\delta^{13}C$ and $\delta^{15}N$), marine productivity (alkenone, β -sitosterol, brassicasterol, dinosterol, TOC, TON, $\delta^{13}C$ and $\delta^{15}N$ concentrations) reconstructions at both sites. We conclude that SST during the early Pleistocene in the GOA was an average of 1°C warmer than during the late Pliocene, the last 500kyr and at modern. The Cordilleran Ice-Sheet developed since 2.8 Ma due to St. Elias tectonic uplift. The Cordilleran Ice-Sheet growth is fed by the humidity of a relatively warm and stratified surface ocean and orographic precipitation since the Pliocene. During the last 500 kyr, warmer SST intervals are associated with a decrease in ocean stratification. Nutrient availability in the GOA is the main control for coccolithophore productivity export reduction since the early Pleistocene. Modern ocean circulation across the North Pacific was established during the LGM and possibly since MIS 4.

This thesis titled “*Climate-ice sheet-ocean interactions in the Gulf of Alaska through the Pliocene and Pleistocene*” produced by Maria Luisa Sánchez Montes and supervised by Dr. Erin L. McClymont and Dr. Jeremy M. Lloyd is submitted to Geography Department, Durham University, Lower Mountjoy, South Road, Durham, United Kingdom for the qualification of Doctor of Philosophy in 2018.

List of Contents

Chapter 1: Introduction

1.1 Rationale Overview	29
1.2 Aim	30
1.3 Research questions and objectives	31
1.4 IODP Expedition 341	33

Chapter 2: Research Background

2.1 The Gulf of Alaska at present	35
2.1.1 Ocean and atmospheric circulation	35
2.1.2 Regional teleconnections	39
2.1.2.1 PDO	40
2.1.2.2 ENSO	42
2.1.2.3 The Arctic Oscillation and North Atlantic Oscillation	43
2.1.3 Marine Productivity in the GOA	44
2.1.3.1. Central GOA	44
2.1.3.2. Coastal GOA	46
2.1.4 Climate of the GOA Summary	48
2.2 Geology and Tectonics	50
2.3 Plio-Pleistocene Climate Evolution	52
2.3.1 The Pliocene (5.3 to 2.6 Ma)	54
2.3.1.1 The Early Pliocene (5.3 to 3.6 Ma)	54
2.3.1.2 The mid (3.3 to 3.1 Ma) and late (3.6 to 2.58 Ma) Pliocene	56
2.3.2 The Plio-Pleistocene Transition and early Pleistocene (2.6 to 1.5 Ma)	64
2.3.3 The mid and late Pleistocene (500 to 0 ka)	66
2.3.3.1 MIS 6 and MIS 5 (MIS 5:130 to 80 ka)	67
2.3.3.2 The Last Glacial Maximum (LGM) 24 to 21 ka)	68
2.4 Cordilleran Ice Sheet History	70
2.4.1 Summary	73

2.5 Reconstructing climate and glaciated environments	74
2.5.1 Palaeotemperature proxy: the $U^{K_{37}}$ and $U^{K_{37}'}$ indices	75
2.5.2 The $\%C_{37:4}$ proxy	78
2.5.3 Productivity proxies	79
2.5.3.1 Alkenones	79
2.5.3.2 Sterols	80
2.5.3.3 Carbon and nitrogen stable isotopes as productivity proxies	81
2.5.3.4 <i>N</i> -alkanes and sterols	82
2.5.3.5 Bulk C and N	83
2.5.4 Additional data sets to this study	84
2.5.4.1 Ice Rafted Debris (IRD)	84
2.5.4.2 Diatoms	85
2.5.4.3 Oxygen isotopes	85
2.6 Summary	85

Chapter 3: Methods

3.1 Site U1417	87
3.1.1 Sediment lithology	87
3.1.2 Sediment recovery and sampling	90
3.2 Site U1418	96
3.2.1 Sediment lithology	96
3.2.2 Sediment recovery and sampling	97
3.3 Sampling protocol and sample storage	100
3.4 Organic biomarker laboratory procedure	100
3.4.1 Glassware and reagent preparation	101
3.4.2 Freeze-dry	102
3.4.3 Lipid extraction	102
3.4.4 Active silica flash chromatography	103
3.4.5 Silylation of the polar fraction	104
3.5 Organic compound identification and quantification	105
3.6 Organic carbon and nitrogen bulk and isotope analysis	108
3.7 Depth-age conversion	110

Chapter 4: Results

4.1 Introduction	113
4.2 Site U1417	113
4.2.1 Palaeo-sea surface temperature and palaeo-salinity from alkenone proxies	113
4.2.2 SST Calibrations during 4 to 1.7 Ma	114
4.2.3 Terrestrial and aquatic proxies	118
4.2.4 Export production proxies	121
4.2.5 Summary of Site U1417	125
4.3 Site U1418	125
4.3.1 Palaeo-temperature and palaeo-salinity proxies	125
4.3.2 Terrestrial and aquatic organic matter proxies	128
4.3.3 Palaeo-marine export production proxies	129
4.4 Summary	132

Chapter 5: Cordilleran Ice Sheet development with warm sea surface temperatures in the Gulf of Alaska

5.1 Introduction	133
5.2 Materials and Methods	136
5.2.1 Site Location and sedimentology	136
5.2.2 Age model	136
5.2.3 Sampling resolution	137
5.3 Results	137
5.3.1 SST	137
5.3.2 $\delta^{13}C_{37:4}$	138
5.3.3 IRD	138
5.3.4 TAR index	139
5.4 Discussion	139
5.4.1 SST Calibration	139
5.4.2 Early to Late Pliocene (4 to 2.6 Ma)	141
5.4.2.1 Non-existent/small Cordilleran Ice Sheet in the early and mid Pliocene	142
5.4.2.2 Terrigenous organic matter input into the GOA	142

5.4.2.3 M2 Glaciation attempt (~3.3 Ma)	143
5.4.2.4 Onset of tidewater Glaciation in the GOA (3 to 2.8 Ma)	144
5.4.3 The intensification (2.8 Ma) of the Cordilleran Ice Sheet and its evolution during the early Pleistocene (2.8-1.7 Ma)	145
5.4.4 Comparison between climatic evolution of the west and east subarctic Pacific during the Plio-Pleistocene transition	147
5.4.5 Comparison across the Pacific during the Plio-Pleistocene	149
5.5 Conclusions	151

Chapter 6: Land-ocean interactions during the Plio-Pleistocene Cordilleran Ice Sheet growth.

6.1 Introduction	153
6.2 Research Site	156
6.3 Material and Methods	157
6.4 Results	157
6.4.1 <i>N</i> -alkane distributions and the TAR index	157
6.4.2 TOC, TON, $\delta^{13}\text{C}$ and $\delta^{15}\text{N}$	158
6.4.3 β -sitosterol	158
6.4.4 Dinosterol	159
6.4.5 Brassicasterol	159
6.4.6 Alkenones	160
6.4.7 Diatoms	160
6.5 Discussion	161
6.5.1 Environmental proxy assessment	161
6.5.2 Main trends during the Pliocene-Pleistocene climate evolution	167
6.5.3 Changes in terrigenous and marine sourced organic input and productivity in relation to SST and the glacial evolution of the Cordilleran Ice Sheet during the Pliocene and Pleistocene	169
6.5.4 Isotopic excursions during the early Pleistocene (2.8 to 2.4 Ma)	174

6.6	Conclusions	176
-----	-------------	-----

Chapter 7: Late Pleistocene ocean temperature dynamics in the Northeast Pacific

7.1	Introduction	179
7.2	Results	181
7.2.1	Site U1418	181
7.2.1.1	$U^{K_{37}}$ and $U^{K_{37}'}$	181
7.2.1.2	SST	181
7.2.1.3	$C_{37:4}$	182
7.2.1.4	TAR	182
7.2.1.5	TOC, TON, $\delta^{13}C$ and $\delta^{15}N$	183
7.2.1.6	Alkenone concentrations	183
7.2.1.7	Sterols	183
7.2.2	Site U1417	184
7.2.2.1	SST	184
7.2.2.2	$C_{37:4}$	184
7.2.2.3	TAR	184
7.2.2.4	TOC, TON, $\delta^{13}C$ and $\delta^{15}N$	185
7.2.2.5	Alkenone concentrations	185
7.3	Discussion	185
7.3.1	Site U1418	185
7.3.1.1	Glacial-Interglacial variability	185
7.3.1.2	Terrigenous organic matter	188
7.3.1.3	Marine productivity at U1418	189
7.3.1.4	Discussion last 500 kyr at Site U1418	192
7.3.2	Climate of the Gulf of Alaska during the last 500 kyr (Comparison between U1418 and U1417)	195
7.3.2.1	The last 200 Kyr in the GOA: High terrigenous and marine organic matter and isotopic excursions during late MIS 7 to MIS 5	199
7.3.2.1.1	MIS 6	199
7.3.2.1.2	MIS 5e	200

7.3.3 Climate of the subarctic Pacific Ocean during the last 500kyr	201
7.3.3.1 Climate drivers	201
7.3.3.2 Establishment of modern subarctic Pacific oceanography	204
7.3.3.3 Pacific and Atlantic teleconnections and implications for the climate of the GOA's climate during the last 500 Kyr	209
7.4 Future climate predictions in GOA based on the past reconstructions	210
7.5 Conclusion	210

Chapter 8: Conclusions and future work

8.1 Conclusions	213
8.1.1. RQ1: What is the magnitude and timing of surface ocean changes during the Pliocene and early Pleistocene, and what impact do they have on ice sheet development in the GOA? Chapter 5	213
8.1.2 RQ2: Did productivity change in the GOA during the Pliocene and early Pleistocene, and how does it relate to the timing of climate changes, terrestrial input into the ocean, and circulation changes? Chapter 6	214
8.1.3 RQ3: What is the response of the GOA to the glacial-interglacial cycles of the last 500 kyr? Chapter 7	215

Appendix	219
-----------------	-----

List of References	299
---------------------------	-----

List of Illustrations

Chapter 1: Introduction

Figure 1.1: Global climate cooling trough the Pliocene to present	30
Figure 1.2: Location of Gulf of Alaska IODP Expedition 341 drill sites	34
Figure 1.3: IODP Expedition 341 stratigraphic logs	34

Chapter 2: Research Background

Figure 2.1: GOA oceanic currents	37
Figure 2.2: North Pacific seasonal atmospheric and ocean circulation	38
Figure 2.3: GOAK 1 hydrographic data	39
Figure 2.4: Synthesis of Pacific climate dynamics and teleconnections	40
Figure 2.5: Positive and negative PDO and SST across the North Pacific	41
Figure 2.6: Atmospheric and ocean circulation during ENSO and NPGO	42
Figure 2.7: PDO, AO and NAO SLP from the N pole view	43
Figure 2.8: GOA atmosphere and ocean circulation	46
Figure 2.9: Surface temperature reconstruction for the past 65.5 Myr	52
Figure 2.10: Mean annual SSTs anomalies Pliocene localities with at 95% confidence	56
Figure 2.11: LR04 Stack compared with sea level, pCO ₂ and sand (%)	59
Figure 2.12: Pliocene-Pleistocene transition over the North Pacific and equatorial Pacific and Atlantic Oceans.	61
Figure 2.13: Freshening in the Bering Sea during a global increase in ice volume	62
Figure 2.14: CLIMAP (1981) SST reconstruction of the LGM annual SST	69
Figure 2.15: Location of DSDP Leg 18 and ODP Leg 145 Pacific drilling sites	71
Figure 2.16: Gulf of Alaska glaciation	71
Figure 2.17: Glacial Intervals in the development of the Surveyor Fan	73
Figure 2.18: Calibration of U ^K _{37'}	76

Chapter 3: Methods

Figure 3.1: Site U1417 Hole D	88
-------------------------------	----

Figure 3.2: Age/depth U1417 core break	89
Figure 3.3: U1417 $U^{K}_{37'}$ data and core break	89
Figure 3.4: Site U1417's shipboard age model	90
Figure 3.5: Site U1417 shipboard sedimentation rates	91
Figure 3.6: Site U1418's shipboard age model	96
Figure 3.7: Site U1418 shipboard sedimentation rates	97
Figure 3.8: Age/depth U1418 core break	98
Figure 3.9: $U^{K}_{37'}$ vs depth and U1418 core breaks	98
Figure 3.10: Schematic organic biomarker laboratory procedure conducted in this study	101
Figure 3.11: Alkenone integration peaks as seen through a GC-MS and GC-FID analysis	107
Figure 3.12: N-alkane samples from the Pliocene (~3 Ma)	108

Chapter 4: Results

Figure 4.1: Alkenone proxies for temperature and salinity	114
Figure 4.2: SST Calibrations Site U1417	117
Figure 4.3: Terrigenous and marine OM input to Site U1417	119
Figure 4.4: Terrigenous and marine OM normalised to sedimentation rates and organic carbon changes at Site U1417	121
Figure 4.5: Marine productivity export proxies at Site U1417	122
Figure 4.6: Marine productivity concentrations normalised to bulk accumulation rate or TOC content at Site U1417	124
Figure 4.7: Alkenone proxies for temperature and salinity at Site U1418	126
Figure 4.8: Terrigenous and marine OM input to Site U1418	127
Figure 4.9: Terrigenous and marine OM normalised to sedimentation rates and organic carbon changes at Site U1418	128
Figure 4.10: Marine productivity export proxies at Site U1418	130
Figure 4.11: Marine productivity concentrations normalised to bulk accumulation rate or TOC content at Site U1418	131

Chapter 5: Cordilleran Ice Sheet development with warm sea surface temperatures in the Gulf of Alaska

Figure 5.1: CO ₂ Plio-Pleistocene reconstructions	135
Figure 5.2: Site U1417 across the Pliocene-Pleistocene transition	140
Figure 5.3: Pliocene-Pleistocene SST across the North Pacific	150

Chapter 6: Land-ocean interactions during the Plio-Pleistocene Cordilleran Ice Sheet growth.

Figure 6.1: Terrigenous and marine organic matter proxies	164
Figure 6.2: Sterol, alkenone and diatom concentrations	165
Figure 6.3: Relationship between terrigenous and marine proxies	167
Figure 6.4: Summary figure	172
Figure 6.5: Isotopic excursions during the PPT	175

Chapter 7: Late Pleistocene ocean circulation changes in the North-east Pacific

Figure 7.1: Glacial-interglacial changes at Site U1418	187
Figure 7.2: Glacial-interglacial cycles and terrigenous and marine OM changes	187
Figure 7.3: Terrigenous and aquatic organic matter source	190
Figure 7.4: Marine productivity export proxies	191
Figure 7.5: Main patterns Site U1418	194
Figure 7.6: Site U1418 and U1418 SST and C _{37:4} comparisons	197
Figure 7.7: Site U1418 and U1417 comparison during the last 500 ka	198
Figure 7.8: Comparison between the SST average values of interglacials represented in Table 7.1	201
Figure 7.9: July insolation at 65 °N compared to U1418 main patterns	208

List of Tables

Chapter 3: Methods

Table 3.1 Polarity Zone interpretation for U1417	91
Table 3.2: Site U1417 sample ID, age range, average, minimum and maximum sedimentation rates (Jaeger et al., 2014) and temporal resolution (kyr)	93
Table 3.3: Polarity Zone interpretation Site U1418	97
Table 3.4: Site U1418 sample ID, age range, average, minimum and maximum sedimentation rates (Jaeger et al., 2014) and temporal resolution (kyr)	99
Table 3.5: Standard details for C and N analyses	109
Table 3.6: U1417 age-depth conversion table	111
Table 3.7: U1418 age-depth conversion table	111

Chapter 5: Cordilleran Ice Sheet development with warm sea surface temperatures in the Gulf of Alaska

Table 5.1: Average SST (°C) and %C _{37:4}	138
--	-----

Chapter 7: Late Pleistocene ocean circulation changes in the North-east Pacific

Table 7.1: Maximum SST for each interglacial at different cores from the North Pacific Ocean	201
--	-----

Appendix

A.1: Alkenone derived SST, %C _{37:4} and alkenone abundances, Site U1417	219
A.2: Alkenone derived SST, %C _{37:4} and alkenone abundances, Site U1418	246
A.3: N-alkane derived data, Site U1417	253
A.4: N-alkane derived data, Site U1418	262
A.5: C and N derived data, Site U1417	266
A.6: C and N derived data, Site U1418	275
A.7: Sterol derived data, Site U1417	278
A.8: Sterol derived data, Site U1418	283

List of Equations

Chapter 2: Research Background

Equation 2.1: $U^{K_{37}}$	75
Equation 2.2: $U^{K_{37}'}$	75
Equation 2.3: $U^{K_{37}'}$ calibration (Müller <i>et al.</i> , 1998)	76
Equation 2.4: $U^{K_{37}'}$ calibration (Sikes <i>et al.</i> , 1997)	76
Equation 2.5: $U^{K_{37}'}$ calibration (Sikes and Volkman, 1993)	76
Equation 2.6: TAR	82

Chapter 3: Methods

Equation 3.1: $Mass_{\text{biomarker}}$	107
Equation 3.2: Biomarker ($\mu\text{g g}^{-1}$)	107
Equation 3.3: Bulk MAR	108
Equation 3.4: Biomarker MAR	108
Equation 3.5: Biomarker ($\mu\text{g g}^{-1} \text{TOC}^{-1}$)	108
Equation 3.6: Ca CO_3 dissolution	110

List of Abbreviations

AC: Alaska Current

ACC: Alaska Coastal Current

AL: Aleutian Low

AMOC: Atlantic Meridional Ocean Circulation

AO: Arctic Oscillation

AS: Alaska Stream

CAS: Central American seaways

DSDP: Deep Sea Drilling Project

ENSO: El Niño Southern Oscillation

GOA: Gulf of Alaska

HNLC: High Nutrient Low Chlorophyll

iNHG: intensification of the North Hemisphere glaciation

IODP: International Ocean Drilling Program

IRD: Ice rafted debris

LGM: last glacial maximum

LNHC: low nutrient high chlorophyll

MAR: mass accumulation rates

MIS: marine isotopic stage

MPWP: Mid Pliocene Warm Period

NAO: North Atlantic Oscillation

NHG: North Hemisphere Glaciation

NPGO: North Pacific Gyre Oscillation

NPO: North Pacific Oscillation

ODP: Ocean Drilling Program

OM: Organic matter

oNHG: Onset of the North Hemisphere glaciation

PDO: Pacific Decadal Oscillation

PPT: Plio-Pleistocene transition

SLP: Sea Level Pressure

SST: Sea surface temperatures

TAR: terrigenous vs. aquatic n-alkane ratio

TOC: total organic carbon

TON: total organic nitrogen

Declaration

I declare that the material contained in this PhD thesis has not been previously submitted for a degree in this or any other institution.

This thesis is based on a joint research from IODP Expedition 341 and includes diatom counts from Dr. Oscar Romero (MARUM, Bremen, Germany), ice rafted debris (IRD) counts from Dr. Ellen Cowan (Appalachian State University, North Carolina, U.S) and $\delta^{18}\text{O}$ from surface dwelling foraminifera *Neogloboquadrina Pachyderma* (sinistral) from Dr. Hirofumi Asahi (Korea Polar Research Institute, Seoul, South Korea). 20 alkenone samples for Site U1417 during the last 0.5 Ma has been shared by Dr. Juliane Muller (AWI, Bremerhaven, Germany): Core U1417C 4H3-35; 4H4-142; 5H3-93; 5H5-42; 6H3-16; 7H2-145; 7H6-46; 8H3-99; 8H5-48; 8H7-46; Core U1417D 3H3-38; 3H6-38; 4H2-76; 4H3-28; 4H4-78; 5H4-17; 6H3-128; 7H3-116; 9H2-46; 9H4-2.

Copyright

The copyright of this thesis rests with the author. No quotation from it should be published without the author's prior written consent and information derived from it should be acknowledged.

Acknowledgements

I am very thankful to my PhD supervisors Erin L. McClymont and Jeremy M. Lloyd for their work and commitment with me and this project. Extended thanks to Erin and the opportunity to get involved in many biomarker projects during the last stages of this PhD.

I would like to thank IODP funding the collection of the samples analysed in this thesis and the hard work during long shifts of the IODP Expedition 341 science party. I also would like to thank Van Mildert College and Durham Doctoral Scholarship that funded this PhD project at Durham. I also thank very much the UK-IODP, Matariki network of universities and IAPETUS for offering support to attend to conferences and research visits where I could expand and share my work. I would like to thank Chris Moy and Christina Riesselman for the chance of collaborative work in the Geology Department in Otago University. I thank the many researches that I met in conferences for their comments that helped shaping this work.

I am very grateful to all the Geography Department laboratory lab staff who created an amazingly happy and supportive environment and were very helpful solving the problems that I encounter during my lab-work. I am very thankful to Jess Frankling for teaching me the biomarker extraction method, to Juliane Müller who taught me about the world of biomarkers at the start of this work and to Paul Bachem and all researches that visited our laboratories for great biomarker and climate discussions. I would like to thank to all the events organised in the Geography that boosted my interest and motivation to keep going through this project. I would also like to thank the department for teaching opportunities and learning new skills while being a PhD student. I thank the Geography department staff and PhD students for all the discussions about science and non-science and to my office mates who created a friendly and hard working environment.

Thanks to all my friends in Durham and so many people that crossed Durham at some point and were a great encounter in life, the Durham dancing community and the piano at Appleby Theatre. Especial thanks for the extraordinary Maialen

Arrieta, Saavidra Perera and Omar F. Sosa Rodriguez. I would also like to thank old friends from Bilbao, Salamanca University, Uppsala University, Sheffield University and Otago University who have been supporting me through this thesis from different parts of the world.

I am very grateful to my parents Maria Luisa Montes Alvaro and Gregorio Sanchez Cuaresma for fostering my curiosity since childhood and providing me with the base of many of skills I have today. Thanks for all the support and commitment to my education. I am also very grateful to Gregorio Sanchez Montes for many discussions. My thanks go also to my extended family, in particular my cousins.

I would like to thank many people around the world who fight for equal opportunities for all. Especial thanks for people who make academia a more diverse, gender equal and a family friendly environment.

To my mother,

Chapter 1: Introduction

1.1. Rationale Overview

Since the Pliocene (5.3 to 2.6 Ma), global climate history is characterised by the transition into a colder world (Figure 1.1), dominated by the onset and intensification of major Northern Hemisphere glaciations which have changed in their duration and intensity. It has been argued that cooling in the surface ocean could be considered one of the driving mechanisms behind increased extent of continental ice sheets (i.e. McClymont *et al.*, 2013). Alternative proposals consider the influences of progressive sub-glacial erosion and feedbacks to explain changing ice-sheet extent and dynamics and/or the potential regional climate impacts of tectonic uplift (Enkelmann *et al.*, 2015) both of which may occur independently of climate change. At present, isolating climate as the driver of evolving continental ice volume since the Pliocene is hindered by the limited long term data sets which directly link climate changes to evidence for ice-sheet advance/retreat, erosion, and tectonic evolution over million year timescales. Data constraining glacial-interglacial cycles from the northeast Pacific is also lacking in comparison to the North Atlantic despite its proximity to the major ice sheets of North America (Otto-Bliesner *et al.*, 2005; Past Interglacials Working Group of PAGES, 2015).

In understanding the global climate history there is a general dominance of research from the North Atlantic region. The role of the North Pacific in the carbon cycle, for instance, remains under explored. It has been suggested that iron limits the marine productivity in the subarctic Pacific at the present day (Martin and Fitzwater, 1988; Martin *et al.*, 1991) but whether this theory holds for the Pliocene is unclear. It is unknown if the east subarctic Pacific was a high productivity region before the Cordilleran Ice Sheet developed (NHG), as it has been recorded in the west (Haug *et al.*, 2005). A detailed understanding of the main controls on marine productivity before the development of modern marine conditions is also lacking. The study of marine productivity could help in the understanding of the role of ocean changes in the North Pacific and its possible influence on the Cordilleran Ice Sheet and the broader development of NHG. Marine productivity and its impact on

past atmospheric CO₂ are important for understanding present day climate change and the impacts of this on future climate.

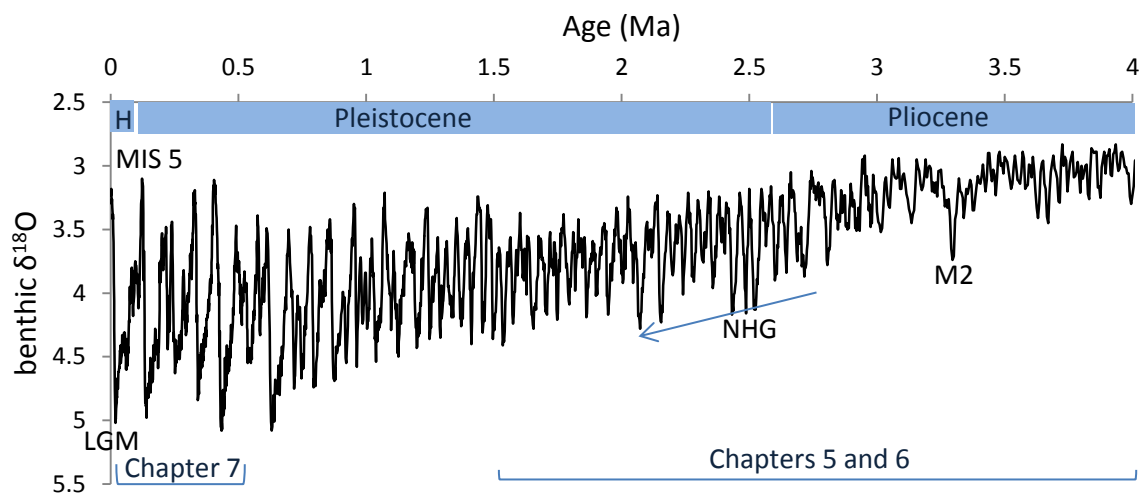


Figure 1.1: Global climate cooling through the Pliocene to present. The global benthic $\delta^{18}\text{O}$ stack, “LR04” (Lisiecki and Raymo, 2005) which represents the global ice volume trend from the Pliocene until the present. Higher $\delta^{18}\text{O}$ values indicate increased global ice volume and colder climate. Annotations of some key climatic events: the cool M2, onset and intensification of the North Hemisphere Glaciation (NHG), the warm interglacial MIS 5 and the Last Glacial Maximum (LGM). The Chapters of this thesis that study specific time periods are also shown, as well as the main geological epochs involved with each Chapter (Pliocene, Pleistocene and Holocene, indicated with a H).

1.2.Aim

The overall aim of this PhD is to assess the ice sheet-ocean-climate interactions in the Gulf of Alaska (GOA) over the last 4 million years (Ma). These interactions are important to study the characteristics of climate settings that allow the development of an ice sheet and how the development of the ice sheet can affect climate and marine environments. Newly recovered marine sediment cores from IODP Expedition 341 in the Gulf of Alaska are analysed. The core sites U1417 and U1418 lie close to the north-western Cordilleran ice sheet, whose evolution is not well understood through the Pliocene and Pleistocene (Jaeger *et al.*, 2011). This research will focus on three time windows of climate change: (1) the Pliocene, a climate state considered to be warmer than present and that precedes the major expansion of the northern hemisphere ice sheets, (2) the Pliocene-Pleistocene

Transition (PPT) during which northern hemisphere ice sheets are argued to have expanded, and (3) the last 500,000 years (ka) when large and pronounced glacial-interglacial cycles mark the global climate record (Lisiecki and Raymo, 2005) (Figure 1.1).

1.3. Research Questions and objectives

In order to meet the above aim, this thesis will focus on 3 main research questions (RQ) that constitute its three main discussion chapters (Chapters 5-7):

RQ1: What is the magnitude and timing of surface ocean changes during the Pliocene and early Pleistocene, and what impact do they have on ice sheet development in the GOA? *Chapter 5*

Objective 1.1: To reconstruct site U1417 sea surface temperatures (SST) and sea surface salinity (SSS) during the period from 4 to 1.5 million years ago (Ma).

Objective 1.2: To compare surface ocean changes from Ob 1.1 to a proxy for ice sheet development (Ice Rafted Debris, IRD) to investigate potential links between the Northeast Pacific Ocean and the Cordilleran ice sheet.

This study has important implications. The warm Pliocene has been proposed as an analogue for future climate scenarios (Hansen *et al.*, 2006). However, our understanding of the North Pacific Ocean from this period of time is lacking (LaRiviere *et al.*, 2012). The Pliocene-Pleistocene transition is the shift towards a world with extensive northern hemisphere glaciation with cycles of major mid and high latitude ice-sheets, as we see periodically in the recent past (last 500 kyr).

RQ2: Did productivity change in the GOA during the Pliocene and early Pleistocene, and how does it relate to the timing of climate changes, terrestrial input into the ocean, and circulation changes? *Chapter 6.*

Objective 2.1: To reconstruct site U1417 organic matter provenance (e.g. marine vs terrestrial source) between 4 to 1.5 Ma.

Objective 2.2: To reconstruct Site U1417 mass accumulation rates of marine phytoplankton.

Objective 2.3: To compare this new reconstruction of organic matter inputs to the sediments with diatom evidence for changing productivity.

It is thought that the North Pacific could act as a major carbon storage basin during glacials (Galbraith *et al.*, 2007). This study would help provide a longer term perspective by assessing relative carbon storage in North Pacific sediments before and after the NHG. A study from the northwest subarctic Pacific (Haug *et al.*, 2005) shows a dramatic decrease in marine productivity after the NHG. It has been suggested that the role of North Atlantic deep water was an important factor for worldwide marine productivity and atmospheric CO₂ decrease during the Pliocene-Pleistocene transition (Lawrence *et al.*, 2013).

RQ3: What is the response of the GOA to the glacial-interglacial cycles of the last 500 kyr?

Objective 3.1: To reconstruct site U1418 and U1417 sea surface temperatures (SST) and sea surface salinity (SSS) during the last 500 kyr.

Objective 3.2: To reconstruct site U1418 and U1417 organic matter provenance during the last 500 kyr.

Objective 3.3: To compare results from Objective 3.1 and 3.2 with IRD data for site U1417 during the last 500 kyr and oxygen isotopes for glacial-interglacial cycle timing for both sites during the last 500 kyr.

By studying the last glacial-interglacial cycles we can assess the ice-ocean-climate interactions that regulate the growing and decaying of ice-sheets. The knowledge of glacial-interglacial cycles for the North Pacific Ocean is limited to only a few data sets (Past Interglacials Working Group of PAGES, 2015), yet the region is important as a potential source region for the moisture which is provided to the larger north America ice sheets (Haug *et al.*, 2005).

Previous research in the GOA has indicated that the first appearance of tidewater glaciation related to the Cordilleran Ice Sheet occurred at 3.5 Ma (Krissek *et al.*, 1995), but we lack detailed reconstructions of ice sheet history and the oceanographic changes which may be related to these is poorly understood. The methods to be used in this thesis will focus on reconstructing SSTs, marine and

terrestrial organic matter inputs and productivity export from biomarkers, using marine sediments recovered by Integrated Ocean Drilling Program (IODP) Expedition 341. Complementary data from other members of the IODP Expedition 341 science party is also presented, including ice rafted debris (IRD) analysis for iceberg/sea-ice presence (by Dr. Ellen Cowan, Appalachian State University, North Carolina, U.S.), oxygen isotopes of surface dwelling foraminifera *Neogloboquadrina pachyderma* (sinistral) for glacial-interglacial timing (by Dr. Hirofumi Asahi, Korea Polar Research Institute, Seoul, South Korea) and diatom counts for diatom productivity export (by Dr. Oscar Romero, MARUM, Bremen, Germany). Organic nitrogen and carbon bulk and isotope studies were carried out in partnership with Dr. Christopher Moy, Otago University, Dunedin, New Zealand. The combined results will allow us to understand the regional relationship between ocean-ice sheets-climate in the North Pacific Ocean and make comparisons to global climatic events.

1.4 IODP Expedition 341

The IODP Expedition 341 (May-July 2013) drilled a cross-margin transect from ice-proximal sites on the continental shelf to distal sites in the deep Pacific (Figure 1.2). This study focuses on the most distal site, (Site U1417, 56° 57' N 147° 6.5' W c. 4190 m water depth) which extends through the Pleistocene, Pliocene and Miocene with average sedimentation rates of 8 cm Kyr⁻¹ for the Pliocene and Early Pleistocene and 13cm cm Kyr⁻¹ for the last 1 Myr. Our second site of interest, Site U1418, lies closer to shore (58°46' N 144° 29.5' W, c. 4218m water depth) with a sedimentation rate averaging 80 cm cm Kyr⁻¹ throughout the sediment sequence (Figure 1.3). Preliminary shipboard analyses indicate that a rich history of climate change, glaciation and tectonics has been recorded, including variable biogenic and terrigenous contributions, and evidence for deposition through pelagic, mass movement and glacial processes (Expedition 341 Scientists, 2014). The analyses undertaken for this thesis will focus on generating a detailed understanding of the interaction between Northeast Pacific palaeoceanography and the history of the north-west Cordilleran Ice Sheet, neither of which are fully understood given limited data which pre-dates the Last Glacial Maximum (LGM).

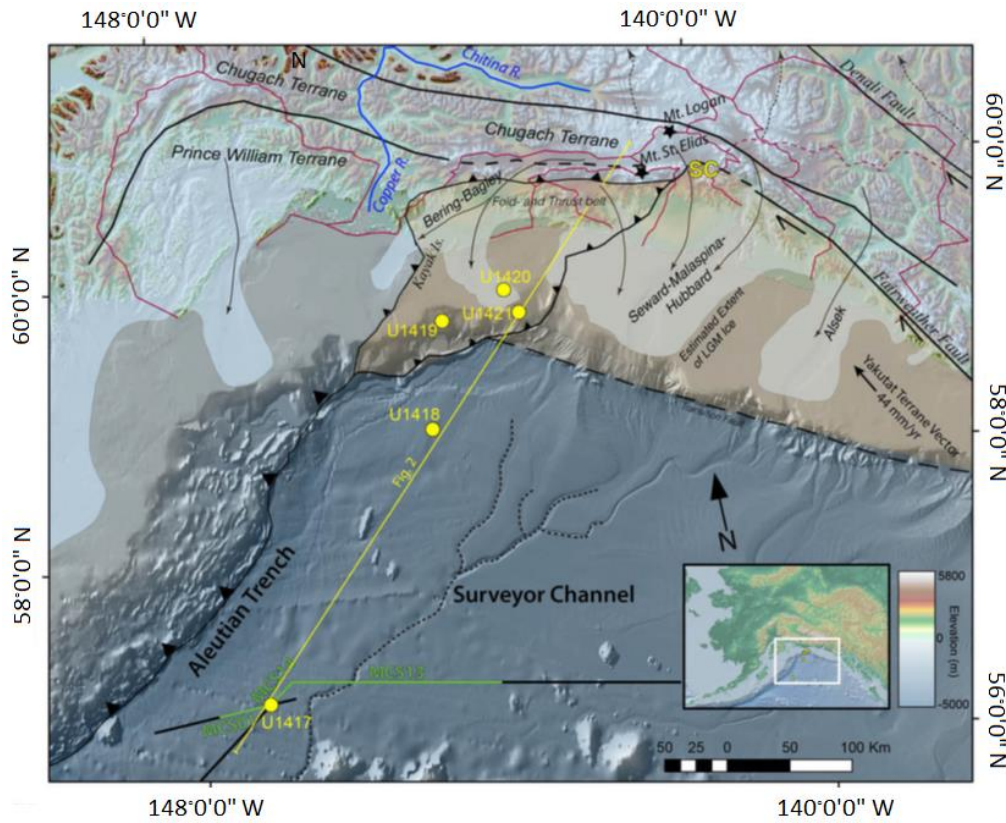


Figure 1.2: Location of Gulf of Alaska IODP Expedition 341 drill sites. Location of Site U1417 to U1421 overlaid on a physical and tectonic map of the Gulf of Alaska (Gulick et al., 2015). Site U1417 and U1418 will be the focus of this study.

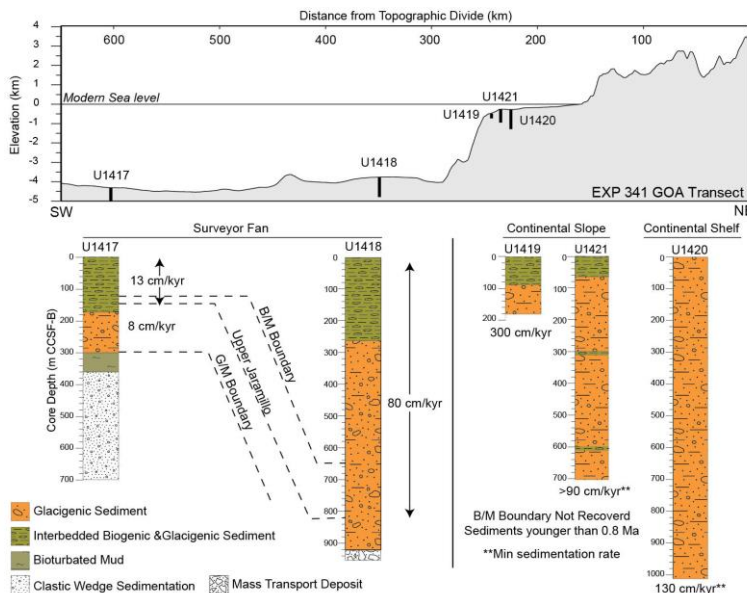


Figure 1.3: IODP Expedition 341 stratigraphic logs. Major lithofacies, location, resolution and shipboard age models according to magnetostratigraphy (Gulick et al., 2015). Site U1417 is the focus of thesis Chapters 5 and 6 and Site U1418 is the focus of thesis Chapter 7.

Chapter 2: Research Background

2.1 The Gulf of Alaska (GOA) at present

The Gulf of Alaska is the sea located in the Northeast Pacific Ocean, from 50° to 60°N and 130° to 170° W. It extends from the Alaska Peninsula in the west to the Alexander Archipelago in the east (Hogan, 2013) and it is delimited by the Bering Sea on the west and the Alaska coast in the north and east, which is, in turn, bounded to the north by the Pacific Mountain System (Molnia, 2008) (Figure 2.1a). The highest peaks of the Pacific Mountain System are Mt. McKinley, Mt. St. Elias and Mt Logan in Canada, of 6,195, 5,489 and 5745 m height respectively (Molnia, 2008). Glaciers cover 20% of the Gulf of Alaska watershed (Spies, 2007). The major rivers draining the St. Elias and Chugach mountains towards the GOA are the Alsek River and the Copper River, fed by glacier discharge which is maximum in August (Figure 2.3b) (Weingartner, 2007). The fluvial discharge into the Gulf of Alaska exceeds 40 % of the discharge of the Mississippi River, and the discharge per unit of area (or yield) is higher than the great equatorial watersheds such as the Amazon River (Spies, 2007). The GOA mean annual freshwater discharge derives from high precipitation, runoff and snow melt from Prince William Sound streams and other river discharges along the SE Alaskan coast (Spies, 2007). High precipitation is due in part to the proximity of the North Pacific Ocean which is a source of moisture, and the high topography of the Pacific Mountain System driving orographic precipitation. Freshwater discharge into the GOA is important because it affects the water column regime by driving density gradients (Spies, 2007). However, wind stress can modify these density gradients through mixing and advection of waters from other locations (Spies, 2007). In the following sections, the main ocean and atmospheric circulation systems of the GOA will be outlined, including their links to wider climate teleconnections.

2.1.1 Ocean and atmospheric circulation

The GOA ocean circulation at present is dominated by the Alaska Gyre which controls the strength and behaviour of the Alaska Current (AC) (Figure 2.1a). The AC flows from offshore of the Alexander Archipelago (SE GOA) to the Kodiak Island

with a northwest component, from where it converts into the Alaskan Stream when exiting the Gulf of Alaska (Figure 2.1a), before flowing towards the Chukchi Sea through the Bering Sea (Kato *et al.*, 2016). The Alaskan Coastal Current (ACC) flows along the GOA coastline and flows westward to the Bering Sea (Figure 1a). The properties of the ACC are characterised by the nutrient and meltwater supply from the coastal Alaskan glaciers. During the 21st century, the ACC has freshened due to enhanced glacial melting rates and increased inland precipitation (Chan *et al.*, 2011). From the start of the melting season (May) and during the rainy season (September to November) (Royer, 1981a, 1982), the AS and the ACC can be easily identified in the Gulf of Alaska (Figure 1b).

The Alaskan Gyre and the western subarctic gyre form the subarctic gyre system of the North Pacific Ocean (Yamamoto and Kobayashi, 2016), which is influenced by atmospheric circulation via the Aleutian Low (AL) and the Pacific High Pressure Systems, which are coupled in an annual cycle: high pressures dominate during the summer season and low pressures dominate during autumn to spring (Hogan, 2013). Over the annual cycle, the AL migrates from the west to the east North Pacific Ocean, and is most intense when it is located in the GOA during winter (Pickart *et al.*, 2009). The AL creates a storm front that travels with it, and the coast of Alaska receives high winter precipitation because of the AL winter position and strength, (Rodinov *et al.*, 2007) but also due to Alaska's high topography which drives orographic precipitation. The GOA can locally receive an annual precipitation of ~800 cm (Powell and Molnia, 1989). During summer, the AL is less intense and almost disappears when it is located in the Bering Sea. A weaker AL is translated into a reduced precipitation over the GOA.

A strong winter AL creates a strong zonal SST gradient in the North Pacific Ocean (Figure 2.2) which is translated into more intense oceanic currents. When the AL is more intense during winter, the ocean responds through southward movement of the cold Arctic waters, and the mid-latitude warm waters sourced in the Kuroshio Current (offshore Japan) flow towards the east through the North Pacific Current and then northwards to the Gulf of Alaska through the AC in a cyclonic anti-clockwise direction. The strong winds associated with the winter AL conditions enhance ocean mixing and lead to a small temperature and salinity gradient

between the surface and subsurface ocean. During summer migration of the AL northwards, the GOA registers higher SSTs due to higher insolation on the North Pacific Ocean, and as the zonal SST gradient is reduced, the storms diminish and the water column stratifies (Pickart *et al.*, 2009).

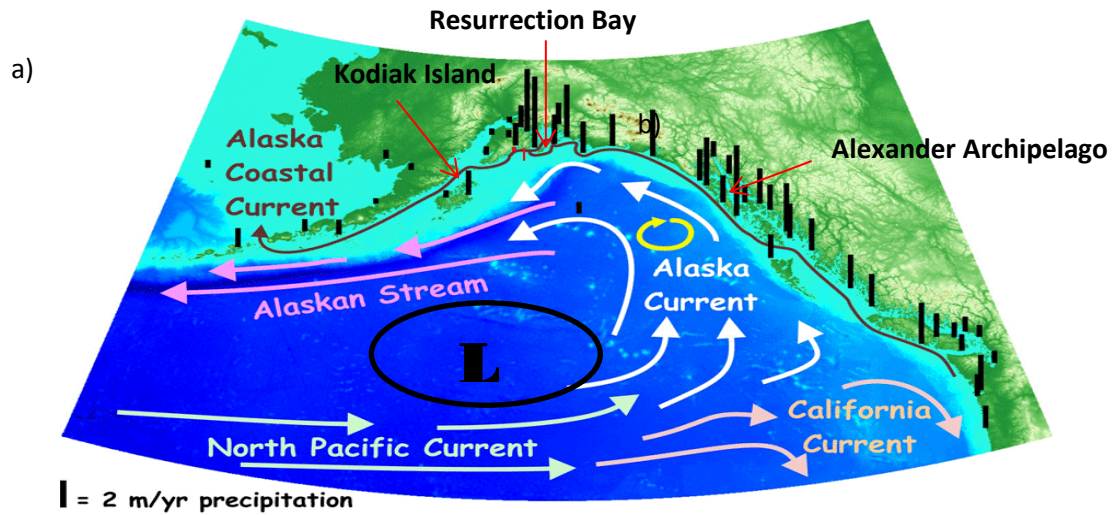


Figure 2.1: GOA oceanic currents. (a) Modern ocean circulation in the Gulf of Alaska and annual precipitation rates (Weingartner *et al.*, 2016) and (b) boundary between coastal waters influenced by glacial weathering (light blue) and offshore waters of the Gulf of Alaska (darker blue). Photograph by Ken Bruland (Schroth and Crusius, 2008).

between the surface and subsurface ocean. During summer migration of the AL northwards, the GOA registers higher SSTs due to higher insolation on the North Pacific Ocean, and as the zonal SST gradient is reduced, the storms diminish and the water column stratifies (Pickart *et al.*, 2009).

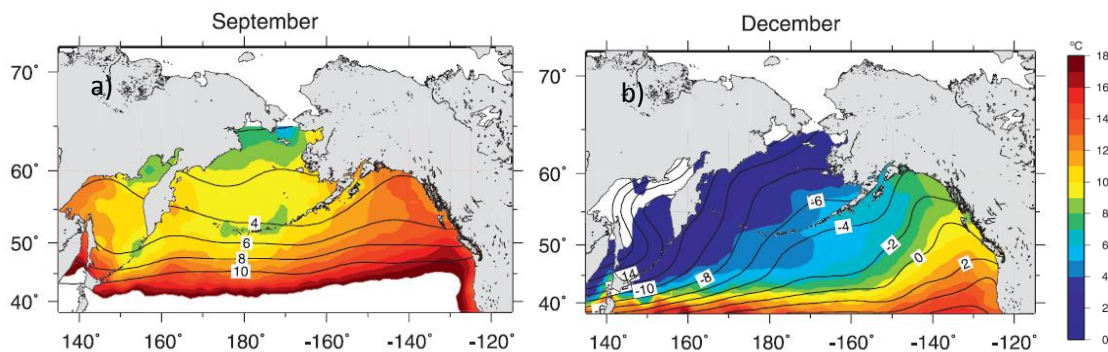


Figure 2.2: North Pacific seasonal atmospheric and ocean circulation. Monthly average SST (colour) from AVRR and 850-mb air temperature (contours) from NCEP for fall 2002 (Pickart et al., 2009).

Current GOA temperature and salinity data taken from the hydrographic station GAK 1 offshore Resurrection Bay (Figure 2.3) shows the ACC annual cycle. Temperatures through the water column are higher during August to October and lower during February to April (Figure 2.3a), and salinities are highest in April and freshest in August (Figure 2.3b) (Weingartner, 2007). Surface waters are the most variable of the water column with SST oscillations of up to 10°C over an annual cycle, and salinity oscillations of 3 psu (Figure 2.3b). The warmest months are late summer (August-September) followed by lower salinities during early fall (October-November), associated with increased glacier meltwater. In contrast, deep water properties at 250 m below the water surface (bottom of the permanent halocline) only vary by 1 °C and 1 salinity unit over an annual cycle (Figure 2.3). During winter, the strong winds enhance ocean mixing and downwelling and the temperature and salinity gradients through the water column are minimal (Figure 2.3b) (Weingartner, 2007). Most of the sea ice in the GOA is formed by the freezing of snow accumulated in the sea surface near fjords during winter (Powell and Molnia, 1989). This process of freezing rejects the seawater salts (“brine rejection”), increasing the salinity of the surface water below the sea ice, which may lead to sinking due to increased density, further enhancing the water column mixing. During summer, downwelling is weak and salinity increases at low water depths. The warm SSTs enhance glacier melting and lead to enhanced cold, fresh melt-water discharge into the GOA, which enhances water column stratification (Powell and Molnia, 1989). The overall low salinity of the North Pacific Ocean is

explained by the low evaporation/high precipitation relationship and the low mixing between the salty subtropical gyre waters and the fresher subpolar gyre systems (Emile-Geay *et al.*, 2003; Stommel, 1961). Humidity is delivered to the subpolar gyre from low latitudes and the East Asian monsoon (Emile-Geay *et al.*, 2003).

The GOA has a CO₂ sink into the deep ocean of 34 and 14 Tg C yr⁻¹ annual mean in the coastal ocean and the continental margin, respectively (Evans and Mathis, 2013). CO₂ sink in the GOA occurs specially in the spring and autumn seasons along the coastal margin, as the surface ocean is under-saturated in CO₂ compared to the atmosphere during these months, and the strong winds help to ventilate the ocean (Evans and Mathis, 2013). The North Pacific ventilation is optimum reaching the intermediate waters (~300-800 m) (Talley, 1993) and the modern surface to deep age difference is ~350 ¹⁴C years as waters from the Southern Ocean and the North Atlantic decrease their density, upwell and travel southward at the mid-depths of the Pacific (Rae *et al.*, 2014). It has been hypothesised that the surface North Pacific could be a source of CO₂ instead of a site of deep ocean carbon storage (Ronge, *et al.*, 2016). The deep North Pacific Ocean is proposed to be a large store of CO₂ during glacial stages, due to enhanced water column stratification (Galbraith *et al.*, 2007).

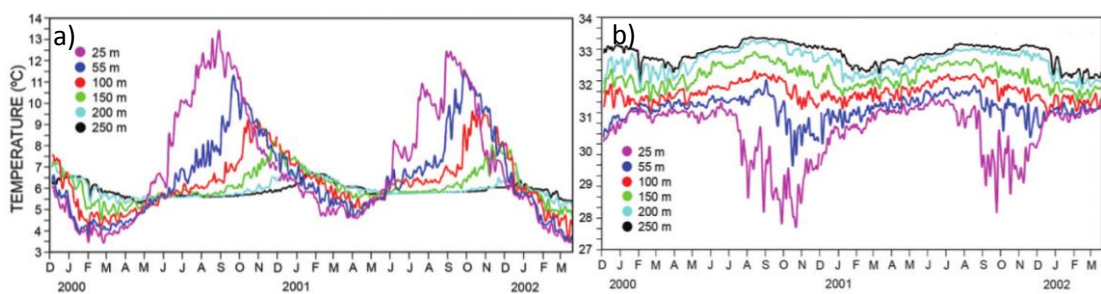


Figure 2.3: GOAK 1 hydrographic data. 2.5 year record of hourly a) temperature and b) salinity profiles through the water column collected at the hydrographic station GAK 1 at the Resurrection Bay offshore of Seward, Gulf of Alaska (Weingartner, 2007).

2.1.2 Regional teleconnections

The GOA shares longer-term climatic signals (i.e. inter-annual and decadal) with other parts of the world, such as the North Atlantic Ocean (Hogan, 2013) or the tropics (Figure 2.4). The AL and North Pacific Oscillation (NPO) mode are

connected to the tropical climatic variability by the El Niño Southern Oscillation (ENSO) (Figure 2.6) and to the North Atlantic circulation by the Arctic Oscillation (AO) and the North Atlantic Oscillation (NAO) (Figure 2.4) (Yamamoto *and Kobayashi*, 2016). It has been suggested that on millennial timescales, comparable teleconnections can account for similarities in the climate events recorded across different basins (i.e. Ravelo *et al.*, 2007).

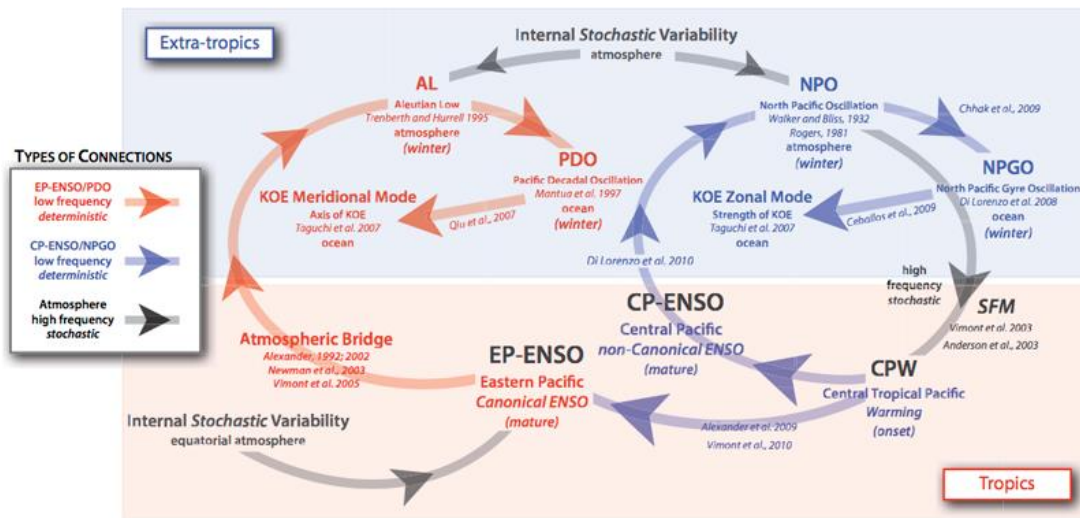


Figure 2.4: Synthesis of Pacific climate dynamics and teleconnections. The PDO (red path) and North Pacific Gyre Oscillation (NPGO) (blue path) outline teleconnections at low-frequency (decadal) time scales. The grey path shows sources of high-frequency stochastic variability in the atmosphere energize the AL, NPO and ENSO systems. In the schematic, the North Pacific Oscillation (NPO) low-frequency variability is linked to the Central Pacific (CP)-El Niño, however, processes internal to the North Pacific atmosphere appear to drive its high-frequency variability (grey path) (Di Lorenzo *et al.*, 2011).

2.1.2.1 PDO

The AL is not only an important factor for the GOA climate but is also tightly linked to the overall North Hemisphere climate due to its influence in the Pacific Decadal Oscillation (PDO) and the North Pacific Gyre Oscillation (NPGO). The PDO and NPGO describe the two leading modes of the North Pacific SST and Sea Level Pressure (SLP) records, which act on decadal time scales. The PDO and the NPGO are the oceanic expressions of the AL and the North Pacific Oscillation (NPO), respectively (Di Lorenzo *et al.*, 2008).

The PDO is the leading mode of the North Pacific SST anomalies and has a periodicity of 20-30 years (Figure 2.5) (Furtado *et al.*, 2011). The positive (negative) phase of the PDO is characterized by negative (positive) SST anomalies in the central North Pacific and surrounded by positive (negative) SSTs along the North American coast and positive (negative) SSTs in the east equatorial Pacific. The surface wind stress reverses from the positive phase (cyclonic) to the negative phase (anticyclonic). During the 1980s, it was observed that a positive PDO and the intensification of the AL triggered a more intense phytoplankton bloom associated with an intensification of the Alaska Gyre, upwelling, and subsequently the enrichment of surface waters in nutrients (Harwell *et al.*, 2010).

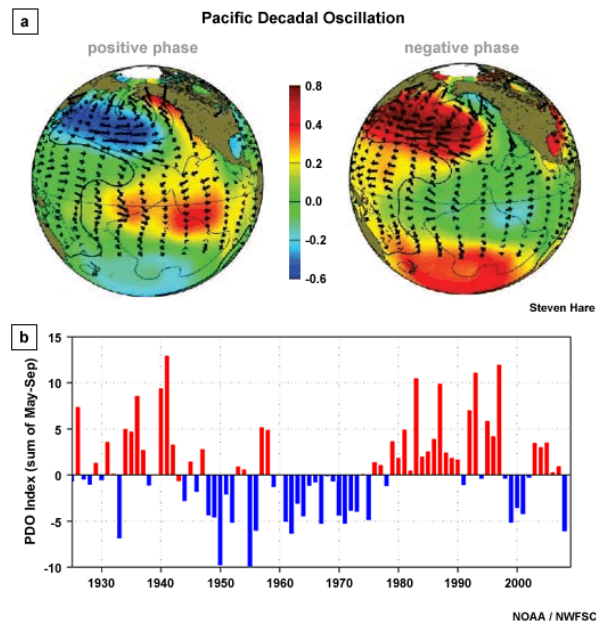


Figure 2.5: Positive and negative PDO and SST across the North Pacific. (a) Wintertime SST (colours), SLP (curves) and surface wind stress (arrows); (b) monthly PDO index from 1925 to 2006 (Lead and Evans, 2011).

The NPGO is the second leading mode of the northeast Pacific sea surface height anomalies (Di Lorenzo *et al.*, 2008; Furtado *et al.*, 2011). The NPGO is associated with changes in the Kuroshio-Oyashio Extension current (Furtado *et al.*, 2011). The SLP from 55 °N 155 °W and 65 °N 170 °E is characterised by a positive correlation from eastern Alaska and western Canada and negative correlations in the Hawaiian latitudes and Japan (Linkin and Nigam, 2008). The NPGO pattern is characterized

by changes in the strength of the sub-tropical and subpolar gyres in the North Pacific which derives to decadal changes in salinity and nutrients in the central and eastern North Pacific (Di Lorenzo *et al.*, 2009).

2.1.2.2 ENSO

ENSO describes a shift in SST anomalies in the equatorial Pacific. During a positive/negative phase or El Niño/La Niña, weaker/stronger winds and warmer/colder equatorial east Pacific results in higher/lower precipitation in the east Pacific compared to the west Pacific. Despite ENSO's characteristic variability of 2-7 years, an ENSO phase can be more predominant during a certain period. Over millennial timescales, the climate in the Pacific can be predominantly El Niño or La Niña-like. This occurs when one of the ENSO phases is evident in SST over the Pacific or through global ENSO teleconnections (i.e. during the Pliocene (Ravelo *et al.*, 2007). In addition, tropical and high latitude climatic modes are tightly linked i.e. ENSO drives the PDO and is strongly linked to the trade winds (Newman *et al.*, 2003). According to climatic models (Furtado *et al.*, 2011), during El Niño phases, the AL shifts towards the GOA and the SSTs in GOA become slightly positive. Under

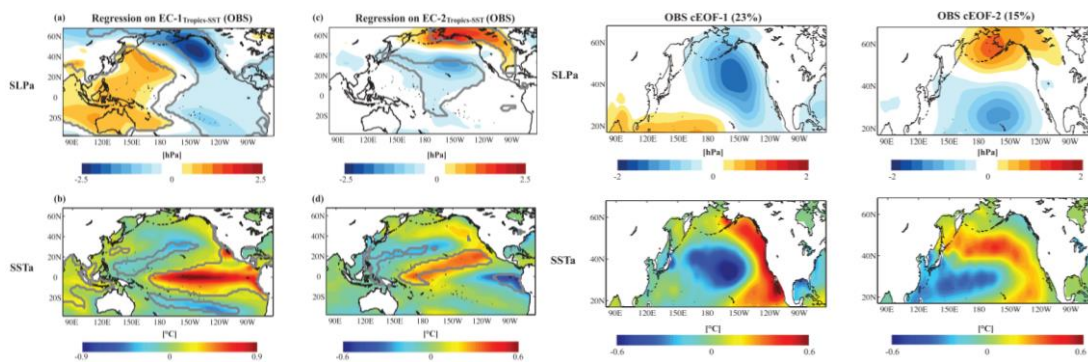


Figure 2.6: Atmospheric and ocean circulation during ENSO and NPGO. (Left) Regression of the observed DJF monthly expansion coefficient time series associated with the leading (1) and second leading (2) mode of variability of the tropical Pacific boreal winter SLPa (top) and SSTa (bottom) and (right) the spatial representation of the leading (1) and second leading (2) mode of variability of North Pacific boreal winter SLPa (top) SSTa (bottom) from observations. Percent covariance explained by the mode in the title (Furtado *et al.*, 2011).

La Niña conditions, the AL shifts towards the central North Pacific and the SST in GOA show a stronger positive anomaly. During El Niño Modoki (when tropical

convection shifts to the central Pacific), the AL is weaker and shifts towards the south of the central North Pacific Ocean, which warms the SSTs of most parts of the North Pacific but the coastal SST of GOA experience slightly negative anomalies (Furtado *et al.*, 2011) (Figure 2.6).

2.1.2.3 The Arctic Oscillation and North Atlantic Oscillation

The Arctic Oscillation (AO) and the North Atlantic Oscillation (NAO) describe changes in pressure systems that result in temperature and storm track changes in the Arctic and North Atlantic regions, respectively. A positive AO phase is characterized by a negative Geopotential Height anomaly associated with a strong polar vortex. This also intensifies the westerly winds, so that the cold air is limited to Scandinavian latitudes. During the negative phase, there is a weaker polar vortex due to the positive anomaly of Geopotential Heights. Westerly winds are also weaker which is translated into a more southerly influence of the polar air which brings storm tracks to the Mediterranean latitudes (Hill *et al.*, 2011).

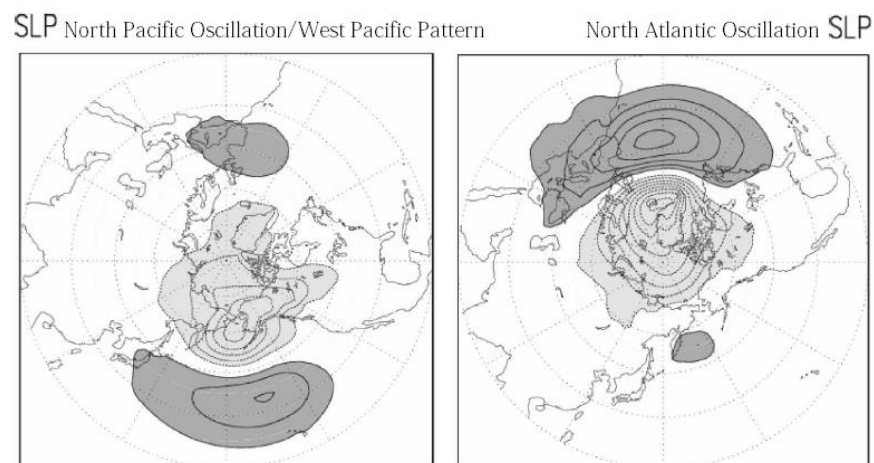


Figure 2.7: PDO, AO and NAO SLP from the N pole view. North Pacific Oscillation/West Pacific Pattern compared with the North Atlantic Oscillation sea level pressure (SLP)
(Modified from Linkin and Nigam, 2008).

The NAO tracks relative changes between pressure systems over the Azores (high) and Iceland (low) (Figure 2.7) and is associated with changes in the alignment of the jet stream, especially around the North America. During a positive NAO phase the Icelandic Low and the Azores High are intensified. This causes a higher pressure gradient over the North Atlantic which intensifies the westerly winds which move dry Arctic cold air from Northern Canada gain humidity while

travelling across the North Atlantic, so is converted into wetter air masses when they arrive to Northern Europe. The opposite is characteristic during the negative phase of NAO, where the pressure systems and therefore the westerlies get weak, cold air masses accumulate and bring cold and dry air further south in North America. Therefore, positive (negative) NAO phases correlate with a positive (negative) AO phases. The positive NAO affects the GOA with stronger negative surface temperature anomalies than during the negative NAO phase (Linkin and Nigam, 2008). Positive NAO and AO could then mean higher storm occurrence and precipitation rates over the GOA.

2.1.3 Marine Productivity in the GOA

Iron bioavailability in the North Pacific is a limiting factor to marine productivity, and more dramatically affects the subpolar NE Pacific (Takeda, 2011; Martin and Fitzwater, 1988). The GOA can be split into two separate regions with regard to nutrient availability and productivity: one at the centre and another on the coast.

2.1.3.1 Central GOA

The central GOA is characterized by iron limited, nitrate-rich and low chlorophyll waters, as part of the wider North Pacific “High Nutrient Low Chlorophyll” (HNLC) region (Hinckley *et al.*, 2009). In other words, the nutrients that are available in the water column in the central GOA are not entirely utilised by primary productivity, as there is the need for light and availability of minor nutrients such as iron to the surface waters to be able to feed phytoplankton growth (Harwell *et al.*, 2010, Martin *et al.*, 1991; Rae *et al.*, 2014).

High concentrations of nitrate are available in the deep waters of the GOA, and so the deep GOA can be the supply of nitrate to the surface if advection of deep-water masses occurs (Stabeno *et al.*, 2004). Despite dissolved iron is more abundant between 250 and 1,000m deep, it is not as abundant as nitrate in the deep ocean and little amount becomes available in the photic zone during upwelling (Boyd and Ellwood, 2010). Iron sources to the photic zone in the Pacific are coastal sediments, atmospheric dust, hydrothermal inputs (Boyd and Ellwood, 2010). Winter water column mixing in the Oyashio-Kuroshio zone has been also observed to increase iron to the photic zone (Nishioka *et al.*, 2011). Other possible processes of iron sources studied in the Southern Ocean include sediment re-suspension,

iceberg melting, sea-ice retreat, dust, eddy transport, island wakes, vertical diffusive flux, volcanism and bottom pressure torque (Boyd and Ellwood, 2010). When iron is available, the particulate organic matter C:N ratio doubles and C:P ratios increase by three times (Martin *et al.*, 1991), which are indicative of big response to iron fertilization in the phytoplankton boom.

In the northeast Pacific, there is a double silica maxima at depths between 2000 and 2500m and at the ocean bottom, attributed to mechanisms such as bio-silica dissolution, bottom sediment dissolution, hydrothermal activity and slope sediment advection (Talley, 1992). Lowest silica is found in the western North Pacific (Talley, 1992).

The marine productivity in the subarctic Pacific has been suggested to respond to mechanisms such as rapid deep ocean circulation and upwelling during interglacials, rather than dust and regional runoff inputs (Rea *et al.*, 1995; Brodeur and Ware, 1995). Wind-induced upwelling occurs in the central GOA during autumn to spring (Stabeno *et al.*, 2004) (Figure 2.8). During summer, upwelling conditions occasionally develop due to the intensifying westerly winds and water column mixing, which helps bringing the nutrients stored in the deep ocean to the surface, increasing productivity (Powell and Molnia, 1989; Harwell *et al.*, 2010) (Figure 2.8). In contrast, during the rest of the year, several factors may explain the lower productivity offshore in the GOA than expected for the abundant nitrate content of the region. One factor could be the reduction of the productivity during the glacier melting season and the subsequent stratification of the water column due to fresh water input into the ocean, limiting the nutrients to the deep ocean (Sarmiento *et al.*, 2004; Stabeno *et al.*, 2004). However, glacier meltwater contains nutrients (Stanley, 2016) which could act as surface ocean fertilisers (Smith *et al.*, 2007). Estimations of river discharge and evapotranspiration makes a total of $849 \pm 121 \text{ km}^3 \text{ yr}^{-1}$ into GOA at present (Hill *et al.*, 2015). However, at modern, meltwater is transported along the southwest coastal Alaska and the Aleutian Arch until the Unimak pass through the ACC (Kipphut, 1990) and evidence for the extension of the meltwater to central GOA has not been published. Positive precipitation/evaporation could drive water stratification in the GOA as precipitation rates are extreme (Hill *et al.*, 2015). During summer, offshore Ekman

forcing could be another potential contributor to nutrient export to the deeper ocean during weaker wind strength (Feely *et al.*, 1979).

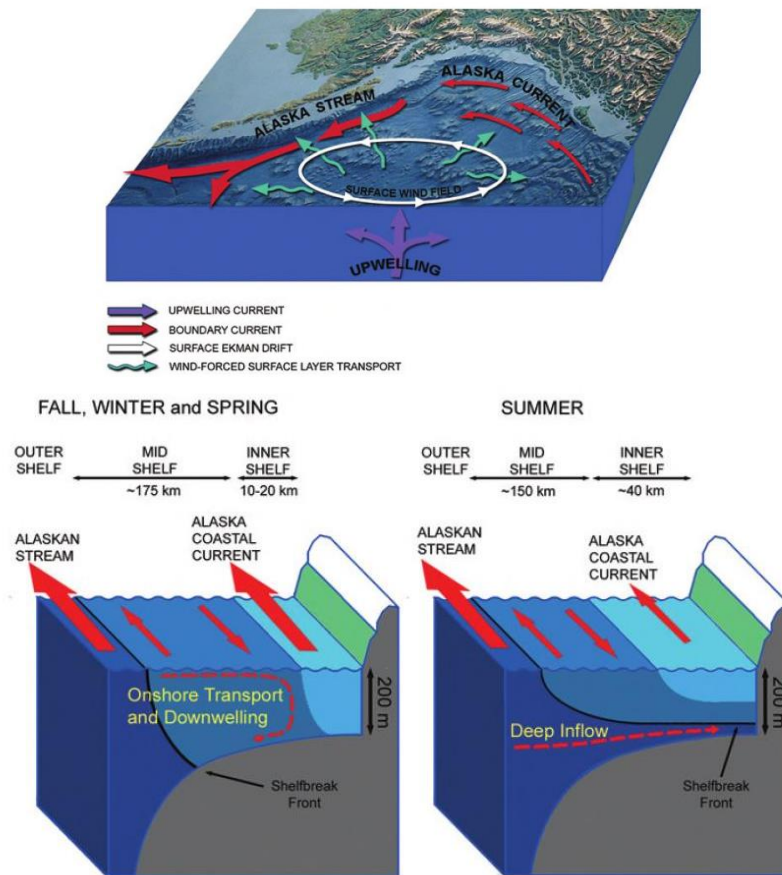


Figure 2.8: GOA atmosphere and ocean circulation. (Top) Major features of the Gulf of Alaska Gyre: upwelling at mid-gyre, Ekman flow away from the centre and currents at the shelf edge; (bottom) schematic circulation in fall, winter and spring (left) and summer (right) over the shelf and slope of the northern Gulf of Alaska (the north is on the right of the figures) (Weingartner, 2007).

2.1.3.2 Coastal GOA

The coastal GOA is characterized by high iron availability, nitrate poor and high chlorophyll waters (LNHC) (Hinckley *et al.*, 2009). Ekman forcing causes downwelling conditions near the coast during most of the year (Stabeno *et al.*, 2004) (Figure 2.8). Downwelling relaxation and eddy propagation along the shelf-break have also been suggested as mechanisms for increasing nutrient availability (Stabeno *et al.*, 2004). However, a number of nutrient sources and mechanisms that contribute to the high productivity along the coastal GOA make this region one

of the richest marine ecosystems on Earth (Ladd *et al.*, 2005). During storms, the sediments on the edge of the shelf are re-suspended and transported due to the disturbance and the wave intensity (Feely *et al.*, 1979) and bathymetric steering in the canyons occur along the GOA shelf (Stabeno *et al.*, 2004). Katabatic winds blowing off the coast can also contribute to increase the terrigenous nutrient delivery to the surface ocean, contributing to nutrient transport to the ocean and enhancing productivity (Bullard *et al.*, 2016). However, the increase of suspended material into the ocean can decrease the sunlight threshold penetration, which is typically the top 50m (Harwell *et al.*, 2010), and so could reduce primary production despite potential higher nutrient availability.

The mechanisms to enhance nutrient availability for marine productivity in the coastal GOA tend to be local. For example, over the nearshore region of the Copper River Delta, the ocean circulation responds to local forcing by wind and river discharge and at the shelf edge, to the Alaska Current (Hill *et al.*, 2015; Kipphut, 1990). Suspended material from Bering, Guyot and Malaspina glaciers are transported via rivers (including the Copper River) to the sea, then directed westward along the coastline and deposited in near-shore environments by the ACC (Feely *et al.*, 1979). Bottom sediments near the shelf edge can be re-suspended by tidal and storm-induced bottom currents during storm events, cold dense near shore water during winters and wind-driven downwelling offshore the Copper River Delta (Feely *et al.*, 1979). Another local example is the region between the Kayak, Middleton Islands and the Copper River. Two gyres: the inner gyre, a cyclonic gyre that creates upwelling on the west of the Kayak Island and the outer gyre, an anticyclonic gyre that creates downwelling in the shelf-edge area both are almost permanent increasing and reducing productivity, respectively (Feely *et al.*, 1979). In Prince William Sound, in contrast, salinity is the most important control for water density, nutrient supply and productivity (Harwell *et al.*, 2010). In summer, rich nutrient deep waters are connected to Prince William Sound by the Hinchinbrook Canyon and their advection causes marine phytoplankton increase (Harwell *et al.*, 2010). During winter, Ekman forcing could be a potential contributor to nutrient export to the deeper ocean during strong wind conditions, as the movement of wind on the water-atmosphere interface creates motion in the

ocean that propagates through the shallow water column and forms downwelling along the coast of GOA (Feely *et al.*, 1979).

The climatic teleconnections discussed above also affect the GOA productivity (Stabeno *et al.*, 2004). During a positive PDO, the Alaskan Gyre strengthens and the California Current weakens (DiLorenzo *et al.*, 2008). The GOA's central upwelling and coastal downwelling zones intensify during positive PDO so that marine productivity increases in central GOA and has been suggested to also increase nutrient availability in coastal regions such as Prince William Sound through GOA water entering the Sound (Harwell *et al.*, 2010). During positive NGPO, the geostrophic circulation intensifies and the North Pacific Current, which travels across the North Pacific and bifurcates to the Alaskan Coastal Current and the California Current, strengthen (see above). Warming in the GOA is associated with positive PDO and NGPO and correlates with negative NAO and positive AO and El Niño events through GOA's climate teleconnections to the North Atlantic and the Arctic (see climate section above). Although general climate teleconnections can be established between the Pacific and the Atlantic Oceans, climate teleconnections are under studied through proxy and model studies (Di Lorenzo *et al.*, 2011; Furtado *et al.*, 2011) and different relationship between climate modes within the Pacific and between oceans can arise through different time scales. As an example, during the late 1970s higher frequency in ENSO events coupled with increase in positive PDO occurrence has been suggested to increase dramatically fish stocks in the North Pacific (Peterson and Schwing, 2003).

2.1.4 Climate of the GOA Summary

The GOA is a contained water body within the North Pacific Ocean that is limited to the east and north with the southeast Alaska coast. The main currents in the GOA are the AC and the ACC. The Alaska Current is sourced in warm mid-latitude currents in the North Pacific travelling eastwards or North Pacific Current. The ACC is characterised by its low salinity content and it is fuelled by glacier and river discharge into the GOA. The ACC travels along the coast of southwest Alaska towards the Aleutian Arch and to the Bering Sea. The Alaska Stream (AS) is a derived current from the AC when travelling along the Aleutian Trench towards the northwestern Pacific. The North Pacific Ocean circulation is influenced by the

Arctic Oyashio Current on the west, which travel southward from the Bering Sea into the Norwest Pacific closing the subpolar Pacific circulation in what is called the Subpolar Gyre.

The climate in the GOA is dominated by the AL pressure system, which travels across the North Pacific in an annual cycle. During winter the AL occupies the centre of the GOA and translates into strong winter wind strength increasing SST gradients in the North Pacific and precipitation over the GOA. During summer, the AL is situated in the Bering Sea and translates to a warmer North Pacific SST and reduced SST gradient between east and west North Pacific. The AL is translated into the PDO over decades. Positive PDO is translated into positive SST anomalies due to advection of warm mid-latitude North Pacific water into the GOA due to a higher frequency of AL presence at the centre of the gyre. Positive PDO is associated with a positive North Pacific Gyre Oscillation and El Niño Southern Oscillation through climate teleconnections leading to a warmer east than west equatorial and North Pacific. Positive PDO climatic teleconnections is associated with positive AO and negative NAO in which the precipitation is increased in east Pacific and reduced in the Atlantic.

The ocean in the GOA is dominated by a water stratification regime at the present day during summer due to increase in glacier meltwater from Alaskan and Canadian glaciers. Two nutrient regimes are established: a high nutrient low chlorophyll (HNLC) region at the centre of the Alaska Gyre circulation offshore of GOA; and a low nutrient high chlorophyll (LNHC) regime under the influence of the Alaska Coastal Current travelling northwards near the north west American coastline diverging to the northwest along the Aleutian Arch. The two nutrient regimes require specific climate conditions and different nutrient supplies for marine productivity. The HNLC region requires advection of deep nutrient rich waters to the surface and micronutrient availability (i.e. iron) from land while the LNHC region requires downwelling relaxation and advection of deep nutrient rich waters for macronutrient availability (i.e. nitrate) in the surface ocean. Upwelling in central GOA associated with strong winds has been suggested to meet nutrient demands to increase marine productivity in both offshore and nearshore GOA, which is associated with a positive PDO, El Niño, positive NGPO, negative NAO and

positive AO by climate teleconnections. However, there are many regional factors that could lead to nutrient supply to the HNLC and LNHC regions during both positive and negative PDO. Similarly, PDO climate teleconnections in the equatorial Pacific, Arctic and Atlantic are under studied through climatic models and are not yet very well understood.

2.2 Geology and Tectonics

Over the Pliocene-Pleistocene timescales examined in this thesis, the tectonically active regional setting of the GOA must be considered. The GOA lies within a tectonically active Pacific belt commonly denominated as the “Ring of Fire”. The GOA is situated over a subduction zone, since the late Eocene-early Oligocene, the Pacific plate has been pushed under the north American plate, with a current rate of $\sim 5.5\text{cm yr}^{-1}$ (Finzel *et al.*, 2011). Alaska was built up through progressive plate convergence and terrain accretion (Powell and Molnia, 1989) building the geology of the South of Alaska with Mesozoic and Cenozoic igneous, metamorphic rocks and alluvial sedimentation (Plafker *et al.*, 1994). The main potential sources of sediments transported to the GOA during the Cenozoic are the Wrangellia, Alexander, Chugach and Yukon-Tanana terrains (Gulick *et al.*, 2015).

Continuous terrain accretion increased the topography (Gulick *et al.*, 2015; Plafker *et al.*, 1994) which is hypothesised to have enhanced glaciation and constituted a source of glacially eroded debris for the GOA (Enkelmann *et al.*, 2015). Evidence for uplift can be found in the deposition of 5 km thick turbidites in the Chugach Terrain of Upper Cretaceous age (Perch-Nilsen, 1985). Offshore, in the Gulf of Alaska, the eroded sediments from the St. Elias Mountain range formed the Surveyor Fan (Figure 1.2).

The Surveyor Fan was deposited from 20 Ma to the present and has been referred to as one of the most unique systems in the world (Reece *et al.*, 2013, Gulick *et al.*, 2015). It is 700 km-long, up to 945m CSF-A deep and late Oligocene oldest approximate basal age system. The Surveyor Fan has no major fluvial or shelf canyon input and has been constructed by glacial erosion (Reece *et al.*, 2013; Gulick *et al.*, 2015; Jaeger *et al.*, 2014). The Chugach-St. Elias orogeny is the highest coastal mountain range in the world and it is still tectonically active (Enkelmann *et*

al., 2009; Reece *et al.*, 2011). Chugach-St. Elias orogen uplift has been estimated to have a starting age of 30 Myr or younger (Lagoe *et al.*, 1993) and new research has enabled to narrow the exhumation age to 4 Ma, which shifted to lower latitudes of the GOA after the Northern Hemisphere Glaciation (NHG) (2.6 to 2 Ma) (Enkelmann *et al.*, 2015).

The potential link between the NHG and exhumation is proposed to confirm the hypothesis that local climate had an effect on tectonics. For the GOA, it has been proposed that climate changes over the Pleistocene (2.6 Ma-present), in particular the shift towards increased magnitude of cooling (Figure 1.1) could have affected the kinematics of the deformation of St. Elias. Specifically, the shift towards increased glaciation in response to climate cooling is hypothesised to have intensified exhumation of the area in response to increasing erosion rates (Enkelmann *et al.*, 2008). The elevation of Mount St. Elias at 5.5 Ma has been speculated to be able to trap precipitation from storms in the form of snow, initiating glaciation (Lagoe *et al.*, 1993). An intensification of glaciation during the late Pliocene has been hypothesised to have occurred around 2.8 Ma, with a doubling of sedimentation rates in the GOA Surveyor Fan and onset of IRD (Gulick *et al.*, 2015).

Glacial erosion can determine topographic elevation and therefore, snow accumulation in the GOA (Molnar and England, 1990). The opposite is also possible, when topographic elevation can determine glaciation. Local precipitation in GOA can reach up to 800cm/a (Powel and Molnia, 1989). High precipitation in tectonically active mountains creates extremely erosive and well fed cool-temperate glaciation, with sedimentation rates the order of 1.5m thick of high basal debris and glacial flow of more than 300m/a (Powell and Molnia, 1989). This has important links to the ocean, delivering low salinity waters into the ocean and favouring column stratification. However, there is little detailed information about when and how the glaciation intensified in the Northwestern Cordilleran Ice Sheet from the Gulf of Alaska, especially since there are no proximal climate records against which to test the hypothesis that cooling was associated with ice sheet expansion. This thesis will focus on this hypothesis and will examine the role of

Pliocene-Pleistocene climate changes in the Northwest Cordilleran ice-sheet evolution.

2.3 Plio-Pleistocene Climate Evolution

The focus of this thesis is to reconstruct the climate history of the GOA, using marine sediment records which extend from the present day back to the globally warmer state of the Pliocene epoch (from 5.3 to 2.6 Ma) and from the late Pleistocene (from 0.5 Ma to the present). In this section, knowledge of the global pattern of climate changes over these time intervals is reviewed, before the links between this knowledge and our limited understanding of the North Pacific (and the GOA in particular) is outlined.

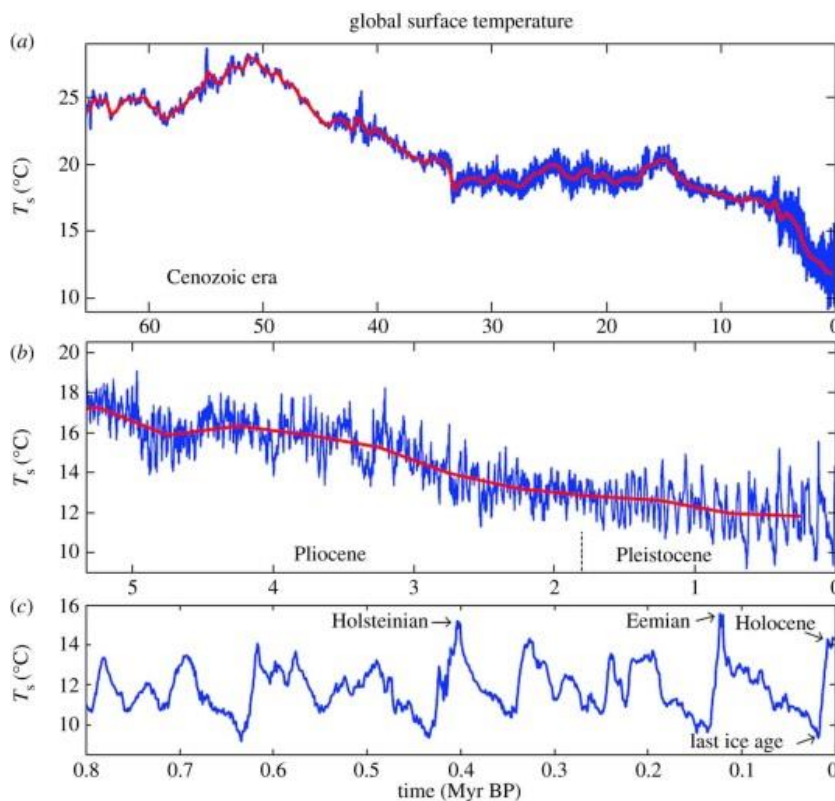


Figure 2.9: Surface temperature reconstruction for the past 65.5 Myr (a), expanded Pliocene-Pleistocene timescale (b) and the last 800,000 years (c). The red curve has a 500 Kyr resolution (Hansen et al., 2013). Note the gradual cooling trend during the Cenozoic, the difference of glacial-interglacial frequency between the Pliocene and early Pleistocene (41 Kyr) and the middle and late-Pleistocene (100 Kyr) and the detail of large glacial-interglacials during the last 0.8 Myr in the last plot.

The climate through the Cenozoic era is known to show a general cooling trend from 65 Ma until the modern time (Figure 2.9a). Within this cooling trend a distinct change in climate called the onset of the North Hemisphere glaciation (oNHG) occurred (Figure 2.9b), which then intensified (iNHG). On a global scale (Figure 2.9) the oNHG occurred in the late Pliocene and early Pleistocene but there are regional differences in the timing of these patterns (note: oNHG and iNHG terms are often used interchangeably). In the Early-Middle Pleistocene there was a transition from the 41 kyr cyclicity that dominated the climate variability of the late Pliocene and Early Pleistocene to the 100 kyr cyclicity called the Mid-Pleistocene Transition (Figure 2.9c) (Lisiecki and Raymo, 2005).

The benthic LR04 stack (Figure 1.1) compiles oxygen isotope data ($\delta^{18}\text{O}$) from benthic foraminifera from 54 sites around the world, and generates a globally averaged signal of ocean temperature and global ice volume for the last 5.2 Ma (Lisiecki and Raymo, 2005). The glacial-interglacial cycles of the LR04 curve are tuned to orbital insolation changes (which provide energy input to the climate system), recognising the overall pacing of the climate system by the Milankovitch orbital cycles of eccentricity (100 kyr), obliquity (41 kyr) and precession (19 to 23 kyr) (Hays *et al.*, 1976). Eccentricity refers to the proximity of Earth's orbit shape around the sun to a circle, obliquity refers to the degree of tilt of the Earth's axis, and precession refers to the position of the north and south poles with respect to the sun (north or south pole facing the sun in different seasons) (Milankovitch, 1941). The eccentricity cycles can, in turn, be gathered into 400 Kyr cycles (Milankovitch, 1941). The Milankovitch astronomical configurations can alter climate by regulating the solar radiation entering the Earth's atmosphere. This alters the heat that is distributed to the Earth's surface and can therefore impact how the Earth re-organizes the heat by changing ocean and atmospheric circulation (Imbrie *et al.*, 1993).

Fluctuations between warm/cold and less/more continental ice can also be identified from Marine Isotope Stages (MIS). The LR04 stack is argued to reflect the global pattern of glacial-interglacial cycles and general climate cooling since the Pliocene. However, due to the very limited data available from the Pacific Ocean in the LR04 stack, this curve has largely been generated from Atlantic

climatic records (Elderfield *et al.*, 2012). There is the need to generate new records to understand local and regional climate changes, to better understand the important mechanisms driving the climate system.

It has been suggested (Maslin *et al.*, 1996) that the onset and expansion of the NHG in the late Pliocene and early Pleistocene responded to orbital changes such as a gradual increase in the amplitude of obliquity between 3.5 and 2.5 Ma and a sharp increase in the amplitude of precession between 2.8 and 2.55 Ma (Maslin *et al.*, 1996). Insolation increase could lead to warmer surface ocean and increased ocean evaporation, which could increase orogenic precipitation in the GOA. Among other suggested climatic drivers are decreasing atmospheric CO₂ concentrations, ocean and atmospheric circulation and tectonics (e.g. Kent and Muttoni, 2008; Beerling and Royer, 2011; De Schepper *et al.*, 2013; Martinez-Boti *et al.*, 2015). In the following sections, the patterns of major climate transitions since the Pliocene will be discussed, and their potential causes outlined.

2.3.1 The Pliocene (5.3 to 2.6 Ma)

The Pliocene epoch comprises a time window that contains a change in climate from globally warm to cold conditions (Figure 2.9b). Due to the warmer-than-modern climate, it has been proposed that the Pliocene had a climate wetter than today, with larger than modern extension of tropical savannas and forests in southwestern Africa and northwestern Australia (Leroy and Dupont, 1994; Dodson and Macphail, 2004). It has been also argued that the Pliocene had permanent El Niño-like condition based on palaeo-precipitation and SST modelling studies (Bonham *et al.*, 2009) but this is not supported by coral data studies (Watanabe *et al.*, 2011).

2.3.1.1 The Early Pliocene (5.3 to 3.6 Ma)

In the early Pliocene (5.3-3.6 Ma) the Earth had a warm, temperate climate with suggested permanent El Niño-like (Wara *et al.*, 2005) or “El Padre” (Ford *et al.*, 2015) conditions. There were lower zonal and meridional SST gradients than the present time (Fedorov *et al.*, 2015; Wara *et al.*, 2005), which intensified around 3.3 Ma in the Nordic Seas (DeSchepper *et al.*, 2013). The eastern Pacific thermocline was deeper (Wara *et al.*, 2005), however, maximum ocean temperatures were similar to present (Fedorov *et al.*, 2013). Modelling the meridional and zonal SST

gradients of the tropics showed a 1:1 relationship and revealed a meridional temperature gradient control over the upper-ocean stratification over the tropics, which controls the zonal gradient along the equator and heat export from the tropical oceans (Fedorov *et al.*, 2015). The intensification of the East Asian winter monsoon from 4.1 Ma increased the aeolian dust accumulation in the North Pacific Ocean (Sites 885 and 996) and lowered the SSTs in the South China Sea (Yamamoto and Kobayashi, 2016; Zhang *et al.*, 2009).

Gateway changes have been proposed to play a key role in the early Pliocene climate (De Schepper *et al.*, 2015). The open central American Seaway has been linked to increased flow from the Pacific to the Atlantic, and a weaker North Atlantic current, causing reduced heat transport to the northern latitudes (DeSchepper *et al.*, 2013). Furthermore, the flow from the Pacific to the Atlantic through the Bering Strait has been suggested to have started between 4.5 and 4 Ma through the opening of the Bering Sea, which started by 5.5-5.4 Ma (Maier-Reimer *et al.*, 1990; Sarthein *et al.*, 2009; De Schepper *et al.*, 2015). Atmospheric CO₂ concentration reconstructions fall within the range 280 to 450 ppm (Pagani *et al.*, 2010; Seki *et al.*, 2010). The warm early Pliocene climate is explained through climatic models by changes in ocean mixing, cloud albedo, and high atmospheric CO₂ (Fedorov *et al.*, 2013; Fedorov *et al.*, 2015). Changes in cloud albedo affects the solar radiation impacting the ocean and ice sheets, and ocean mixing limits the extent of heat exchange between the atmosphere and the deep ocean.

Despite the overall global warmth of the early Pliocene, ice rafted debris (IRD) pre-dating the Pliocene has been found at 14 Ma on the East Greenland margins (Fram Strait and Yermak Plateau) (Wolf-Welling *et al.*, 1996), at ~8 Ma at the West Greenland margin (Baffin Bay) (Thiebault *et al.*, 1989), at 7.3 Ma offshore of southeast Greenland (St. John and Krissek, 2002), and at 5.5 Ma in the Nordic Seas (Jansen and Sjöholm, 1991) and the North Pacific Ocean (Krissek, 1995, Figure 2.10). The appearance of IRD in the Nordic Seas (Bachem *et al.*, 2017), central Arctic Ocean (e.g. Herman, 1970) and North Atlantic (Schaeffer and Spiegel, 1986) started at 5.3 and 4.5 and 10.2 Ma respectively. IRD appearance is interpreted as indicating the onset of the oNHG (Yamamoto and Kobayashi, 2016) and its age has been re-located to 3.6 Ma through globally distributed increase in planktonic and

benthic foraminifera oxygen isotope records (Mudelsee and Raymo, 2005). Despite the evidence for tidewater glaciation to explain the IRD appearance, it has been suggested that these regional glacial events did not expand into a glaciation covering a large part of the Northern Hemisphere, and some of them were not sustained until the late Pliocene (Mudelsee and Raymo, 2005).

2.3.1.2 The mid (3.3 to 3.1 Ma) and late (3.6 to 2.58 Ma) Pliocene

Within the Pliocene, the period from 4 Ma to the present is characterized by a general cooling trend of SST (Fedorov *et al.*, 2014) (Figure 2.9b). Much attention has focussed on the time period during the general cooling trend, the mid Pliocene warm period at 3.3-3.1 Ma, when the climate was globally warm (Hansen *et al.*, 2006), with interglacials 2 or 3°C warmer than pre-industrial levels (Haywood *et al.*, 2010). However, data is lacking from the GOA despite its proximity to the Cordilleran Ice Sheet (Figure 2.10).

The late Pliocene or Piacenzian (3.6-2.58 Ma) is the most recent stage of the Pliocene epoch. During the late Pliocene, the climate is marked by a more dramatic cooling than during the early Pliocene; the climate shifts from a warm climate with

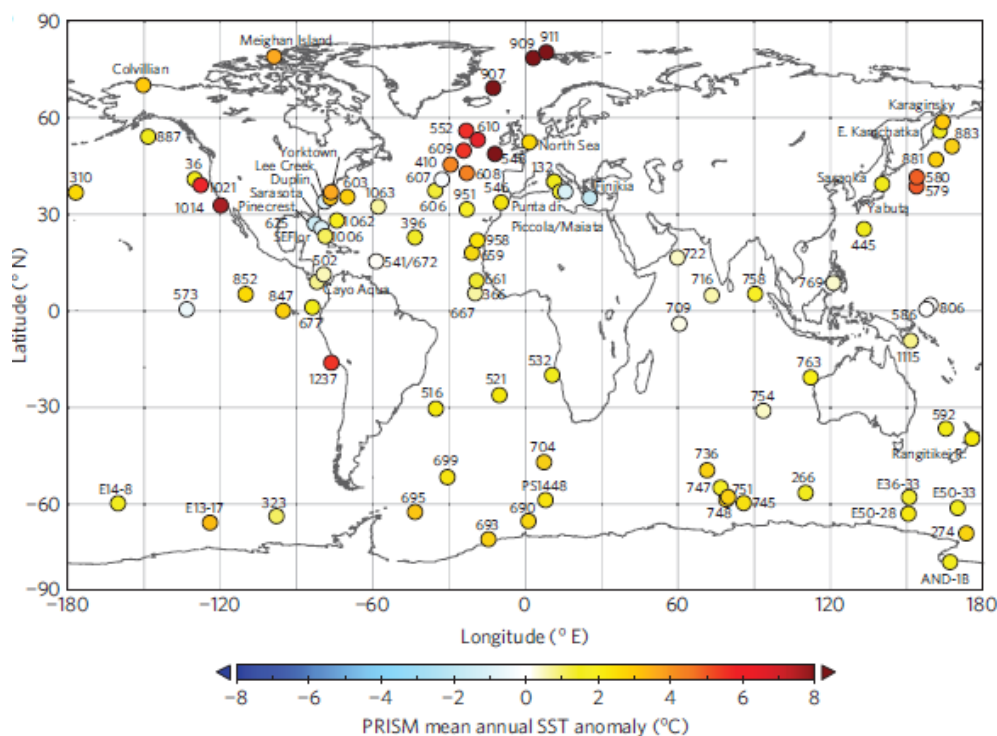


Figure 2.10: Mean annual SSTs anomalies Pliocene localities with at 95% confidence assessment from PRISM dataset (Dowsett *et al.*, 2012). Note the gap in data from the GOA.

little glaciation to repeated glaciations extending across large parts of the Northern Hemisphere by the end of this period at 2.58 Ma (Figure 1.1). The late-Pliocene overall cooling trend is matched by the long-term sea level drop, however within these trends there are significant climatic variations which are also evidenced by changes in atmospheric CO₂ concentration and changes in the Atlantic Meridional Ocean Circulation (AMOC) strength (Figure 2.11) (De Schepper *et al.*, 2013). The most studied windows of the Piacenzian are the mid-Piacenzian warm period (MPWP) (3.29-2.97 Ma) (Dowsett *et al.*, 2012) and the cold M2 event (~3.3-3.26 Ma) (De Schepper *et al.*, 2013).

Climate analogues are important for end of century climate projections. Climate analogues are selected based on the similarity with present climate characteristics. One of the key characteristics is a similar to present atmospheric CO₂ concentration (i.e. Martinez-Boti *et al.*, 2015). There are many past climates in Earth history that could potentially be good analog of present-future climate, but the mid-Pliocene offers a major advantage compared to older time-periods by having a continental configuration close to the present (Salzmann *et al.*, 2011; Raymo *et al.*, 1996).

The MPWP has gained much interest due to the similarity with projections for the end of this century in relation to the current climate change and the global temperatures above pre-industrial levels (Dowsett *et al.*, 2013; Hansen *et al.*, 2006). The MPWP was characterized by average global temperatures 2-3 °C warmer than present, amplified in polar regions (7 to 8°C warmer and 400 mm wetter than today), and more specifically in the Northern Hemisphere (Burckle *et al.*, 1996 ; Barron, 1996; Robinson, 2009; Ballantyne *et al.*, 2010). The MPWP been argued to be due to an increase of atmospheric CO₂ compared with the early Pliocene (Brigham-Grette *et al.*, 2013; Lunt *et al.*, 2012). Due to the higher concentration of CO₂ during the MPWP, the size of the ice sheets were reduced, and the global mean sea level was 25±20 m above the current values (Dowsett *et al.*, 2010; Raymo *et al.*, 2009). However, there are some disparities between CO₂ records, which are based on different producers e.g. tree species for stomata and different foraminifera species used to analyse δ¹¹B for CO₂ reconstructions (Martinez-Boti *et al.*, 2015).

The PRISM project has reconstructed the palaeoenvironmental conditions of the MPWP window (Dowsett *et al.*, 2012). They conclude that the global climatic models and sea surface temperature data agree very well in most regions except in the North Atlantic, where models underestimate warming (Dowsett *et al.*, 2012). The limited data from some regions (Figure 2.10) and the use of data averages to characterize conditions over a wide time window (~200 kyr) which includes multiple glacial-interglacial cycles, is a potential limitation of PRISM. Differences between data-model simulations of Pliocene permanent warm climate intervals also present a challenge for climate models (Haywood *et al.*, 2013a). For example, the North Atlantic Ocean data sets present an increase in the amplitude of the warm SST anomaly with latitude, but the models do not show such a strong gradient (Dowsett *et al.*, 2012). This disagreement could be due to a reduction in sea-ice in the Northern Hemisphere and the positive feedbacks or differences in the position of the Gulf Stream-North Atlantic Drift in the models compared with the geological reconstruction (Dowsett *et al.*, 2012) and enhanced thermohaline circulation during the Pliocene, in turn enhancing the heat transport to the poles (Raymo *et al.*, 1996). Furthermore, an enhanced thermohaline circulation disagrees with the estimations of future scenarios of the current “global warming”, where the thermohaline circulation is expected to weaken in a warming climate (Lin *et al.*, 2006). Models of future climate are focussing on a regional scale, a greater number of high resolution proxies, and a finer window of time (a ‘time slice’) to try to narrow down the reasons for data-model discrepancy and better understand the controls on Pliocene climate (Dowsett *et al.*, 2013; Dowsett *et al.*, 2016).

Despite continental configurations during the MPWP being closer to the present day in comparison to the early Pliocene (Salzmann *et al.*, 2011; Raymo *et al.*, 1996), there were still some differences. Uplift and modified present-day orography due to erosion (Salzmann *et al.*, 2011) could have modified circulation patterns and SST during a warm interval (Rind and Chandler, 1991) in relation to the present. As an example, it has been suggested that during the MPWP, the Antarctic Bottom Water became weaker in the Pacific rather than in the Atlantic Ocean (Haywood and Valdes, 2004) perhaps as a consequence of the closure of the Panama seaway

since the early Pliocene (Haug *et al.*, 2005). It has also been suggested that the closure of Bering and Canadian Arctic Archipelago Straits reduced the connection of less salty waters from the subarctic Pacific through the Arctic Ocean and to the North Atlantic, resulting in a warmer climate in the North Atlantic during the MPWP (Otto-Bliesner *et al.*, 2016) which could have led to a fresher and more stratified northern Pacific Ocean. Lunt *et al.* (2012) attribute the MPWP warmth to orographic changes in the northern hemisphere, including the Rockies; to changes in ice cover in the Arctic; and to changes in precipitation in the southern hemisphere. Regional cooling of 1 to 3°C due to changes in orography during the MPWP in the west Canadian Rockies is driven by a reduction in ascending air over the mountains and decrease in cloud cover and precipitation (Lunt *et al.*, 2012). Lunt *et al.* (2012) also suggests a warming in the Arctic and in the Barents Sea due to a reduced ice cover and an increase ice cover in Antarctica due to a warmer climate and increased precipitation. A potential similar response could be expected in the Cordilleran Ice Sheet. However, Haywood and Valdes (2004) attribute the warmth of the MPWP to the reduction of the ice-sheets and the sea ice cover and

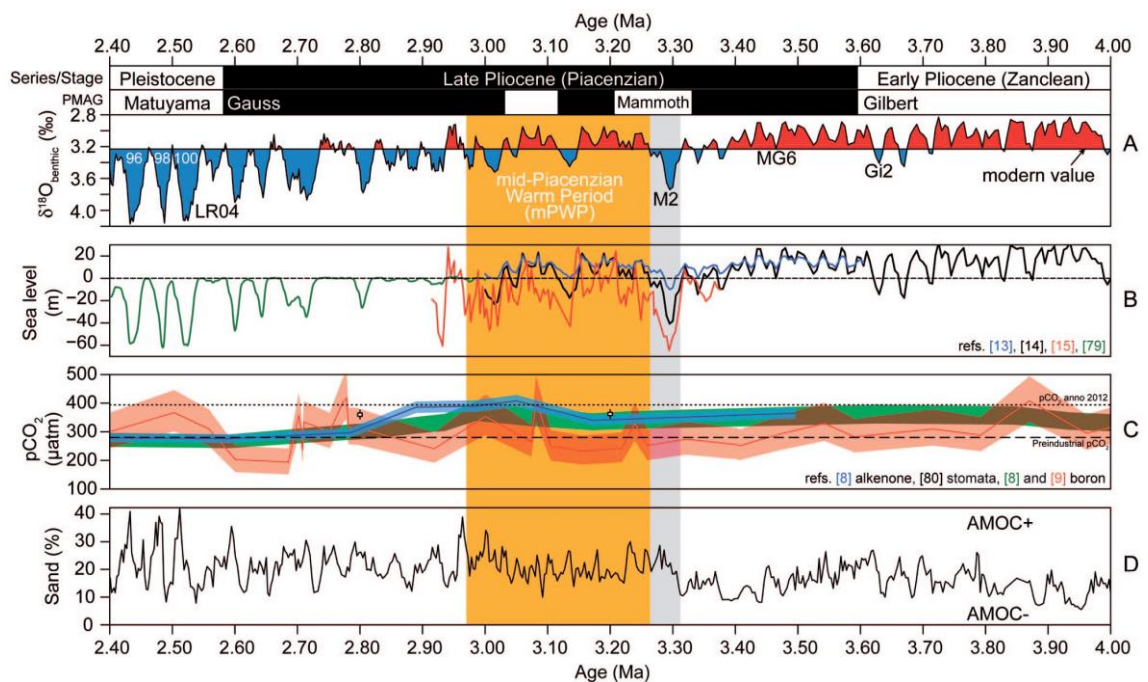


Figure 2.11: LR04 Stack compared with sea level, pCO_2 and sand (%). The latter is used to represent water flow from the Pacific into the Atlantic through the Central American Seaway and AMOC strength (De Schepper *et al.*, 2013).

the associated ice-albedo feedback in a 400 ppm atmospheric CO₂ world. Another difference from present is that the climate sensitivity, or global temperature response to doubling of CO₂ forcing, during the warm Pliocene was half as strong as for the colder late Pleistocene epoch (Martínez-Botí *et al.*, 2015). Martínez-Botí *et al.* (2015) explained this difference in the radiative impacts of the continental ice-albedo feedback during the late Pleistocene that was not present with more restricted glaciation during the warm Pliocene. A long term similar to present equatorial Pacific state “El Padre” (Ford *et al.*, 2015), could have caused some variations in the SSTs of the western equatorial Pacific and broken the normal pCO₂ equilibrium between the atmosphere and the surface ocean (Raymo *et al.*, 1996). Some uncertainty in the CO₂ reconstructions during the MPWP also relates to the SST data which is used in the CO₂ calculations: a 1.5°C error in reconstructed SST results in a 25 ppm error in atmospheric CO₂ (Raymo *et al.*, 1996), although Martínez-Botí *et al.* (2015) minimises the error by considering the average SST between 4 kyr time intervals. However, not many sediment sequences can extract this level of temporal resolution in the data.

Within the overall warmth of the mid Pliocene there is a pronounced glacial stage termed MIS M2. During MIS M2, it has been proposed that the climate was colder than present and sea level dropped around 64 m with respect to present day, although the exact size of the M2 ice sheets is still under debate (Dolan *et al.*, 2015). Despite the M2 cooling event, the climate was unable to develop a full glacial stage (Haug and Tiedemann, 1998). Prior to M2 (~3.3 Ma), the Atlantic and Pacific Oceans (and their circulation systems) were connected through the Panama Seaway, weakening the heat transport to the Arctic and driving colder climate in higher latitudes. This Arctic cooling and the climate evolution towards a glaciation stage are difficult to reconcile with high atmospheric CO₂ levels (Lunt *et al.*, 2008; De Schepper *et al.*, 2013). A feedback is suggested, whereby the expansion of the North Hemisphere ice sheets during MIS M2 led to a drop in global sea level which is argued to have stopped the inflow of Pacific waters into the Atlantic across the resulting shallow Panama seaway, in turn developing the present Pacific Warm Pool, enhancing the North Atlantic circulation and heat transport to the North Atlantic, and thus terminating the glaciation (De Schepper *et al.*, 2013).

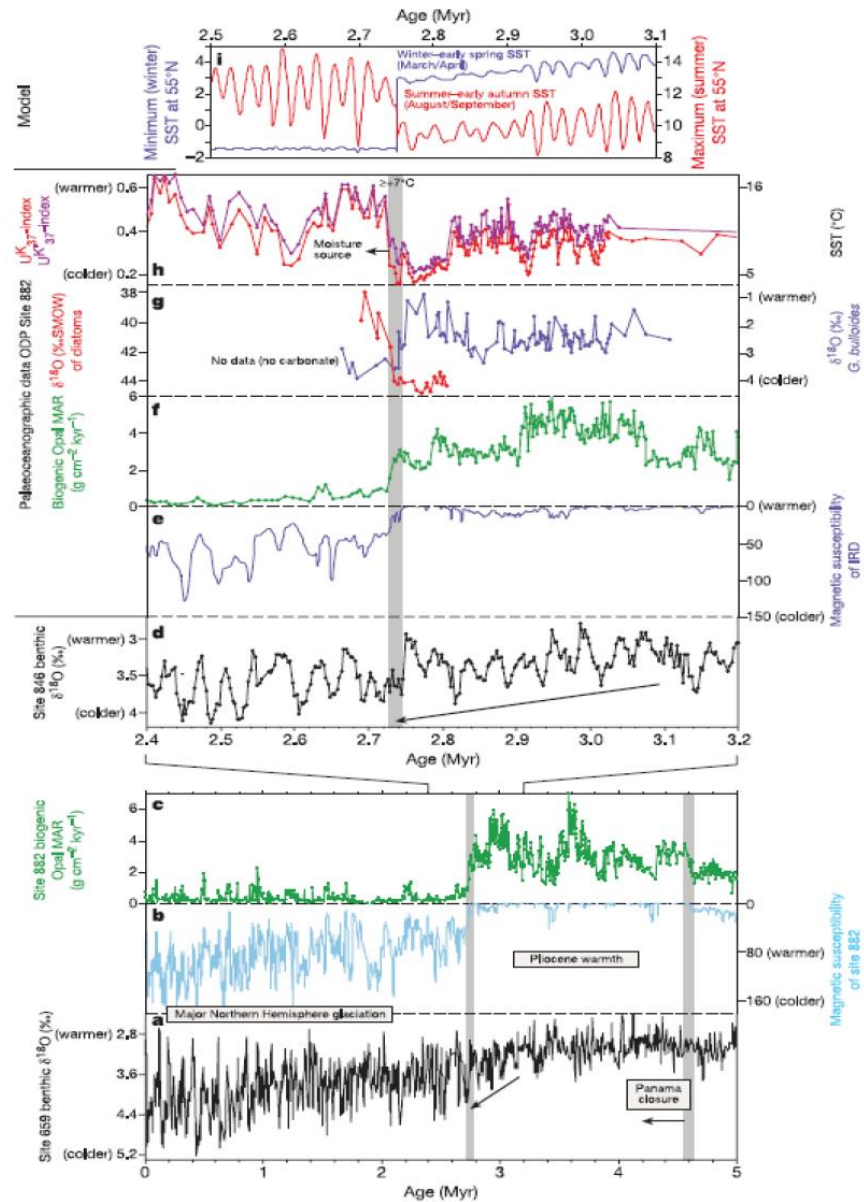


Figure 2.12: Pliocene-Pleistocene transition over the North Pacific and equatorial Pacific and Atlantic Oceans. Shifts in summer and winter insolation at 55°N during 3.1 to 2.5 Ma, $U^{K_{37}}$, $U^{K_{37}'}$, SST, $\delta^{18}O$ from diatoms and planktonic foraminifera, biogenic opal MA and magnetic susceptibility from ODP 882; benthic $\delta^{18}O$ from ODP 846 (equatorial Pacific) during 3.2 to 2.4 Ma, zoom in biogenic opal and magnetic susceptibility from ODP 882 and benthic $\delta^{18}O$ from ODP 659 (equatorial Atlantic). The Northern Hemisphere Glaciation is highlighted in grey (Haug *et al.*, 2005).

For the North Pacific Ocean, the only sites analysed to identify glacial-interglacial cycles in the Pliocene climate are ODP 882 (northwest Pacific; Haug *et al.*, 2005)

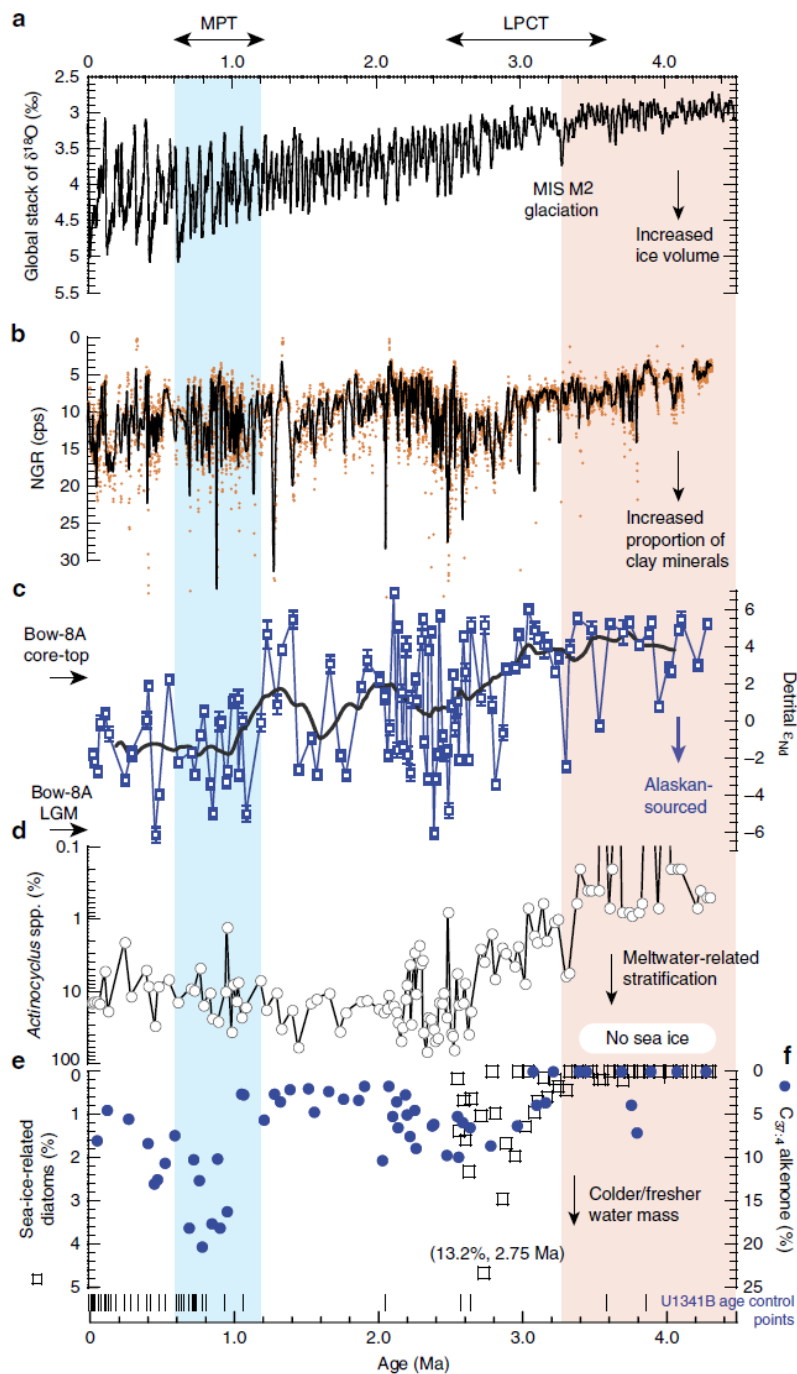


Figure 2.13: Freshening in the Bering Sea during a global increase in ice volume.

Bering Sea climatic records (Horikawa et al., 2015).

and ODP 887 (northeast Pacific; Rea *et al.*, 1995). From 3.5 to 2.5 Ma, a climatic linkage has been observed between the Northwest Pacific (Site 882), equatorial Pacific (ODP 846) and the North Atlantic Ocean (Site 659), both describing a cooling SST trend (Figure 2.12). In comparison with the North Atlantic Ocean, the SST in the Pacific Ocean has experienced stronger variations, which could be

consistent with the suggestion that the SSTs of the North Pacific could have been sensitive to CO₂ and orography (Lunt *et al.*, 2012; LaRiviere *et al.*, 2012) with changes in the Panama Seaway configuration (Haug *et al.*, 2005). New studies from the Bering Sea (Horikawa *et al.*, 2015) suggest that glaciers of Alaska were present as far back as 4.2 Ma and a long term trend towards fresher waters (revealed from $\delta^{13}C_{37:4}$ analysis) started since MIS M2 (3.3 Ma). During the M2 event the Bering Sea surface became colder and fresher, due to an input of low-salinity water from the Arctic Ocean (Horikawa *et al.*, 2015). The Bering Sea oceanography suggest a disruption in the North Atlantic Deep Water formation and has been argued as a trigger for long term global climate cooling (Horikawa *et al.*, 2015)(Figure 2.13). East Asian summer monsoon intensification and the co-occurrence of climate cooling during the late Pliocene suggest that a joint closure of Panama Seaway, surface water freshening across the equatorial and North Pacific and ice volume increase culminated in the oNHG, with possible contributions from the Tibetan plateau uplift (Nie *et al.*, 2014).

Modern salinity differences between east equatorial Pacific and Caribbean Sea were established around 4.2 Ma (Nie *et al.*, 2014). In the North Pacific, late Pliocene intensification of the East Asian summer monsoon and change in Panama Seaway was translated into fresher surface North Pacific waters and enhanced sea ice formation (Nie *et al.*, 2014). The closure of the CAS has also been associated with an enhanced North Atlantic Thermohaline Circulation (Bartoli *et al.*, 2005). Models suggest that sea ice formation would have driven an enhanced atmospheric circulation and east Asian monsoon increasing moisture transport and meridional and high latitude (Nie *et al.*, 2014). As a result, the GOA could have developed warmer sea surface due to increase ocean circulation and increase heat supply from lower latitudes as well as and fresher surface waters due to the restriction from the modern saltier North Atlantic waters. A cooling climate and an enhanced moisture supply to the GOA could have played an important role in the development of the Cordilleran Ice Sheet (Haug *et al.*, 2005). However, there is a lack of data in the GOA to be able to assess the paucity of this theory (Figure 2.10). In addition, the timing of the Panama Seaway closure has been extensively debated in the science community, with studies arguing its occurrence as a cause or pre-

condition for the intensification of the NHG (i.e. Haug *et al.*, 2005) and other studies do not consider the CAS a necessary mechanism for glaciation (De Schepper *et al.*, 2015). Some other studies have re-defined the timing of this event as far as the mid-Miocene (Montes *et al.*, 2015).

2.3.2 The Plio-Pleistocene Transition and early Pleistocene (2.6 to 1.5 Ma)

The Plio-Pleistocene transition involves the onset/intensification of the NHG, which refers to the first evidence of an expanded glaciation in the Northern Hemisphere after the warm Pliocene epoch. The onset of the NHG is measured by the increase in frequency and abundance of ice rafted debris (IRD) pulses which are more or less synchronous in the polar and subpolar oceans of the Northern Hemisphere. The widespread increase in IRD indicates the expansion of tide-water glaciers across several regions of the Earth, and therefore, a globally cooler climate. The timing of the NHG is generally set around 2.64 Ma (Bailey *et al.*, 2013) or 2.7 Ma (Haug *et al.*, 2005), but varies slightly from region to region. For instance, IRD from the North Atlantic shows that the onset of the NHG happened first in Greenland and Europe (2.72 Ma) and then North America (2.64 Ma) (Bailey *et al.*, 2013), whereas in the Nordic Seas there is evidence for small inputs of IRD developing from 5.3 Ma (Bachem *et al.*, 2017). The intensification of the NHG is most often referred to as occurring at 2.7Ma based on a pronounced cooling period in the LR04 stack (Liesecki and Raymo, 2005) and the abrupt increase of IRD in the Nordic Seas and the North Pacific (Yamamoto and Kobayashi, 2016; Bailey *et al.*, 2013). However, Mudelsee and Raymo (2005) discuss an earlier onset of the NHG from 3.6 Ma to 2.4 Ma. The timing of the intensification of the NHG thus lies close to the Plio-Pleistocene transition and can be attributed from 2.6 to 2.4 Ma.

Before the Plio-Pleistocene transition, various regional cooling events took place (Figure 2.12 and 2.13) but overall SSTs were still warmer than present for Arctic summers until 2.7 Ma (Haug *et al.*, 2005). Two possible explanations for the global-scale cooling associated with NHG could be tectonic changes such as the closure of the Indonesian and Panamanian/Central American seaways (CAS) during 3-2.5 Ma (Bartoli *et al.*, 2005; De Schepper *et al.*, 2013) and the uplift of the Tibetan plateau during the late Pliocene (although this is still controversial) (Nie *et al.*, 2014). Regardless of the exact timing of the Panama seaway closure, it has been argued

that isolation would not be sufficient in explaining the occurrence of the NHG (Lunt *et al.*, 2008). Orogenic uplift and an increase in erosion can increase weathering on land and has been proposed to decrease atmospheric CO₂ concentrations during the Phanerozoic (Otto-Bliesner, 1995). The NHG is associated with a drop of CO₂ to pre-industrial levels around 2.8 Ma (Seki *et al.*, 2010; Fedorov *et al.*, 2013; Martínez-Botí *et al.*, 2015). Orogenic changes have been proposed to lead to an increase in heat transport to the North Atlantic region during the Pliocene, and may have increased precipitation in higher latitudes and led to the glacial development during the Plio-Pleistocene transition (Haug *et al.*, 2005; Lawrence *et al.*, 2010; Bringham-Grette *et al.*, 2013; Fedorov *et al.*, 2013; Sarnthein *et al.*, 2013).

In regions where there is an absence of IRD, other proxies can also record a dramatic change across the Pliocene-Pleistocene boundary, which can be indicative of the NHG development. As an example, in the subarctic Northwest Pacific (Haug *et al.*, 2005) the alkenone SST warming at 2.7 Ma is indicative of strong-high latitudinal feedback mechanism during autumn and enhanced moisture supply to the north American Ice Sheet. Global ocean reorganization and restriction of North Pacific-North Atlantic waters through the Bering Sea prior to the intensification of the Northern Hemisphere glaciation (Yamamoto and Kobayashi, 2016) translated in a southward shift of the North Atlantic Drift at 2.7 Ma (Kamikuri *et al.*, 2007). Radiolarian assemblages from the subpolar Northwest Pacific also revealed a severe glacial stage at 2.7 Ma that impacted radiolarian sedimentation rates and assemblage composition (Kamikuri *et al.*, 2007). The intensification of the East Asian Monsoon and the re-organization of the atmospheric circulation are suggested to have contributed to the decrease in atmospheric CO₂ by increased sediment erosion and weathering and have triggered the onset of the NHG (Zhang *et al.*, 2009; Yamamoto and Kobayashi, 2016). However, the global ocean reorganization with an increase in stratification and decrease in water exchange between oceans is suggested to have decreased marine productivity affecting the opal content in the sediments in the Pacific, Atlantic and Southern Oceans above latitudes of 50°N and 50°S (Sikes *et al.*, 1991; Raymo *et al.*, 1992; Lawrence *et al.*, 2013; Yamamoto and Kobayashi, 2016). The dust record from ODP 885 in the Northeast Pacific shows an increase in aeolian

mass accumulation rate (MAR) input from $<100 \text{ cm}^2/\text{kyr}$ (from 4 to 2.67 Ma) to ~ 100 to $150 \text{ cm}^2/\text{kyr}$ during the last 2.6 Ma (Snoeckz *et al.*, 1995). Dust input into the middle extratropical North Pacific (Site 885) peaks with the onset of the NHG (2.6-2 Ma) (Snoeckx *et al.*, 1995) which could locally increase marine productivity. A permanent halocline was established since the NHG (~ 2.7 Ma) and it is currently reset at depths of 100 and 200 m in the subarctic Pacific Ocean (Yamamoto and Kobayashi, 2016). The establishment of the halocline derived in a drop in macronutrients to the surface ocean and decrease in opal accumulation at ODP 882 (Haug *et al.*, 2005). However, whether comparable changes in ocean circulation were also observed in the NE Pacific, and in proximity to the ice sheets (i.e. in the GOA) remains unclear. A sea surface temperature record from the Gulf of Alaska is needed in order to access more proximal ice-ocean-climate interactions.

2.3.3 The mid and late Pleistocene (500 to 0 Ka).

Between the PPT and the late Pleistocene (1.5 to 0.5 Ma), global climate is defined by the development of glacial and interglacial cycles which are dominated by 41 kyr cyclicity. The Mid Pleistocene Transition (MPT; 1.2 Ma to 700 ka) marks the transition from a world of 41 kyr cycles to 100 kyr cycles (Elderfield *et al.*, 2012). Since the MPT, glacial-interglacial cycles have a cyclicity of 100 Kyr, with a distinctive 'saw-tooth' shape (Figure 2.9c). Although comparable in time to eccentricity forcing, the 100 kyr climate cycles are not solely explained by astronomical configurations (Abe-Ouchi *et al.*, 2013, Imbrie *et al.*, 2011, Imbrie *et al.*, 1993). Feedbacks between climate, ice sheets and the carbon cycle must be considered in order to explain the 100 Kyr cycles, since the forcing from eccentricity is insufficient to explain their dominance in the climate record (Imbrie *et al.*, 1993). Whilst much research has focussed on explaining the feedbacks during glacial stages, the length and timing of interglacials can vary between regions, as well as the intensity and response to regional or global climatic feedbacks (Wolff, 2015). Little information is known about the role of the Northeast Pacific regional climate and impact on global climate during late Pleistocene glacial and interglacials (e.g. Lang and Wolff, 2011; Candy and McClymont, 2013; Wolff *et al.*, 2015).

Iron input into in the GOA has been observed from higher sea level and rapid inundation of the continental shelves (Davies *et al.*, 2010). The potential for increased iron input into in the GOA poses the question whether iron limited waters offshore the GOA (Martin *et al.*, 1991) could allow enhanced marine productivity during deglacials, as it has been discovered during the warm Holocene in coastal GOA (Addison *et al.*, 2012; Davies *et al.*, 2010). Another hypothesis focusses in iron fertilization as key trigger of enhanced marine productivity in the GOA (Martin *et al.*, 1988) during glacial stages, especially if helped by increased glacial dust (Naafs *et al.*, 2012). The dynamics of the Cordilleran Ice Sheet could regulate regional sea level changes and so the flooding of the continental shelves of south Alaska, which could be a source of iron supply and fertilization of GOA waters.

Two of the most debated yet best studied time intervals during the last 500 ka are MIS 5e and the Last Glacial Maximum (LGM).

2.3.3.1 MIS 6 and MIS 5 (MIS 5: 130 to 80 Ka)

The transition from MIS 6 to MIS 5 is evidenced by a sharp rise in SST of 5 °C in the Bering Sea (Max *et al.*, 2014) and in some other records from marine coastal records and Arctic lakes which show an abrupt warming of 4 to 10 °C (Kienast *et al.*, 2011; Melles *et al.*, 2012). MIS 5e peak SST in the subarctic Pacific is similar North Atlantic SST and less intense as at El'gygytgyn lake in Arctic Russia (Max *et al.*, 2014). Glacial stages in Arctic Russia, Greenland and the North Atlantic share similar characteristics during the last 140 ka with increase in IRD and sea ice in the Bering Sea and weaker AMOC strength (Max *et al.*, 2014). During MIS 6, IRD peaks become more abundant around Antarctica and it is linked to a weaker of the North Atlantic Deep Water formation leading to enhanced Southern Ocean water stratification (Broecker and Henderson, 1998). Marine iron fertilization due to dust transport around Antarctica leading to changes in productivity has been proposed to play a key role (Broecker and Henderson, 1998). Millennial scale oscillations during cold periods follow certain steps: an increase of subpolar species, an increase in IRD synchronous with a cooling in SSTs of 3-5 °C and finally an abrupt warming which sets them to their initial state (Kandiano *et al.*, 2004).

Similar Arctic and Antarctic glacial-interglacial feedbacks could characterise the GOA record during the last 500 kyr.

SST in the subarctic Pacific and Atlantic were at a maximum and 2 °C warmer than present during the substadal MIS 5e (128-126 Ka) (Max *et al.*, 2014; Kandiano *et al.*, 2004). MIS 5e climate in the Arctic and subarctic is characterised by weakening in the subpolar gyre circulation, absence of IRD and active AMOC (Max *et al.*, 2014). Millennial scale climate variability involves important mechanisms to explain climate transitions between glacial and interglacials. Millennial scale climate variability during MIS 5e has been suggested to be caused by changes in the Atlantic Meridional Overturning Circulation (AMOC) (Galaasen *et al.*, 2014) and rapid atmospheric propagation from the North Atlantic to the subarctic Pacific climate, such as via the East Asian winter monsoon teleconnection (Max *et al.*, 2014; Sun *et al.*, 2012). Other model simulations attribute freshwater in the Northern Hemisphere and reduced AMOC as an important player in the evolution of the colder than present North Atlantic during early Last deglacial climate (130 ka) and warmer than present Southern Ocean by bipolar seesaw mechanisms (Stone *et al.*, 2016). However, there is currently very limited data availability for the NE Pacific, and specifically in the GOA, to test some of these hypotheses to explain climate fluctuations within MIS 5e. As with the Pliocene, MIS 5e has been proposed to be a good target to better understand current and future climate change. However, it is important to consider that the different climatic forcings such as seasonal astronomical changes and greenhouse gas concentrations does not make MIS 5e a good modern climate analogue (Stone *et al.*, 2016). Rather, it is a useful time period to study mechanisms of climate and environmental change that operate under warm climates (Stone *et al.*, 2016).

2.3.3.2 The Last Glacial Maximum (LGM) (24 to 21 Ka)

Global SSTs record a large longitudinal gradient in all oceans during the LGM (MARGO, 2009). The Nordic Seas were ice free and, based on alkenone studies, the North Atlantic was colder than present during the LGM, whereas some areas of the Northwest Pacific were warmer during the LGM than at present (MARGO, 2009). A study from the California Current concludes that the increase in wind stress during the LGM increased ocean upwelling at 42°N (Ortiz *et al.*, 1997). Atmospheric CO₂

levels dropped to 180 ppm during the LGM (Anklin *et al.*, 1997). The North Pacific has been suggested as a location of deep carbon storage during the LGM due to ocean stratification (Rae *et al.*, 2014). High North Pacific pH could be associated with shoaling of the AMOC and increase in deep water alkalinity and CaCO_3 preservation or changes in marine phytoplankton (Rae *et al.*, 2014). Ocean stratification is often associated with low marine productivity as nutrients are normally reduced in the surface ocean and an additional nutrient supply is required e.g. Asian desert dust. In the subarctic Pacific, Asian dust and drifting icebergs were higher during MIS 2 than during the last interglacial, which might be expected to stimulate productivity (Jaccard *et al.*, 2009). Marine productivity was lower in the northwest Pacific but higher in the northeast Pacific in the California margin (McManues *et al.*, 1998) (Jaccard *et al.*, 2009). Data from the north Pacific (e.g. LaRiviere *et al.*, 2012) and the GOA (Rea *et al.*, 1995) is scarce and the above questions remains unanswered for the Northeastern Pacific.

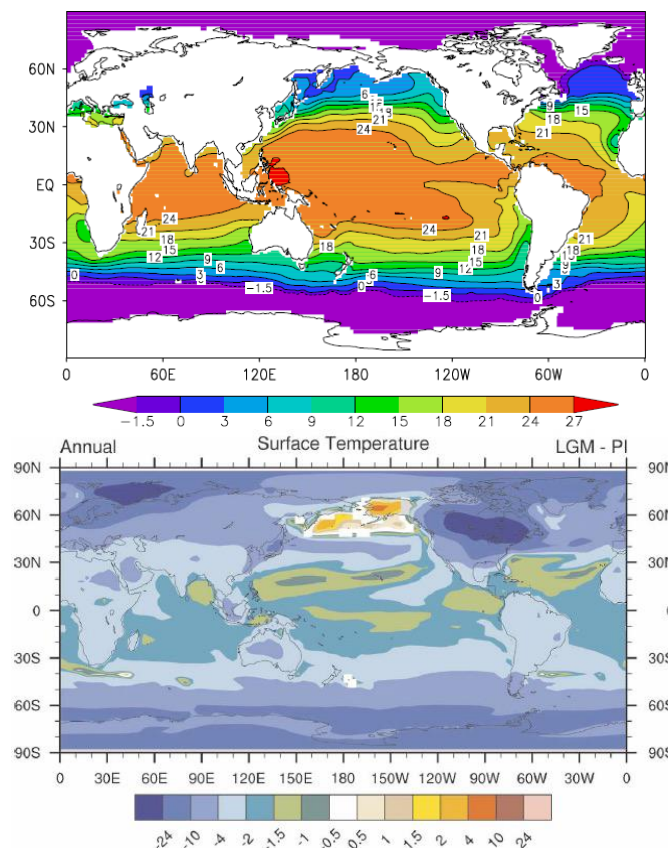


Figure 2.14: CLIMAP (1981) SST reconstruction of the LGM annual SST (left) and LGM minus PI reconstructed annual surface temperature change (Otto-Bliesner *et al.*, 2005) (right).

CLIMAP data show SST across the GOA during the LGM of about 4-5 °C, which is around 1°C colder than annual modern SST (Figure 2.14) (Locarnini, 2006). Climate models suggest that the air temperature was in fact warmer over central Alaska and the GOA in comparison with the pre-industrial climate (Figure 2.15) (Otto-Bliesner *et al.*, 2005), but were warmer in east Alaska and colder in west Alaska and the GOA compared with modern which can be associated with changes in AL position (Kim *et al.*, 2008).

The role of the North Pacific as a source of deep water formation has been suggested to play an important role in CO₂ rise during the Holocene, due to changes in ocean surface salinity and enhanced intermediate water ventilation and climate change (Rae *et al.*, 2014). The North Pacific does not form deep water today, thus, mechanisms proposed for glacial stage deep water formation suggest an increase in surface salinity due to a reduction in monsoonal freshwater flux (Rae *et al.*, 2014).

2.4 Cordilleran Ice Sheet History

The reconstruction of the Laurentide Ice Sheet has been given much attention to date (e.g Naafs *et al.*, 2013; Bailey *et al.*, 2013; Rabassa and Ponce, 2013), but less attention has been paid to its northwestern component, the Cordilleran Ice Sheet. The Gulf of Alaska has been previously drilled (Figure 2.15) in two expeditions: Deep Sea Drilling Project (DSDP) Leg 18 (Leg 145 Scientific Party, 1992) and Ocean Drilling Program (ODP) Leg 145 (Von Huene *et al.*, 1971a, b, c, d and e). DSDP Leg 19 and 18 recovered sediments from the Lower Eocene to the upper Pleistocene (Scholl and Creager, 1973; Leg 145 Scientific Party, 1992), ODP Leg 145 Site 887 recovered sediments from lower Miocene to Quaternary (Leg 145 Scientific Party, 1992). Despite these drilling sites adding valuable information about the climate in the GOA undertaking studies that determined that coarse sand had an IRD origin and revealed glacial duration, the timing of the increase in IRD was an aim that was not met during Leg 18 (Von Huene *et al.*, 1971a, b, c, and e) and the biostratigraphy palaeoceanography and palaeoclimatology were the scientific objectives of Leg 18 (Creager *et al.*, 1971). Both drilling expeditions were limited to low sediment recovery, low sediment accumulation (25mm/yr during the Pliocene and lower

Pleistocene, Site 887) and age constrain difficulties (Zahn *et al.*, 1991; McDonald *et al.*, 1999; Galbraith *et al.*, 2007; Gebhardt *et al.*, 2008).

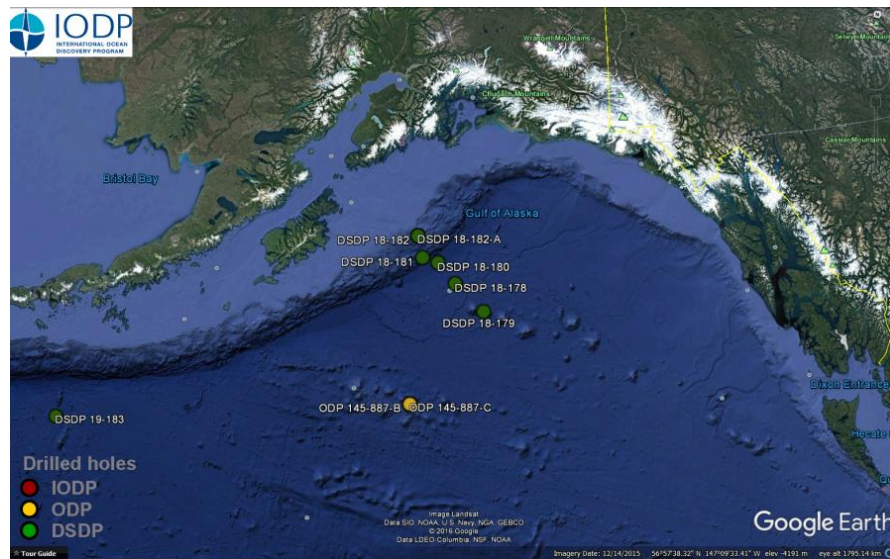


Figure 2.15: Location of DSDP Leg 18 and ODP Leg 145 Pacific drilling sites. DSDP in green and ODP in yellow (Image source: Google Earth and IODP, 2016). Yellow and green dots were drilled sites in the GOA during 1992 and 1971, respectively.

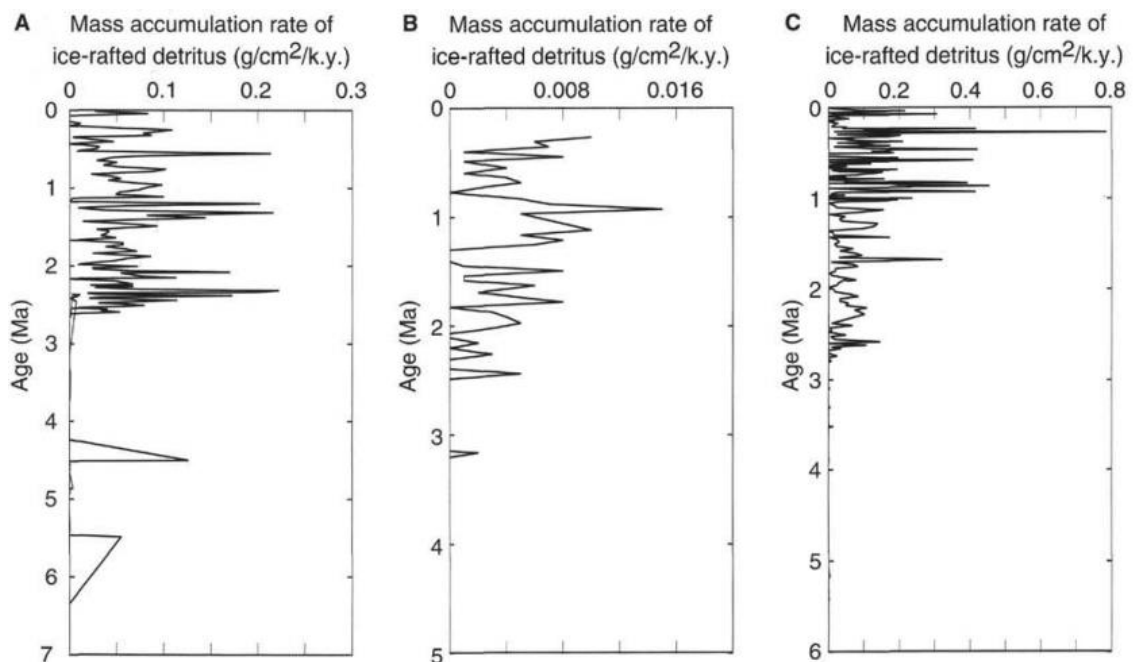


Figure 2.16: Gulf of Alaska glaciation. Sites 881 (A), 883 (B) and 887 (C) IRDs ($\text{g}/\text{cm}^2/\text{kyr}$) (Krissek *et al.*, 1995).

Dust input into the middle extratropical North Pacific (Site 885) peaks with the onset of the NHG (2.6-2 Ma) (Snoeckx *et al.*, 1995). The first sustained IRD

appearance across the North Pacific is at 2.8 Ma during the late Pliocene (Rea *et al.*, 1995), which suggests tidewater glaciers were present in the GOA during the onset of the Pleistocene due to the proximity of the Alaska coast to the drilling sites (Figure 2.16).

Seismic-reflection profiles of the Surveyor Fan in the GOA prior to Expedition 341 revealed important changes in sedimentation rates (which were interpreted responses to climatic events) preserved in three sequences, which started during the Miocene (Jaeger *et al.*, 2011). It is argued that glacial-interglacial cycles and sea valley formation controlled the variations in the sedimentation of the Surveyor Fan. Thus, the model of the evolution of the Surveyor Fan sedimentation and onshore glaciation prior to the drilling of Expedition 341 was interpreted as comprising 4 stages (Figure 2.17):

- 1- Glacial Interval A (~5.5 Ma). First evidence of tide-water glaciation in the Gulf of Alaska.
- 2- Warm mid-Pliocene with diminished glacial activity
- 3- Glacial interval B: Return to glaciation associated with the ONHG (~2.9-2.4 Ma).
- 4- Glacial Interval C: Intensification of the glacial activity at ~1 Ma associated with the MPT.

However, the direct links between stages 1-4 and our understanding of Neogene climate change are poorly understood due to the lack of climate data and well-constrained glacial chronologies for the GOA. Since the climate of the GOA is important for modern glacial advance/retreat and meltwater supply, it was argued that the stratigraphy of the Surveyor Fan could provide important new insights into climate-glaciation interactions from an ice-proximal location (Reece *et al.*, 2011). This was part of the rationale for the activities of Expedition 341.

The sedimentation of the Surveyor Fan has been interpreted as a product of fluvial and then glacial erosion from the Chugach-St Elias ranges, and records of exhumation and uplift, as well as evidence for glaciation and climatic changes within the GOA (Reece *et al.*, 2013, Gulick *et al.*, 2015). The timing of the glaciation was not well constrained, and before Expedition 341 a major seismic reflector had

been interpreted as evidence for glacial advance either related to the onset of NHG or as a result of the MPT (Gulick *et al.*, 2015). Previous analysis of a site further offshore (ODP 887) had revealed that the terrigenous sedimentation doubled at the NHG and again at the MPT (Krissek *et al.*, 1995; Reece *et al.*, 2011). This two-step pattern of increasing sedimentation rates associated with the NHG and MPT was confirmed at Sites U1417 and U1418 during Expedition 341 (Gulick *et al.*, 2015).

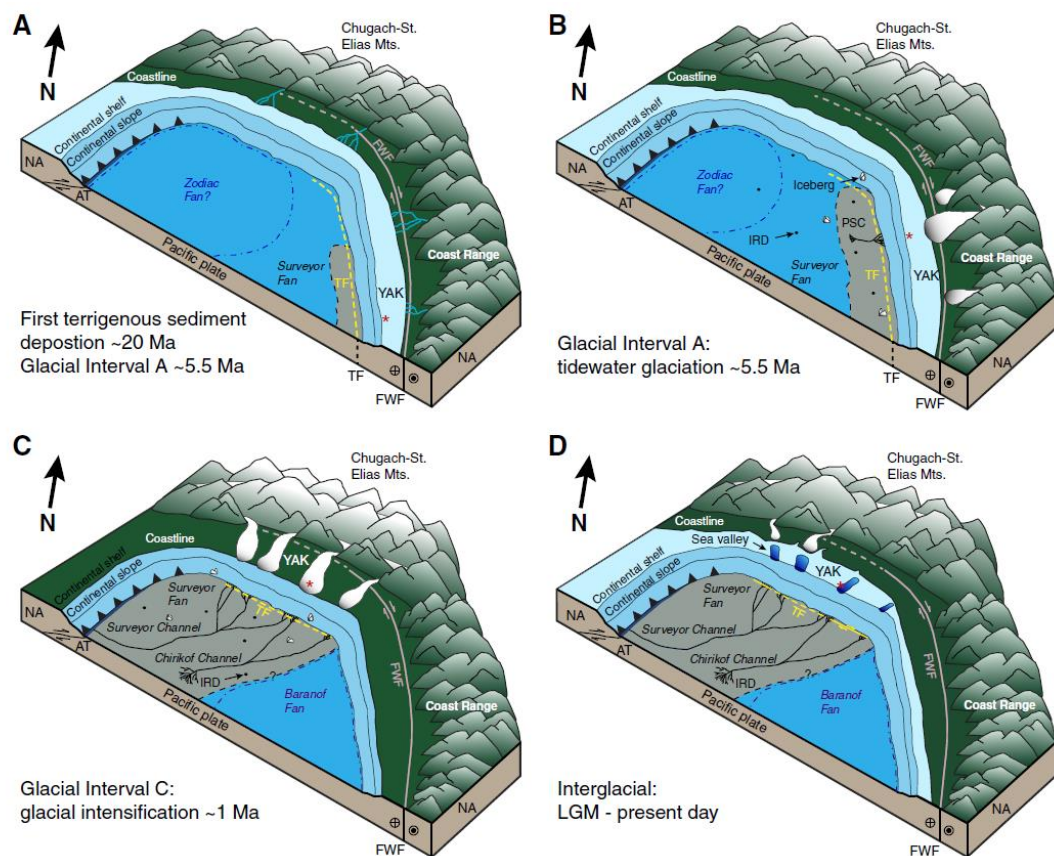


Figure 2.17: Glacial Intervals in the development of the Surveyor Fan from 20 Ma until the present day (Reece *et al.*, 2013).

What remains unclear is whether these times of increased glaciation are climatic or tectonically-driven (Gulick *et al.*, 2015), because there is no local climate history for the region, and nor is the precise timing of the glaciation well-constrained. This uncertainty provides the rationale for generating histories of climate and ice-sheet history for the GOA over the Pliocene and Pleistocene, the focus of this project.

2.4.1 Summary

Previous drilling expeditions to the GOA, DSDP Leg 18 and ODP Leg 145 have failed to produce a continuous Pliocene and Pleistocene climate record due to poor sediment recovery and sedimentation rates and age model constrains. A new drilling expedition (IODP Expedition 341) offers the opportunity to complement the scarce existing data on the timing and intensity of different glacial periods during the Pliocene and Pleistocene and to assess climate-ocean interactions as well as study the role of St. Elias mountain uplift in the climate changes.

2.5 Reconstructing climate and glaciated environments

In this thesis, the palaeoceanography and palaeoenvironmental history of the GOA will be reconstructed using proxy evidence preserved in the marine sediments collected by IODP Expedition 341. Climatic proxies are indirect records of past climates preserved in various sequences, including trees, ice sheets, corals and sediments. This thesis will focus on a specific set of proxies: called 'biomarkers'. Biomarkers are organic molecules that are preserved in sediments, are produced by known organisms, and preserve signatures of Earth's climate or environmental conditions over millions of years (Rosell-Melé and McClymont, 2007). Organic components need to fulfil a number of characteristics to be biomarkers: these include having good preservation over time; to be indicative of a determined environment; to be related to a natural producer; and to be widely found in global sediments (Rosell-Melé and McClymont, 2007).

Several organic biomarker proxies preserve a climatic and environmental record in marine sediments and so they represent an appropriate methodology to reconstruct past ocean temperatures, salinity, organic terrestrial and marine inputs, and marine productivity changes (Rosell-Melé and McClymont, 2007). Therefore, biomarker studies are a good approach to study climate-ocean-ice-sheet interactions. One of the advantages of biomarkers is that they are often identifiable to one type of environment or biological source, narrowing down the window of speculation in the interpretation of the results in comparison with other non-biomarker proxies and especially those analysing bulk sediments (i.e. C and N). Another advantage is that some of the biomarkers show relative resistance to degradation (Kim *et al.*, 2006; Rosell-Melé and McClymont, 2007). However, it

has been shown that, as organic molecules, biomarkers can be affected by processes of preservation and advection of fine-grained sediment under certain environmental settings (Ohkouchi *et al.* 2002). This thesis will utilise biomarkers for palaeotemperature, palaeosalinity, marine productivity and terrestrial organic matter provenance. Additional proxy information which has been provided by other members of the IODP Expedition 341 science party include diatom counts, IRD and foraminifera $\delta^{18}\text{O}$.

2.5.1 Palaeotemperature proxy: the $U^{K_{37}}$ and $U^{K_{37}'}$ indices

SSTs provide important climate information which includes the ocean response to radiative forcing and changes in ocean circulation. The $U^{K_{37}}$ and $U^{K_{37}'}$ index uses the relative abundance of the alkenone biomarkers to reconstruct past SSTs. Alkenones are long chain ketones synthesised by algae of the division Haptophyta and class Prymnesiophyceae (Marlowe *et al.*, 1984). In the case of *Emiliania huxleyi*, the most common coccolithophore of the world's oceans at modern, alkenones constitute $8.0 \pm 2.9\%$ of the total organic carbon present on the living cells (Prahl *et al.*, 1988). Alkenones can serve as palaeothermometers, since C_{37} alkenones have 2, 3, or 4 unsaturations depending on the water temperature in which the haptophytes grew (Brassell *et al.*, 1986; Rosell-Melé, 1998). Two indices are used depending on the latitude of the sediment core location: $U^{K_{37}}$ or $U^{K_{37}'}$ (Equation 2.1) for polar and sub-polar locations, because the $C_{37:4}$ alkenone is generally only found in cold environments, and $U^{K_{37}'}$ (Equation 2.2) for temperate locations in the absence of $C_{37:4}$:

$$\textbf{Equation 2.1: } U^{K_{37}} = (C_{37:2} - C_{37:4}) / (C_{37:2} + C_{37:3} + C_{37:4}) \text{ (Brassell et al., 1986)}$$

$$\textbf{Equation 2.2: } U^{K_{37}'} = C_{37:2} / (C_{37:2} + C_{37:3}) \text{ (Prahl and Wakeham, 1987)}$$

It has been shown that the inclusion of the $C_{37:4}$ alkenone does not strengthen the temperature calibration using $U^{K_{37}}$ calibration, but, instead, it leads to increased scatter in the correlation between $U^{K_{37}}$ and SSTs (Sikes and Sicre, 2002). As a result, it is recommended that the $U^{K_{37}'}$ index is used to reconstruct SSTs in most oceanographic regimes (Rosell-Melé and McClymont, 2007) and considering the abundance of $\%C_{37:4}$ (Bendle *et al.*, 2005). The SST calibration of Müller *et al.* (1998) (Equation 2.3) was generated by analysing the $U^{K_{37}'}$ index from core tops

from 370 sites spanning 60°S to 60°N around the world (Atlantic, Indian and Pacific Oceans) and correlating these to the annual mean SST from 0m water depth (Figure 2.18).

Equation 2.3: $U^{K_{37}'} = 0.033SST + 0.044$ (Müller *et al.*, 1998)

The Müller *et al.* (1998) SST calibration has been used for SST between 0 to 29°C, it is within the error limits of other SST calibrations such as Prahll and Wakeham (1987) and Prahll *et al.* (1988) and offers a SST with a 1.5 °C error confidence (Müller *et al.*, 1998).

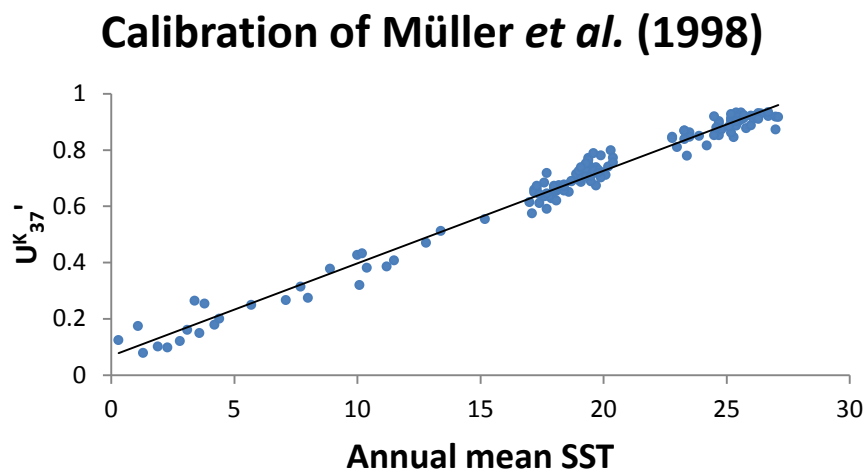


Figure 2.18: Calibration of $U^{K_{37}'}$ into annual mean sea surface temperatures based on core tops across 60°S to 60°N in the Atlantic, Indian and Pacific Oceans (Müller *et al.*, 1998).

In a core-top study for the central North Pacific, the $U^{K_{37}'}$ SST calibration of Müller *et al.* (1998) offers a 2°C SST interval of confidence for the region in waters between 4 and 9°C and led to overestimations of the mean annual SST (Meheust *et al.*, 2013). The Sikes *et al.* (1997) SST calibration from the Southern Ocean (Equation 2.4) has been suggested to be more reliable for the Northeast Pacific and Bering Sea, and is calibrated to summer temperatures (Meheust *et al.*, 2013). This calibration has a similar slope as the calibration from Sikes and Volkman (1993) (Equation 2.5) also from the Southern Ocean and for temperature ranges of 4 to 25 °C (Sikes and Volkman, 1993). However, below that value, the calibration fits better with an exponential regression (Sikes and Volkman, 1993).

Equation 2.4: $U^{K}_{37'} = 0.038T - 0.082$ ($r = 0.960$, $r^2 = 0.921$)

Equation 2.5: $U^{K}_{37'} = 0.0414T - 0.156$

Global core top analysis shows that $U^{K}_{37'}$ correlates best with the annual sea surface temperatures following the calibration of Müller *et al.* (1998) rather than with seasonal SSTs in the 0-10m water depth (Herbert, 2001). $U^{K}_{37'}$ has been widely used to reconstruct sea surface temperatures over the Pliocene and Pleistocene (e.g. McClymont *et al.*, 2005a; Petrick *et al.*, 2015a; Bachem *et al.*, 2016; Lawrence *et al.*, 2013; Naafs *et al.*, 2012), including in the Pacific (McClymont *et al.*, 2008; McClymont *et al.*, 2012; Herbert *et al.*, 2010; La Riviere *et al.*, 2012). However, Pliocene alkenone SST data from the subarctic Pacific is limited to ODP Site 882 in the Northwest (Martinez-Garcia *et al.*, 2010; McClymont *et al.*, 2008). At Site 882, a seasonality signal in the $U^{K}_{37'}$ index due to water stratification regime was used to explain a signature of warming across the Pliocene-Pleistocene transition and cooling in other temperature proxies (Haug *et al.*, 2005).

In a study of prymnesiphyte algae productivity, a consistent late spring seasonal maximum was shown between three sites on a transit of the northeast Pacific, yet despite this seasonality in production a constant integrated annual flux of alkenones was observed (Prah *et al.*, 1993). Walinsky *et al.* (2009) quantified the C_{37} alkenones on the continental shelf in the Gulf of Alaska and discovered a decrease in abundance relative to organic carbon with increasing latitude above 58.5 °N, especially sites proximal to land.

The $U^{K}_{37'}$ index does not show significant differences in its calibration to SST when the species of Haptophyte algae that synthesises the alkenones changes (Müller *et al.*, 1998; McClymont *et al.*, 2005). Zooplankton herbivory does not alter the index, which would invalidate the alkenones as palaeotemperature proxies (Grice *et al.*, 1998). Similarly, algae growth rate and nutrient availability does not influence $U^{K}_{37'}$ in open oceans (Müller *et al.*, 1998). Alkenone degradation within the water column and sediments does not significantly change the U^{K}_{37} index, as all 3 C_{37} alkenones appear to have similar susceptibility to degradation, and the index remains unaltered after diagenesis (Rosell-Melé and McClymont, 2007; Prah and Muehlhausen, 1989). As an example, in a culture study under oxic conditions

(which are the most aggressive conditions for organic matter degradation), the $U^{K_{37}}$ increased only by 0.03 units which is equivalent to less than a 1°C temperature change (Teece *et al.*, 1998). Alkenones thus provide a robust method for reconstructing GOA SSTs.

2.5.2 The % $C_{37:4}$ proxy

The $C_{37:4}$ alkenone has been identified in its highest concentrations within cold and fresh subpolar waters (Bendle *et al.*, 2005). The relative abundance of $C_{37:4}$ is expressed as a percentage of the total C_{37} alkenones (% $C_{37:4}$). $C_{37:4}$ is present in oceans with salinities from 33.8 to 35.1 ‰ and temperatures colder than 13°C (Sikes and Sicre, 2002; Liu *et al.*, 2007) which corresponds to polar and sub-polar waters, but it is not found in temperatures above 15°C (Brassell and Englinton., 1986).

Although there is a temperature control over the abundance of $C_{37:4}$ (it is most abundant at low temperatures), it has also been shown that it may also be influenced by salinity (Bendle *et al.*, 2005). At low salinities the % $C_{37:4}$ was shown to increase, and could comprise up to 77% of the C_{37} alkenones (Bendle *et al.*, 2005). In the open ocean it has been discussed to be dependent on changes in growth rate, light or nutrient input (Sikes and Sicre, 2002) based on culture works (e.g. Conte *et al.*, 1998). Bendle *et al.* (2005) suggested that alkenone temperature calibrations should include $C_{37:4}$, but the lack of data on $C_{37:4}$ abundance from the subarctic Pacific limits the calibration of $U^{K_{37}}$ in this region (McClymont *et al.*, 2008). In a study from the Nordic seas, Bendle *et al.* (2005) established a threshold to discriminate between coastal and subpolar/subarctic water masses ($>5\%$ $C_{37:4}$) and open marine settings in mid to low latitudes ($<5\%$ $C_{37:4}$). In the subarctic Pacific, high $C_{37:4}$ is associated with cooler and fresher water masses (Harada *et al.*, 2006), but there are few $U^{K_{37}}$ data and widely spread around this region (i.e. McClymont *et al.*, 2008) which limits the creation of a regional calibration for the Northern Pacific. The use of the $C_{37:4}$ alkenone as a proxy for freshwater inputs has been previously suggested (e.g. Bendle *et al.*, 2009; Martrat *et al.*, 2007). In these examples, Martrat *et al.* (2007) interpreted their $C_{37:4}$ in the Iberian margin as evidence for freshwater inputs to the North Atlantic driven by high inputs of iceberg discharges to the North Atlantic, perhaps driven by ice-sheet surging

Bendle *et al.* (2009) further applied the %C_{37:4} proxy to determine the transition from marine to brackish waters in response to sea level change, from sediments in northwest Scotland.

2.5.3 Productivity proxies

Marine export production is the term used to quantify plankton deposition in the deep ocean sediment. In this section, we will outline the alkenones, sterols, carbon and nitrogen stable isotopes as productivity export proxies.

2.5.3.1 Alkenones

It has been observed (Prahl *et al.*, 1988) that there is a correlation between the amount of alkenones synthesised and the number of synthesiser cells present. Higher C₃₇ alkenone abundance in marine sediments could then be used as an indicator of higher marine production, specifically from the haptophytes which include the coccolithophores. Yet only a small portion (35%) of alkenones which are produced in the surface water reaches the sea floor and about 1% of alkenones are present in the total OC (Goni *et al.*, 2004, Cariaco Basin). Total alkenone concentrations are more representative of the overall export production of the coccolithophores (Rosell-Melé and McClymont, 2007). There is also the potential for the alkenone signal to be diluted when sedimentation rates increase. The alkenone mass accumulation rate (MAR) eliminates the sedimentation rate factor that can mask the “real” alkenone export signal when expressed by alkenone per gram of sediment analysed. When used in conjunction with SST, alkenone concentrations/MAR has been used to provide indications of changing haptophyte production due to upwelling or water column stratification (Herbert, 2003). For example, high (low) obliquity has been linked to El Niño (La Niña)-like conditions and lower (higher) productivity in the tropical Pacific during the MPWP (e.g. Lawrence *et al.*, 2006).

In addition to the C₃₇ alkenones, the haptophytes also synthesise a suite of C₃₈ alkenones which can have an ethyl or methyl alkylation as well as 2 or 3 unsaturations (Marlowe *et al.*, 1984a). The C₃₇ alkenones to C₃₈ alkenones ratio (K₃₇/K₃₈) increase in growth temperature (Prahl and Muehlhausen, 1989). Due to a distinct range of alkenone distributions during their synthesis (Prahl *et al.*, 1988), the K₃₇/K₃₈ has been suggested to indicate different relative contributions of

Emiliania huxleyi to *Gephyrocapsa oceanica* at the time of alkenone production (Yamamoto *et al.*, 2000). Sikes *et al.* (1997) showed that in the South Pacific, K_{37}/K_{38} between the values of 0.6 to 0.8 show a provenance of *G. oceanica* and values between 0.8 to 2 show syntheses by *E. huxleyi*. Another study from core top material (Herbert, 2001) also shows a similar provenance of alkenones using K_{37}/K_{38} . Alkenone production by *G. oceanica* differs in their growth water temperature in comparison with the alkenone production of *E. huxleyi* (Herbert, 2003). McClymont and Rosell-Melé (2005) shows that despite evolutionary events in coccolithophores, the stability in alkenone based ratios (e.g. K_{37}/K_{38}) suggested that the process of alkenone synthesis appeared to have been unaffected and so modern calibrations could be applied.

2.5.3.2 Sterols

Sterols are lipids synthesised by a variety of eukaryotic organisms. Brassicasterol is a biomarker synthesised by diatoms and haptophytes (Volkman, 2006; Volkman, 1986; Kanazawa *et al.*, 1971). It has been used as an open-water proxy (Müller *et al.*, 2011) and as a diatom export productivity proxy (Lei *et al.*, 2012). Brassicasterol is sourced from marine and freshwater phytoplankton (Stein *et al.*, 2003). The marine or terrigenous environment provenance of brassicasterol (Kanazawa *et al.*, 1971; Stein and McDonald, 2004) needs to be carefully argued to avoid proxy misinterpretation. Dinosterol is a biomarker synthesised by dinoflagellates (Boon *et al.*, 1979) and it is used as a dinoflagellate marine export proxy (D'Anjou *et al.*, 2013). Dinosterol is absent from terrestrial environments (Volkman, 1986). However, dinosterol is not synthesized by all dinoflagellate species (Rampem *et al.*, 2010) and has been found in cultured diatoms (Volkman *et al.*, 1993). Still, it can be a useful biomarker to assess dinoflagellate productivity (Castaneda *et al.*, 2011). Dinosterol is more abundant in glacial sediments of the eastern tropical Pacific and it peaks prior to or synchronously with the alkenones during glacial maxima (Brassell, 1993). In southern California, the downcore profile of dinosterol corresponds to dinoflagellate blooms recorded in marine sediments (Brassell, 1993). Comparing dinosterol and brassicasterol inputs to a sediment sequence can be used to determine the broad shifts in phytoplankton community structure (Lei *et al.*, 2012).

The advantages of these sterols as proxies is their wide distribution that covers a range of different environments (Brassell and Eglinton, 1983a,b) and ages, despite their vulnerability to degradation due to the hydroxyl group (Gaskell *et al.*, 1974). Caveats of sterol proxies include their higher susceptibility to degradation in comparison with the alkenones, which are very resistant to degradation (Wakeham *et al.*, 2002).

2.5.3.3 Carbon and Nitrogen stable isotopes as productivity proxies

Carbon and nitrogen have naturally occurring isotopic forms: the lighter ^{12}C and ^{14}N and the heavier ^{13}C and ^{15}N . Lighter isotopes are more frequent in nature ($^{12}\text{C}=98.9\%$ and $^{14}\text{N}=99.6\%$) than heavy ones ($^{13}\text{C}=1.1\%$ and $^{15}\text{N}=0.4\%$) (CIAAW, 2007-2015). Relative carbon and nitrogen isotopic composition is often represented as the heavier vs. the lighter form and written as $\delta^{13}\text{C}$ and $\delta^{15}\text{N}$. The $\delta^{13}\text{C}$ and $\delta^{15}\text{N}$ values can vary between reservoirs. For example, in a process called isotope fractionation, photosynthesis from plants and phytoplankton preferably uptakes the lighter isotopes ^{12}C and ^{14}N from air or water masses, as it requires less energy consumption to generate food (e.g. Galbraith *et al.*, 2004). In the ocean, when phytoplankton die they are transported into the deep ocean leaving the surface water enriched in the heavy isotopes (e.g. Ryabenco, 2013; Galbraith *et al.*, 2004). Early diagenetic alterations have been considered in sedimentary $\delta^{13}\text{C}$ and $\delta^{15}\text{N}$ of organic carbon, but these processes have been suggested to act uniformly not altering the ratio (De Lange *et al.*, 1994). However, changes in dominant phytoplankton producers have been suggested to drive changes in organic $\delta^{13}\text{C}$ and $\delta^{15}\text{N}$ (Zohary *et al.*, 1994; Gu *et al.*, 1999; Syväranta *et al.*, 2006). The $\delta^{13}\text{C}$ and $\delta^{15}\text{N}$ of organic carbon is a useful analysis to determine the chemistry of the water according to the fractionation of $\delta^{13}\text{C}$ and $\delta^{15}\text{N}$ from biota (Knudson and Ravelo, 2015).

A second process called denitrification accounts from N fractionation losses in the water column (20 to 60%) and deep sediments (60 to 100%). Denitrification is the process of converting nitrate molecules into N_2 by bacterial reduction. The ineffective denitrification leaves a residue of heavy $\delta^{15}\text{N}$ organic carbon in the water column of 9 to 18% heavier than the global average. This heavy $\delta^{15}\text{N}$ organic

carbon signature can be advected to the surface ocean and be incorporated into marine organic structure (Galbraith *et al.*, 2004; Addison *et al.*, 2012).

2.5.3.4 *N-alkanes and sterols*

The presence of terrestrial biomarkers in marine sediments can give valuable information on environmental change onshore and/or the processes that might have transported those biomarkers from land, through wind-blown dust, or sediments eroded and transported within rivers or by glaciers (Ikehara *et al.*, 2000). These terrestrial biomarkers include *n*-alkanes (leaf waxes) and more complex lipids derived from soils and peats (e.g. branched glycerol dialkyl glycerol tetraether (Walsh *et al.*, 2008). This thesis focusses upon the terrigenous biomarkers (*n*-alkanes and sterols) found within the GOA sediments.

The *n*-alkanes are termed 'long chain' or 'short chain', which are synthesised by dominantly terrestrial or marine plants and algae, respectively. Terrestrial C₂₇, C₂₉ and C₃₁ alkanes are synthesized by vascular plants (Rieley *et al.*, 1991). The C₃₁/C₂₉ *n*-alkane ratio has been previously used to reconstruct terrestrial vegetation and therefore, climate (Lei *et al.*, 2013), because woody plants typically display *n*-alkane distributions of C₂₇ or C₂₉ and indicate humid climate whereas grass typical *n*-alkane distribution is C₃₁, which is associated with dry climate. Aquatic C₁₅, C₁₇ and C₁₉ alkanes are synthesised by algae (Bourbonniere and Meyers, 1996) and C₁₇ to C₂₀ alkanes are also synthesized by cyanobacteria (Han and Calvin, 1969). Both cyanobacteria and microalgae (i.e. diatoms, coccolithophores and dinoflagellates) are included in the term "phytoplankton". Therefore, *n*-alkanes are an indicator of both the production and/or preservation of organic matter from terrestrial and marine sources (Lei *et al.*, 2012). However, short chain *n*-alkanes have been also interpreted as terrigenous source OM (Stein *et al.*, 2003).

The *n*-alkanes serve as tracers for marine or terrestrial organic matter and are often presented as a "terrestrial to aquatic" ratio (TAR) Cranwell (1973). High TAR values indicates a higher accumulation of long chain *n*-alkanes in relation to short chain *n*-alkanes, typically attributed to increase in higher plant contribution to the sediment in detriment of marine productivity export production. The opposite is indicative of low TAR values.

$$\text{Equation 2.6: } TAR = ([C_{27}] + [C_{29}] + [C_{31}]) / ([C_{15}] + [C_{17}] + [C_{19}])$$

Different degradation rates from terrestrial and marine biomarkers make the use of *n*-alkanes difficult (Damsté *et al.*, 2002a). Longer chain *n*-alkanes are more resistant to degradation than short chain *n*-alkanes (Pancost and Boot, 2004) and the *n*-alkanes are more resistant overall than other compounds of plant waxes such as *n*-alkanoic acids and *n*-alkanols (Cranwell, 1981).

In the GOA, there are several petrogenic organic matter sources i.e. coal (Walinsky *et al.*, 2009; Jaeger *et al.*, 2014), that can complicate the TAR index, since older organic matter containing long chain *n*-alkanes may be transported to the marine sediments (Walinsky *et al.*, 2009). However, the carbon preference index (CPI) can also be used to determine the organic matter maturity (Bray and Evans, 1961). High CPI indicates low maturity and predominantly land-plant input, and low CPI (below 1) indicates low maturity carbonates and/or hypersaline environments (Peters *et al.*, 2005). In the GOA, CPI values are between 1.2 to 2.9, showing a mixture of terrestrial plants (CPI~ 3-10) and fossil hydrocarbons (CPI~1) (Walinsky *et al.*, 2009), which may complicate interpretations of provenance or changing transport pathway to the core sites examined here.

β-sitosterol is a sterol that has been previously used as terrigenous source biomarker in near shore Siberia Arctic marine environments (Xiao *et al.*, 2013). β-sitosterol can have both terrestrial and marine sources from phytoplankton (Huang and Meinschein, 1976; Volkman, 1986) and bacteria but have been interpreted as dominantly terrestrial in Russian Arctic rivers (van Dongen *et al.*, 2008).

2.5.3.5 Bulk C and N

The sedimentary content of Carbon (C) and nitrogen (N) and their relative abundance (C/N ratio), can all be used as indicators of source of OM and productivity. Because of the different OM constituents, terrestrial plant contains a higher C/N ratio than marine algae (Killops and Killops, 2005). This difference resides in the function of C chains to the vertical growth of plants. Low C/N ration suggests increased abundance of marine algae (e.g. Walisky *et al.*, 2009) or terrigenous aquatic plant material, high C/N ratio indicates increased abundance

of more complex plants (terrestrial source) (Nasir *et al.*, 2016). Some of the problems with using bulk C and N ratio for determining the terrestrial or marine source of sediments is that C and N are elements present in many substances as they are very common chemical elements. TOC and TON records can be used as overall marine productivity and terrestrial OM export to the deep ocean (Hopkinson and Vanillo, 2005). As an example, one of the difficulties with TOC and TON widespread occurrence is the erosion of older records of TOC and TON unlocked in the bedrock (i.e. erosion of coal from land) into the ocean (Stein and McDonald, 2003). The TOC and TON are susceptible to degradation and changing sedimentation rates. Therefore, it is often represented as mass accumulation rates. The differential TOC and TON degradation can alter the TOC/TON ratio.

2.5.4 Additional data sets to this study

In addition to the biomarker and bulk elemental composition data produced in this thesis, the assessment of ocean and ice sheet history in the GOA benefits from collaboration with a number of scientists from Expedition 341, who have provided their data for comparison here.

2.5.4.1 Ice Rafted Debris (IRD)

Dr Ellen Cowan has provided IRD data for Site U1417 in order to examine ice sheet behaviour since the Pliocene. IRD (>125 μ m) transport to the distal ocean and lakes can only be explained by iceberg or sea ice transport, as they are too heavy to be transported by wind (Jansen *et al.*, 2000). Glaciers are highly erosive agents that incorporate eroded material into the ice at the ice-rock interface as the glacier advances. Once the glacier has reached the sea and begins calving, the sediment incorporated within the ice can be transported in icebergs, before melting out and being deposited on the seafloor (e. g. Kuijpers *et al.*, 2014). An alternative transport mechanism for IRD is via sea ice, which originates at the sea surface, but in shallow and coastal areas sea ice can thicken to freeze onto the sea floor or the coastline thus incorporating material into the sea ice itself (e .g. Turner *et al.*, 2015; Cowan *et al.*, 2008; Kuijpers *et al.*, 2014). IRD has been widely used to track re-advance of glaciers around the world (e.g. Bailey *et al.*, 2012) and there is debate regarding how the IRD iceberg delivery is related to glacier advance or retreat (e.g.

Bohaty and Harwood, 1998; Bachem *et al.*, 2016; Kandiano *et al.*, 2004; Krissek *et al.*, 1995).

2.5.4.2 Diatoms

Dr. Oscar Romero has provided counts of diatoms identified in Site U1417 for the Pliocene and early Pleistocene. Total diatom count is a valuable record to assess changes in diatom productivity and/or diatom preservation, the latter dependent on changes in water column and sediment chemistry, which can be aggressive for silica preservation (Crosta and Koc, 2007). Diatom production is very dependent upon Si nutrient supply into the ocean which can be delivered by glacier runoff and river input (Dugdale and Wilkerson, 2001). The concentration of silicic acid with respect to other macronutrients explains the dominance of calcareous or siliceous productivity (Ragueneau *et al.*, 2000). In the northeast Pacific, a maximum in silica concentrations is found in intermediate and deep waters, due to dissolution of sinking particles (Talley, 1992).

2.5.4.3 Oxygen isotopes

Planktonic foraminiferal shells are the most common material used for climate reconstruction (Kucera, 2007). Planktonic foraminifera are single-cell calcium carbonate shelled marine phytoplankton algae. Their preservation in the sediment record and organic and inorganic molecular structure provide numerous chemical studies of the environment from nutrient availability and marine isotope fractionation (e.g. Walinsky *et al.*, 2009) and water temperature and salinity (Mg/Ca, $\delta^{18}\text{O}$). Dr. Hirofumi Asahi has provided the $\delta^{18}\text{O}$ record from *Neogloboquadrina pachyderma* (sin) 150-250 μm , a planktonic foraminifera from high latitudes. Benthic foraminifera $\delta^{18}\text{O}$ is an indicator of global ice volume (e.g. Lisieki and Raymo, 2005), however, planktonic $\delta^{18}\text{O}$ can be influenced by changes in surface water temperature and/or dominance of evaporation/precipitation during glacial and interglacials as well as global volume (Tiedeman *et al.*, 1994).

2.6 Summary

The evolution of the North Pacific Ocean over the Pliocene and Pleistocene still remains largely unknown. However, there is potential to advance our understanding of both how the North Pacific Ocean evolved as well as the development of the Cordilleran Ice Sheet, with implications also for the tectonic

history of the region. Understanding the North Atlantic and North Pacific linkages during past warm intervals similar to the present climate are important to resolve climatic equations about the functioning of the Earth in order to simulate future climate scenarios, key for a current changing climate and uncertain future. The mid-Pliocene period constitutes a potential analogue of future climatic scenarios, yet data is lacking from the North Pacific to understand the patterns and causes of climate change in this region. Our understanding of the development and later expansion of the northern hemisphere ice sheets over the Pliocene-Pleistocene is also dominated by evidence from the North Atlantic region. In this thesis, newly recovered marine sediment cores from the Gulf of Alaska offer an outstanding opportunity to address these Pliocene and Pleistocene climate questions. A suite of biomarker analyses are undertaken in order to reconstruct changes to GOA oceanography and links to environmental changes onshore. In the following Chapters, the detailed methodology applied in this thesis will be outlined (Chapter 3), before presenting (Chapter 4) and discussing (Chapters 5-7) the results which have been obtained and their implications for the research questions posed in Chapter 1.

Chapter 3: Methods

3.1 Site U1417

3.1.1. Sediment lithology

Site U1417 (56° 57.38'N, 147° 7.86 'W, 4218m water depth) recovered 700 m of marine sediments during IODP Expedition 341 (29th May to 29th July 2013). Site U1417 extends through the Miocene until the Holocene (Figure 3.1; Jaeger *et al.*, 2014). Throughout this thesis, the depths of sediment recovered will always be referred to using the initial shipboard composite depth model, also known as “the splice” and termed CCSF-A (Jaeger *et al.*, 2014), which allows correlation across the different holes drilled at each site (Figure 3.2; Figure 3.3).

Site U1417 can be divided in six lithostratigraphic units. Lithostratigraphic unit VI consists of dark grey mud interbedded with dark sandy mud and silt. It also contains non-glaciated but gravity flow related thin diamict beds (Jaeger *et al.*, 2014). Lithostratigraphic unit VH consists of greenish grey biosiliceous ooze (Jaeger *et al.*, 2014). Lithostratigraphic unit VF consists mainly of greenish grey diatom ooze (Jaeger *et al.*, 2014). Lithostratigraphic unit VE consists of grey and dark greenish grey banded mud with diamict and silt beds. It contains traces of organic matter and wood detritus (Jaeger *et al.*, 2014). Lithostratigraphic unit VD consists of diatom ooze and mud (Jaeger *et al.*, 2014). Lithostratigraphic unit VC consists of a dark grey diamict with variable abundance of clasts of variable sizes and sources (i.e. mud and coal), interbeds of mud and plant debris (Jaeger *et al.*, 2014). Lithostratigraphic unit VB consists of dark grey to greenish diatom with mud and diatom ooze intervals. Bioturbation occurs at different degrees (Jaeger *et al.*, 2014). Lithostratigraphic unit VA consists of dark grey bioturbated mud with diamict, sand and diatom ooze intervals and possible coal content (Jaeger *et al.*, 2014). Lithostratigraphic unit IV consists of dark grey to greenish bioturbated mud with diatom intervals (Jaeger *et al.*, 2014). Lithostratigraphic unit III consists of a diamict with variable abundance of clasts and with bioturbated grey mud (Jaeger *et al.*, 2014). Lithostratigraphic unit II consists of grey to greenish-grey mud with

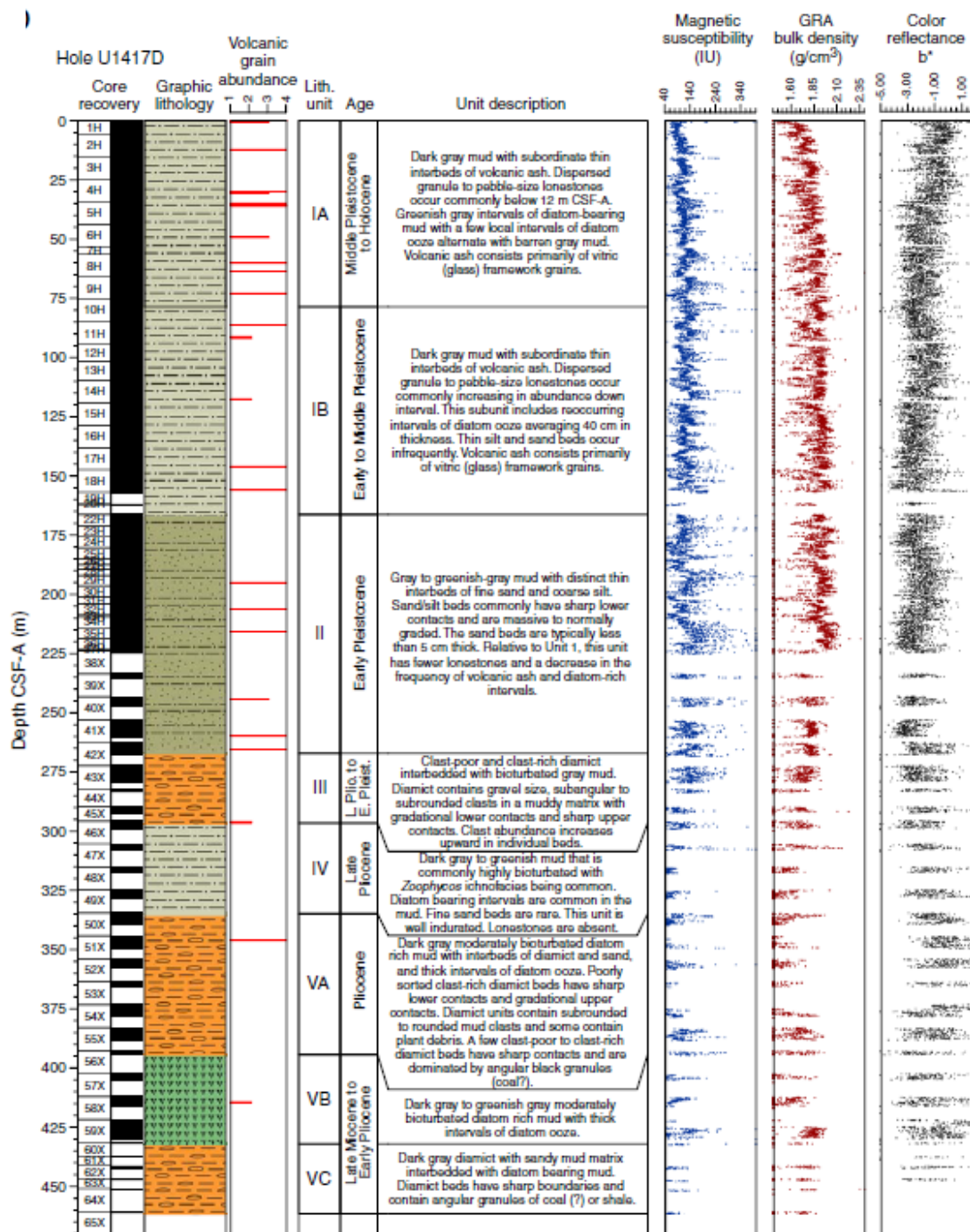


Figure 3.1: Site U1417 Hole D. From left to right: CSF-A depth, sample label, core recovery, graphic lithology, volcanic grain abundance, lithostratigraphic units, age, unit descriptions, magnetic susceptibility, GRA bulk density and color reflectance (Jaeger et al., 2014).

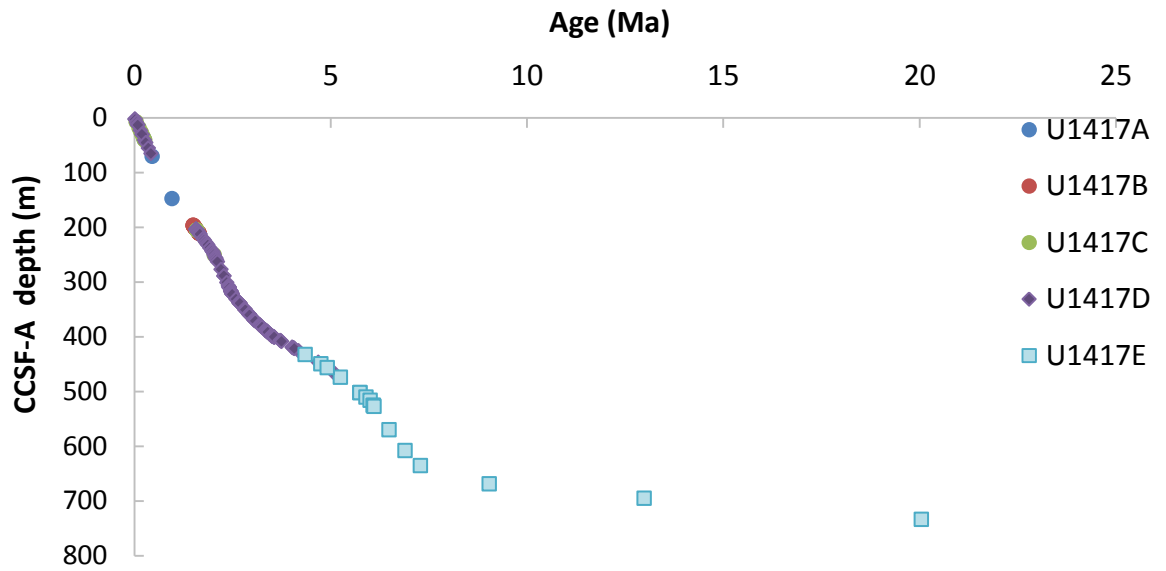


Figure 3.2: Age/depth U1417 core break. Age (Ma) and CCSF-A depth (m) showing the core breaks, U1417A (blue), U1417B, (red), U1417C (green), U1417D (purple diamond) and U1417E (blue square).

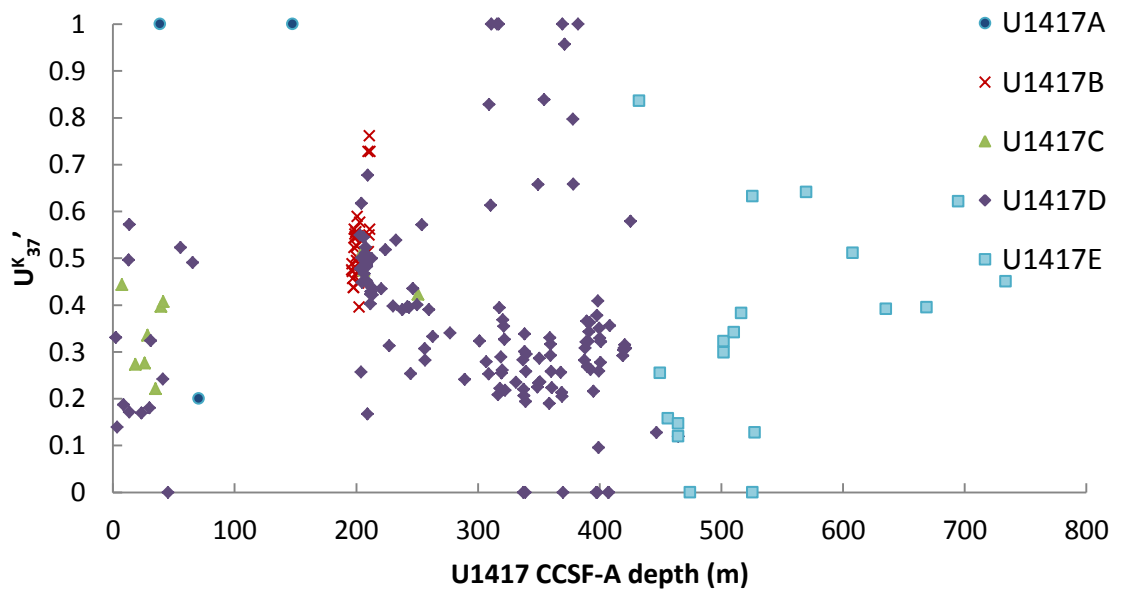


Figure 3.3: U1417 U^{k}_{37}' data and core break. U1417 U^{k}_{37}' vs Age (Ma) and CCSF-A depth (m). U^{k}_{37}' vs vs U1417 CCSF-A depth (m) showing the core breaks, U1417A (light blue star), U1417B, (purple cross), U1417C (green triangle), U1417D (blue diamond) and U1417E (red square).

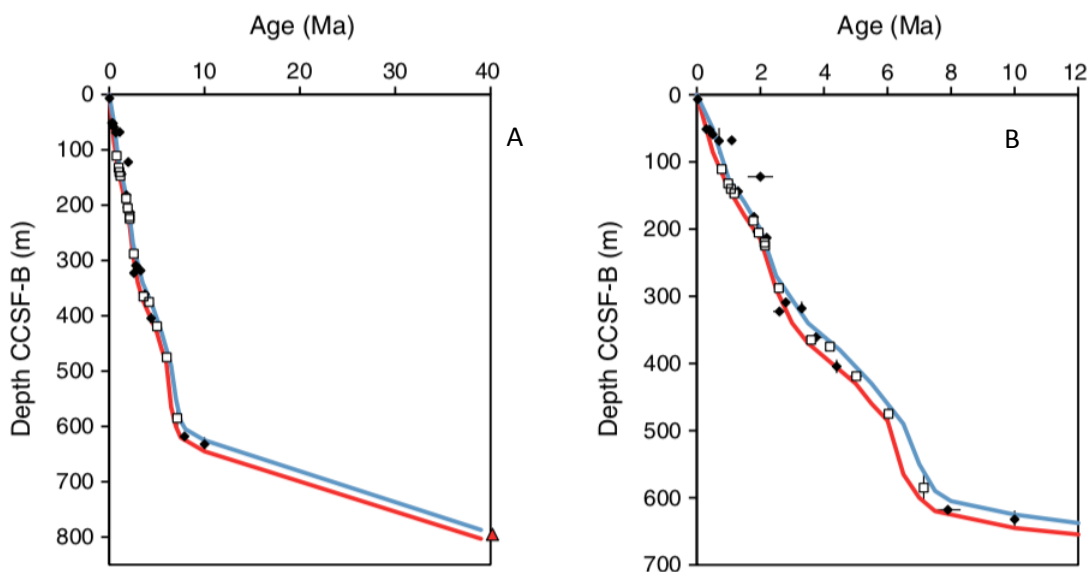


Figure 3.4: Site U1417's shipboard age model. Red and blue curves represent the minimum and maximum age, the dashed curve represents the maximum age and the red curve represent the average age. Diamonds, squares and triangles represent ages obtained by biostratigraphy, paleomagnetism and Site 178 basement, respectively (Jaeger *et al.*, 2014).

sand and silt beds with lonestones, volcanic ash and diatom intervals (Jaeger *et al.*, 2014). Lithostratigraphic unit IA consists of dark grey mud with volcanic ash, lonestones, diatom mud, ooze and mud intervals (Jaeger *et al.*, 2014). Figure 3.1 shows some of these lithostratigraphic units contained in Core U1417D.

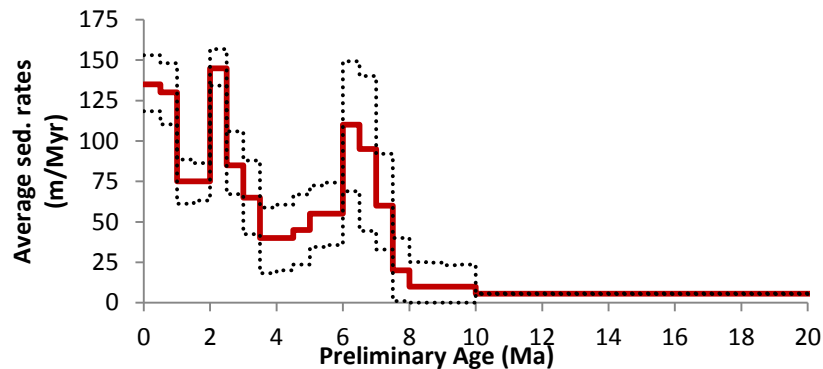
Site U1417 contains several magnetic reversals such as the Gauss/Matuyama Boundary, the Upper Jaramillo and the Brunhes/Matuyama, and a radiolarian age of 0.4 ± 0.1 Ma at 60.24 ± 3.07 m CCSF-A, which have been used to reconstruct this site's age model (Figure 3.4 and Table 3.1). Poor carbonate preservation across the Pliocene and early Pleistocene prevents production of a stable isotope stratigraphy using foraminifera. Shipboard magneto- and bio-stratigraphy indicates that, at Site U1417, average sedimentation rates varied as shown in Figure 3.5 (Jaeger *et al.*, 2014).

3.1.2 Sediment recovery and sampling

IODP 341 Exp. was able recover 70% of the sediment after drilling Site U1417 (Expedition 341 Scientists, 2014). However, for the Pliocene sections this led to a number of core breaks, preventing a continuous sequence. Overall, 27 samples

Table 3.1: Polarity Zone interpretation for U1417 (Jaeger et al., 2014).

Polarity zone interpretation			Age	\pm (Ma)	Depth CCSF-B (m)	\pm (m)
C1n	(B)	Matuyama/Brunhes	0.781	0.02	111	1
C1r.1n	(T)	Jaramillo	0.988	0.02	133	1.5
C1r.1n	(B)	Jaramillo	1.072	0.02	140	1
C1r.2n	(M)	Cobb Mountain	1.179	0.02	150.5	1.5
C2n	(T)	Olduvai	1.778	0.02	186	2
C2n	(B)	Olduvai	1.945	0.02	205.5	1
C2r.1n	(T)	Reunion	2.128	0.02	220.5	2
C2r.1n	(B)	Reunion	2.148	0.02	224.5	4
C2r.2r	(B)	Gauss/Matuyama	2.581	0.02	287.5	1
C2An.3n	(B)	Gilbert/Gauss	3.596	0.02	365	5
C3n.1n	(T)	Cochiti	4.187	0.02	375	5
Middle of C3n.3n (B) Sidufjal to C3n.4n (B)						
Thvera			5.017	0.218	419	5
C3An.1n	(T)		6.033	0.1	475	10
C3Bn	(T)		7.14	0.1	585	20

**Figure 3.5: Site U1417 shipboard sedimentation rates detailed for the last 20 Ma (Jaeger et al., 2014).**

were analysed for the 20 to 4 Myr record, which makes a sampling resolution of 1.68 samples/Myr, 173 samples were analysed for the 4 to 1.5 Ma, which corresponds to a sampling resolution of 69,2 samples/Myr and 28 samples were analysed for the last 0.5 Myr, which corresponds of a sampling resolution of 56 samples/Myr. Samples collected for biomarker analysis were around 4 cm thick, and taken every 44 cm between 700-420 m CCSF-A (1.6 to 4 Ma) and every 21 cm

along the top 200 m CCSF-A. Based on shipboard sedimentation rates (Figure 3.5), Table 3.2 outlines temporal average, minimum and maximum represented in U1417 samples and their sample spacing.

Samples from Site U1417 analysed in this study span cores U1417E to U1417A from bottom to top of the record (U1417E 37R-1 to U1417E 7R-2; U147D 59X-2 to U1417D 1H-1W 44-48; U1417C 25H-3 to U1417C 2H-2W 49-53; U1417B 22H-4W 45-46 to U1417B 20H-2W 83-87; U1417A 16H-3 to U1417A 4H-5) (Figure 3.2; Figure 3.3).

The oldest sample analysed for this study from Site U1417, U1417E 37R-1 (733.7 m CCSF-A, ca.20 Ma) (Figure 3.2), belongs to lithostratigraphic unit VI (Jaeger *et al.*, 2014). The next oldest sample, U1417E 32R-2 (694.7 m CCSF-A and 12.9 Ma), belongs to lithostratigraphic unit VH (Jaeger *et al.*, 2014). U1417E 29R-5 (668.6 m CCSF-A and 9 Ma) belongs to lithostratigraphic unit VF. U1417E 26R-1 to 20R-1 (midpoint CCSF-A depth of 635.3 to 527.5 m and 6.3 to 6.1 Ma) belongs to lithostratigraphic unit VE. U1417E 15R-4 (of 525.7 m CCSF-A and 6 Ma) belongs to lithostratigraphic unit VD. U1417E 14R-1 to U1417E 13R-1 (516.3 m to 501.9 m CCSF-A and 6 to 5.7 Ma) belong to lithostratigraphic unit VC. U1417E 10R-2 to 7R-2 (474.3 to 449.6 m CCSF-A and 5.2 to 4.7 Ma) belongs to lithostratigraphic unit VB. U147D 59X-2 to 57X-1 (464.5 to 446.6 m CCSF-A and 5.0 to 4.7 Ma) belong to lithostratigraphic unit VB. U1417D 54X-4W 70-74 to U1417D 50X-1W 55-59 (421.4 to 378.3 m CCSF-A and 4.0 to 3.2 Myr old) belong to lithostratigraphic unit VA. U1417D 49X-3W 49-53 to U1417D 46X-1W 0-4 (371.1 to 336.6 m CCSF-A and 3 to 2.7 Ma) belong to lithostratigraphic unit IV. U1417D 45X-2W 70-74 to U1417D 43X-1W 10-14 (332.2 to 315.8 m CCSF-A and 2.6 to 2.4 Ma) belongs to lithostratigraphic unit III. U1417D 42X-CCW 23-27 to U1417D 24H2W 9-13 (311 to 203.2 m CCSF-A and 2.4 to 1.6 Ma) belongs to lithostratigraphic unit II. U1417D-9H 5-10 to U1417D 1H-1W 44-48 (83.6 to 2.1 m CCSF-A and 0.5 to 0.02 Ma) belong to lithostratigraphic unit IA. U1417B 20H-7W 12-16 to U1417B 20H-2W 113-117 (202.9 to 196.6m CCSF-A and 1.6 to 1.5 Ma) that belongs to lithostratigraphic unit II. U1417A 9H-3 to U1417A 2H-6 (72.4 to 19.5 m CCSF-A and 0.5 to 0.1 Ma) belongs to lithostratigraphic unit IA.

Table 3.2: Site U1417 sample ID, age range, average, minimum and maximum sedimentation rates (Jaeger et al, 2014) and temporal resolution (kyr) of the sediment samples analysed in this PhD.

Sample ID	Section age (Ma)	Aver. sed rates (m/Myr)	Min sed. rates (m/Myr)	Max sed. rates (m/Myr)	Aver. Temp. res. (kyr)	Min. temp. res. (kyr)	Max. temp. res. (kyr)	Aver. Sample Spacing (kyr)	Min. Sample Spacing(kyr)	Max Sample Spacing(kyr)
U1417E 37R-1	20	5.5	5.3	5.7	7.3	7.5	7.0	80	83.0	77.2
U1417E 32R-2	12.9	5.5	5.3	5.7	7.3	7.5	7.0	80	83.0	77.2
U1417E 29R-5	9	10.0	0.0	24.7	4	N/A	1.6	44	N/A	17.8
U1417E 26R-1 - U1417E 24R-1	7 - 6.5	95	44.4	140.2	0.4	0.9	0.3	4.6	9.9	3.1
U1417E 20R-1 - U1417E 14R-1	6.5 - 6	110	68.9	149.2	0.4	0.6	0.3	4.0	6.4	2.9
U1417E 13R-1	6 - 5.5	55	35.6	74.3	0.7	1.1	0.5	8.0	12.4	5.9
U1417E 10R-2 - U1417D 59X-2	5.5 - 5	55	34.5	72.5	0.7	1.2	0.5	8.0	12.7	6.1
U1417E 8R-3 - U1417D 57X-1	5 - 4.5	45.0	23.5	66.9	0.8	1.7	0.6	9.8	18.7	6.6

U1417E 10R-2 - U1417D 54X-2W 36-40	4.5 - 4	40.0	20.1	66.6	1	2.0	0.6	11.0	21.9	6.6
U1417D 54X-1W 76-80 - U1417D 52X-1W 134-138	4 - 3.5	40.0	18.3	58.9	1	2.2	0.7	11.0	24.0	7.5
U1417D 52X-1W 97-101 - U1417D 49X-1W 35-39	3.5 - 3	65.0	42.3	88.0	0.6	0.9	0.4	6.8	10.4	5.0
U1417D 48X-2W 106-110 - U1417D 44X-1W 18-23	3 - 2.5	85.0	67.1	106.0	0.5	0.6	0.4	5.2	6.6	4.1
U1417D 43X- CCW 41-45 - U1417D 32H-2	2.5 - 2	145.0	134.2	156.9	0.3	0.3	0.2	3.0	3.3	2.8

U1417D 32H-2W 17-21 - U1417B 20H-2W 83-87	2 - 1.5	74.0	63.2	86.4	0.5	0.6	0.5	6.0	7.0	5.1
U1417A 9H-3 - U1417D 1H-1W 44-48	0 - 0.5	135.0	118.4	153.0	0.3	0.3	0.3	1.5	1.8	1.4

3.2 Site U1418

3.2.2 Sediment lithology

Site U1418 (58°46.60' N, 144° 29.55' W, 3667 m water depth) recovered 950 m of marine sediments, during IODP Expedition 341. Site U1418 extends back to the early Pleistocene to the Holocene. Lithostratigraphic unit IIB which consists of dark grey to dark greenish grey mud with laminations, clasts, diamict with low abundance of clasts of iceberg rafting or sea-ice origin, bioturbated volcanic ash and lonestones (Jaeger *et al.*, 2014). Lithostratigraphic unit IIA which consists of dark grey to dark greenish grey muddy diamict with low abundance of clasts of iceberg rafting or sea-ice origin and dark grey mud with clasts, sand, lonestones and granules (Jaeger *et al.*, 2014). Lithostratigraphic unit I, which consists of dark grey to dark greenish grey silt and mud intervals with intermittent diatom abundances, sand, volcanic sediments and lonestones (Jaeger *et al.*, 2014).

Site U1418's age is constrained by the Upper Jaramillo and the Brunhes/Matuyama Boundary (Figure 3.6 and Table 3.3). Site U1418 average sedimentation rates varies from 575 m/Myr from 0.5 to 0.4 Ma, 825 m/Myr from 0.4 to 0.2 to 1275 m/Myr from 0.2 to 0.0 Ma (Jaeger *et al.*, 2014) (Figure 3.7).

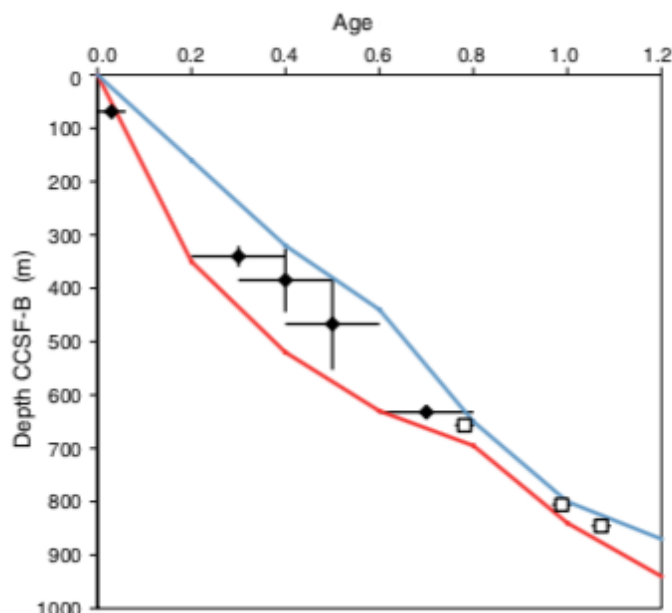
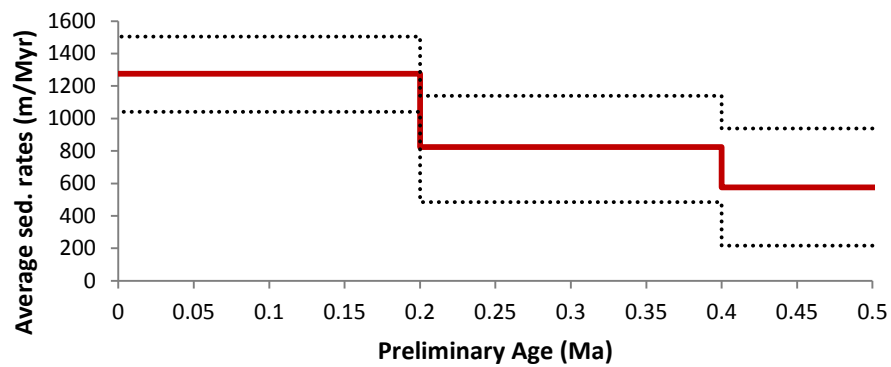


Figure 3.6: Site U1418's shipboard age model (Jaeger *et al.*, 2014). Red, black and blue diamonds are dates obtained from magnetostrigraphy, biostratigraphy and a low-magnetic susceptibility interval suspected to correspond to MIS 5e, respectively.

Table 3.3: Polarity Zone interpretation for U1418 (Jaeger et al., 2014).

Polarity chron interpretation	Age (Ma)	Core, section, interval (cm)	Depth	Depth
			CSF-A (m)	CCSF- B (m)
		341-U1418F		
C1n (B)			645.43	
Matuyama/Brunhes	0.781	Top 41R-5, 115	645.43	
		Base 44R-1, 15	668.1	668.1
C1r.1n (T) Jaramillo	0.988	Top 57R-6, 55	801.58	801.58
		Base 58R-5, 75	809.89	809.88
C1r.1n (B) Jaramillo	1.072	Top 62R-2,90	844.25	844.25
		Base 62R-4, 35	846.35	846.35

**Figure 3.7: Site U1418 shipboard sedimentation rates (Jaeger et al., 2014).**

3.2.3 Sediment recovery and sample resolution for study

Samples from U1418 analysed span core sites U1418A to U1418F from top to bottom of the record (U1418A 3H-2 145-150 to U1418 32H-1 115-130; U1418B 1H-1 145-150 to U1418B 2H-1W 145-150; U1418C 22H-4W 24-26 to U1418C 30H-3W 124-126; U1418D 6H-3W 44-46 to U1418D 36X-4W 59-61; U1418E 2H-2W 64-66 to U1418E 6H-5W 104-106; U1418F 5R-3W 94-96 to U1418F 22R-5W 104-106) (Figure 3.8 and 3.9). The oldest samples analysed for this study from Site U1418 are from core Site U1418F. U1418F 22R-5W 104-106 to U1418F 10R-2W 88-90 (94-96 to 471.4 to 303.1 m CCSF-A and 503.1 to 382.1 ka) belong to

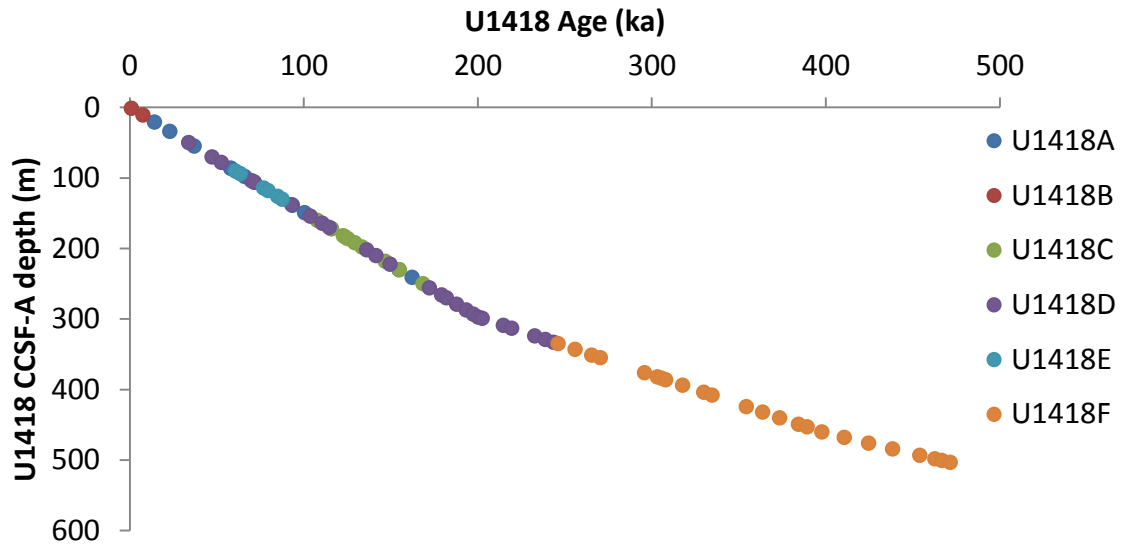


Figure 3.8: Age/depth U1418 core break. Age (ka) and CCSF-A depth (m) showing the core breaks, U1418A (blue), U1418B, (red), U1418C (green), U1418D (purple diamond), U1418E (light blue square) and U1418F (orange).

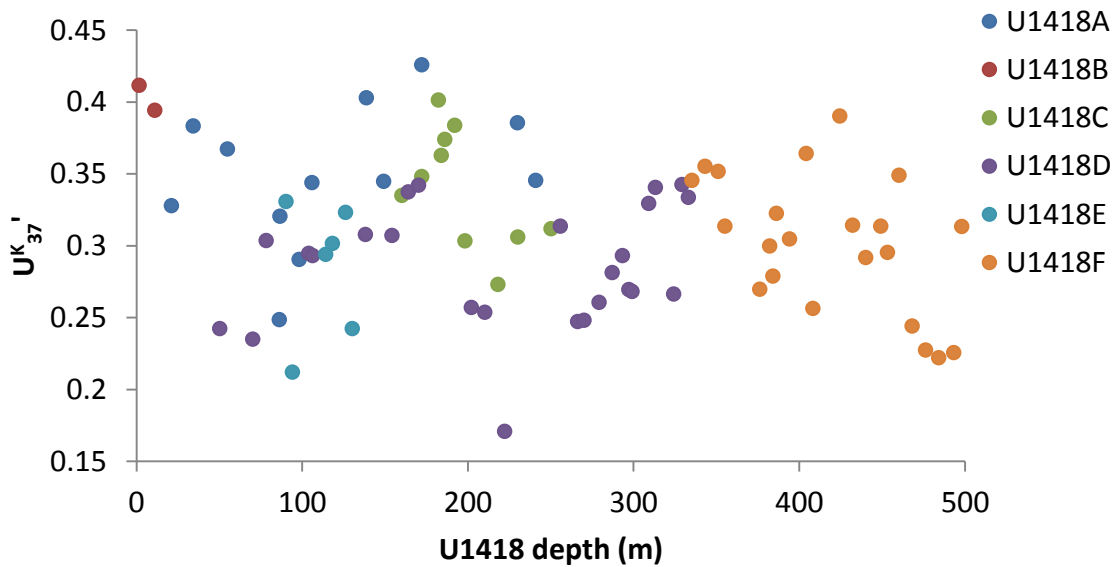


Figure 3.9: U^k_{37}' vs depth and U1418 core breaks. U1418 Age (Ma) vs U1418 CCSF-A depth (m). U^k_{37}' vs vs U1418 CCSF-A mid-point depth (m) showing the core breaks, U1418A (dark blue), U1418B, (red), U1418C (green), U1418D (purple), U1418E (light blue) and U1418F (orange).

Table 3.4: Site U1418 sample ID, age range, average, minimum and maximum sedimentation rates (Jaeger et al., 2014) and temporal resolution (kyr) of the sediment samples analysed in this PhD thesis.

Sample ID	Section age (Ma)	Aver. sed rates (m/Myr)	Min sed. rates (m/Myr)	Max sed. rates (m/Myr)	Aver. Temp. res. (yr)	Min. temp. res. (yr)	Max temp. res. (yr)	Aver. Sample Spacing (yr)	Min. Sample Spacing (yr)	Max Sample Spacing (yr)
U1418F 22R-5W 104-106- U1418F 19R-1W 113-115	0.5-0.4	575	216	939	34.8	92.6	21.3	111.3	296.3	68.2
U1418F 18R-2W 135-150- U1418D 32H-2W 21-23	0.4-0.2	825	484	1139	24.2	41.3	17.5	77.6	132.2	56.2
U1418D 31H-2W 97-99- U1418B 1H-1 145-150	0.2-0	1275	1041	1505	15.7	19.2	13.3	50.2	61.5	42.5

lithostratigraphic unit IIB. U1418F 9R-5W 14-16 to U1418F 5R-3W (295.8 to 246.1 m CCSF-A and 376.1 to 335.1 ka) belongs to lithostratigraphic unit IIA. U1418D 36X-4W 59-61 to U1418D 34X-1W 4-6 (243.6 to 214.6 m CCSF-A and 333.0 to 309.1 ka) belongs to lithostratigraphic unit II. U1418D 32H-3W 74-76 to U1418D 6H-3W 44-46 (202.5 to 33.8 m CCSF-A and 299.1 to 50.1 ka), U1418C 30H-3W 124-126 to U1418C 22H-4W 24-26 (168.4 to 107.8 m CCSF-A and 240.9 to 160.1 ka), U1418B 2H-1W 145-150 to U1418B 1H-1 145-150 (7.5 to 1.0 m CCSF-A to 11.1 to 1.4 ka) and U1418A 32H-1 115-130 to U1418A 3H-2 145-150 (162.2 to 14.1 m CCSF-A and 240.9 to 21.0 ka) belong to lithostratigraphic unit I.

IODP 341 Exp. was able to recover 86.4% of material drilled at Site U1418 (Jaeger et al, 2014). Our sample resolution for U1418 is approximately one sample every 6kyr for SST and alkenone abundance analyses. Most the samples are 2 cm thick with an average separation between samples of 6.4 m. Average, minimum and maximum sedimentation rates have been used to reconstruct the time represented in each sediment sample included in this study, as well as the separation between samples (Table 3.4).

3.3 Sampling protocol and sample storage

The IODP Expedition 341 sampling party minimised the contamination of organic compounds during the sampling of the marine sediment cores for biomarker studies. All samples were collected using metal tools, and were wrapped in foil before being placed in individual plastic bags for posting. Samples arrived to Durham University on the 12th December 2013. Since arrival samples were kept stored in a fridge with temperatures below 5°C to control organic matter decomposition, and freeze dried as soon as possible.

3.4 Organic biomarker laboratory procedure

The organic biomarker laboratory procedure starts with the preparation of glassware and reagent material needed and the following microwave lipid extraction, silica columns for flash chromatography, and the silylation of the polar compounds (Figure 3.10).

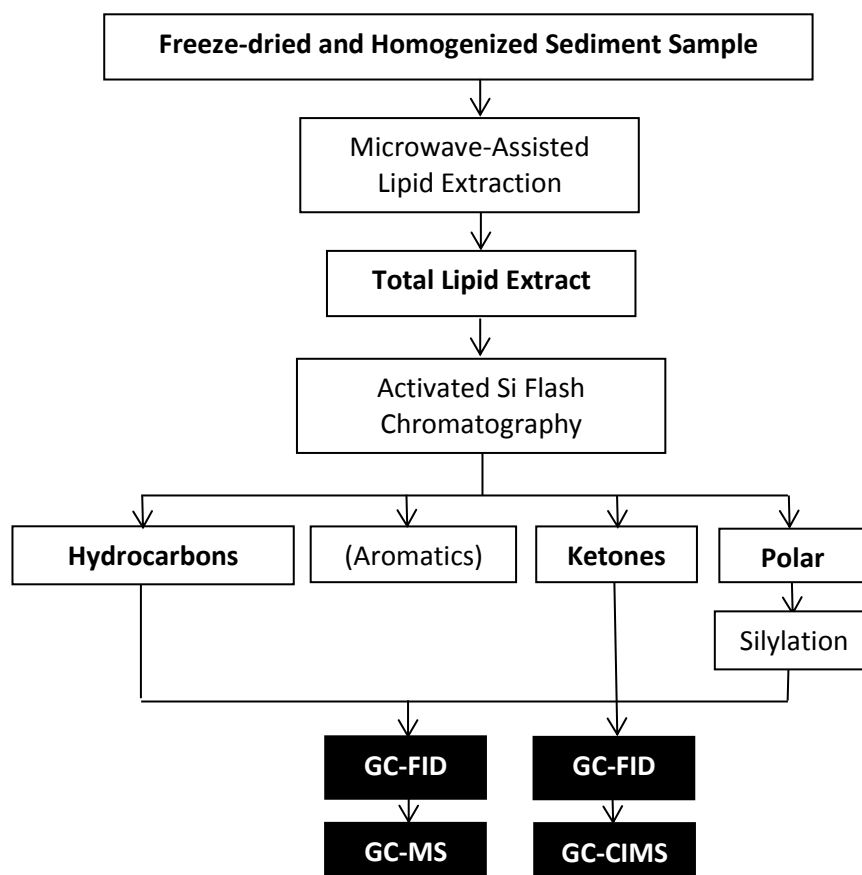


Figure 3.10: Schematic organic biomarker laboratory procedure conducted in this study.

3.4.1 Glassware and reagent preparation

Contamination minimisation is a key component of biomarker laboratory routine. In the laboratory, contamination is avoided with various stages of, often repetitive, cleaning of the different equipment. Glassware was cleaned with a brush and tap water removing all sediment and ink labels and left overnight in a 1% dilution of ©Decon in deionised water. The following day, glassware was rinsed with tap water and deionised water and left to dry. The glassware was wrapped in aluminium foil and heated at 450 °C for 4 hours, then stored in a dry cupboard.

Teflon tubes and lids for the microwave system were cleaned with tap water and deionized water and left to dry, then stored wrapped in aluminium foil in a dry cupboard. Before their use, they were rinsed with a mixture of dichloromethane and methanol (DCM:MeOH) 3:1 and allowed to dry. Plastic tops for screw top test tubes were soaked overnight in a beaker filled with 1% ©Decon diluted in

deionized water. The following day they were rinsed with tap water and deionised water and left to dry. Magnetic stirrers for the microwave are cleaned by sonicating in a DCM:MeOH (3:1) mix for 5 minutes. Silica (Si) gel high purity grade pore size 60 Å, 220-440 mesh particle size, 35-75 µm particle size (©Sigma Aldrich) was cleaned and activated by heating to 450°C during 4 hours in a beaker covered with aluminium foil for flash chromatography. After that it was stored in a desiccator cupboard to avoid humidity. Cotton wool was rinsed with DCM and left to dry covered with aluminium foil. After that it is also stored in a desiccator cupboard.

Hexane and DCM wash bottles in the different Gas chromatography (GC) instruments were cleaned and refilled with “fresh” solvent prior setting a run of samples. DCM blanks were run before samples and within sample sequences, alongside extracted standards, to monitor potential contamination and to monitor performance.

3.4.2 Freeze-dry

To prepare the samples for lipid extraction, sediment samples were freeze-dried to control organic matter degradation and to eliminate moisture from the sediments. In contrast with air drying, freeze-drying has been suggested as the best method to dry sediment samples for SST studies, as choosing freeze-drying as a drying method has been observed to have no significant impact in altering the $U^{K_{37}}$ index up to 0.035, reducing the error distribution of SST up to 0.5 °C (McClymont *et al.*, 2007).

Samples were cooled to -80 °C overnight or longer, then freeze dried over two days. Samples were stored at room temperature until being analysed.

3.4.3 Lipid extraction

Lipids were extracted from sediment samples using the microwave-assisted extraction method of Kornilova and Rosell-Melé (2003). Temperature has been the only determinant factor influencing the yields of the biomarkers and 70°C has presented a better alkenone extraction recovery (68% higher alkenones per gram of sediment) than the ultrasonication extraction (Kornilova and Rosell-Melé, 2003). The microwave-assisted biomarker extraction did not show a bias towards

the determination of the $U_{K_{37}}$ index in comparison with the traditional ultrasonic method for biomarker extraction (Kornilova and Rosell-Melé, 2003). To quantify each fraction from the chromatography, a mixed internal standard contained similar compounds as the targeted compounds to conduct the analysis of this study. In this study, we added 5α -cholestane and C_{36} *n*-alkane for *n*-alkanes fraction (F1), 2-nonadecanone for the ketone fraction (F2) and 5α -androstan- 3β -ol for the sterol fraction (F3); Sigma Aldrich).

Microwave extraction involves weighting freeze-dried sediments into microwave Teflon tubes, adding the internal standard, the solvent DCM:MeOH 3:1 and a magnetic stirrer. The samples are then microwaved, heating to 70°C during 5 minutes for a total lipid extraction. The sediments are centrifuged at 2500 rpm for 5 minutes and the decanted supernatant solvent is placed into round bottom flasks. Most of the remaining solvent is removed with the rotary evaporator to obtain the lipid extracts. Separation of the total lipid extract into three fractions was undertaken by silica flash chromatograph (Section 3.4.4).

The first “test” batches of “squeeze cakes” (or samples used for pore water analysis) extracted contained sediment samples across U1417. For these, the recommended 3.5 g of sediment was extracted with 15 ml of a solution of dichloromethane: methanol (DCM:MeOH 3:1), including $20\mu\text{l}$ of a mix standard containing known concentrations of 5α -cholestane, hexatriacontane and 2-nonadecanone (Sigma-Aldrich). However, method development was necessary to adjust to the low organic matter content characteristics of our samples (<1 wt (%); Jaeger *et al.*, 2014) and to old organic material found in some samples. The weight of sediment extracted increased to 5 g, the solvent volume added for extraction to 18 ml and the silica column separation of lipids changed (Section 3.4.4).

3.4.4 Active silica flash chromatography

The active silica flash columns method is used to separate the total lipid extract into the compounds of interest. Si columns preparation start with the activation of the Silica gel (high purity grade pore size 60\AA 220-440 mesh particle size, 35-75 μm particle size for flash chromatography, ©Sigma Aldrich) by heating it to 450°C during 4 hours. Silica columns are prepared by plugging a clean glass pipette with

clean cotton wool, then adding 4 cm of active silica above. Two column volumes of hexane are run through the column to clean and prepare it for chromatography. For each fraction, a different solvent is used depending on the chemical behaviour of the compounds due to be collected. During the “test” batches, 4 column volumes of Hexane, DCM and MeOH were added for the collection of hydrocarbons (F1), ketones (F2) and the polar fraction (F3). However, the F2 chromatograms presented a hump in the baseline from the presence of aromatic compounds which was masking the ketone fraction compounds. A more exhaustive lipid separation to ensure a clean F2 was developed according to the following: 3 ml of Hexane for hydrocarbons collection (F1), 1.5 ml of a mixture of Hexane and DCM (Hexane:DCM 9:1) for aromatics (added to F1), 5.5 ml of DCM for ketones (F2) and 16 ml of a mixture of Ethyl Acetate and Hexane (Ethyl Acetate: Hexane 20:80) for polars (F3). Once collected, F1 and F2 fractions are transferred to GC vials and run by gas chromatography analysis (Section 3.5) or stored in the fridge for future analyses (Killops and Killops, 2005).

3.4.5 Silylation of the polar fraction

The most polar fraction, or F3, is the least volatile fraction and the most retained on the GC system. To make the polar fraction more volatile and decrease the reactivity of these compounds with the GC column, we derivatized the F3 of the samples. Derivatisation involves the modification of a chemical compound into a more suitable product for analysis. Silylation is a type of derivatization which involves the replacement of a OH-group of a compound with a trimethylsilyl (-SiMe₃) group. *N,O*-Bis(trimethylsilyl)trifluoroacetamide (BSTFA; Sigma Aldrich) is used to convert the alcohols and sterols into trimethylsilyl derivatives, which change the properties of the compound to a more volatile nature.

Polar fraction (F3) samples were dried under a stream of N₂. Once completely dried they were silylated using 50 µl of *N,O*-Bistrifluoroacetamide (BSTFA) and 50 µl of DCM, warmed to 70 °C for 1 hour and then allowed to cool overnight. The silylated polar fractions were dried under a stream of N₂ and re-dissolved in 25 µl of DCM for analysis by gas chromatography.

3.5 Organic compound identification and quantification

All lipid fractions were dried using a flux of N₂ and re-dissolved in DCM for gas chromatography mass spectrometer (GC-MS) and gas chromatography flame ionization detector (GC-FID) and re-dissolved in 25 µl 2,2,4-trimethylpentane for gas chromatography-chemical ionization mass spectrometry (GC-CIMS) analysis. Samples are first run in a GC-FID to quantify the biomarker concentration in comparison with the quantity of internal standard present on each sample (5 α -cholestane and C₃₆ *n*-alkane for hydrocarbon fraction, 2-nonadecanone for the alkenone fraction and 5 α -androstane-3 β -ol for the polar fraction; Sigma Aldrich) (Equation 3.1). Then samples are run in a GC-MS to identify the organic compounds present of the sample via their molecular weight spectrometry. Fraction 2 samples are run in a GC-CIMS, adapted from the method of (Rosell-Melé et al., 1995), which is used to increase the resolution of the alkenone signal for a more accurate U^K₃₇ index quantification and SST calculation when samples are low in organic carbon %. The full instrument details for these three approaches are now outlined.

A Thermo Scientific Trace 1310 GC-MS was equipped with a programmable temperature vaporizer (PTV) injector and with a temperature program set at 60°C during 2 min and then raised at 12°C min⁻¹ until reaching 150 °C and then raised again to 310 at 6 °C min⁻¹ and hold during 25 mins. 0.8 ml of sample was injected and He was used as a carrier flow. *N*-alkanes, ketones and sterols were separated using a 60m x 0.25 mm i.d., Restek RXi-5ms column (0.25µm 5% diphenyl-95% dimethyl polysiloxane coating). GC-MS was used for identification of the organic matter represented in the GC-FID chromatograms of the sediment samples.

A Thermo Scientific Trace 1310 gas chromatograph was fitted with flame ionization detector (GC-FID) and a split-splitless injector. Compressed air is set as the air flow, helium (He) is set as the carrier flow, nitrogen (N) as a make-up flow and hydrogen (H) helps with ignition. The oven temperature is set at 70°C for 2 minutes 70°C for 2 mins, then increased to 170°C at 12°C min⁻¹, then increased to 310°C at 6.0 °C min⁻¹, then held at 310°C for 35 mins. *N*-alkanes, ketones and sterols were separated using a 60m x 0.25 mm i.d., Restek RXi-5ms column

(0.25 μ m 5% diphenyl-95% dimethyl polysiloxane coating). 1 ml of sample is injected. The samples were quantified with reference to internal standards (5 α -cholestane, 2-nonadecanone, and 5 α -androstan-3 β -ol) and normalised to the original extracted dry weight of sediment (Equation 3.2), a sedimentation rate changes calculating the mass accumulation rate (MAR) (Equation 3.3 and Equation 3.4) and total organic carbon of the samples (Equation 3.5).

Alkenone relative abundance was achieved by gas chromatography (GC) coupled with chemical ionisation mass spectrometry (GC-CIMS), adapted from the method of (Rosell-Melé *et al.*, 1995). Analyses were performed using a Trace Ultra gas chromatograph directly coupled to a Thermo DSQ single quadrupole mass spectrometer, fitted with a programmed temperature vaporising (PTV) injector. 1.2 ml of sample is injected. Alkenones were separated using a 30m x 0.25 mm i.d., Restek RXi-5ms column (0.25 μ m 5% diphenyl-95% dimethyl polysiloxane coating). Helium was employed as the carrier gas (2 ml min⁻¹). The injector was held at 120°C and splitless mode (1.2 min) during injection, and then immediately temperature programmed from 120°C to 310° at 10°C s⁻¹, then held for 0.6 min. The oven was programmed to hold at 175°C for 1.7 min, then increased to 310°C at 11 min⁻¹, and held at from 310°C for 12 min. The mass spectrometer was operated in positive chemical ionisation mode (PCI), using high-purity anhydrous ammonia (N6.0, BOC) introduced to the ion source through the CI gas inlet. Selected ion monitoring was performed, targeting the 8 ions corresponding to the [M + NH₄]⁺ adducts of the target C₃₇ and C₃₈ alkenones and the internal standard (nonadecanone), each with a SIM width of 1 m/z and a dwell time of 30 ms. The target m/z were: 300 (nonadecanone), 544 (C_{37:4}), 546 (C_{37:3}), 548 (C_{37:2}), 560 (C_{38:3Et} and C_{38:3Me}), 562 (C_{38:2Et} and C_{38:2Me}), 564 and 578 (C₃₆ alkyl alkenoates) as detailed by (Rosell-Melé *et al.*, 1995).

The CIMS method increases the resolution of the alkenone signal to allow for a more accurate U^K₃₇ and U^K_{37'} index quantification (Figure 3.11) (for more info, see Chapter 2). We use the SST calibration from Müller *et al.* (1998) to convert the U^K_{37'} index into annual mean sea surface temperatures (see Chapter 2).

The relative abundance of the C_{37:4} alkenone is expressed as a percentage of the total C₃₇ alkenones (%C_{37:4}) (See Chapter 2). Using the n-alkane fraction, the

relative input of terrigenous (C₂₇, C₂₉ and C₃₁) and marine (C₁₅, C₁₇ and C₁₉) n-alkanes were quantified, using the TAR index (Figure 3.12) (See Chapter 2). The

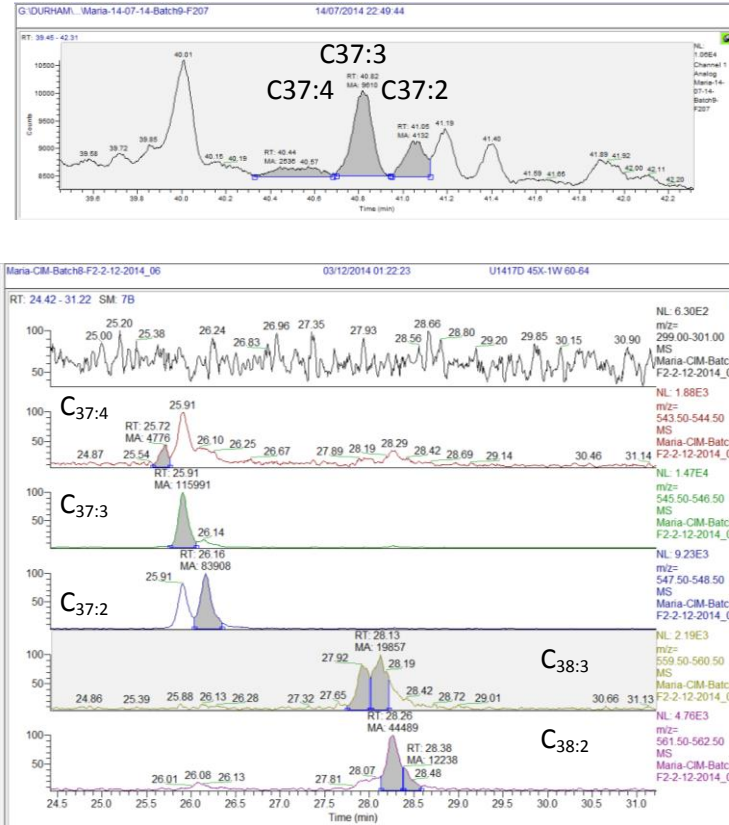


Figure 3.11: Alkenone integration peaks as seen through a GC-MS and GC-FID analysis (top) and GC-CIMS analysis (bottom). C_{37:4} and C_{38:3} are hard to quantify in both analysis but easier in GC.

relative abundance of each of the biomarkers (total C₃₇ alkenones, sterols, n-alkanes) was calculated using a known concentration of internal standard (Equation 3.1):

$$\text{Equation 3.1: } \text{Mass}_{\text{biomarker}} = \text{Mass}_{\text{standard}} / [\text{Area}_{\text{standard}}] * ([\text{area}_{\text{biomarker}}])$$

The biomarker mass per sample was normalised to the weight of the sample ($\mu\text{g g}^{-1}$) (Equation 3.2), the sediment mass accumulation rate ($\mu\text{g cm}^{-2} \text{Kyr}^{-1}$) (Equation 3.3 and 3.4) and changes to the total organic carbon content of the sediment ($\mu\text{g g}^{-1} \text{TOC}^{-1}$) (Equation 3.5).

$$\text{Equation 3.2: } \text{Biomarker } (\mu\text{g g}^{-1}) = \text{Mass}_{\text{biomarker}} * \text{weight}_{\text{sample}}^{-1}$$

Equation 3.3: Bulk MAR ($\text{g cm}^{-2} \text{Kyr}^{-1}$) = Dry bulk density (g cm^{-3}) * Sedimentation rates (cm Kyr^{-1})

Equation 3.4: Biomarker MAR ($\mu\text{g cm}^{-2} \text{Kyr}^{-1}$) = Bulk MAR * Biomarker ($\mu\text{g g}^{-1}$)

Equation 3.5: Biomarker ($\mu\text{g g}^{-1} \text{TOC}^{-1}$) = Biomarker ($\mu\text{g g}^{-1}$) * TOC^{-1}

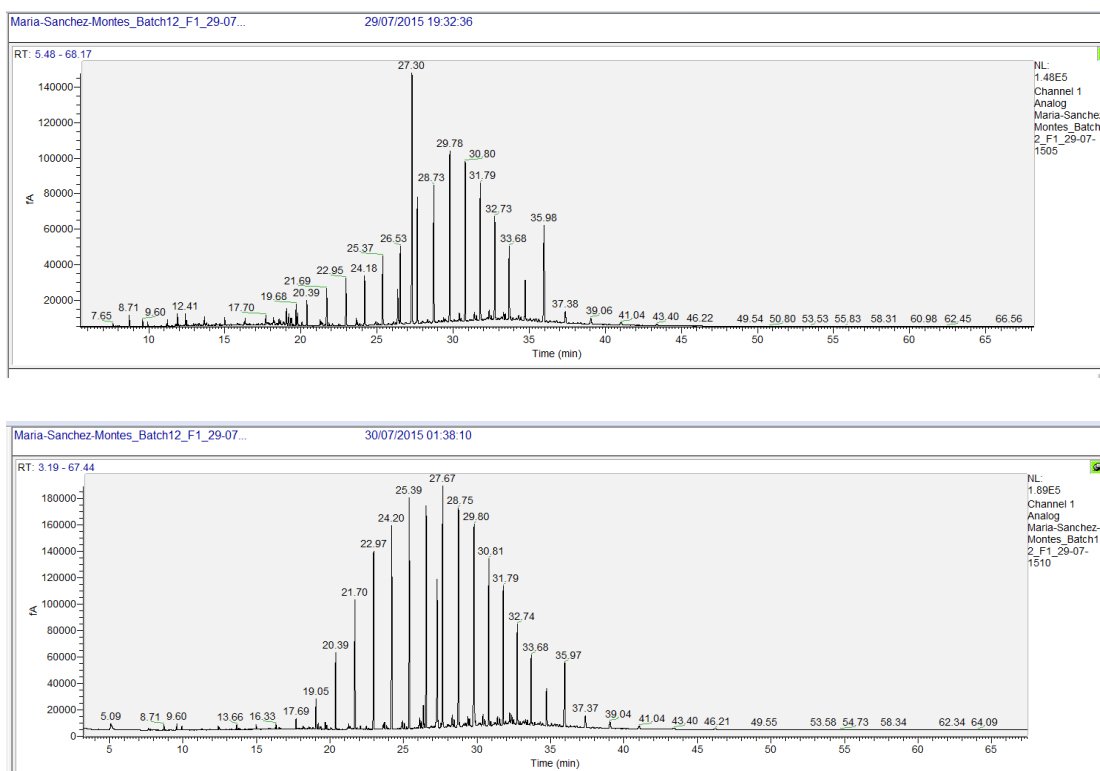


Figure 3.12: *N-alkane samples from the Pliocene (~3 Ma). Top sample has higher TAR than lower sample (GC-FID).*

3.6 Organic carbon and nitrogen bulk and isotope analysis

Freeze-dried and homogenized sediment samples were transported to the geology department of The University of Otago (New Zealand) for carbon (C) and nitrogen (N) bulk (TOC and TON) and isotopic ($\delta^{13}\text{C}$ and $\delta^{15}\text{N}$) analyses. A first test of samples was made by weighing 40 mg of dried sediment into tin and silver capsules to investigate the best method to implement for this analysis according to the characteristics of our samples. Some standards (Acetanilide Reference (TN $4.52 \pm 0.1\%$ w/w and TC 9.52% w/w) and Control (TN 71.09% w/w and TC 10.36% w/w) and MESS-2 (TN $0.170 \pm 0.009\%$ w/w and TC $2.052 \pm 0.042\%$ w/w) were alternated in the run to monitor the preparation and instrument

performance. As a result of the low total nitrogen (TN) concentration (<0.1% w/w) and the total carbon (TC) (<3 % w/w) present in the samples, the weight of sediment for analysis was increased, and silver caps were used to acidify the samples.

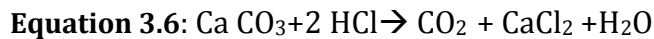
Approximate 70 mg of sediment was weighed into silver caps and acidified with sulfuric acid H₂SO₄ (1M) to remove the inorganic carbon efficiently (Equation 3.11) however without compromising organic matter preservation. Acidification was repeated until no further bubbling was observed in the sample under the microscope. Samples were oven-dried between acidifications at 40°C. To guarantee the full combustion of the sample, 6 mg of Tungsten VI oxide (WO₃) was added into each sample. A gas chromatography isotope ratio mass spectrometry was used to analyse the isotopic values of carbon and nitrogen and quantify the ¹³C, ¹²C, ¹⁵N, ¹⁴N and total organic carbon (TOC) and total organic nitrogen (TON). Analysis was controlled placing some standards in between the samples in the same run (Table 3.5).

Table 3.5: Standard details for C and N analyses. $\delta^{15}\text{N}$ (‰), TON (%), $\delta^{13}\text{C}$ (‰) and TOC (%) details of the standards used for analysis accuracy monitoring of carbon and nitrogen studies.

Standard	$\delta^{15}\text{N}$ (‰)	TON (%)	$\delta^{13}\text{C}$ (‰)	TOC (%)
EDTA-OAS	-0.73 ± 0.12	9.59	-38.52 ± 0.20	41.1
USGS-40	-4.52	9.52	-26.39	40.8
USGS-41	47.57	9.76	37.63	41.9
MESS-2	3.09 ± 0.78	0.170 ± 0.009	-26.07	1.384 ± 0.050
AA#1	1.18	10.37	-29.53	71.09

Replications of samples and standards were also placed within the same batch to control analysis. These quantified an overall standard deviation of the method of 0.58 ‰ for $\delta^{15}\text{N}$, 0.006 % for TON, 0.26 ‰ for $\delta^{13}\text{C}$ and 0.031% for TOC, a within-batch standard deviation of 0.6‰ for $\delta^{15}\text{N}$, 0.003% for TON, 0.24 ‰ for $\delta^{13}\text{C}$ and 0.021% for TOC and a between-batch standard deviation of 0.78‰ for $\delta^{15}\text{N}$, 0.11% for TON, 0.4‰ for $\delta^{13}\text{C}$ and 0.053% for TOC. The test samples (tin capsules) were run with a Carlo Erba and rebuilt Sercon MS combination (Carlo Erba NA

3500 elemental analyser and a PDZ Europa 20-20 isotope ratio mass spectrometer (Sercon Ltd., Cheshire, UK). A combination of a Varian elemental analyser and a gas chromatograph combustion isotope ratio mass spectrometer (EA-IRMS) was used for the analysis of the acidified silver capsules, to generate the downcore data presented here.



Many studies have examined the effect of acidification on organic C and N bulk and isotopes in invertebrates (Jaschinski *et al.*, 2008; Mateo *et al.*, 2008; Vafeiadou *et al.*, 2013; Serrano *et al.*, 2008) and in marine sediments (Ryba and Burgess, 2002; Kennedy *et al.*, 2005). For marine sediments, the direct addition of acid to the sediments has been proved to remove most of carbonates (Ryba and Burgess, 2002) (Equation 3.6). A more detailed study of the acidification process with different acids: HCl (1M, 2M and 6M), H₂SO₃ (6%) and H₃PO₄ (1M), suggests that acidification carried out with 6M HCl, 6% H₂SO₃ and 1M H₃PO₄ resulted in higher organic carbon concentrations and $\delta^{13}\text{C}$ than with the 1 and 2M HCl acids. This is interpreted as a non-effective acidification process where inorganics are still present in the sample (Kennedy *et al.*, 2005). Acidification carried out with 6% H₂SO₃ and 1M H₃PO₄ resulted also in lower $\delta^{15}\text{N}$ than the non-acidified sediment, which could not be explained (Kennedy *et al.*, 2005). A weak acid (i.e. 1 to 2 M HCl) solution is advised to use for the removal of inorganic carbon without a significant bias in the bulk TOC and TON and $\delta^{13}\text{C}$ and $\delta^{15}\text{N}$ (Kennedy *et al.*, 2005). Alteration of nitrate by diagenesis (Jaeger *et al.*, 2014) in our study sediments was an incentive for inorganic removal. We followed the Kennedy *et al.* (2005) acidification of samples and compared it with a non-acidification method of samples and concluded the acidification was a more appropriate approach where values were on the range of the instrument detection.

3.7 Depth-age conversion

Age-depth conversion and plots of the different cores and the core breaks the sediment samples analysed in this study are shown in Table 3.6 and Figures 3.6 and 3.7 (U1417) and Table 3.7 and Figures 3.8 and 3.9 (U1418).

Table 3.6: U1417 age-depth conversion table.

Age (Ma)	Average depth CCSF-A (m)
0.0	0.00
0.5	78.03
1.0	153.18
1.5	196.53
2.0	245.12
2.5	323.26
3.0	365.76
3.5	398.26
4.0	418.26
4.5	438.26
5.0	460.76
5.5	488.26
6.0	515.76
6.5	570.76
7.0	618.26
7.5	648.26
8.0	658.26
8.5	663.26
9.0	668.26
9.5	673.26
10.0	678.26
39.0	838.26

Table 3.7: U1418 age-depth conversion table.

Age (Ma)	Average depth CCSF-A (m)
0	0
0.2	297.1
0.2	297.1
0.4	462.1
0.4	462.1
0.6	577.1

Chapter 4: Results

4.1 Introduction

This PhD thesis has produced a number of records: sea surface temperature (SST) reconstruction and sea surface salinity from alkenone analysis, terrestrial and aquatic organic matter delivery to the site from *n*-alkane and total organic carbon (TOC) and total organic nitrogen (TON) analysis, and marine productivity export from carbon ($\delta^{13}\text{C}$) and nitrogen ($\delta^{15}\text{N}$) isotope, alkenone and sterol analyses. This Chapter will outline only results of the analysis performed in this PhD thesis, by site. Alkenone records have been produced by Dr. Juliane Müller through the early-middle Pleistocene transition (1.5 Ma to 0.5 Ma) gap in Site U1417 data below. Interpretations and implications of the results presented here will be discussed in Chapters 5 (U1417) and 6 (U1417) and 7 (U1418) together with other climatic records as mentioned in Chapter 1.

4.2 Site U1417

4.2.1 Palaeo-sea surface temperature and palaeo-salinity from alkenone proxies

$U^{K_{37}}$ index at Site U1417 ranges from 0 to 0.6 and has an average value of 0.3 (Figure 4.1), excluding samples where no alkenone could be detected. Negative $U^{K_{37}}$ values correspond to samples with >20% $C_{37:4}$ alkenone. Through the 800 to 0 m CCSF-A sediment depth, the $U^{K_{37}}$ shows considerable scatter, although values ranging from 0.6 to 0.15 during the Miocene (800 to 400 m CCSF-A; Figure 4.1), from 0.42 to 0.17 during the Pliocene (475 to 340m CCSF-A) from 0.44 to 0.09 during the early Pleistocene and from 0 to 0.37 during the Late Pleistocene (340 to 196m CCSF-A). Thus, $U^{K_{37}}$ at Site U1417 shows an overall decreasing trend from the Miocene to present. The $U^{K_{37}'}$ values range from 0 to 0.7 and have average value of 0.3, and shows a similar overall trend to $U^{K_{37}}$ (Figure 4.1). $U^{K_{37}}$ shows a wider range of values than $U^{K_{37}'}$, which is a result of the $U^{K_{37}}$ index containing the $C_{37:4}$ alkenone (Section 2.5.2), which also varies downcore (Figure 4.1c). $C_{37:4}$ concentrations range from 0 to 33.2%, with an average of 3.2 % (Figure 4.1c).

There is a long-term trend towards increased $C_{37:4}$ from the Miocene to present at Site U1417.

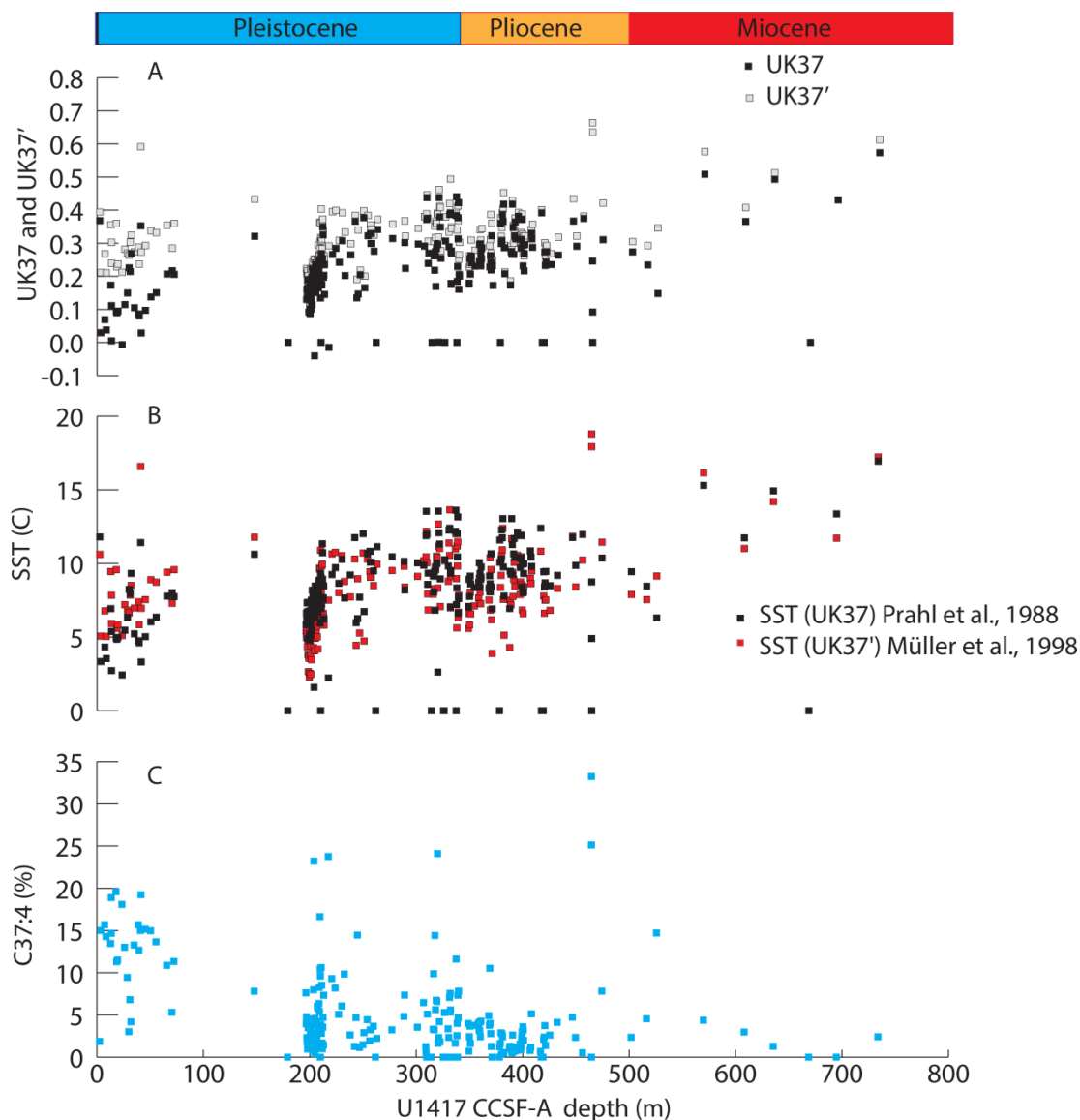


Figure 4.1: Alkenone proxies for temperature and salinity (a) $U^{K_{37}}$ (black) and $U^{K_{37}'}$ (white), (b) SST ($^{\circ}$ C) calculated from $U^{K_{37}}$ (black) (Prah et al., 1988) and $U^{K_{37}'}$ (red) (Müller et al., 1998) and (c) $C_{37:4}$ (%), plotted against composite depth for Site U1417 (m CCSF-A). The absence or unquantifiable alkenones in the record are indicated with 0 value data points.

4.2.2 SST Calibrations during 4 to 1.7 Ma

The SST calibration of Prah and Wakeham (1987) and Prah *et al.* (1988) is based on the $U^{K_{37}}$ index, which incorporates the $C_{37:4}$ alkenone: in high latitudes, the co-registration of SST and salinity information by the $C_{37:4}$ alkenone (Bendle *et al.*, 2005) introduces complexities for the reconstruction of SSTs. In contrast, the $U^{K_{37}'}$

index excludes the $C_{37:4}$ alkenone from the index and has a better linear correlation to growth temperatures (Prahl and Wakeham, 1987) including a global core-top calibration (Müller *et al.*, 1998 and Conte *et al.*, 2006). High $\%C_{37:4}$ has been thought to be restricted to East Greenland (Bendle *et al.*, 2005) however at Site U1417 $\%C_{37:4}$ concentrations reach 25 %. The $\%C_{37:4}$ concentration ranges between 0 to 35% at Site U1417 and confirms the freshwater characteristics in our site. For $\%C_{37:4}$ concentrations higher than 5% it has been suggested that the linear correlation between $U^{K_{37}}$ and SST is less precise (Rosell-Melé, 1998). When $C_{37:4}$ concentrations are higher than 5 %, more scatter between SST and $U^{K_{37}}$ has been observed, and the $U^{K_{37}}$ index has been identified as being more reliable (Bendle and Rosell-Melé, 2004). However, there needs to be a future better assessment of whether $C_{37:4}$ should be incorporated into the SST calibration in the northeast Pacific, given that few Pacific data points are found in the global calibrations.

Site U1417 $C_{37:4}$ range of concentrations (Figure 4.1) is comparable to the North Atlantic $\%C_{37:4}$ range at modern (Sikes and Sicre, 2002). However, Site U1417 $C_{37:4}$ range is ~25% higher range than found in salinity reconstructions from the North Atlantic during the last 65 kyr (Naafs *et al.*, 2013) and ~20% lower range as found in the Sea of Okhotsk during the last 120kyr (Harada *et al.*, 2008). All of these studies used the $U^{K_{37}}$ index for SST calibrations according to Müller *et al.* (1998) (Naafs *et al.*, 2013) to Prahl *et al.*, 1988 (Harada *et al.*, 2008) whereas the study of Sikes and Sicre (2002) is used to create a new $U^{K_{37}}$ -SST calibration.

At Site U1417, the $U^{K_{37}}$ index is applied to reconstruct SSTs, acknowledging the relatively high presence of $\%C_{37:4}$. The $U^{K_{37}}$ index has been converted into SST according to the core-top to annual mean SST correlation constructed with samples spanning 60°S to 60°N, which includes the Pacific Ocean (Müller *et al.*, 1998) (Figure 4.1 and Figure 4.2). This calibration has been applied to samples from the North Pacific Ocean (Meheust *et al.*, 2013, McClymont *et al.*, 2008, Herbert *et al.*, 2010, LaRiviere *et al.*, 2012, McClymont *et al.*, 2012). However, the core-top calibration of Sikes *et al.* (1997) has been suggested as the best calibration for summer SST in the east North Pacific and Bering Sea (Meheust *et al.*, 2013). The Sikes *et al.* (1997) calibration is similar to the calibration of Sikes and Volkman *et*

al. (1993), and both arose from analysis of Southern Ocean core top and surface water samples (see Section 2.5.1). Applied to our results, the summer SST of Sikes *et al.* (1997) is overall 2.0 °C warmer than the SST calibration of Müller *et al.* (1998), whereas the Sikes and Volkman (1993) SST calibration is overall 2.9 °C warmer than the SST calibration of Müller *et al.* (1998) (Figure 4.2). However, the Sikes *et al.* (1997) calibration for the eastern North Pacific is based only on three samples with $U^{K_{37}}$ values ranging from 0.4 (SO202/1 26-1 and SO202/1 27-1) to 0.37 (SO202/1 28-1) 400 and 300 km away from Site U1417 (Meheust *et al.*, 2013), respectively, whereas our $U^{K_{37}}$ data ranges from 0 to 0.7. Given that the calibration of Sikes *et al.* (1997) is dominated by samples from the Southern Ocean, has a small number of samples from the Gulf of Alaska being tested against that calibration, and the narrow window of $U^{K_{37}}$ index values represented, it is difficult to accept this calibration as the most reliable for application to the GOA samples presented here.

Alkenones are synthesized by prymnesiophytes, a classification that includes the coccolithophores (e.g. Volkman *et al.*, 1980a). Coccolithophore blooms peak during different season at different locations (Rosell-Melé and Prahl, 2013). At subpolar latitudes blooms are more intense from summer to early autumn (Brown and Yoder, 1994) based on Nimbus 7 CZCS imagery data from 1978 and 1986, although they bloom all year around. Seasonal peak coccolithophore blooms occur during late spring in the northeast Pacific (Prahl *et al.*, 1993) based on sediment traps, and during late summer through to late autumn in the subpolar northwest pacific (Haug *et al.*, 2005; Yamamoto and Kobayashi, 2016) based on top core studies. The seasonality in the production of alkenones could mean that the Sikes *et al.* (1997) calibration for summer SST could be more appropriate to use in these regions in the ocean. However, the seasonality bloom is still under debate (Rosell-Melé and Prahl, 2013).

Both the Müller *et al.* (1998) and Sikes *et al.* (1997) calibrations have similar SST ranges to current ocean conditions in the GOA and show similar SST to the Holocene of 10°C (Müller *et al.*, 1998) and 12 °C (Sikes *et al.*, 1997) at 15 kyr in our site (our top-most sample), which corresponds to similar modern SST average and to late summer-early fall SST on the top 25 m of the water column at Resurrection

Bay (Weingartner, 2007), respectively. Average Pliocene SST calibrated by Müller *et al.* (1998) is 8°C and 10 °C calibrated with Sikes *et al.* (1997), which reflects mean annual and summer SST, respectively.

In this study, we use the calibration of Müller *et al.* (1998), as the sedimentary temperature signal from alkenones has been suggested to average out any seasonal fluctuations in productivity, to allow the reconstruction of annual sea surface temperatures (Rosell-Melé, 1998). Furthermore, the presence of 4 hours of sunlight during the month of December (State of Alaska, 2001-2007) makes the coccolithophore blooms possible all year around in the Gulf of Alaska (Brown and Yoder, 1994). The calibration that captures the known variations in coccolithophore and alkenone production is that of Müller *et al.* (1998), which also includes the samples of the study of Sikes *et al.* (1997) but calibrates the data to mean annual sea surface temperature. Sediment trap studies are lacking from the GOA, however, to confirm the season of maximum alkenone flux to the deep ocean.

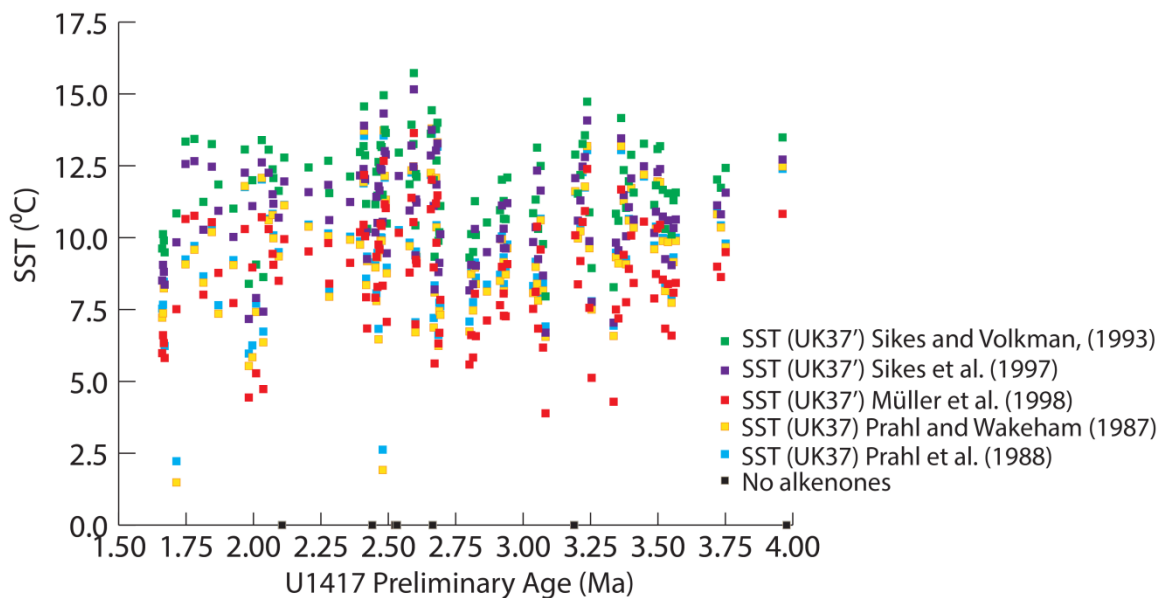


Figure 4.2: SST Calibrations Site U1417. SST (°C) calibrations based on the $U^{K_{37}}$ index applied to the complete data set of Site U1417: Sikes and Volkman (1993) in green, Sikes *et al.* (1997) in purple and Müller *et al.* (1998) in red and SST (°C) calibrations based on the $U^{K_{37}}$ index: Prahl and Wakeham (1987) in yellow and Prahl *et al.* (1988) in blue during 4 to 1.66 Ma. Samples where alkenones could not be detected are shown in black.

4.2.3 Terrestrial and aquatic proxies

TOC concentrations range from 0.1 to 1.1 % with average concentrations of 0.4% (Figure 4.3). TON concentrations range from 0.01 to 0.1‰ with an average of 0.04‰ (Figure 4.3). Shipboard analyses of Site U1417 determined that there was an inorganic N contribution to the bulk N (Jaeger *et al.*, 2014). Despite the inorganic contribution of N, bulk N and C/N ratios can be used to assess changes in nutrient input and utilization. Inorganic C was removed from the samples before bulk stable isotope analysis (Section 3.6). Organic $\delta^{13}\text{C}$ ranges from -26.0 to -20.3, with average concentrations of -24.5, and organic $\delta^{15}\text{N}$ ranges from -0.4 to 6.4‰, with average concentrations of 3.2‰ (Figure 4.3). All of the bulk organic matter data sets show an increasing long term trend towards the present, and a decrease in variability. Thus, the Pliocene-early Pleistocene has the highest variability in the bulk sediment data (Figure 4.3).

‰TOC concentrations are similar to the Arctic Ocean concentrations (Schubert and Calvert, 2001). $\delta^{13}\text{C}$ at Site U1417 show an approximate of 4 times lighter concentrations than $\delta^{13}\text{C}$ in a transect from the east Equatorial Pacific through the Miocene through the Pliocene and Pleistocene range ($\delta^{13}\text{C}$ =2.5 to -0.5‰; Reghelling *et al.*, 2015). $\delta^{13}\text{C}$ concentrations follow a trend towards enrichment in the light isotope through the Miocene until the mid-Pliocene which then reverses until the present (Reghelling *et al.*, 2015). $\delta^{15}\text{N}$ concentrations at Site U1417 are similar than previously analysed samples from the GOA and other marine sediment samples across the globe during the last 200 kyr (Galbraith *et al.*, 2004).

The terrestrial/aquatic ratio (TAR) is the ratio between the terrigenous and the aquatic source of organic matter (Section 2.5.3.4). The TAR index at Site U1417 ranges from 0.4 to 17 with an average value of 3.8 (Figure 4.3a). Excluding the samples where no *n*-alkanes could be detected during the Pliocene and early Pleistocene, Miocene TAR values range from 1.8 to 6.4, Pliocene TAR values range from 2.2 to 17, early Pleistocene values range from 0.7 to 8.6 and late Pleistocene values from 0.5 to 3.5 (Figure 4.3). The range of TAR at Site U1417 is similar to other lake and terrestrial TAR studies across the globe (e.g. TAR= 1 to 8, D'anjou *et al.*, 2013, Lake El'gygytgyn; TAR=1 to 12, Yadav *et al.*, 2017, Southern India; TAR= 0.5 and 0.9, Sanches-Filho *et al.*, 2013; Brasil). The highest TAR at Site U1417 are

registered around 400 m CCSF-A, and the lowest around 320 m, 200 m, and the top 90 m CCSF-A. The highest values of TAR correspond to a relative increase of the terrestrial *n*-alkanes, and the lowest TAR to a relative increase of aquatic *n*-alkanes (Figure 4.3). However, at 350 m CCSF-A, there is a decrease in TAR synchronous

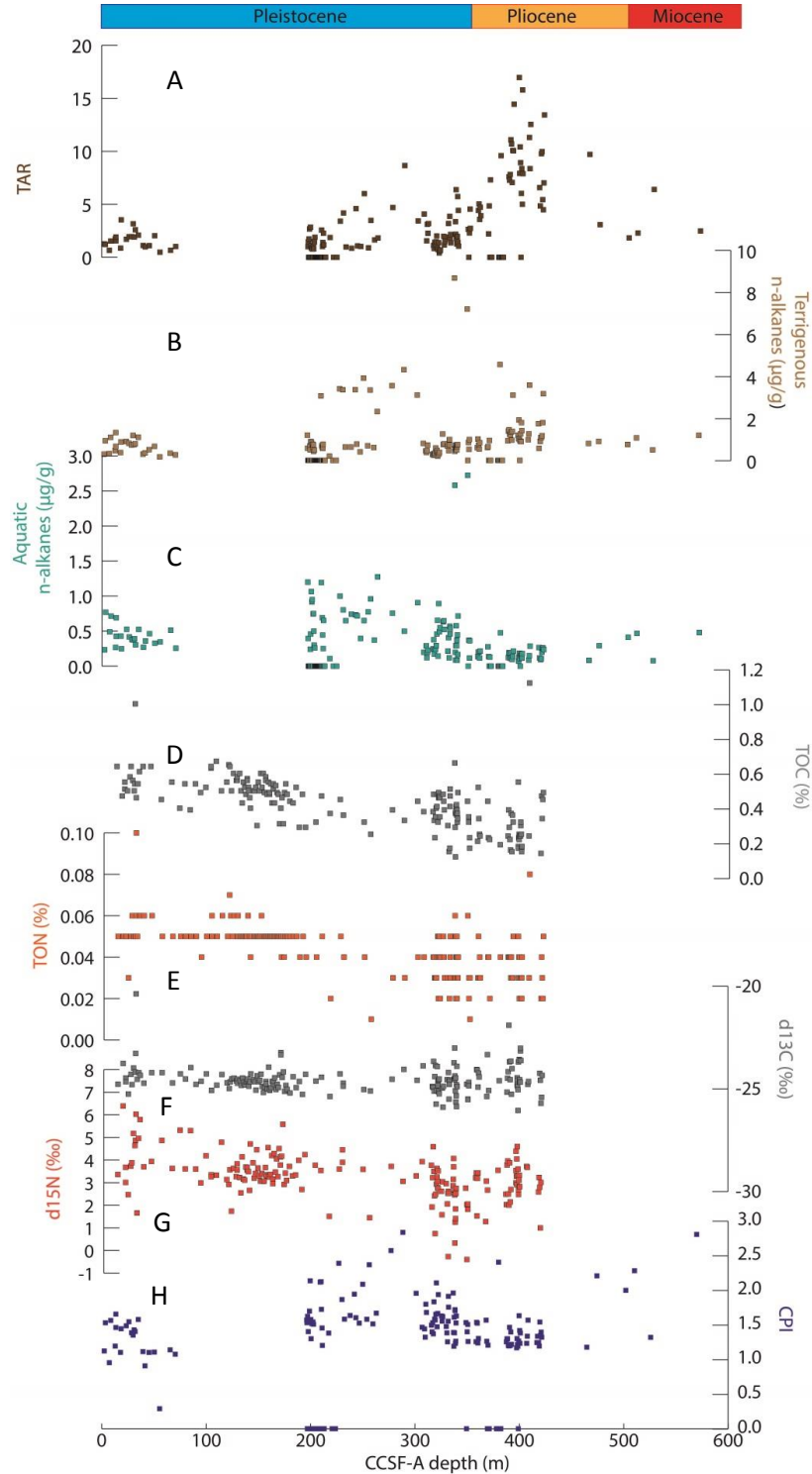


Figure 4.3: Terrigenous and marine OM input to Site U1417. (a) TAR ratio, (b) terrestrial $[[C_{27}]+[C_{29}]+[C_{31}]]$ (brown) and (c) marine $[[C_{15}]+[C_{17}]+[C_{19}]]$ (green) *n*-alkanes, (d) total

bulk organic carbon (TOC), (e) total organic nitrogen (TON) (%), (f) $\delta^{13}\text{C}$, (g) $\delta^{15}\text{N}$ (‰) and (h) CPI index plotted by composite depth for site U1417 (m CCSF-A).

with high terrigenous *n*-alkane concentrations and much lower aquatic *n*-alkanes. This can be explained by the larger decrease in marine in relation to terrigenous *n*-alkanes, which is translated into a lower ratio despite a loss of terrigenous *n*-alkanes.

The aquatic *n*-alkanes are low during the Miocene (0.1 to 0.5 $\mu\text{g g}^{-1}$, 2.1 to 7.0 $\mu\text{g cm}^{-2}\text{ kyr}^{-1}$), decrease during the Pliocene and reach their maximum during the Plio-Pleistocene transition (up to 2.7 $\mu\text{g g}^{-1}$ at 348.8 m CCSF-A, 31.6 $\mu\text{g cm}^{-2}\text{ kyr}^{-1}$ at 336.6 m CCSF-A and 6.4 $\mu\text{g g}^{-1}\text{ TOC}^{-1}$ at 348.8 m CCSF-A). During the Pleistocene, the aquatic *n*-alkane concentration decreases towards present, ranging between 0.2 to 0.7 $\mu\text{g g}^{-1}$, 1.8 to 8.8 $\mu\text{g cm}^{-2}\text{ kyr}^{-1}$ and 0.4 to 1.1 $\mu\text{g g}^{-1}\text{ TOC}^{-1}$ (Figure 4.3 and Figure 4.4). Terrigenous *n*-alkane concentrations range from 0.5 to 1.2 $\mu\text{g g}^{-1}$ and 3.4 to 17.4 $\mu\text{g cm}^{-2}\text{ kyr}^{-1}$ during the Miocene and increase during the Pliocene to values from 0.5 to 4.6 $\mu\text{g g}^{-1}$, 5.2 to 39.5 $\mu\text{g cm}^{-2}\text{ kyr}^{-1}$ and 6.7 to 11.8 $\mu\text{g g}^{-1}\text{ TOC}^{-1}$ (Figure 4.3 and Figure 4.4). During the Pleistocene, the terrigenous *n*-alkanes peak at the start of the early Pliocene to concentrations up to 8.7 $\mu\text{g g}^{-1}$, 106.1 $\mu\text{g cm}^{-2}\text{ kyr}^{-1}$ and 17.0 $\mu\text{g g}^{-1}\text{ TOC}^{-1}$ and decrease during the Pleistocene to values of 0.3 to 1.3 $\mu\text{g g}^{-1}$, 2.3 to 17.4 $\mu\text{g cm}^{-2}\text{ kyr}^{-1}$ and from 0.8 to 2.4 $\mu\text{g g}^{-1}\text{ TOC}^{-1}$. Overall, aquatic *n*-alkanes range from 0 to 35 $\mu\text{g cm}^{-2}\text{ kyr}^{-1}$, with an average value of 5 $\mu\text{g cm}^{-2}\text{ kyr}^{-1}$. Terrigenous *n*-alkanes range from 0 to 120 $\mu\text{g cm}^{-2}\text{ kyr}^{-1}$, with an average value of 9 $\mu\text{g cm}^{-2}\text{ kyr}^{-1}$ through the Miocene to the present.

The carbon preference index (CPI) is a way of quantifying the maturity of the organic matter (Section 2.5.3.4). Values close 1 are traceable to thermal mature terrestrial organic matter eroded from bedrock, whereas a CPI value of 1.5 comes from more immature sources (Peters *et al.*, 2005). The average CPI at Site U1417 is 1.5, and ranges from 0.3 to 2.8. The long-term CPI trend is similar to the terrigenous *n*-alkane concentrations and TAR index with the highest CPI values (2 to 3) recorded during the Miocene and early Pleistocene and lowest values (around 1) recorded during the late Pleistocene. The CPI results can be interpreted

as indicating a higher abundance of immature soils during the Miocene and during the Plio-Pleistocene transition (CPI \sim 1.5 to 3). CPI values between 1.5 and 1 occur during the Pliocene, and the later samples of the early Pleistocene, which suggest a mix between mature and immature OM and/or a higher abundance of mature soils during the late Pleistocene. CPI values close to 1 might reflect coal particles found in sediments in the Gulf of Alaska (Rea *et al.*, 1995; Gulick *et al.*, 2015). High TAR values during the Pliocene might suggest a higher concentration of coal particles in the sediment in comparison with other *n*-alkanes.

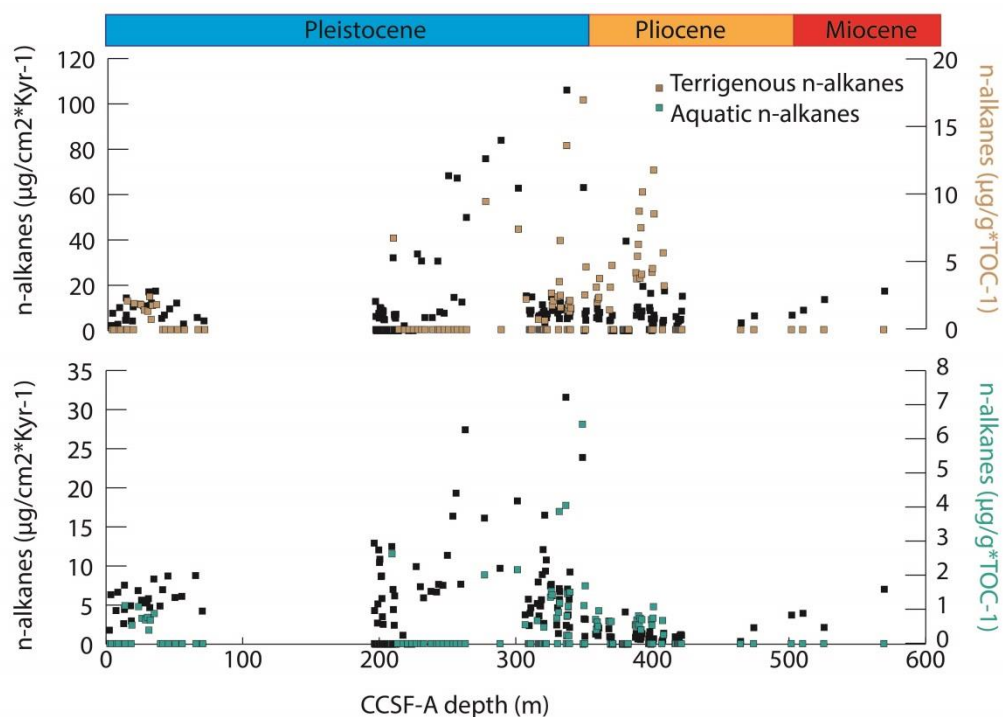


Figure 4.4: Terrigenous and marine OM normalised to sedimentation rates and organic carbon changes at Site U1417. Terrigenous (brown) and aquatic (turquoise) *n*-alkanes ($\mu\text{g g}^{-1} \text{ TOC}^{-1}$, right axes) and both in black ($\mu\text{g cm}^{-2} \text{ kyr}^{-1}$, left axes).

4.2.4 Export production proxies

All export productivity proxies are presented as their original concentration (per g sediment dry weight, $\mu\text{g g}^{-1}$), normalised to sediment mass accumulation rate ($\mu\text{g cm}^{-2} \text{ kyr}^{-1}$) and normalised to TOC ($\mu\text{g g}^{-1} \text{ TOC}^{-1}$). Note that the normalisation to TOC could not be completed on all samples due to an incomplete TOC data set.

Alkenone concentration ranges from 0 to $6.1 \mu\text{g g}^{-1}$, with an average value of 0.2 (Figure 4.5). Considering the accumulation rates of alkenones and TOC, the alkenone concentration varies from 0 to $53.7 \mu\text{g cm}^{-2} \text{kyr}^{-1}$, with an average of $1.6 \mu\text{g cm}^{-2} \text{kyr}^{-1}$ and from 0 to $1.2 \mu\text{g g}^{-1} \text{TOC}^{-1}$, with an average of $0.1 \mu\text{g g}^{-1} \text{TOC}^{-1}$ (Figure 4.6). All alkenone records show low values during the Miocene, an abrupt increase in alkenone concentration during the middle to late Pliocene, a later small decrease during the early Pliocene, and lower values during the late Pleistocene.

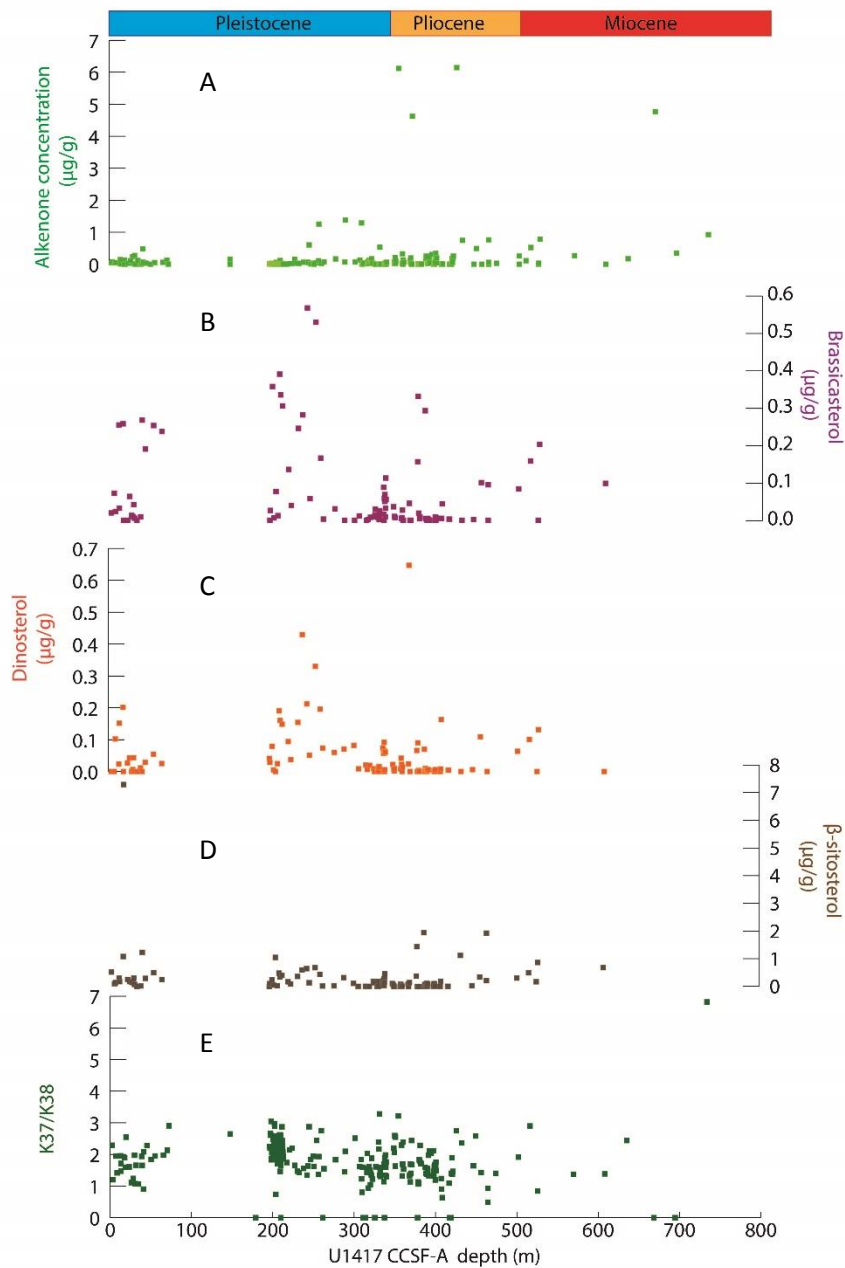


Figure 4.5: Marine productivity export proxies at Site U1417. (a) Alkenone concentration ($\mu\text{g g}^{-1}$) (b) Brassicasterol concentration ($\mu\text{g g}^{-1}$), (c) dinosterol concentration

($\mu\text{g g}^{-1}$), (d) β -sitosterol concentration ($\mu\text{g g}^{-1}$) (e) K_{37}/K_{38} alkenone ratio vs U1417 CCSF-A depth (m).

Alkenone MAR concentrations at Site U1417 are 10 times lower than Pliocene and Pleistocene records from the California Margin (ODP 1012, Liu *et al.*, 2008), 4 times lower than records from the east Equatorial Pacific (ODP 846, Lawrence *et al.*, 2006) and half compared to the Sea of Okhotsk (MD01-2412, Harada *et al.*, 2008). In comparison with the Atlantic, Site U1417 alkenone MAR concentrations through the Pliocene and Pleistocene are comparable to Equatorial Atlantic records (ODP 662, Lawrence *et al.*, 2013) and around 10 times higher than records from the North Atlantic (ODP 907, Lawrence *et al.*, 2013; ODP 982, Lawrence *et al.*, 2009; ODP 607, Lawrence *et al.*, 2013) and South Atlantic (ODP 1091, Cortese *et al.*, 2004).

The C_{37} alkenone to C_{38} alkenones ratio (K_{37}/K_{38}) show values ranging from 0.5 to 3.3 with a single point with a value 6.8 during the Miocene (Figure 4.5). The K_{37}/K_{38} record has a long-term mean of 1.9. There is no long-term trend nor change in variability in the K_{37}/K_{38} record. The K_{37}/K_{38} data from Site U1417 are within the same range as the modern North Pacific Ocean (Prah1 *et al.*, 1988).

Brassicasterol concentrations range from 0 to $0.6 \mu\text{g g}^{-1}$ (0 to $11.2 \mu\text{g cm}^{-2} \text{ kyr}^{-1}$ and from 0 to $0.9 \mu\text{g g}^{-1} \text{ TOC}^{-1}$) with an average value of $0.1 \mu\text{g g}^{-1}$, $0.9 \mu\text{g cm}^{-2} \text{ kyr}^{-1}$ and $0.06 \mu\text{g g}^{-1} \text{ TOC}^{-1}$. Brassicasterol concentrations increase during the uppermost 50 m CCSF-A of Site U1417, and between 380 to 400 m, with values around $0.3 \mu\text{g g}^{-1}$ (double those recorded between 200 to 300 m CCSF-A). This pattern is replicated by brassicasterol mass accumulation rates (Figure 4.6).

Dinosterol concentrations range from 0 to $0.6 \mu\text{g g}^{-1}$, from 0 to $7.0 \mu\text{g cm}^{-2} \text{ kyr}^{-1}$ and from 0 to $0.3 \mu\text{g g}^{-1} \text{ TOC}^{-1}$, with an average value of $0.05 \mu\text{g/g}$, $0.6 \mu\text{g cm}^{-2} \text{ kyr}^{-1}$ and $0.04 \mu\text{g g}^{-1} \text{ TOC}^{-1}$ (Figure 4.5 and 4.6). As observed for brassicasterol, dinosterol concentrations are lower overall during the Miocene, Pliocene and late Pleistocene than during 200 to 300 m CCSF-A range (which corresponds to the early Pleistocene), where values are the highest of the records. A slight increase in dinosterol concentration synchronous to an increase in brassicasterol around 500 m CCSF-A is also appreciable.

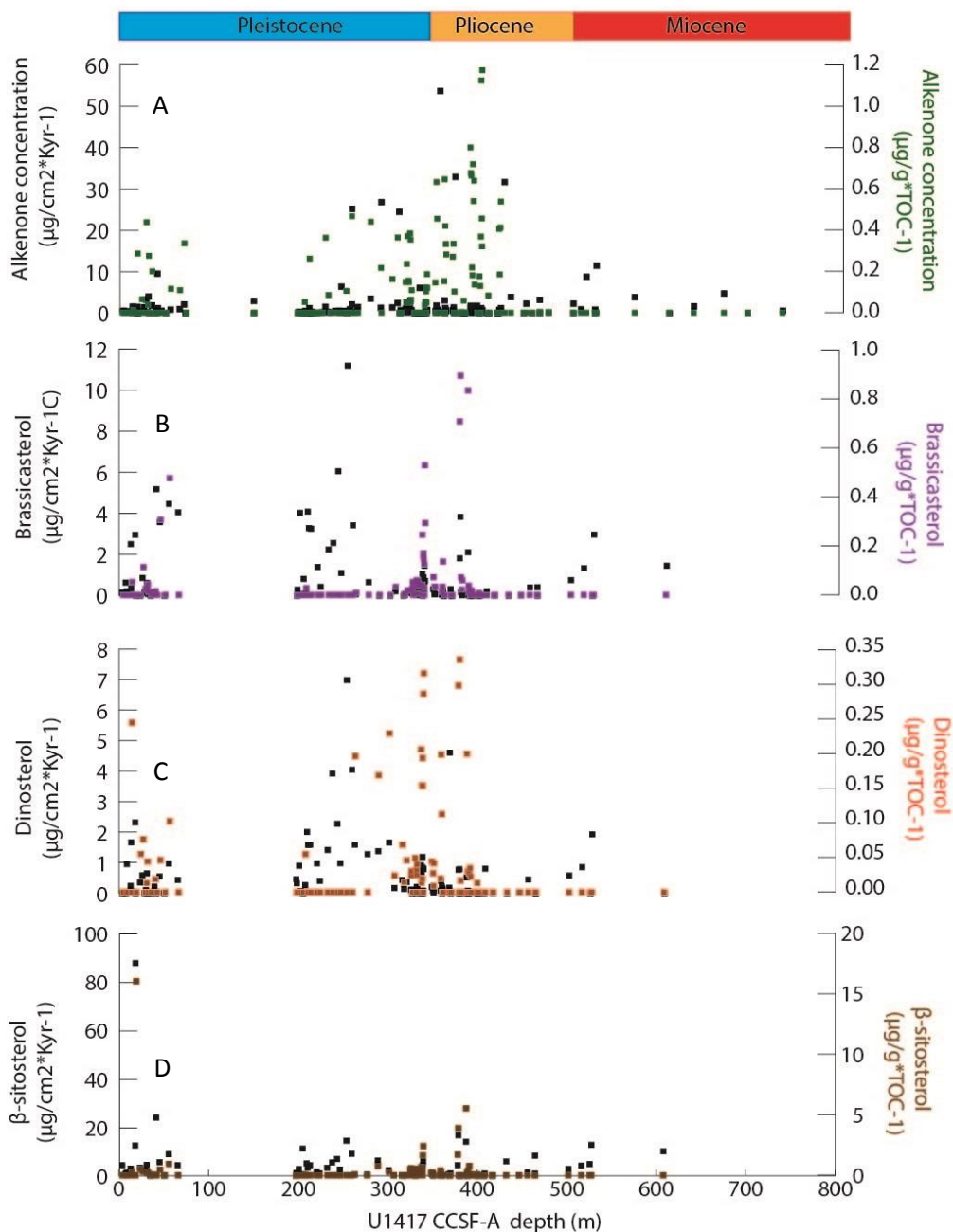


Figure 4.6: Marine productivity concentrations normalised to bulk accumulation rate or TOC content at Site U1417. (a) Alkenone concentrations, (b) brassicasterol, (c) dinosterol and (d) β -sitosterol (coloured data in $\mu\text{g g}^{-1} \text{TOC}^{-1}$, right axes; black in $\mu\text{g}/\text{cm}^2/\text{kyr}$) vs U1417 CCSF-A mid-point depth (m).

β -sitosterol concentrations range from 0 to $7.3 \mu\text{g g}^{-1}$, from 0 to $87.7 \mu\text{g cm}^{-2} \text{kyr}^{-1}$ and from 0 to $16.0 \mu\text{g g}^{-1} \text{TOC}^{-1}$, with an average value of $0.3 \mu\text{g g}^{-1}$, $3.5 \mu\text{g cm}^{-2} \text{kyr}^{-1}$ and $0.4 \mu\text{g g}^{-1} \text{TOC}^{-1}$ (Figure 4.5 and 4.6). Excluding some isolated samples with concentrations (~ 1 to $2 \mu\text{g g}^{-1}$ between 400 to 500 m CCSF-A), β -sitosterol

concentrations increase consistently during 350 to 450 m CCSF-A depth from concentrations of below 1 to values above 1 $\mu\text{g g}^{-1}$ and remain low for the rest of the record. β -sitosterol $\mu\text{g cm}^{-2} \text{ kyr}^{-1}$ concentrations show concentrations approximately 10 times higher than for other marine sterols in Figure 4.6. β -sitosterol concentration increase consistently during 350 to 450 m CCSF-A depth from values of below 1 to values above 1 $\mu\text{g g}^{-1}$ and remain low for the rest of the record. Mass accumulation rates of dinosterol and dinosterol normalised to TOC records follow the same trend described above.

4.2.5 Summary of Site U1417

This thesis explores proxies for palaeo-temperatures, salinity and organic matter provenance and maturity at Site U1417. From the Miocene to the present, Site U1417 reveals a gradual long term cooling trend, with an increase in freshwater input, a gradual long term increase in %TOC, %TOC, organic $\delta^{13}\text{C}$ and $\delta^{15}\text{N}$. Increasing contributions from terrestrial and aquatic *n*-alkanes and alkenone, brassicasreol, dinosterol and β -sitosterol concentrations occur during the late Pliocene-early Pleistocene. Changes to sedimentation rates or total organic carbon contents did not control the patterns of biomarker accumulation; however TOC values were insufficient to create a complete record of phytoplankton concentration according to TOC flux to the deep ocean. The CPI and K_{37}/K_{38} records do not show notable long term variations. In detail, all of the records (excluding the CPI and K_{37}/K_{38} ratios) show a shift in behaviour from the early Pliocene to the late Pliocene and early Pleistocene. Chapter 5, 6 and 7 will discuss the interpretations and implications of the patterns observed here for Site U1417.

4.3 Site U1418

4.3.1 Palaeo-temperature and palaeo-salinity proxies

$U^{K_{37}}$ values at Site U1418 range from -0.09 to 0.4, and have an average value of 0.1, across the 0-500 m CCSF-A interval studied here (Figure 4.7). There is an overall decrease in $U^{K_{37}}$ towards the present. $U^{K_{37}'}$ values range from 0.2 to 0.4 and have average value of 0.3. In contrast to the $U^{K_{37}}$, the $U^{K_{37}'}$ does not show any major trend throughout the top 500 m CCSF-A. $U^{K_{37}}$ shows a wider range of values than $U^{K_{37}'}$ due to the former index containing the $C_{37:4}$ alkenone, as also observed for

Site U1417 (see 4.2.1). As outlined above, the $U^{K_{37}}$ index will be discussed as the record of SST in the following chapters (Chapter 7). $C_{37:4}$ concentrations range from 1.5 to 27.5 % with an average of 14.9% (Figure 4.7). There is an overall increase in $\%C_{37:4}$ towards the present in the upper 500 m CCSF-A at Site U1418.

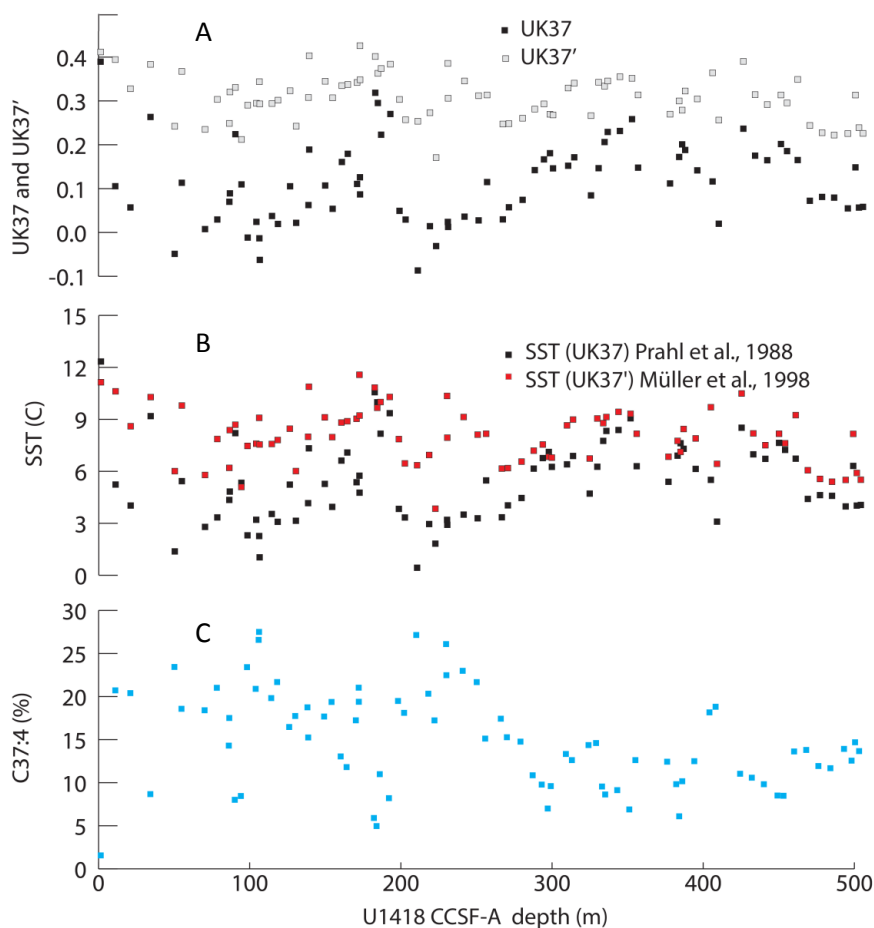


Figure 4.7: Alkenone proxies for temperature and salinity at Site U1418 proxies for Records of SST at Site U1418. (a) $U^{K_{37}}$ (black) and $U^{K_{37}'}$ (white), (b) SST ($^{\circ}$ C) calculated from $U^{K_{37}}$ (grey) and $U^{K_{37}'}$ (red) and (c) $C_{37:4}$ (%) vs U1418 CCSF-A depth (m).

$U^{K_{37}}$ based SST calibration of Prah et al. (1988) range from 0.4 to 12.3 $^{\circ}$ C with an average value of 5.4 $^{\circ}$ C. $U^{K_{37}'}$ based SST values calibrated according to Müller et al. (1998) range from 3.8 to 11.5 $^{\circ}$ C and have an average value of 8.0 $^{\circ}$ C. The SST based on the calibration of Prah et al. (1988) shows a decreasing trend over the upper 500 m CCSF-A of U1418. SST based on the $U^{K_{37}'}$ index (Müller et al., 1998) shows a small long term increasing trend throughout the top 500 m CCSF-A towards the present. Within the longer-term trends some shorter-term variability can also be

seen with most dramatic cyclicity above 300m CCSF-A, with cooling at ~200m, 100m and 50m CCSF-A (Figure 4.7).

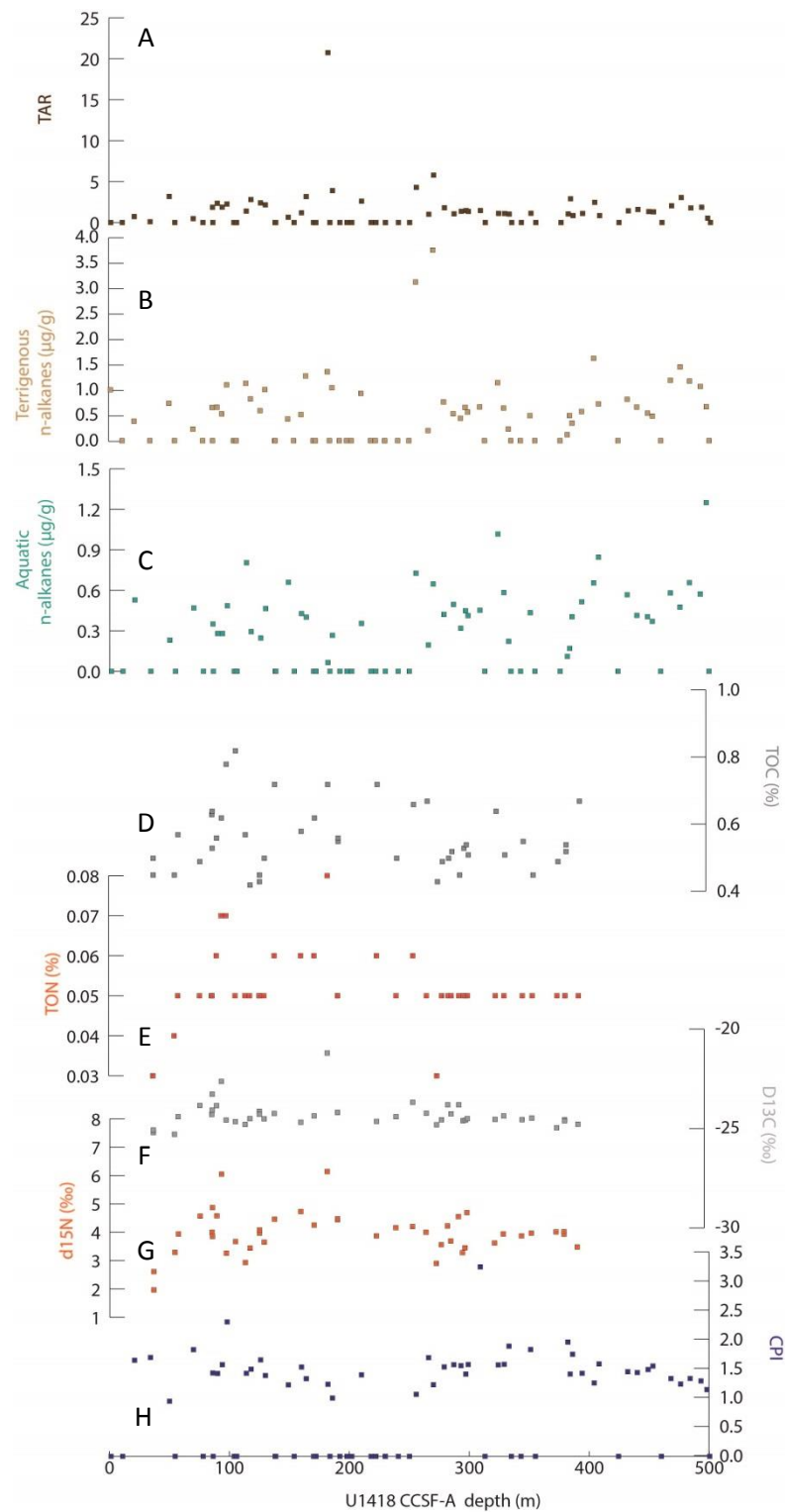


Figure 4.8: Terrigenous and marine OM input to Site U1418. (a) TAR ratio, (b) terrestrial $[[C_{27}]+[C_{29}]+[C_{31}]]$ (brown) and (c) marine $[[C_{15}]+[C_{17}]+[C_{19}]]$ (green) n-alkanes, (d) total

bulk organic carbon (TOC), (e) total organic nitrogen (TON) (%), (f) $\delta^{13}\text{C}$, (g) $\delta^{15}\text{N}$ (‰) and (h) CPI index plotted by U1418 CCSF-A depth (m).

4.3.2 Terrestrial and aquatic organic matter proxies

TOC concentrations range from 0.4 to 0.8 % with an average value of 0.6%. TOC values increase moving upwards through the core, with values from 0.4 to 0.8 % from 500 to 100 m CCSF-A, but this trend is reversed in the uppermost 100m CCSF-A, with a drop in TOC to values between 0.4 to 0.6 % (Figure 4.8). TON concentrations range from 0.03 to 0.08 % and have an average value of 0.05 % (Figure 4.8). TON concentrations are close to the detection limit of the analyser.

Organic $\delta^{13}\text{C}$ values range from -25.5 to -21.3 ‰ and have an average value of -24.3 ‰ (Figure 4.8). There is a trend towards increase in $\delta^{13}\text{C}$ concentrations from 500 to 70 m CCSF-A and a decreasing trend during the last 70 m CCSF-A depth. Organic $\delta^{15}\text{N}$ values range from 2 to 6.1 ‰ and have an average value of 4 ‰ (Figure 4.8). There is an increasing trend in $\delta^{15}\text{N}$ values from 500 to 70 m CCSF-A and a drop during the last 70 m CCSF-A.

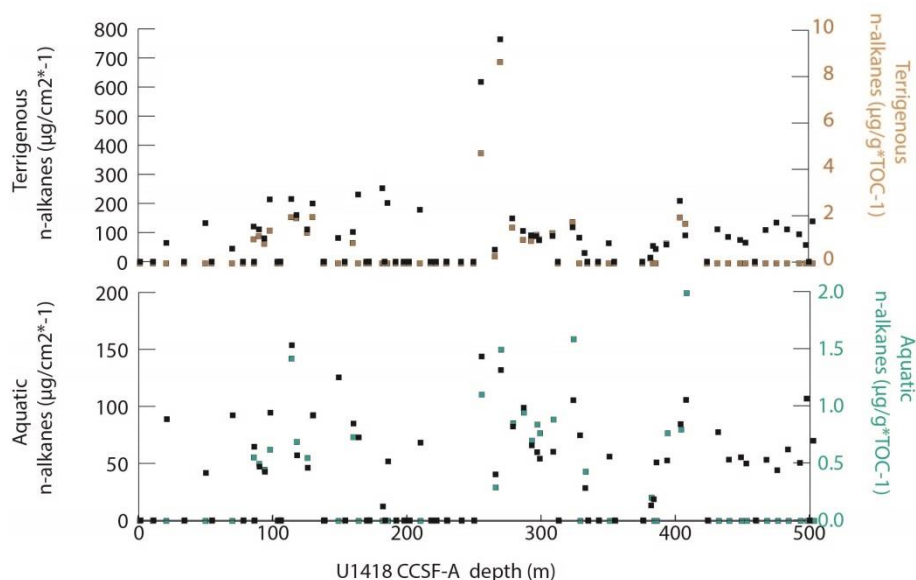


Figure 4.9: Terrigenous and marine OM normalised to sedimentation rates and organic carbon changes at Site U1418. Terrigenous (brown) and aquatic (turquoise) n-alkanes ($\mu\text{g g}^{-1} \text{TOC}^{-1}$, right axes) and both in black ($\mu\text{g cm}^{-2} \text{kyr}^{-1}$, left axes).

TAR values at Site U1418 range from 0 to 20.7 and have an average value of 1.3 (Figure 4.8). An outlying high TAR of 20.7 (182.2 m CCSF-A), reflects both very low ($0.06 \mu\text{g g}^{-1}$) aquatic *n*-alkane and a high ($1.0 \mu\text{g g}^{-1}$) terrigenous *n*-alkane inputs. Elsewhere, TAR values show an increasing trend towards the present day in the uppermost 280 m CCSF-A. Terrestrial *n*-alkane concentrations range from 0 to $3.7 \mu\text{g/g}$ (0 to $8.6 \mu\text{g g}^{-1} \text{TOC}^{-1}$; 0 to $764.0 \mu\text{g cm}^{-2} \text{kyr}^{-1}$), with an average value of $0.5 \mu\text{g g}^{-1}$ ($0.5 \mu\text{g g}^{-1} \text{TOC}^{-1}$; $79.2 \mu\text{g cm}^{-2} \text{kyr}^{-1}$). Aquatic *n*-alkane concentrations range from 0 to $1.2 \mu\text{g g}^{-1}$ (0 to $2.0 \mu\text{g g}^{-1} \text{TOC}^{-1}$; 0 to $153.7 \mu\text{g cm}^{-2} \text{kyr}^{-1}$) with an average value of $0.3 \mu\text{g g}^{-1}$ ($0.3 \mu\text{g g}^{-1} \text{TOC}^{-1}$; $40.3 \mu\text{g cm}^{-2} \text{kyr}^{-1}$) (Figure 4.8 and Figure 4.9).

N-alkane concentrations are double (terrestrial, $0.61 \mu\text{g g}^{-1}$; aquatic, $0.35 \mu\text{g g}^{-1}$) those recorded during the 500-250m interval than during the last 250 m (terrestrial $0.36 \mu\text{g g}^{-1}$ and aquatic $0.17 \mu\text{g g}^{-1}$) (Figure 4.8).

CPI values range from 0 to 3.3 and have an average value of 0.9. The CPI shows variations but no clear trend across the uppermost 500 m CCSF-A (Figure 4.8). Slight increases in CPI are recorded between 300 and 400 m CCSF-A and at 100 m CCSF-A.

4.3.3 Palaeo-marine export production proxies

Alkenone concentrations range from 0 to $13.4 \mu\text{g g}^{-1}$, from 0 to $0.14 \mu\text{g g}^{-1} \text{TOC}^{-1}$ and from 0 to $1685.6 \mu\text{g cm}^{-2} \text{kyr}^{-1}$ and have an average value of $0.2 \mu\text{g g}^{-1}$, $0.03 \mu\text{g g}^{-1} \text{TOC}^{-1}$ and $219.6 \mu\text{g cm}^{-2} \text{kyr}^{-1}$ (Figure 4.10). Alkenone concentrations have a small long term decreasing trend during the last 500 m CCSF-A at Site U1418.

Brassicasterol concentrations range from 0.01 to $0.8 \mu\text{g g}^{-1}$ and have an average value of $0.2 \mu\text{g g}^{-1}$ (Figure 4.10). Brassicasterol concentrations increase up to $0.8 \mu\text{g g}^{-1}$ between 50 to 200 m CCSF-A, and up to $0.35 \mu\text{g g}^{-1}$ from 400 to 500 m CCSF-A. Brassicasterol mass accumulation rates (Figure 4.11) range from 1.0 to $27470.5 \mu\text{g cm}^{-2} \text{kyr}^{-1}$ with an average of $5163.6 \mu\text{g cm}^{-2} \text{kyr}^{-1}$. Brassicasterol concentration normalized by the TOC ranges from 0 to $0.5 \mu\text{g g}^{-1} \text{TOC}^{-1}$ with an average value of $0.05 \mu\text{g g}^{-1} \text{TOC}^{-1}$ (Figure 4.11). Brassicasterol shows a decreasing trend during the last 500 m CCSF-A.

Dinosterol abundance values range from 0 to $0.9 \mu\text{g g}^{-1}$ and have an average value of $0.1 \mu\text{g g}^{-1}$. Dinosterol abundances increase during the 50 to 200 m CCSF-A interval (up to around $0.4 \mu\text{g g}^{-1}$) and from 400 to 500 m CCSF-A (up to $0.3 \mu\text{g g}^{-1}$) but there is not a clear long term trend in dinosterol abundances (Figure 4.10). Dinosterol mass accumulation rates ranges from 0.0 to $35737.6 \mu\text{g cm}^{-2} \text{kyr}^{-1}$ with an average of $3799.4 \mu\text{g cm}^{-2} \text{kyr}^{-1}$ (Figure 4.11). Dinosterol abundances normalized by the TOC ranges from 0 to $0.6 \mu\text{g g}^{-1} \text{TOC}^{-1}$ with an average value of $0.06 \mu\text{g g}^{-1} \text{TOC}^{-1}$.

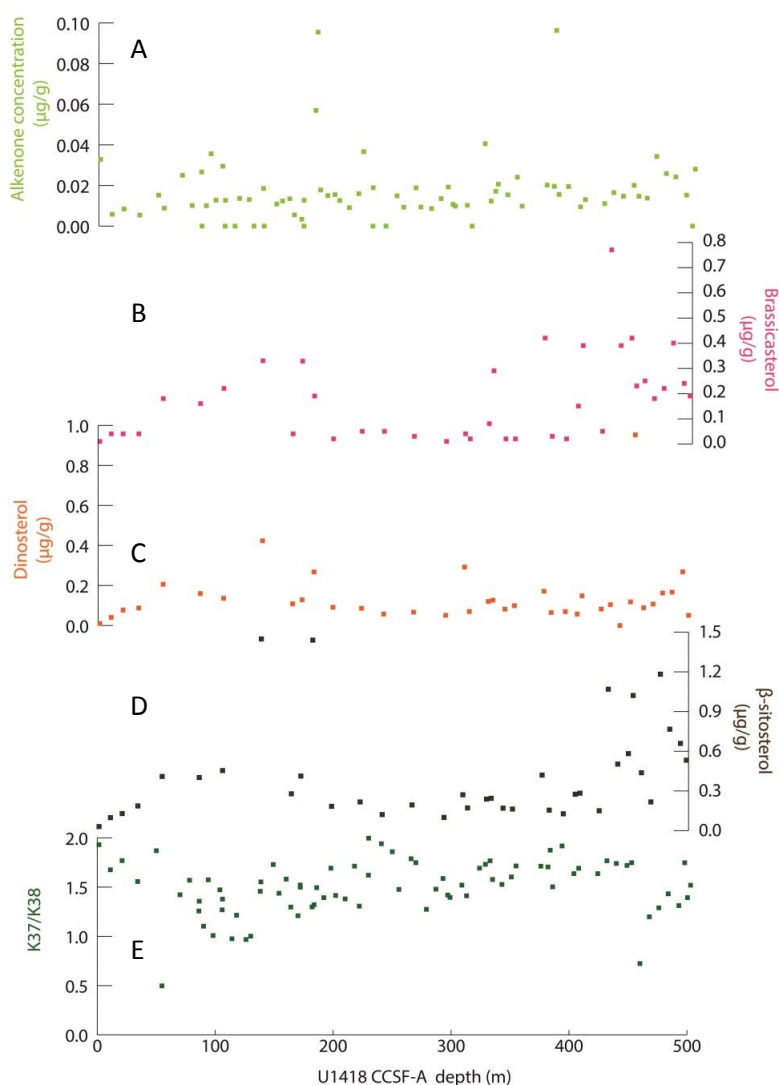


Figure 4.10: Marine productivity export proxies at Site U1418. (a) Alkenone abundances ($\mu\text{g/g}$), (b) Brassicasterol, (c) dinosterol ($\mu\text{g/g}$), (d) β -sitosterol and (e) C_{37}/C_{38} alkenone ratio (K_{37}/K_{38}) vs U1418 CCSF-A mid-point depth (m).

β -sitosterol abundance concentration range from 0 to $1.4 \mu\text{g g}^{-1}$ and have an average value of $0.4 \mu\text{g g}^{-1}$ (Figure 4.10). β -sitosterol abundances increase between 50 to 200 m CCSF-A, up to $1.5 \mu\text{g g}^{-1}$, and from 400 to 500 m CCSF-A, up to $1.2 \mu\text{g g}^{-1}$. β -sitosterol mass accumulation rates ranged from 4.0 to $38303.7 \mu\text{g cm}^{-2} \text{kyr}^{-1}$ with an average of $11122.0 \mu\text{g cm}^{-2} \text{kyr}^{-1}$ (Figure 4.11). β -sitosterol abundances normalized by the TOC ranges from 0 to $2.0 \mu\text{g g}^{-1} \text{TOC}^{-1}$ with an average value of $0.1 \mu\text{g g}^{-1} \text{TOC}^{-1}$ (Figure 4.11).

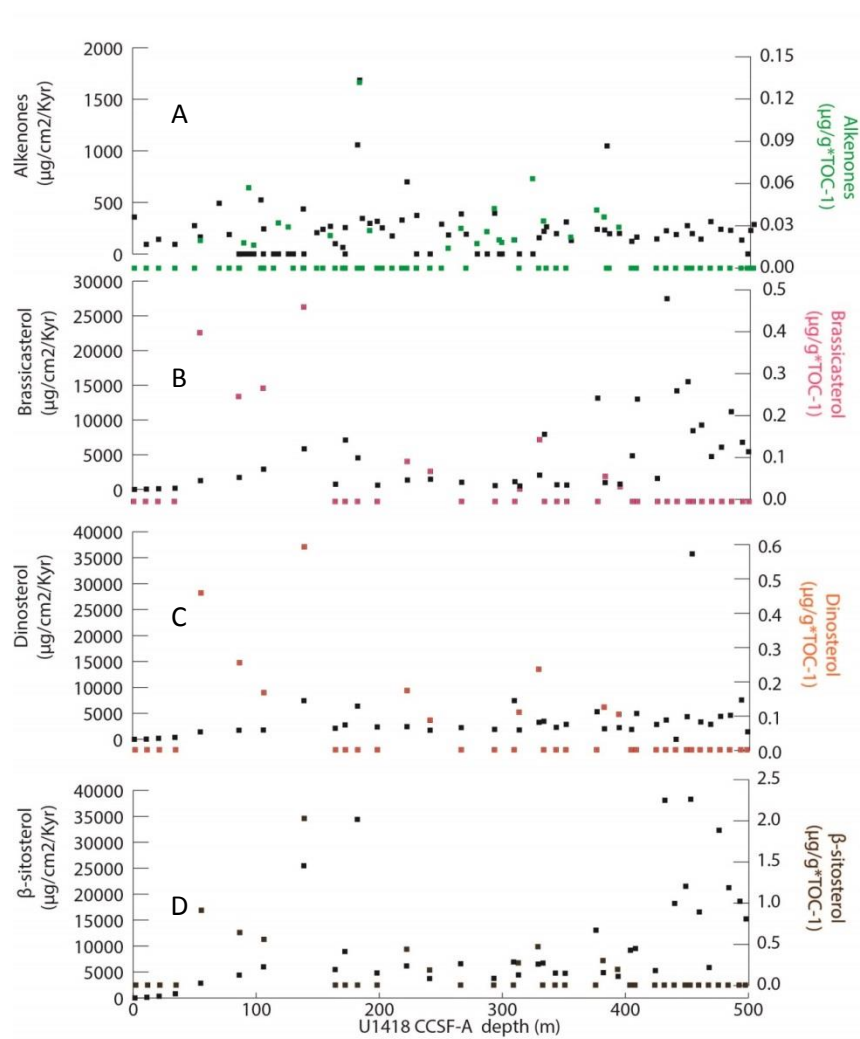


Figure 4.11: Marine productivity concentrations normalised to bulk accumulation rate or TOC content at Site U1418. Alkenone abundances, brassicasterol, β -sitosterol and dinosterol (coloured data in $\mu\text{g g}^{-1} \text{TOC}^{-1}$, right axes; black in $\mu\text{g cm}^{-2} \text{kyr}^{-1}$) vs U1418 CCSF-A depth (m).

The K_{37}/K_{38} ranges from 0.5 to 2.0 with an average value of 1.5. The K_{37}/K_{38} ratios at Site U1418 show an overall decrease moving up the core towards present, although there is an increase in the uppermost 100 m CCSF-A (Figure 4.10).

4.4 Summary

Overall trends at Site U1418 show a slight long term warming towards present, and development of a fresher ocean surface. Lower resolution data on terrigenous and aquatic *n*-alkanes, sterol, TOC and TON, $\delta^{13}\text{C}$ and $\delta^{15}\text{N}$ concentrations inputs do not reveal any long term trends. However, alkenone concentrations and K_{37}/K_{38} ratio show a long term decrease during the 500 to 50 m CCSF-A. Sterol concentrations show synchronous changes over the last 500 kyr. All terrestrial and marine proxies show a truncation in their increasing long term trends or variability in the last 50 m CCSF-A. Chapter 7 will assess the interaction between the reconstructed SSTs and evidence for ice sheet development over the late Pleistocene.

Chapter 5: Cordilleran Ice Sheet development with warm sea surface temperatures in the Gulf of Alaska

5.1 Introduction

During the Neogene, the climate transitioned from a globally warm to a globally cooler climate that enabled the development of ice masses in both hemispheres (Zachos *et al.*, 2001a). The MPWP (3.3-3.0 Ma) is a warm period that interrupts the cooling trend during the Pliocene, with global temperatures around 2-3 °C above pre-industrial levels (Jansen *et al.*, 2007; Haywood *et al.*, 2004), and warming suggested to have been more intense at higher latitudes (Haywood *et al.*, 2013; Dolan *et al.*, 2015). The MPWP has been suggested as a potential analogue to the 21st century climate due to the atmospheric CO₂ levels (400 ppmv) and largely equivalent continental configurations relative to the present (Salzmann *et al.*, 2011; Raymo *et al.*, 1996, Jansen *et al.*, 2007).

Overall, the mid-Pliocene ice masses were smaller than modern (Dolan *et al.*, 2011), except during the “M2 event” (~3.3 Ma) (De Schepper *et al.*, 2013). The M2 event is a dramatic cooling in the ocean which is considered to be a premature attempt of a glaciation which was unsuccessful (De Schepper *et al.*, 2013). Climate model experiments suggest that during M2, the area of formation of the North Atlantic Deep Water (NADW) was more extensive and shifted northwards, and high-latitude vegetation shifted from tundra to conifers (Dowsett *et al.*, 1994; Dowsett *et al.*, 2009).

However, some aspects of the Pliocene continental configuration were different than at present, which may have had regional climate impacts. For example, the Central American Seaway (CAS) final closure has been stipulated by models (Haug and Tiedeman., 1998) and data (Bartoli *et al.*, 2005) to have occurred by 2.74 Ma, although the timing of the CAS closure is still under debate (Section 2.3.2). The CAS closure has been suggested to be responsible for an increase in the poleward transport of salt and heat and increased moisture supply to the northern latitudes

culminating in the NHG (Bartoli *et al.*, 2005). It has also been associated with an enhanced North Atlantic Thermohaline Circulation (Bartoli *et al.*, 2005). The Indonesian Throughflow was reduced between 3 to 4 Ma (Cane and Molnar, 2001) and more recently that time frame has been reduced to between 3.5 to 3.0 Ma (Karas *et al.*, 2011a and 2011b). This tectonic change has been associated (Karas *et al.*, 2011a) with the increased heat transport to the Southwest Pacific and a decrease in meridional temperature gradients during the gradual global climate cooling trend.

Events which may have affected the North Pacific, and the Gulf of Alaska, include the opening of the narrow Bering Sea gateway at 4.5 Ma, which produced a cooler Nordic Seas and, together with changes in the CAS, led to the intensification of the North Atlantic Meridional Overturning Circulation (AMOC) (De Schepper *et al.*, 2015). Climate modelling results indicate that the closure of both the Bering Strait and Canadian Arctic Archipelago are both associated with warmer SSTs in the North Atlantic and intensification of the AMOC (Otto-Bliesner *et al.*, 2016). It remains unclear what impact these events had on the North Pacific.

Topographic changes also occurred during the mid-Pliocene with mountain uplift in the Himalayas (main uplift started at 4.5 Ma-present, Zheng *et al.*, 2000) and the European Alps (Plio-Pleistocene, Spencer, 1965). The St. Elias Mountains, situated in coastal Alaska, is the highest coastal mountain range in the world at present (Enkelmann *et al.*, 2015). The uplift of the St Elias Range from early Pliocene to early Pleistocene led to an increase in orographic precipitation and subsequent increase in sedimentation rates. The high erosional pathway shifted to the southern St Elias Range at 2.6 Ma (Enkelmann *et al.*, 2015). It has been proposed that mountain glaciation developed in the St Elias mountains from 5.5 Ma (Reece *et al.*, 2013), ultimately developing into tidewater glaciers, which still shape the regional landscape. It is still debated whether climatic or tectonic forcing was the main driver of the NHG (Haug *et al.*, 2005), as it cannot be explained solely by changes in isolation (Lunt *et al.*, 2008). An alternative mechanism to grow and expand ice-sheets independent of climate forcing is through changes in topography and its impact on orographic precipitation (Bartoli *et al.*, 2005, Haug *et al.*, 2005).

Independent regional records of climate such as in the Gulf of Alaska could test these hypotheses.

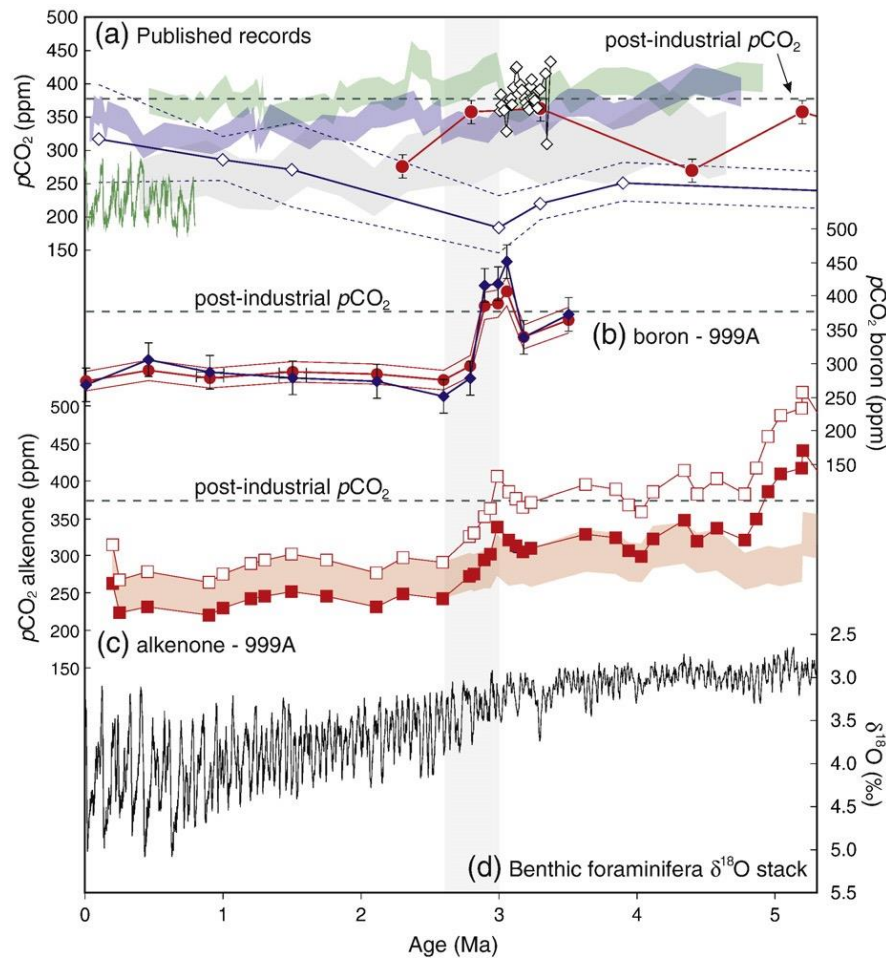


Figure 5.1: CO₂ Plio-Pleistocene reconstructions from (a) EPICA (green; Lüthi *et al.*, 2008), $\delta^{11}\text{B}$ from ODP Sites 871 and 872 in the west equatorial Pacific (blue diamonds; Pearson and Palmer, 2000), and stromata fossil leaves (red circles; Kürschner *et al.*, 1996), $\delta^{13}\text{C}$ of bulk organic material from ODP Site 806 in the west Equatorial Pacific (white diamonds, Raymo *et al.*, 1996) and alkenones from the ODP Sites 925 in the west Equatorial Atlantic (blue), 806 (green) and 1208 (grey) in the west Equatorial Pacific (Pagani *et al.*, 2010) multiproxy $p\text{CO}_2$ reconstructions; (b) from $\delta^{11}\text{B}$ from ODP Leg 165, Site 999 in the Caribbean Sea (Seki *et al.* 2010) and (c) from alkenones from ODP Leg 165, Site 999 in the Caribbean Sea (Seki *et al.* 2010) compared to benthic $\delta^{18}\text{O}$ LR04 stack (Lisiecki and Raymo, 2005) and modern reconstructions $p\text{CO}_2$ (Keeling *et al.*, 2009). (Figure from Seki *et al.* (2010)).

Amongst the mechanisms for the climatic shift from the start of the MPWP to the cold NHG is a drop in atmospheric CO₂ concentration (Seki *et al.*, 2010). The

cooling trend of the Pliocene is synchronous with a decrease in CO₂ (Figure 5.1) which likely promoted ocean cooling via reduced radiative forcing and the expansion of the continental ice sheets. The overall CO₂ decrease in the late Pliocene becomes more abrupt during the Plio-Pleistocene transition around 2.8 Ma (Martínez-Botí *et al.*, 2015; Seki *et al.*, 2010) (Figure 5.1). Despite the global drop in atmospheric CO₂, timing of the onset of the NHG varies between locations based on IRD delivery to northern oceans and at some locations the NHG has been set as far back as at 3.5 Ma (Nordic Seas, Mudelsee and Raymo, 2005). However, the timing of the intensification of the NHG (iNHG) has been set to around 2.5 Ma based on IRD counts from the North Atlantic (Shackleton *et al.*, 1984) and at 2.7 Ma based on IRD from the North Pacific (Haug *et al.*, 1999).

Here, we present new data sets from the Gulf of Alaska to examine the evidence for past climate change in the Northeast Pacific Ocean and for the advance and retreat of the Cordilleran Ice Sheet across the Pliocene-Pleistocene transition. We analyse marine sediments collected by IODP Expedition 341, which indicated that the onset of a significant glaciation and enhanced erosion developed at the Pliocene-Pleistocene boundary (Gulick *et al.*, 2015). IODP Site U1417 (56° 57.38'N, 147° 7.86 'W, water depth 4218m) is examined from 4 to 1.5 Ma through the alkenone SST proxy (the U^K_{37'} index), the abundance of the cold water alkenone C_{37:4}, the mass accumulation rate of ice rafted debris (IRD, from Ellen Cowan) and the terrestrial-to-aquatic ratio (TAR) of *n*-alkane biomarkers. We test the hypothesis that the late Pliocene expansion of the Cordilleran Ice Sheet responded to cooling associated with the Pliocene-Pleistocene transition.

5.2 Materials and Methods

5.2.1 Site location and sedimentology

The detailed modern oceanography and sedimentology of Site U1417 are described in Chapters 2 and 3. Here we focus on the sediments spanning the transition from lithostratigraphic unit V to IV, marked most prominently by the onset of lone stones considered to indicate ice rafting at the Pliocene -Pleistocene boundary (Jaeger *et al.* 2014).

5.2.2 Age model

The shipboard age model was calculated using bio- and magnetostratigraphy (Jaeger *et al.*, 2014) (See Chapter 3 for more details). The Gauss/Matuyama magnetic reversal (2.581 ± 0.02 Ma and 287.5 ± 1 m CCSF-B) was very well constrained in multiple holes to provide an important age control point for this study. Poor carbonate preservation across the Pliocene and early Pleistocene prevents production of a higher resolution stable isotope stratigraphy. The shipboard age model sedimentation rates show a marked but temporary increase between 2.0-2.5 Ma (Chapter 3), which has been attributed to a first major erosion of the landscape by expansion of the Cordilleran ice sheet (Gulick *et al.*, 2015). The recovery of the Pliocene-early Pleistocene sediments was 70% on average (Expedition 341 Scientists, 2014), which leads to a number of core breaks in the record. However, glacial- interglacial cyclicity and longer-term trends in the data sets can be still examined.

5.2.3 Sampling resolution

119 biomarker samples were analysed between 4 and 1.7 Ma, which corresponds to a sampling resolution of 1 sample every 21,000 years (See Chapter 3 for more details). The samples spanned around 3 cm core depth: based on the Pliocene and early Pleistocene average sedimentation which ranges between 156 cm kyr^{-1} between 2.5 to 2 Ma to 18.3 cm kyr^{-1} during the 4 to 3.5 Ma (Jaeger *et al.*, 2014) this means that each sample represents an average of 0.4 kyr (minimum: 0.2 kyr, maximum: 2.2 kyr). Samples were spaced c. 44 cm across the Pliocene and early Pleistocene (1.5-4.0 Ma), which is translated into an average temporal spacing of 14.4 kyr (minimum: 2.8 kyr, maximum: 24 kyr) (See Chapter 3).

5.3 Results

5.3.1 SST

The alkenone-based SST record at Site U1417 shows orbital-scale variability throughout 4.0 to 1.7 Ma (Figure 5.2). Overall, the $U^{K'_{37}}$ -SSTs calculated using the Müller *et al.* (1998) calibration shows a range of $9.7 \text{ }^{\circ}\text{C}$ (from 3.9 to $13.6 \text{ }^{\circ}\text{C}$) (Figure 5.1). Using the $U^{K'_{37}}$ -SST calibration from Prahl *et al.* (1988), SST range of

11.4 °C, which is heavily influenced by the %C_{37:4} (Section 5.3.2; white, Figure 5.1). Average SST for different time intervals are outlined in Table 5.1.

Table 5.1: Average SST (°C) and %C_{37:4}. Average SST (°C) is the average of all the data points of the time interval, peak SST (°C) average is the average of the highest data points of each interval selected (Figure 5.2), trough SST (°C) average is the average of the lowest data points of each interval selected (Figure 5.2) and the average SST (°C) variability is the average amplitude of SST changes or difference between the peak SST average and the trough SST average for the 4 time intervals detailed in Figure 5.2 and for the Pliocene (4 to 2.8 Ma) and Pleistocene (2.7 to 1.7 Ma). In grey, data calculated from U^K₃₇ (Prahl et al., 1988) and in black, data from U^K₃₇' (Müller et al., 1998).

Age intervals (Ma)	Average SST (°C)	Peak SST (°C) average	Trough SST (°C) average	Average SST variability (°C)	Average C _{37:4} (%)	Peak C _{37:4} (%)
4.0-3.0	10.0/8.6	13.0/10.6	6.9/4.4	6.0/6.2	1.9	10.5
3.0-2.8	8.7/7.4	10.0/8.6	7.1/6.4	3.0/2.2	3.2	4.9
2.7-2.4	10.0/9.5	13.6/12.1	2.6/6.5	11.0/5.6	4.8	24.1
2.4-1.7	8.8/8.3	12.0/10.5	2.2/5.0	9.8/5.5	5.4	23.8
Pliocene	9.3/8.0	11.5/9.6	7.0/5.4	4.5/4.2	2.6	7.7
Pleistocene	9.4/8.9	12.8/11.3	2.4/5.2	10.3/6.1	5.2	23.9

5.3.2 %C_{37:4}

C_{37:4} values range from 0 to 24% (Figure 5.2). Values are lower than 5% from 4 to 3 Ma with an average of 1.7%. After 3 Ma values often exceed the 5% threshold suggested to indicate the presence of subpolar water masses (Bendle *et al.*, 2005), with a mean average value of 4.8%. Average %C_{37:4} for different time intervals are outlined in Table 5.1.

5.3.3 IRD

IRD is not present in Site U1417 sediments until 2.8 Ma, where the first and highest peak in IRD of our record appears with a value of 4.5 g cm⁻² kyr⁻¹ (Figure 5.2). After this peak, IRD remains very low (≤ 0.03 g cm⁻² kyr⁻¹) until 2.6 Ma. From 2.6 to

2.42 Ma, IRD increases again with values up to $4 \text{ g cm}^{-2} \text{ kyr}^{-1}$. From 2.4 to 1.7 Ma, IRD remains present but low ($0.588 \text{ g cm}^{-2} \text{ kyr}^{-1}$).

5.3.4 TAR index

The TAR index at Site U1417 ranges from 0.8 to 17 between 4 and 1.7 Ma, with an average of 5 (Figure 5.2). The average value is used as an indicator to visualise the dominance of the terrigenous versus marine sources of organic matter at Site U1417 during the 4 to 1.6 Ma time period. The highest TAR values are registered between 4 to 3.06 Ma, with an average value of 9.36, showing a higher terrigenous than aquatic source of the organic matter. The TAR decreases from 3.04 to 1.66 Ma to an average value of 2.73, showing an increased contribution from aquatic sources into Site U1417 (Chapter 4) in comparison with terrigenous sourced OM. After 3.046 Ma, there are three intervals of relatively higher terrigenous organic matter inputs, at 2.68, 2.66, 2.27 and 2.03 Ma (Figure 5.2), where TAR exceeds the overall average value of our record.

5.4 Discussion

5.4.1 SST Calibration

Regardless of whether the $U^{K_{37}}$ or $U^{K_{37}'}$ index is used, SSTs do not show any long-term trend between 4 to 1.7 Ma. However, the absolute values and amplitude variability is different (Figure 5.2). As detailed in Chapter 4, it is important to consider and evaluate the different alkenone indices and calibrations: here, the $U^{K_{37}'}$ index has been converted into SST according to the core-top to annual mean SST correlation constructed with samples spanning 60°S to 60°N (including from the Pacific Ocean) (Müller *et al.*, 1998), and this is our preferred calibration to be applied. The SST calibration of Prahla *et al.* (1988), which includes the $C_{37:4}$ alkenone, is also displayed here for comparison.

Regardless of the calibration, the SST show similar range of 9°C variability throughout the 2.34 Myr (4 to 1.66 Ma). This variability is comparable with modern SST variability in the top 25 m water column of the Gulf of Alaska of 10°C (Spies, 2007). The modern SST range in the Gulf of Alaska is 3.5 to 13.5°C (Levitus *et al.*, 2015), which is very similar to our SST range during the 4 to 1.5 Ma period

using the Müller *et al.* (1998) calibration (average SST of 9.7 °C). The Pliocene SST average is 8.0°C and the Pleistocene average SST is 9°C (Table 5.1). Regardless of the calibration used, the Pliocene was 2°C cooler than the Holocene and the Pleistocene was 1°C cooler than the Holocene.

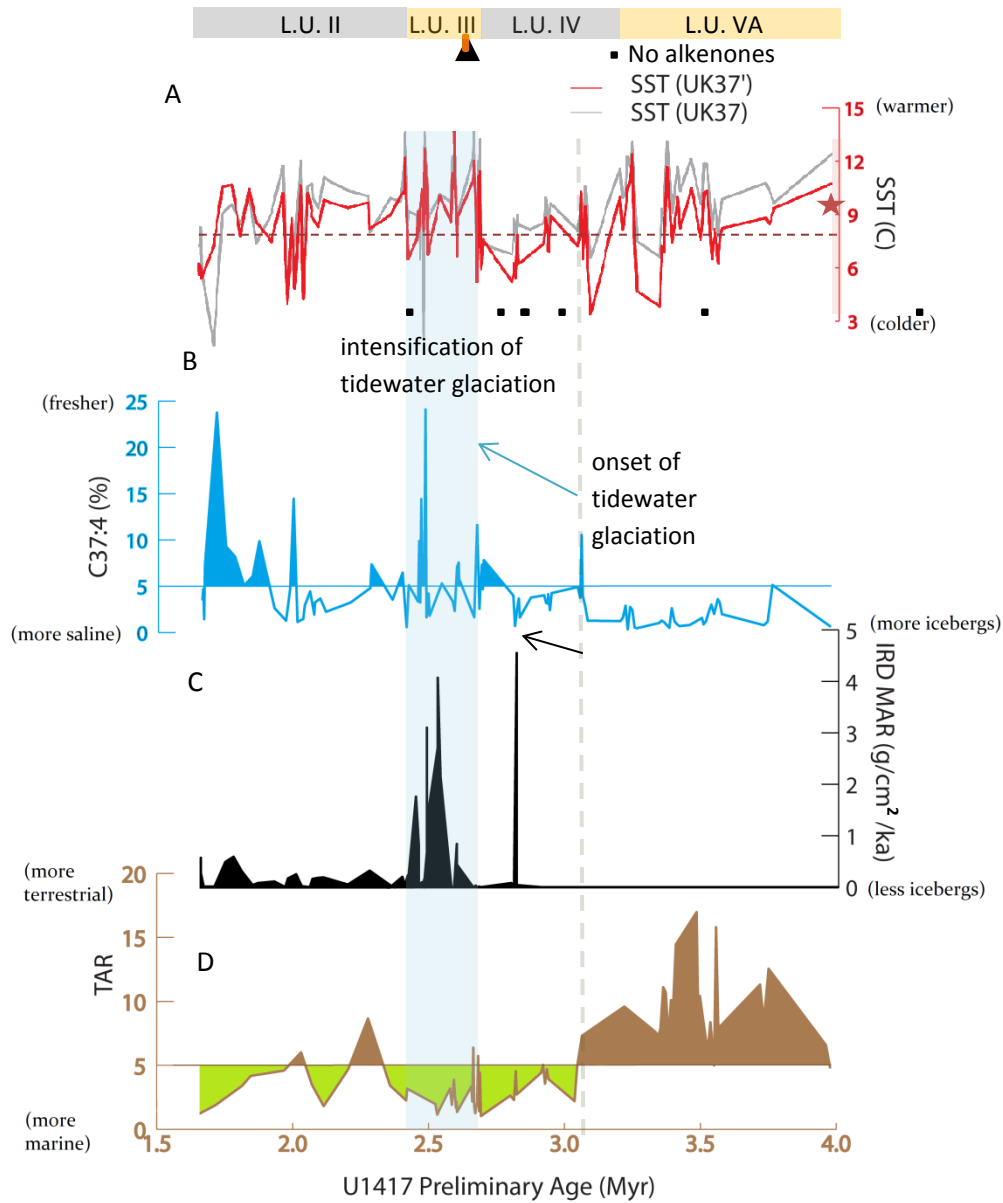


Figure 5.2: Site U1417 across the Pliocene-Pleistocene transition. (a) red line: SST from UK_{37}' index according to Müller *et al.* (1998) calibration; grey line: SST from UK_{37} index according to Prah *et al.* (1988) calibration; U1417 SST (calibrated according to Müller *et al.* (1998) in red and according to Prah *et al.* (1988) in grey. Dashed red line: Modern monthly average SST during the 1970-2016 time intervals for the 0-100 m water column depth (Weingartner *et al.* 2016) in the Gulf of Alaska and average SST through the 2005-2012 time

period (Levitus *et al.*, 2015) at Site U1417; Red star on y-axis: value of our youngest sample analysed at Site U1417 (0.01 Ma), SST calculated from Müller *et al.* (1998) calibration; Pink rectangle: modern SST range during 2000-2002 at the hydrographic station GAK 1 at the Resurrection Bay offshore of Seward, Gulf of Alaska (Weingartner, 2007) and summer and winter annual SST average (2005-2012) at Site U1417 (Levitus *et al.*, 2015). (b) abundance of the cold and freshwater alkenone $C_{37:4}$ (%). Horizontal line shows the threshold of Bendle *et al.* (2005) above which subarctic/subpolar water masses were determined for the Nordic Seas; (c) IRD MAR ($g\ cm^{-2}\ ka^{-1}$); (d) TAR index. Horizontal line shows the average TAR value from Site U1417. Lithostratigraphic units (L.U.) VA, IV, III and II of the samples and their main lithology (diamict and mud) (Jaeger *et al.*, 2014) are indicated (orange=diamict, brown=mud) at the top of the plot. Vertical dashed lines show the transition between different stages of the NHG outlined in Table 5.1: Note that the subdivision of the record into the arbitrary chosen intervals and lithostratigraphic units of the samples are often offset. Black triangle is the Gauss –Matuyama magnetic reversal (at 2.581) and the orange mark the top x-axis is the Plio-Pleistocene boundary (at 2.58); black squares: no alkenones detected;

5.4.2 Early to Late Pliocene (4 to 2.6 Ma)

The mid- to late-Pliocene SST values at Site U1417 shows that the GOA had a variable warm average of 8.6 °C (Figure 5.2; Table 5.1), which is equivalent to around 1.6 °C warmer than modern (here “modern” refers to the annual average SST of 7 °C during the 2005 to 2012 time period), with monthly SST average of 4 and 12°C during winter and summer, respectively (Levitus *et al.*, 2015). Average Pliocene SST (4 to 2.6 Ma) at Site U1417 is 0.7 °C colder than the Pleistocene (2.6 to 1.5 Ma). This means that there was a gradual warming across the late Pliocene to the early Pleistocene. A Pliocene-Pleistocene warming is consistent with ODP Site 882 in the subarctic Pacific (Martínez-García *et al.*, 2010), DSDP Site 593 in the Tasman Sea (McClymont *et al.*, 2016) and Site 1090 (Martínez-García *et al.*, 2010) in the South Atlantic, but inconsistent with the North Atlantic i.e. ODP Site 982 (Lawrence *et al.*, 2009), where there is a surface gradual cooling from the Pliocene to present. The variable SST values during the MPWP have an average of 7.3°C, similar to modern SST average, but contains peak SST values 2 to 3°C warmer than

modern average (Figure 5.2). This is important for considering the mid Pliocene warm period as an analogue for the future (Hansen *et al.*, 2006).

Both $C_{37:4}$ and IRD increase between 4 and 1.7 Ma, when TAR is observed to decrease. From 4 to 2.6 Ma the $\%C_{37:4}$ values remain low, IRD is not present in Site U1417, yet there is high terrigenous input in relation to the rest of the record. In the following sections, the processes likely to be driving these trends are assessed, in the context of an early to late Pliocene sea surface which shows minimal change in SST.

5.4.2.1 Non-existent/small Cordilleran Ice Sheet in the early and mid Pliocene

The absence of IRD from 4 to 3.05 Ma suggests that the Cordilleran Ice Sheet, if at all present, was not yet extensive enough to deliver icebergs to the GOA. However, our records from Site U1417 cannot exclude the possibility of small glaciers developing in Alaska since 4 Ma, as indicated from neodymium and lead isotope records from the Bering Sea (Horikawa *et al.*, 2015). Furthermore, the absence of IRD at Site U1417 contrasts with the first appearance of IRD at ODP 887, which shows evidence for development of tidewater glaciation in the GOA from 5.5 Ma, and which was attributed to the uplift of the Yakutat formation (Reece *et al.*, 2013). However, the IRD mass accumulation rates at ODP 887 before 2.6 Ma is very small, being close to 0 and $<0.2 \text{ g cm}^{-2} \text{ Ky}^{-1}$ (Krissek *et al.*, 1995). Early Pliocene and even Miocene evidence of tidewater glaciation ($\delta^{18}\text{O}$, IRD) have been found also at other locations in the North Atlantic (Mudelsee and Raymo, 2005; Bachem *et al.*, 2016). However, as also observed in the GOA, these are also considered to be minor in scale compared to during the major glaciations of the late Pliocene and Pleistocene.

5.4.2.2 Terrigenous organic matter input into the GOA

There is a shift of TAR at 3 Ma, which we interpret as a change in relative importance of marine or terrigenous organic matter input into U1417 (Lei *et al.*, 2012). One potential mechanism to explain increased terrigenous organic matter inputs is due to glaciation increasing the erosion rates on land (Childress, 2016). Between 4 to 3 Ma, the high TAR and an absence of IRD suggests that the south-

eastern Alaskan coast was a heavily vegetated landscape, eroded by rivers and possibly mountain glaciers whose extension was limited to the land.

High Pliocene TAR values (5 to 16) occur with relatively low sedimentation rates at Site U1418. River transport and ocean currents could transport terrigenous material from the Yakutat Terrain (Childress, 2016) to Site U1417, 700 km offshore the Alaskan coast. The Kulthieth rocks have high TAR signature of a maximum value of 2 (Childress, 2016) and could imprint the sediments delivered to the ocean with an ancient signal of terrigenous organic matter, rather than reflecting erosion of contemporary 'fresh' organic matter from vegetation and soils. However, site U1417 CPI values >1 (Chapter 4, Figure 4.3) do not overlap with CPI values found in Alaska's lithology <1 (Childress, 2016).

The sedimentology of Site U1417 also shows evidence for downslope transport from the Alaska coast to the benthic regions of U1417 (Jaeger *et al.*, 2014). Gravity flow and suspension fallout from surface water plumes (Jaeger *et al.*, 2014) could have contributed to the transport of the plant waxes offshore Site U1417. Alternatively, dust transport from North America has been presented as a key process for plant wax transportation to the North Atlantic during the NHG (Naafs *et al.*, 2012). Some climate model outputs (McClymont *et al.*, 2012) suggest that a deeper AL and intense winds blowing offshore Alaska can develop during cold periods such as the LGM (McClymont *et al.*, 2012). If the colder SST during the Pliocene in comparison with the Pleistocene reflected a deeper AL, and/or the Yakutat terrain was already covered by ice during the Pliocene (Reece *et al.*, 2013), dust driven transport of terrigenous organic matter may have developed. Site U1417 low sedimentation rates, absence of IRD and high TAR during the Pliocene in comparison with the early Pleistocene cannot resolve the hypothesis above.

5.4.2.3 M2 Glaciation attempt (~3.3 Ma)

Two intervals of significant cooling are recorded during the Pliocene at Site U1417: during MIS M2 and KM2. Both intervals are punctuated by core breaks, suggesting a change in the sediment lithology which made core recovery difficult. Both cool stages reach SSTs only subsequently seen during the early Pleistocene (Figure 5.3). The M2 has been proposed as a significant Pliocene glaciation, but it did not reach

the same extension as the early Pleistocene glaciations, possibly due to the prevalent high atmospheric CO₂ levels (De Schepper *et al.*, 2013). Among the mechanisms proposed for this glaciation attempt (Haug and Tiedemann, 1998) is the *a priori* enhanced ocean flow by the Panama Seaway closure and the increase in heat transport to the North Atlantic (De Schepper *et al.*, 2013). This mechanism could mean an increase in precipitation in the GOA by increased westerly winds through positive AO and NAO atmospheric teleconnections (Hill *et al.*, 2011) (Chapter 2). However, if this event triggered the appearance of glaciation in Alaska at all (De Schepper *et al.*, 2013), the glaciation was not intense enough to grow an ice sheet or tidewater glaciers which were able to deliver icebergs to Site U1417, as no IRD is recorded here until after 2.8 Ma. Critically, the new SST data presented here is the first climatic data for the GOA (and one of only a few for the North Pacific), and may therefore be important for improving assessment of climate model outputs during this time (Dolan *et al.*, 2015).

5.4.2.4 Onset of tidewater Glaciation in the GOA (3 to 2.8 Ma)

At 3 Ma, the TAR diminishes, as organic matter from higher plants transported to Site U1417 slightly decreases and marine OM increases. One possibility to explain a fall in terrigenous organic matter is that the land could have become increasingly ice covered, in turn limiting the growth of vegetation and so the abundance of terrigenous organic matter that could be eroded to the ocean. Terrigenous sediment transport in small river systems might have decreased due to glaciation (Childress, 2016) compared to before the NHG. Arid conditions in Asia have been previously proposed from 3.5 Ma with the initiation of the NHG in the North Pacific Ocean from aeolian MAR studies from the central North Pacific (Snoeckx *et al.*, 1995). An alternative explanation for the changing TAR is that a change in erosional pathways after tectonic uplift of the Chugach/St. Elias mountain (although this change is constrained to 2.7 Ma by Enkelmann *et al.* (2015) and the glaciation could have altered the main path of terrestrial input to the Surveyor Channel to higher metamorphic and plutonic sources (Childress, 2016).

The onset of falling TAR coincides with an increase in average sedimentation rates to 85 m Myr⁻¹, and is marked by the first % C_{37:4} value to reach above the 5%

threshold proposed by Bendle *et al.* (2005) to discriminate coastal and subpolar/subarctic water masses in the Nordic Seas. This increase in sedimentation rates indicates that the erosive agent was more efficient than before 3 Ma (despite the relative reduction in terrigenous organic matter) and suggests that glaciers were present in land, although their signal is not yet visible in IRD because they had not developed calving margins. Although $\%C_{37:4}$ has been linked to the presence of subpolar water masses (Bendle *et al.*, 2005), it also, in part, reflects the association of $C_{37:4}$ with a colder and fresher surface ocean. An alternative explanation for the increase in $\%C_{37:4}$ at 3 Ma is that meltwater from the expanding glaciation onshore influenced the sea surface in the GOA, as is observed today in the Alaska Coastal Current (Chapter 2). At 3 Ma, average SSTs remain warm (around 10 °C, since 4 Ma), yet the evidence from Site U1417 suggests that environmental changes are already developing onshore. From 3 Ma, there is some evidence for cooling at Site U1417, but there is also less SST variability (Figure 5.2) so that the coldest SSTs observed during the Pliocene are not repeated.

5.4.3 The intensification (2.8 Ma) of the Cordilleran Ice Sheet and its evolution during the early Pleistocene (2.8-1.7 Ma)

TAR values remain low (between 1 to 6) and IRD counts, after their first appearance at 2.8 Ma ($4.5 \text{ MAR g cm}^{-2} \text{ Kyr}^{-1}$), decrease from 2.8 to 2.6 Ma to values of between 0 and $1 \text{ g cm}^{-2} \text{ Kyr}^{-1}$ and increase from 2.6 to 2.4 Ma (up to $4 \text{ g cm}^{-2} \text{ Kyr}^{-1}$). The low TAR values and the high IRD counts appear synchronous with the higher SSTs and the high $\%C_{37:4}$ over this time period. The first big pulse of IRD ($4.5 \text{ MAR g cm}^{-2} \text{ Kyr}^{-1}$) and doubling of sedimentation rates at 2.8 Ma (from 85 to 145 m Myr^{-1} average) is the first evidence that tidewater glaciers were present in the GOA and delivered icebergs to the sea, and it has been suggested to be the maximum Cordilleran Ice Sheet extension during the Pliocene (Gulick *et al.*, 2015). These records together suggest that the Cordilleran Ice Sheet remained extensive after the NHG and now developed a higher discharge of icebergs into the sea. Yet this “intensification of the Alaskan tidewater glaciation” occurred with a GOA that was either warmer than, or of comparable warmth to, the late Pliocene.

Due to the lack of SST data from 2.8 to 2.69 Ma, we can't be certain of the cause of the decrease in IRD after the first major peaks at 2.8 Ma. However, with the onset of the Pleistocene, between 2.69 to 1.66 Ma, Site U1417 is marked by the highest sustained IRD and $\%C_{37:4}$ of the record presented here. $C_{37:4}$ often exceeds 5%, and especially between 2.8 to 2.5 Ma when $C_{37:4}$ values reach their maximum (up to 24%). The average $\%C_{37:4}$ value for the early Pleistocene is 5.2%. Despite the attributable influence of subpolar water masses on GOA sea surface characteristics, the study of Bendle *et al.* (2005) in the Nordic Seas determines that the range of $\%C_{37:4}$ of 0 to 25% is too high to be associated with truly polar water masses. These values are similar to those of the East Greenland Current, and the North and East Icelandic Currents, which have a mix of polar and Atlantic waters (Bendle *et al.*, 2005). Although stratification of the water column due to glacier discharge in the north Pacific results in warmer sea surface in comparison with the water body underneath it (Meheust *et al.*, 2013), there is no information about the origin of $C_{37:4}$ from the North Pacific to explain the high values recorded at Site U1417.

Furthermore, the overall increase in $\%C_{37:4}$ in the GOA during the early Pleistocene occurs as SSTs warm by around 1°C relative to the Pliocene (Figure 5.2), although cooler SST are accompanied by high $C_{37:4}$ (up to 25%), a pattern which also supports the idea of a mixture of water masses influencing the GOA (Bendle *et al.*, 2005). One possibility to reconcile these patterns is that the sea surface water masses in the GOA do not directly relate to the subpolar/subarctic sources, but that the $C_{37:4}$ may be related to salinity and not to SST changes. A possible explanation for the co-existence of warmer GOA SSTs, the lower (250 to 400 ppm) atmospheric CO_2 levels during this time than in the Pliocene (Seki *et al.*, 2010; Martínez-Botí *et al.*, 2015), with potential freshening of surface water masses, could be the stratification of the water column due to increased evaporation and precipitation (Haug *et al.*, 2005) and/or due to increased glacier meltwater. The inputs of IRD and terrigenous OM to Site U1417 show the potential for terrigenous sediment to reach the site. Therefore, despite the location of Site U1417 700 km away from land, the overall correspondence between $\%C_{37:4}$ increase and the IRD delivery supports the interpretation of the $\%C_{37:4}$ as a glacier meltwater signal.

Pliocene-Pleistocene SSTs differ by ~ 1 °C, with the early Pleistocene warmer than the late Pliocene. This pattern has not been observed in the North Atlantic (Lawrence *et al.*, 2009) and is not consistent with a linear response to global CO₂ concentrations at this time, even given CO₂ proxy uncertainties (Martínez-Botí *et al.*, 2015; Seki *et al.*, 2010). Ocean stratification and a less mixed water column would help in surface ocean fast warming, which would be a source of moisture to the land and trigger orographic precipitation (Haug *et al.*, 2005) in the uplifted coastal terrain. These processes would have been key for a fast Cordilleran Ice Sheet growth (Haug *et al.*, 2005; Enkelmann *et al.*, 2015), since there is also evidence in further uplift of the St. Elias Mountains at 2.7 Ma which may have amplified the response in development of the Cordilleran Ice Sheet during a period of warm SST (Enkelmann *et al.*, 2015).

Between 3.2 to 2.8 Ma, atmospheric CO₂ concentrations decreased from higher than present values between 280 and 450 ppmv before 3.2 Ma (Pagani *et al.*, 2010; Seki *et al.*, 2010) to pre-industrial concentrations of 250-300 ppmv by about 2.4 Ma (Seki *et al.*, 2010). However, Martínez-Botí *et al.* (2015) reconstructed a decrease in pCO₂ between 2.8 to 2.6 Ma to below, or close to, the modelled threshold for the NHG (280 μ atm). A decrease in CO₂ can decrease surface air temperature around 1 to 2 °C in the Gulf of Alaska area (Lunt *et al.*, 2012). It has already been suggested after MIS 5e in the Nordic Seas (Risebrobakken *et al.*, 2007) that moisture source could be a major factor in ice-sheet built-up without changes in tectonics and during a period of low insolation. In modelling experiments, a 50% reduction in the elevation of the Rockies in the Pliocene led to a 2-3°C lowering of surface air temperature in the GOA, due to a reduction in cloud cover and precipitation, and is further associated with warming in the Barents Sea and Arctic which can be increased with reduced ice cover (Lunt *et al.*, 2012). However, vegetation changes attributed to low albedo from boreal forests can increase the surface air temperature about 3 to 4°C in a localized area of the St. Elias Mountains (Lunt *et al.*, 2013). Changes in vegetation and albedo could be considered during ice sheet growing with no change in SST.

5.4.4 Comparison between climatic evolution of the west and east subarctic Pacific during the Plio-Pleistocene transition.

Mean annual SST in the modern subarctic North Pacific Ocean are 1 °C warmer in the east than in the west. Modern oceanography in the north Pacific describes a subpolar gyre in the GOA that drives oceanic currents from the west, off the coast of Japan, to the east and then to the north near the south coast of Alaska and then along the Aleutian Islands (Chapter 2, Figure 2.1). The new data presented here, indicates that during the Pliocene and early Pleistocene the opposite pattern of SSTs occurs compared to the modern: SSTs are 3-4 °C warmer in the west than in the east (8.7 °C for U1417 and 12 °C for ODP 882) (Figure 5.3). Thus, in comparison with the modern (Chapter 2, Figure 2.2), the subarctic west Pacific was around 1-2°C warmer and the subarctic east Pacific was 1-2°C colder during the Plio-Pleistocene. We do not find a modern analogy where the east Pacific becomes colder and the west Pacific warmer, only that the seasonal changes in the AL position drives the subarctic Pacific to become colder in winter with an increase in storminess and associated water column mixing in the GOA, and a warmer subarctic Pacific occurs in summer with associated water column stratification in the GOA (Chapter2). Therefore, the temperature inversion between the west and east Pacific cannot be explained by changes in the intensity of the AL alone.

During the Pliocene, ODP 882 (northwest Pacific) is colder and ODP 1021 (mid-latitude east Pacific) is warmer. During the PPT and the NHG, both sites have similar SSTs. After the NHG, Site 882 gets warmer and Site 1021 gets colder. Pliocene SST differences could be explained by the ice-free behaviour of the Arctic Ocean during the Pliocene and the modern permanent and seasonal Arctic sea-ice cover. A reduction of Arctic sea ice and Northern Hemisphere Ice Sheets before the NHG in comparison with the present, a restriction between North Pacific and North Atlantic water and more southern North Atlantic drift through the Arctic into the west Pacific (Yamamoto and Kobayashi, 2016) could explain a warmer west than east subarctic Pacific during the Pliocene. However, März *et al.* (2013) and Swann *et al.* (2016) suggest that an explanation to a colder northeast Pacific could be a higher leak of Southern Ocean intermediate waters to the surface waters of the subarctic north Pacific and a Bering Sea that would help in the formation of sea ice.

This is consistent with a strong AL affecting the GOA SST. This theory considers the similarities between the climate of Siberia and the Pacific during the Plio-Pleistocene explained above due to an enhanced thermohaline circulation. This theory is further explored in Chapter 6 with the study of marine productivity export changes.

5.4.5 Comparison across the Pacific during the Plio-Pleistocene

SST trends across the North Pacific during the 4 to 1.7 Ma interval do not follow the pattern of cooling from the MPWP as observed in the North Atlantic Ocean between 18 and 13 °C in ODP Site 982 (Lawrence *et al.*, 2009). Instead, the early Pleistocene was often warmer than the Pliocene across the subarctic Pacific (Figure 5.3). Across the PPT there is evidence in the tropical Pacific of a long term increase in the zonal SST gradient (Fedorov *et al.*, 2013). Changing zonal and/or meridional SST gradients are expected to change heat transport poleward. This could have been triggered by ENSO and a permanent and positive PDO state during the Pleistocene in comparison with the Pliocene. Increase of heat transport to the Northeast Pacific under strong ENSO conditions is consistent with model climate outputs that have been modelled for the Pliocene (Bonham *et al.*, 2009), but the lack of data from the Northeast Pacific limits the confirmation of these results.

Explanations for the NHG include the closure of the Indonesian Seaway between 3 and 4 Ma (Cane and Molnar, 2001), and the associated drier GOA due to a reduction in heat transport between the tropics and the high latitudes and the cooling of the SST in the GOA due to melting of northern ice sheets. However, the timing of the closure of the Indonesian Seaway is not well constrained. The gradual closure of the Bering Sea and changes in the Canadian Arctic Archipelago are associated with warmer North Atlantic SSTs during the MPWP (Otto-Bliesner *et al.*, 2016). The gradual closure of the Bering Sea and changes in the Canadian Arctic Archipelago are also associated with enhanced (De Schepper *et al.*, 2015; Otto-Bliesner *et al.*, 2016) and northwards shifted (Dowsett *et al.*, 1994; Dowsett *et al.*, 2009) AMOC and could be responsible for the restriction of fresh, stratified and cooler waters in the Pacific during M2 observed in Figure 5.3.

Across the PPT there are larger changes in SSTs at high latitudes. During the NHG, these ~10 °C SST variations are due to the shoaling of the thermocline, ocean stratification and ocean’s heat capacity (Haug *et al.*, 2005; La Riviere *et al.*, 2012). This is due to the higher climatic variability that higher latitudes experience from

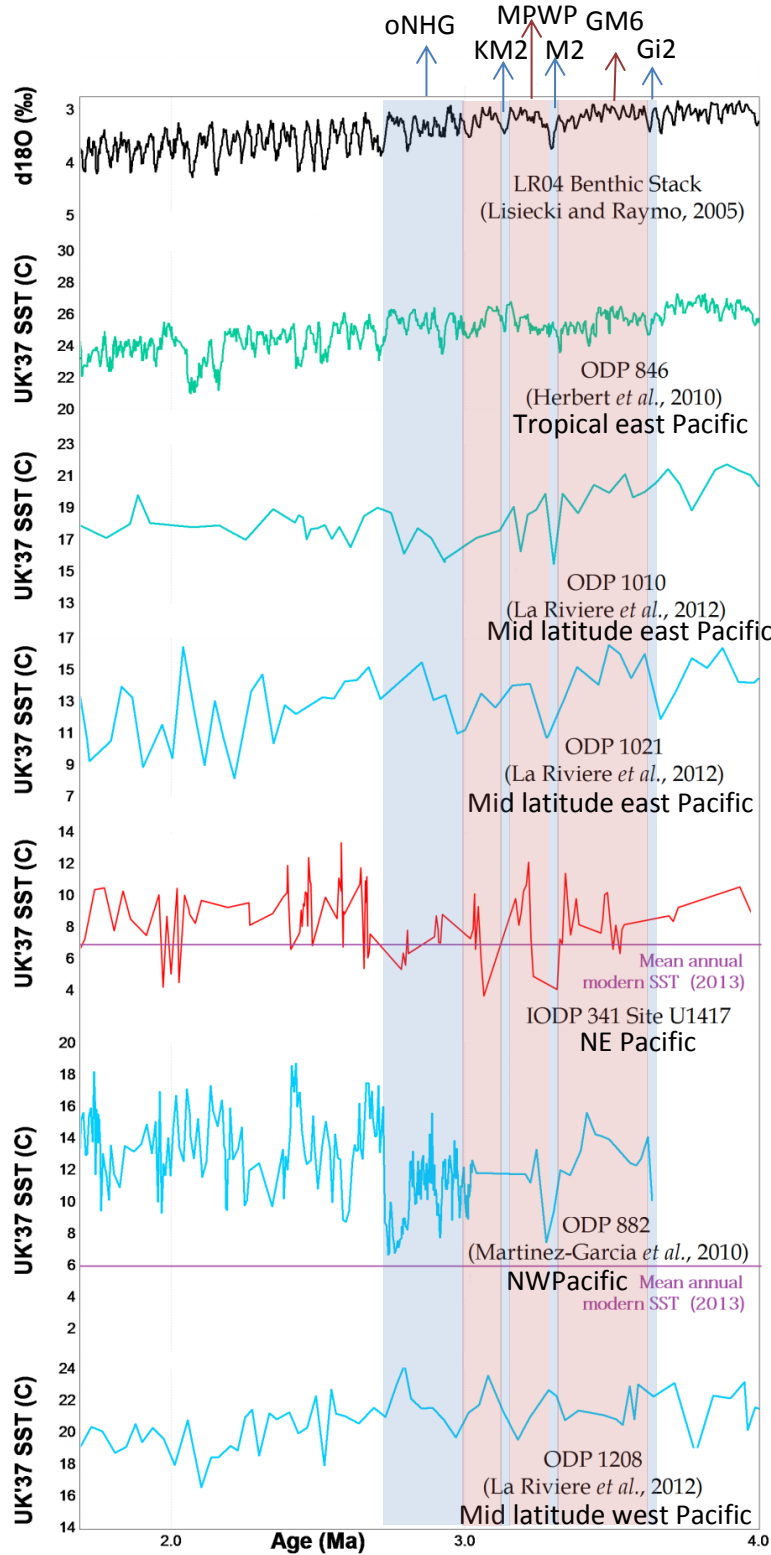


Figure 5.3: Pliocene-Pleistocene SST across the North Pacific. SST (C) from UK_{37}' comparison between IODP 341 Exp. Site U1417 (pink horizontal line indicates the Modern Annual SST average in GOA), ODP Site 846 (Herbert et al., 2010), ODP Site 1208, Site 1010 and Site 1021 (LaRiviere et al., 2012), ODP Site 882 (Martínez-García et al., 2010). LR04 Benthic Stack (Lisiecki and Raymo, 2005) on top.

seasonal solar radiation and ice sheet influence into the ocean. In the modern Pacific Ocean, the El Niño Southern Oscillation (ENSO) phenomenon influences SST of the tropics that in turns influences SST in the northern high latitudes. Warmer conditions in the GOA have been attributed to a more positive PDO and ENSO during the Holocene (Barron and Anderson, 2010). These changes have altered the climatic system in the GOA by shifting the AL eastward and intensifying it, as well as increasing winter precipitation on land (Barron and Anderson, 2010). In the rest of the Pacific, the Holocene changes have been marked by a shift southward of the North Pacific High, increased SST variability in mid-latitudes ($\sim 30^\circ\text{N}$) and the increase in SST during autumn to winter around 40°N (Barron and Anderson, 2010).

5.5 Conclusions

The onset and intensification of glaciation in the St. Elias range of the GOA occurred in two steps. Firstly, at 3 Ma, a decrease in terrestrial/aquatic organic matter is suggestive of increased land ice coverage, and occurs with an increase in $\%C_{37:4}$ that we interpret as an increase in freshwater input into the ocean, likely from glacial meltwater. Secondly, at 2.8 Ma there is the development of tidewater glaciers in the Gulf of Alaska. From 2.8-2.4 Ma, we hypothesise that the intensification of the glaciation in GOA occurred due to high efficiency in the ice-ocean-climate coupling where the warm sea surface temperatures increased the precipitation as snow over land, which in turn led to increased high freshwater delivery from glacier meltwater. Higher snowfall led to a growing Cordilleran Ice Sheet, and bedrock erosion allowed the delivery of IRD into the ocean (and an overall increase in sedimentation rates) during the Pleistocene.

The SST evolution from the Pliocene to the Pleistocene in the GOA is very different from the North Atlantic, with a colder late Pliocene than early Pleistocene. The

unusual SST pattern in the GOA could be explained by a regional high latitude ocean circulation in the Pacific delivering more heat to the GOA during the Pleistocene than during the Pliocene, although the drivers of such connections remains unclear. Finally, it remains possible that tectonic uplift could also help explain the development of the Cordilleran Ice Sheet during warm SST in the GOA after the NHG, but this explanation requires testing through improved constraints on the timing and location of uplift in the region.

Chapter 6: Land-ocean interactions during the Plio-Pleistocene Cordilleran Ice Sheet growth.

6.1 Introduction

Marine productivity is controlled by a complex range of processes involving the interaction between ocean and atmospheric circulation and the flux of terrestrially derived nutrients. In the modern Gulf of Alaska there are two different marine productivity regimes: one offshore, in the centre of the gyre and another one along the coast. This chapter will focus on the productivity changes offshore of the GOA. Offshore, the GOA is a high nutrient low chlorophyll region (Hinckley *et al.*, 2009). This is caused by micronutrient limitation and leads to nitrate rich deep waters (Harwell *et al.*, 2010, Martin *et al.*, 1991; Rae *et al.*, 2014; Stabeno *et al.*, 2004). Despite the apparent micronutrient limitation (Martin *et al.*, 1988), the GOA is one of the richest ecosystems of the planet (Ladd *et al.*, 2005). In the central GOA, wind-induced upwelling occurs during autumn to spring (Stabeno *et al.*, 2004) and during summer. Upwelling conditions occasionally develop due to intensification of the westerly winds, which helps to mix the nutrients stored in the deep ocean up to the surface, increasing marine productivity (Powell and Molnia, 1989; Harwell *et al.*, 2010). Outside of the higher productivity seasons (spring-autumn), the lower productivity may reflect the weaker wind strength in the Gulf of Alaska, associated with a weaker AL (Chapter 2).

In addition to the role of wind outlined above, rivers and/or glaciers can also impact the ocean circulation by altering stratification and can, therefore, impact marine productivity (Addison *et al.*, 2012). Wind, rivers and glacial melt can also bring nutrients from land to the ocean, such as iron, a micronutrient that limits productivity in the modern GOA (Martin *et al.*, 1991). Generally, wind transport is maximum during winter and glaciers are faster when more lubricated (more meltwater production and ocean nutrient input), which occurs during summer.

Dust input to the GOA from the coastal rivers is maximum during autumn lower river level and river sediment exposure (Crusius *et al.*, 2011).

Over decadal time-scales, a positive PDO (see Chapter 2) and the presence of a low-pressure system over the GOA is associated with stronger winds and precipitation, positive SST anomaly in the GOA and Prince William Sound and increase downwelling in coastal GOA and upwelling at the centre of the GOA (Harwell *et al.*, 2010). This is translated into an increase in primary and secondary marine productivity in the central GOA and decrease in coastal GOA (Harwell *et al.*, 2010). Reversed conditions occur during negative PDO (Harwell *et al.*, 2010).

On glacial-interglacial timescales during the last 500 kyr, marine productivity changes are globally very distinctive. Increases in marine productivity during interglacials have been observed in the subarctic Pacific (Jaccard *et al.*, 2005), which has also been observed during warm episodes after the NHG (Jakob *et al.*, 2016) and during the last deglaciation (i.e. Lam *et al.*, 2013; Galbraith *et al.*, 2007). Marine productivity during interglacials is high, yet it is during glacials that it is thought there would be more deep ocean storage of carbon in the North Pacific (Galbraith *et al.*, 2007).

Around 14.5 ka, a rapid warming and freshening of the sea surface of the northwest Pacific was attributed to an increase of meltwater from the Cordilleran Ice Sheet, which is directly followed by a deglacial productivity peak (Lam *et al.*, 2013). At this site, the stratification of the upper ocean driven by enhanced meltwater inputs was not an impediment to increased productivity, since increased iron and nitrate supply from the continent provided nutrient inputs (Lam *et al.*, 2013, Davies *et al.*, 2010). Iron sources have been proposed to be a crucial fertilizer of central GOA marine productivity (Martin *et al.*, 1991, Davies *et al.*, 2010). Sources of iron to the GOA are Asian dust, volcanic ash and submarine lateral transport from the continental margin (Jackson and Hart, 2006; Gutjahr *et al.*, 2008, Yokoo *et al.*, 2004, VanLaningham *et al.*, 2009). In the northwest Pacific Ocean, despite iron being the main productivity control at present (Martin *et al.*, 1991), over glacial and deglacial periods iron is considered to have a secondary role in controlling marine productivity, because peaks of iron are not coexistent

with peaks in productivity (Lam *et al.*, 2013). Instead, the availability of macronutrients and light have been suggested to be more important than iron to trigger marine productivity in the past. For example, in the subarctic northwest Pacific, meltwater input and upper ocean stratification has been suggested to be critical for maintaining sunlight penetration of the surface ocean and aiding productivity (Lam *et al.*, 2013). In coastal GOA, iron availability has been attributed to dust transport from exposed glacial sediments and river mouths (such as the Copper River) in coastal Alaska during autumn (Crusius *et al.*, 2011), sea level rise and flooding (Davies *et al.*, 2010) and sediment storage at the shelf and slope (Praetorius *et al.*, 2015) during deglaciation. The proximity of the GOA to the Cordilleran Ice Sheet allows direct examination of how the evolution of a large ice mass affects the supply of nutrients from fluvial and/or glacial sources. These nutrients are sourced from similar bedrock lithology erosion as during the LIG or if enhanced hydrological regime would increase nutrient availability in the ocean during the Pliocene.

Glacial periods during the Late Pliocene (2.7 Ma) were accompanied by the strengthening of the North American dust sources into the Atlantic (Naafs *et al.*, 2012). In the Southern Ocean, which is a HNLC region, increase in dust input to the ocean has been proposed as the cause of an increase in marine productivity export (Lawrence *et al.*, 2013). In other subarctic or subpolar waters (the subarctic Pacific (Haug *et al.*, 2005), Bering Sea (März *et al.*, 2013), Southern Ocean (Sigman *et al.*, 2004) and North Atlantic (Lawrence *et al.*, 2013; Lawrence *et al.*, 2009) marine productivity is higher before the NHG. However, in some sites from the North Atlantic (Site 607; Lawrence *et al.*, 2013), South Atlantic (Cortese *et al.*, 2004; Martínez-García *et al.*, 2010) and the subtropical, equatorial Pacific (Liu *et al.*, 2008; Lawrence *et al.*, 2006; Lawrence *et al.*, 2013) the alkenone MAR export is higher after the NHG. Marine productivity could be important as a mechanism for drawing down atmospheric CO₂ and storing it in the deep ocean. It is, therefore, important to consider how marine productivity has changed across the NHG where there was an abrupt decrease in atmospheric CO₂ (Seki *et al.*, 2010). Polar stratification and its impact in ocean-atmosphere CO₂ limitation could impact climate cooling globally (Haug *et al.*, 2005). It remains unclear how marine

productivity in the Northeast Pacific responded to the transition from the warm Pliocene to the onset and intensification of northern hemisphere glaciation (NHG).

Based on the previous research, one hypothesis is that the marine productivity in the GOA was higher before the NHG, and the ocean stratification that followed the NHG (Chapter 5) could have caused marine productivity to contribute to atmospheric CO₂ drawdown and global cooling. Here this hypothesis is tested through a multi-proxy approach, focussing on evidence for marine productivity and inputs of terrestrial OM as proxies for terrestrial inputs of dust/river/glacial sediment which might also provide nutrients. Terrestrial and marine organic matter sources have been assessed using the distributions of leaf-wax *n*-alkanes and ratios of TOC/TON. Marine productivity and nutrient utilization has been assessed using bulk $\delta^{13}\text{C}$ and $\delta^{15}\text{N}$, alongside biomarkers for diatoms (brassicasterol), dinoflagellates (dinosterol) and coccolithophores (alkenones), and diatom counts. To understand the climatic context of the evolution of these records, the data are compared with the SST history and IRD reconstructed in Chapter 5.

6.2 Research Site

This chapter investigates Site U1417 during the same interval of time (4.0-1.7 Ma) as in Chapter 5. This includes the increase in sedimentation rates close to the Pliocene-Pleistocene boundary at 2.56 Ma, and a transition in the core lithology at 2.6 Ma (Gulick *et al.*, 2015). As shown in Chapter 5 there is a warming of SSTs into the early Pleistocene.

Site U1417 is currently located under the Aleutian Low (AL), in a High Nutrient Low Chlorophyll (HNLC) region of the Subarctic Pacific. Strong climate-ocean-productivity linkages are characteristic of this area: cooler SSTs are associated with the presence of the AL pressure system in the centre of the Gulf, which is associated with increased precipitation, an increase in ocean mixing and upwelling in the Alaskan Gyre between November and March, which enhances marine productivity (Addison *et al.*, 2012; Davies *et al.*, 2010). In spring and summer, the opposite effect occurs due to a weakening of the AL. However, the supply of iron from glacier meltwater in coastal GOA mixes with the high nitrate concentration of

the surface water resulting in phytoplankton blooms (Addison *et al.*, 2012; Meheust *et al.*, 2013). Currently, the eastern Pacific is poorer in silicic acid than the western North Pacific (Maier *et al.*, 2015). The spring phytoplankton bloom is dominated by diatom species and late summer-fall phytonplankton bloom is dominated by coccolithophore species, although in central North Pacific this seasonality could be extended over a longer period (Meheust *et al.*, 2013).

6.3 Material and Methods

The same samples which were analysed for SST reconstructions (Chapter 5) are presented here. The full details of the analytical methodology are provided in Chapter 3. Organic matter concentrations in the sediment are always presented as mass accumulation rates (MAR), to take into account the influence of changing sedimentation rate and sediment density on original concentrations (Chapter 4). The biomarkers have also been normalised to TOC content, to take into account the possible influence of overall organic matter degradation (Chapter 4). Original biomarker concentrations are shown in Chapter 4.

6.4 Results

6.4.1 *N*-alkane distributions and the TAR index

The MAR of long chain or terrigenous *n*-alkanes ranges from 0 to 106.2 $\mu\text{g cm}^{-2} \text{kyr}^{-1}$, with an average value of 12.5 $\mu\text{g cm}^{-2} \text{kyr}^{-1}$ (Figure 6.1b). Short chain or aquatic *n*-alkanes range from 0 to 31.6 $\mu\text{g cm}^{-2} \text{kyr}^{-1}$ with an average value of 4.5 $\mu\text{g cm}^{-2} \text{kyr}^{-1}$ (Figure 6.1b). Both long chain and short chain *n*-alkanes show a long term increase in MAR, during the Pliocene-early Pleistocene. Long chain and short chain MAR are low during the Pliocene with average values of 7 and 1.32 $\mu\text{g cm}^{-2} \text{kyr}^{-1}$, respectively. During the Plio-Pleistocene transition, long chain *n*-alkanes remain low and short chain *n*-alkanes increase compared to the late Pliocene concentrations. During the early Pleistocene the long chain and short chain MAR values decrease slightly, but still record higher values than during the Pliocene. The long chain *n*-alkanes average concentrations during the early Pleistocene are 17.7 $\mu\text{g cm}^{-2} \text{kyr}^{-1}$. The short chain *n*-alkanes have an average value of 7.5 $\mu\text{g cm}^{-2} \text{kyr}^{-1}$ during the early Pleistocene.

TAR is a ratio of long chain (terrestrial sourced i.e. higher plants) and short chain (aquatic sourced i.e. phytoplankton) *n*-alkanes (See Chapter 2) (Cranwell, 1973). Our TAR index ranges from 0 to 17 with an average value of 4 (Figure 6.1c). The highest TAR values of our record are registered between 4 to 3.06 Ma, with an average value of 6.5, showing a dominant terrestrial source of the organic matter in the Pliocene. The TAR concentrations decrease during 3.05 to 1.66 Ma to average values of 2.4, showing a reduction in the importance of terrestrial *n*-alkanes compared to aquatic sources in comparison with the Pliocene. During the 3 to 1.66 Ma, terrestrial inputs still dominate in our record. After 3.05 Ma there are four short punctual increases in TAR, at 2.68, 2.66, 2.27 and 2.03 Ma.

6.4.2 TOC, TON, $\delta^{13}\text{C}$ and $\delta^{15}\text{N}$

TOC ranges from 0 to 1.1%, with an average value of 0.3% during the Pliocene-early Pleistocene (Figure 6.1d). Total organic nitrogen (TON) ranges from 0.01 to 0.08%, with an average value of 0.035% during the Pliocene-early Pleistocene (Figure 6.1d). Bulk organic carbon isotope ($\delta^{13}\text{C}$) values range from -26.0 to -21.9‰, with an average value of -24.5‰ during the Pliocene and early Pleistocene (Figure 6.1f). Bulk organic nitrogen isotope ($\delta^{15}\text{N}$) values range from -0.4 to 4.6‰, with an average value of 2.8‰ during the Pliocene and early Pleistocene (Figure 6.1f).

TOC MAR ranges from 729.8 to 10484.9 $\mu\text{g cm}^{-2} \text{kyr}^{-1}$, with an average value of 4601.3 $\mu\text{g cm}^{-2} \text{kyr}^{-1}$ (Figure 6.1e). TON MAR ranges from 91.7 to 1002.9 $\mu\text{g cm}^{-2} \text{kyr}^{-1}$, with an average value of 486.1 $\mu\text{g cm}^{-2} \text{kyr}^{-1}$ (Figure 6.1e).

All TOC, TON, $\delta^{13}\text{C}$ and $\delta^{15}\text{N}$ show very similar trends during the Pliocene and early Pleistocene, with lower average MAR (TOC=2399.5 $\mu\text{g cm}^{-2} \text{kyr}^{-1}$, TON=302.4 $\mu\text{g cm}^{-2} \text{kyr}^{-1}$) during the Pliocene and higher average MAR values during the early Pleistocene values (TOC=6319.8 $\mu\text{g cm}^{-2} \text{kyr}^{-1}$, TON=629.5 $\mu\text{g cm}^{-2} \text{kyr}^{-1}$), with the peak values of each record at the Plio-Pleistocene boundary (Figure 6.1d, e and f).

6.4.3 β -sitosterol

All β -sitosterol abundance calculations (in $\mu\text{g g}^{-1}$, $\mu\text{g g}^{-1}\text{TOC}^{-1}$ and $\mu\text{g cm}^{-2} \text{kyr}^{-1}$) show very similar trends (Figure 6.1a and Figure 6.2a). For details on the $\mu\text{g g}^{-1}$ and $\mu\text{g g}^{-1}\text{TOC}^{-1}$ data sets please see Chapter 4.

β -sitosterol MAR ranges from 0 to 16.7 $\mu\text{g cm}^{-2}\text{kyr}^{-1}$ (black curves in Figure 6.1a and Figure 6.2a), with an average value of 1.9 $\mu\text{g cm}^{-2}\text{kyr}^{-1}$ through the Pliocene and early Pleistocene. β -sitosterol average values are 2.6 $\mu\text{g cm}^{-2}\text{kyr}^{-1}$ during the Pliocene and 1.3 $\mu\text{g cm}^{-2}\text{kyr}^{-1}$ during the early Pleistocene. β -sitosterol MAR long term trend is not clear. β -sitosterol MAR are very low between 4 to 3.3 Ma with an average value of 0.3 $\mu\text{g cm}^{-2}\text{kyr}^{-1}$, values increase during 3.3 to 3.2 Ma with an average value of 6.1 $\mu\text{g cm}^{-2}\text{kyr}^{-1}$, values decrease from 3.2 to 2.1 Ma with an average value of 1.2 $\mu\text{g cm}^{-2}\text{kyr}^{-1}$ and increase again from 2.1 to 1.7 Ma with an average value of 5.4 $\mu\text{g cm}^{-2}\text{kyr}^{-1}$.

6.4.4 Dinosterol

All dinosterol abundance calculations (in $\mu\text{g g}^{-1}$, $\mu\text{g g}^{-1}\text{TOC}^{-1}$ and $\mu\text{g cm}^{-2}\text{kyr}^{-1}$), as with β -sitosterol abundances, show very similar trends (Figure 6.2b). For details on the $\mu\text{g g}^{-1}$ and $\mu\text{g g}^{-1}\text{TOC}^{-1}$ data sets please see Chapter 4.

Dinosterol MAR ranges from 0 to 7 $\mu\text{g cm}^{-2}\text{kyr}^{-1}$, with an average value of 0.6 $\mu\text{g cm}^{-2}\text{kyr}^{-1}$. Pliocene dinosterol MAR have an average value of 1 $\mu\text{g cm}^{-2}\text{kyr}^{-1}$ and early Pleistocene dinosterol MAR have an average value of 0.3 $\mu\text{g cm}^{-2}\text{kyr}^{-1}$ through the Pliocene and early Pleistocene. Dinosterol long term trend is not clear. Dinosterol MAR increases from 3.2 to 3 Ma with an average of 1.66 $\mu\text{g cm}^{-2}\text{kyr}^{-1}$ and from 2.4 to 1.6 Ma with an average of 2.2 $\mu\text{g cm}^{-2}\text{kyr}^{-1}$. From 4.0 to 3.2 Ma, dinosterol MAR remains very low with an average of 0.11 $\mu\text{g cm}^{-2}\text{kyr}^{-1}$ and from 3.0 to 2.4 Ma, with an average of 0.26 $\mu\text{g cm}^{-2}\text{kyr}^{-1}$.

6.4.5 Brassicasterol

All brassicasterol abundance calculations (in $\mu\text{g g}^{-1}$, $\mu\text{g g}^{-1}\text{TOC}^{-1}$ and $\mu\text{g cm}^{-2}\text{kyr}^{-1}$) show very similar trends (Figure 6.2c). For details on the $\mu\text{g g}^{-1}$ and $\mu\text{g g}^{-1}\text{TOC}^{-1}$ data sets please see Chapter 4.

Brassicasterol MAR ranges from 0 to 12 $\mu\text{g cm}^{-2}\text{kyr}^{-1}$, with an average value of 0.9 $\mu\text{g cm}^{-2}\text{kyr}^{-1}$ through the Pliocene and early Pleistocene. Brassicasterol MAR during the Pliocene has a 1.1 $\mu\text{g cm}^{-2}\text{kyr}^{-1}$ and 0.3 $\mu\text{g cm}^{-2}\text{kyr}^{-1}$ during the early Pleistocene. Brassicasterol MAR long term trend is not clear. Brassicasterol MAR increases from 3.3 to 3.0 Ma with an average of 1.3 $\mu\text{g cm}^{-2}\text{kyr}^{-1}$, and from 2 to 1.6 Ma with an average of 3.5 $\mu\text{g cm}^{-2}\text{kyr}^{-1}$. From 4 to 3.3 brassicasterol MAR remains

very low with an average of $0.04 \mu\text{g cm}^{-2} \text{kyr}^{-1}$ and from 3 to 2 Ma, with an average of $0.24 \mu\text{g cm}^{-2} \text{kyr}^{-1}$.

6.4.6 Alkenones

Both alkenone abundance calculations show similar trends (Figure 6.2d). We will use the $\mu\text{g g}^{-1} \text{TOC}^{-1}$ units to account for the degradation of the biomarkers, as this is an important process to account for when considering marine productivity (see Chapter 2).

Alkenone abundance show higher values than the sterol biomarker abundances. Alkenone concentration are higher before 2.5 Ma (average value of $0.5 \mu\text{g g}^{-1} \text{TOC}^{-1}$) than during 2.5 to 1.7 Ma (average value of $0.3 \mu\text{g g}^{-1} \text{TOC}^{-1}$). This record has a lower resolution than the SST as the GC-CIMS method for sea surface temperature reconstructions could also quantify weak alkenone samples whereas the GC-FID method for alkenone abundance quantification could not quantify weak alkenone samples.

6.4.7 Diatoms

Total diatom abundance is highly variable ranging from 0 to 17 million valves g^{-1} (Figure 6.2E), with an average of 971,000 valves g^{-1} . Diatom abundance reaches maximum levels from 4.0 to 3.55 Ma, with an average of 7.6 million valves g^{-1} . At 3.55 Ma, diatom abundances show an abrupt reduction, with an approximate average concentration of 552,000 valves g^{-1} during 3.55 to 2.8 Ma. After 2.8 Ma, diatoms concentrations are absent from the sediments except for two intervals, at 2.46 and 1.96 Ma, where diatom counts reach values of 15,600 and 8,000 valves sample^{-1} , respectively (Figure 6.2e).

Total diatom MAR ranges from 0 to 83,662,002 valves $\text{cm}^{-2} \text{kyr}^{-1}$, with an average value of 5,215,437 valves $\text{cm}^{-2} \text{kyr}^{-1}$ through the Pliocene and early Pleistocene. Total diatom MAR are highest from 4 to 3.55 Ma with an average value of 32,968,233 valves $\text{cm}^{-2} \text{kyr}^{-1}$ and decrease from 3.55 to 2.8 Ma with an average value of 4,189,762 valves $\text{cm}^{-2} \text{kyr}^{-1}$. After 2.8 Ma, total diatom counts disappear with the exception at 2.4 Ma with a value of 317,666 valves $\text{cm}^{-2} \text{kyr}^{-1}$.

6.5 Discussion

6.5.1 Environmental proxy assessment

N-alkanes and bulk organic carbon and nitrogen are often used to estimate aquatic and marine sources of organic matter (OM) (Meheust *et al.*, 2013, Walinsky *et al.*, 2009). At Site U1417, TAR and TOC/TON ratio have opposite trends through the Pliocene and early Pleistocene; TAR long term trend shows an increase/decrease in marine/terrigenous *n*-alkanes whereas the TOC/TON ratio shows a trend towards increasing terrigenous OM input (Figs. 6.1c). TAR is a ratio of long chain (terrestrial sourced i.e. higher plants) and short chain (aquatic sourced i.e. phytoplankton) *n*-alkanes (See Chapter 2) (Cranwell, 1973).

The "aquatic" C₁₅, C₁₇ and C₁₉ alkanes are dominantly synthesised by algae (Bourbonniere and Meyers, 1996) and the C₁₇ to C₂₀ alkanes are also dominantly synthesized by cyanobacteria (Han and Calvin, 1969), both part of the phytoplankton, which can be from marine or terrestrial freshwater environments. In contrast, terrestrial C₂₇, C₂₉ and C₃₁ *n*-alkanes are dominantly synthesized by vascular plants (Rieley *et al.*, 1991). In this manner, it is possible to use the TAR to assess whether the source of OM was from terrestrial plants or phytoplankton productivity.

The TOC/TON ratio reflects the relatively higher organic C content in terrestrial OM (higher plants) and the relatively higher N content in the marine realm (algae) based on their elementary biological structure (Walisky *et al.*, 2009). However, the TOC and TON also contains a mix of material from different sources. Despite the overall interpretation of increase/decrease in the TAR and TOC/TON ratios as higher/lower terrigenous organic matter, the different provenance of the *n*-alkane and the bulk organic carbon and nitrogen might be the cause of the long term disagreement between the two records. However, perhaps there is "marine signal" of TOC and TON that is eroded into the sea from land i.e. carbon (See Chapter 5) or freshwater phytoplankton (fluvial/lacustrine) together with the terrigenous material input to the sea.

Similarly, the TAR could be imprinted with terrestrial (freshwater) phytoplankton and bacterial OM. To distinguish the terrestrial source component of marine sediments we compare the terrigenous OM signal from the geological record of the

coastal Gulf of Alaska. The *n*-alkane signature of rock formations from the Yakutat terrain in Alaska is typical petroleum chain lengths shorter than C₂₀ (Childress, 2016). The Kulthieth and Poul Creek Formations contain higher chain lengths of C₂₁ to C₂₉ and up to C₃₂, respectively (Childress, 2016). The overall low TAR values of terrestrial rock formations in Alaska are likely due to their maturity, being the greatest TAR values in the Kulthieth Formation rocks (TAR <2). Our *n*-alkane data cover a wider range of values than the ones found on coastal south Alaska geology, which suggest additional contributions from an aquatic productivity signal to the geological *n*-alkane signal in the ocean as well as terrigenous OM input. However, both aquatic and terrigenous could still have a terrestrial source (i.e. rivers).

Bulk and isotopic C and N records are used here to reconstruct both terrigenous and marine OM input and past productivity. In previous investigations from the Gulf of Alaska, oceanic TOC, $\delta^{13}\text{C}$, $\delta^{15}\text{N}$ and N/C records show a similar range of values compared to our records at Site U1417 (Walinsky *et al.*, 2009; Addison *et al.*, 2012). $\delta^{15}\text{N}$ follows the same trend of other terrigenous and marine records outlined above, with a long term trend towards the enrichment of heavier nitrogen isotopes during the early Pleistocene. The increase towards heavier $\delta^{15}\text{N}$, despite similar $\delta^{13}\text{C}$, and increase TON and TOC and marine and terrigenous *n*-alkanes during the early Pleistocene in comparison with the late Pliocene suggest synchronous increase in terrigenous and marine source of OM during the early Pleistocene.

Past productivity interpretations draw on the preferential utilisation of the lighter isotopes during production, which is then transferred to the marine sediment organic matter record. However, N isotopes have multiple controls, and can be contaminated by clay composition or be influenced by oceanic currents i.e. the Kuroshio Current is characterized by a low $\delta^{15}\text{N}$ signal, which is associated with N₂ fixation (Ryabenko, 2013). Most of our $\delta^{13}\text{C}$ values are between -24 and -25 ‰ and the $\delta^{15}\text{N}$ values are concentrated between 4.5 and 1.5‰, though there are some spikes with higher and lower isotopic values. The higher and lower spikes in the $\delta^{13}\text{C}$ and $\delta^{15}\text{N}$ occur during the same events in both records. According to the study of Yu *et al.* (2010) from estuary and coastal sediments from south China, these values are indicative of a freshwater environment and increase to -21‰ in marine

environments. Based on measurements of particulate organic carbon (POC), Yu *et al.* (2010) identify values ranging from 24.5 to 25.5‰ corresponding to a brackish water environment (Yu *et al.*, 2010). A study from rock formations in the GOA revealed the $\delta^{13}\text{C}$ values from the Yakutat terrane range from -27 to -22 ‰ and $\delta^{15}\text{N}$ values from the Kulthieth Formation range from 1 to 3 ‰ and from Poul Creek and Yakataga formations values range from 3 to 5 ‰ (Childress, 2016). The $\delta^{13}\text{C}$ record from Alaska geology has similar range of concentrations as Site U1417 $\delta^{13}\text{C}$ record. However, the $\delta^{15}\text{N}$ values from Alaskan rocks have lower range than our records from marine sediments which suggests an additional provenance of the lower $\delta^{15}\text{N}$ values at the GOA during these low $\delta^{15}\text{N}$ intervals.

$\delta^{15}\text{N}$ often shows lighter isotopes from 2.8 to 2.4 Ma, with $\delta^{15}\text{N}$ ranges from 0 to 1‰. The low $\delta^{15}\text{N}$ values are rapidly followed by heavier $\delta^{15}\text{N}$ of up to 2.5 ‰ (biomass preferentially uptakes the lighter isotope). The high $\delta^{15}\text{N}$ variability is also evident in the $\delta^{13}\text{C}$ concentrations (Figure 6.4). Lighter $\delta^{13}\text{C}$ concentrations have been previously interpreted as biomass consumption (Brunelle *et al.*, 2007). During the 3.2 to 2.8 Ma, the atmospheric CO_2 levels decreased from higher than post-industrial values between 375 and 450 ppm before 3.2 Ma (Pagani *et al.*, 2010; Seki *et al.*, 2010) to pre-industrial 250-300 at about 2.4 Ma (Seki *et al.*, 2010). Decreasing atmospheric CO_2 levels could have driven a lighter $\delta^{13}\text{C}$ and $\delta^{15}\text{N}$ signature (Raymo *et al.*, 1996) before 3.2 Ma and heavier isotopic signature after 3.2 Ma.

Literature often presents dinosterol and brassicasterol as marine productivity indicators synthesised from dinoflagellate and diatom species, respectively (D'anjou *et al.*, 2013; Schulte *et al.*, 1999). Brassicasterol, if interpreted as a diatom productivity export proxy, would be expected to correlate with the diatom abundance record (Figures 6.2 C and E). The fact that this is not the case suggests that something might be biasing the biomarker and/or diatom record, such as differential silica and/or OM preservation or a different brassicasterol synthesiser other than diatoms (Volkman, 2006). Due to the almost anti-phase correlation between diatom abundance and brassicasterol abundance during the Pliocene-Pleistocene (Figure 6.4e) and the similarity between dinosterol and brassicasterol trends (Figure 6.2), the dinosterol and brassicasterol could represent a common

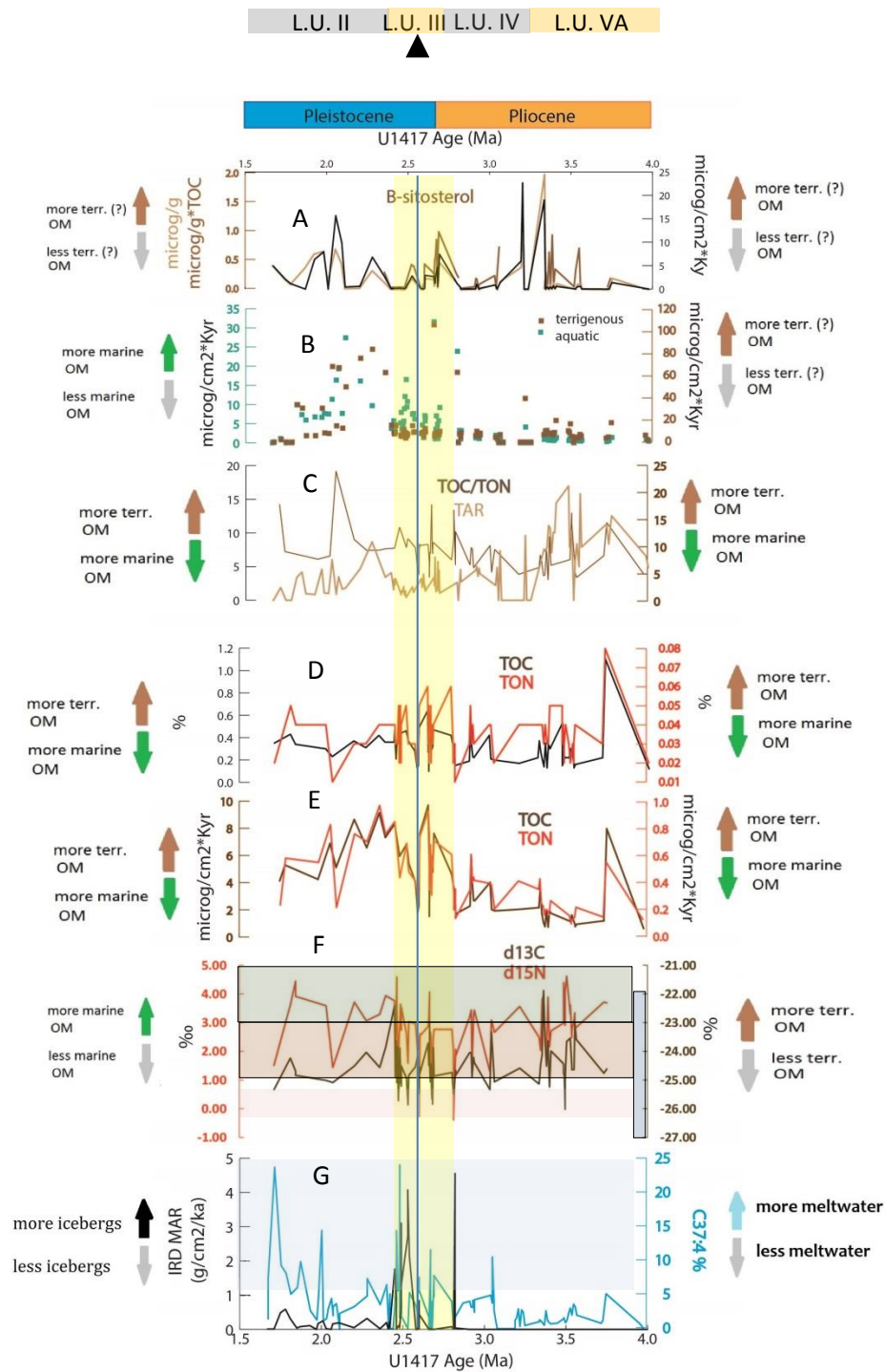


Figure 6.1: Terrigenous and marine organic matter proxies. A) β -sitosterol in $\mu\text{g/g}$ (light brown), $\mu\text{g g}^{-1}$ TOC $^{-1}$ (dark brown) and in $\mu\text{g cm}^{-2} \text{kyr}^{-1}$; B) terrigenous (brown) and aquatic (blue) n-alkane MAR ($\mu\text{g cm}^{-2} \text{kyr}^{-1}$); C) terrigenous and aquatic n-alkane ratio (TAR) (light brown) and total organic carbon (TOC) and total organic nitrogen (TON) ratio (TOC/TON) (dark brown), D) total organic carbon (TOC) (grey) and total organic nitrogen (TON) (red) in %; E) total organic carbon (TOC) (grey) and total organic nitrogen (TON) (red) in $\mu\text{g cm}^{-2} \text{kyr}^{-1}$; F) $\delta^{13}\text{C}$ (grey) and $\delta^{15}\text{N}$ (red) in ‰. Coloured boxes are values found in the Yakutat terrane range (blue box in $\delta^{13}\text{C}$ y axis), Kulthieth Formation (orange box $\delta^{15}\text{N}$

axis) and the Poul Creek and Yakataga formations (green box in $\delta^{15}\text{N}$ axis) (Childress, 2016); G) IRD MAR ($\text{g cm}^{-2} \text{ kyr}^{-1}$) (black) and $\text{C}_{37:4}$ in % (blue) vs U1417 Age (Ma). Lithostratigraphic units II, III, IV and VA (grey for mud and orange for diamict, see chapter 3). Black triangle on top shows the age of the Gauss-Matuyama magnetic reversal in our core (2.58 Ma). Pliocene and Pleistocene boundary shown above graph. Lateral arrows highlight the increase/decrease of environmental factors. Vertical and horizontal shadows highlight features highlighted in the text.

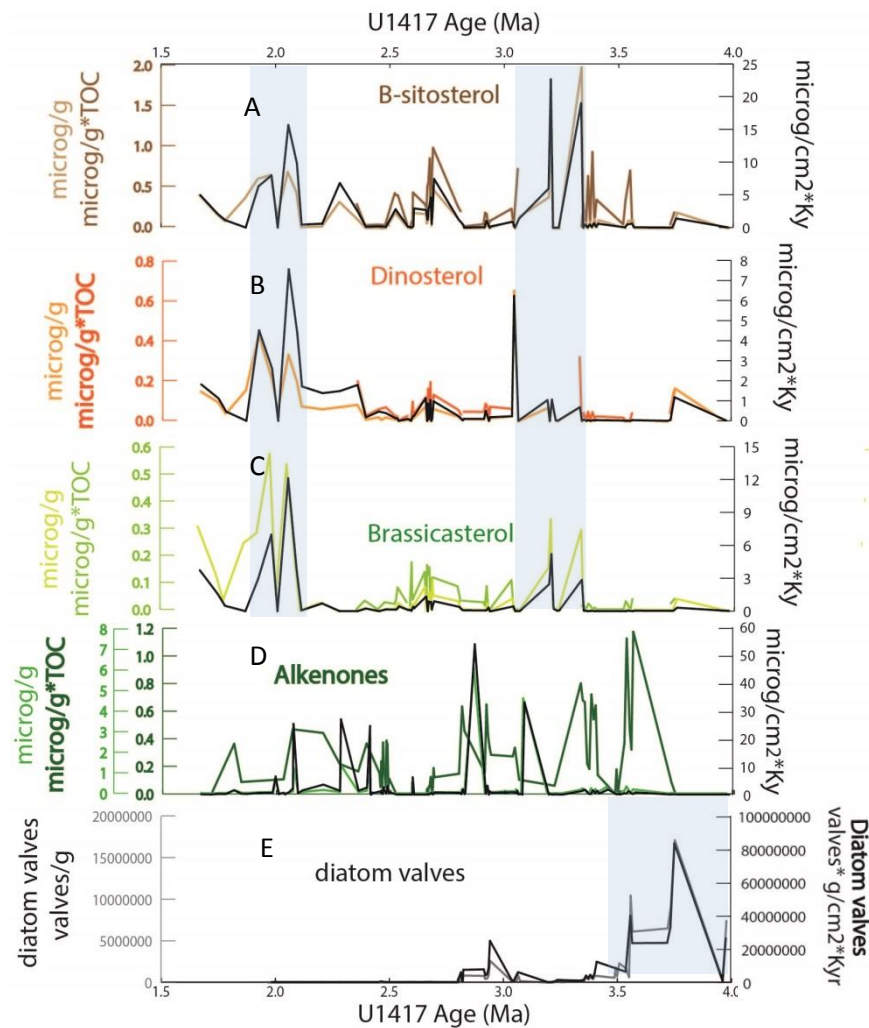


Figure 6.2: Sterol, alkenone and diatom concentrations. A) β -sitosterol in $\mu\text{g/g}$ (light brown), $\mu\text{g/g*TOC}$ (dark brown) and $\mu\text{g cm}^{-2} \text{ kyr}^{-1}$ (black); B) Dinosterol in $\mu\text{g/g}$ (light orange), $\mu\text{g/g*TOC}$ (dark orange) and $\mu\text{g cm}^{-2} \text{ kyr}^{-1}$ (black); C) Brassicasterol in $\mu\text{g/g}$ (light green), $\mu\text{g/g*TOC}$ (yellow) and $\mu\text{g cm}^{-2} \text{ kyr}^{-1}$ (black); D) alkenone abundances in $\mu\text{g/g}$ (light green), $\mu\text{g/g*TOC}$ (dark green) and $\mu\text{g cm}^{-2} \text{ kyr}^{-1}$ (black) E) diatom valves in valves g^{-1} (grey) and in valves $\text{cm}^{-2} \text{ kyr}^{-1}$ (black) vs U1417 Age (Ma). Colour shadows highlight intervals of data mentioned in the text.

synthesiser in the Gulf of Alaska, such as dinoflagellates (Goad and Withers, 1982). The difference between brassicasterol and alkenones MAR (Figure 6.2c and d) supports the assumption of a different synthesiser between the two biomarkers and the possibility of dinoflagellate and coccolithophore synthesis of these biomarkers, respectively. However, we cannot discard the differential OM degradability between alkenones and sterols; alkenones being more resistant to degradation than sterols. Sterol degradability could explain the similar patterns between all sterol records in our site.

Finally, the interpretation of the β -sitosterol record as a terrigenous OM proxy is assessed by comparing the trends with the other terrigenous records presented here (Figure 6.1). β -sitosterol MAR does not replicate the long term trends of other terrigenous proxies (terrigenous *n*-alkanes and TOC). Further evidence suggesting the β -sitosterol record is not an accurate proxy for terrigenous input in our site comes from the weak correlation between brassicasterol and β -sitosterol values (Figure 6.3b), the low r^2 value of 0.33 between the two sterols suggests a weak relationship. In comparison, a bi-plot of long and short chain *n*-alkanes values shows a much stronger linear relationship between terrigenous and marine *n*-alkanes with an $r^2=0.83$ (Figure 6.3a). The linear relationship between *n*-alkanes could be interpreted as a similar increase in both terrigenous and marine *n*-alkanes or similar *n*-alkane preservation, The relationship between increase in terrigenous and increase aquatic *n*-alkanes is lost during highest *n*-alkane concentrations. Highest terrigenous and aquatic *n*-alkane concentrations are recorded between 2.4 and 2.0 Ma and increase in alkenone MAR and sedimentation rates (Figure 4.3).

The relationship between brassicasterol and β -sitosterol (Figure 6.3b) do not follow a clear linear relationship as the terrigenous and marine *n*-alkanes above (Figure 6.3a). The increase in β -sitosterol concentrations does not seem connected to the concentration of brassicasterol however higher brassicasterol values are linked to higher values of β -sitosterol (Figure 6.3b). Despite both records seem to share a common degradability history (Figure 6.2a and c) they seem to have different environmental source with no clear relationship between them (Figure

6.3b). Sterol biomarker provenance interpretations proved to be difficult and these records will not be the focus of the discussion in this chapter.

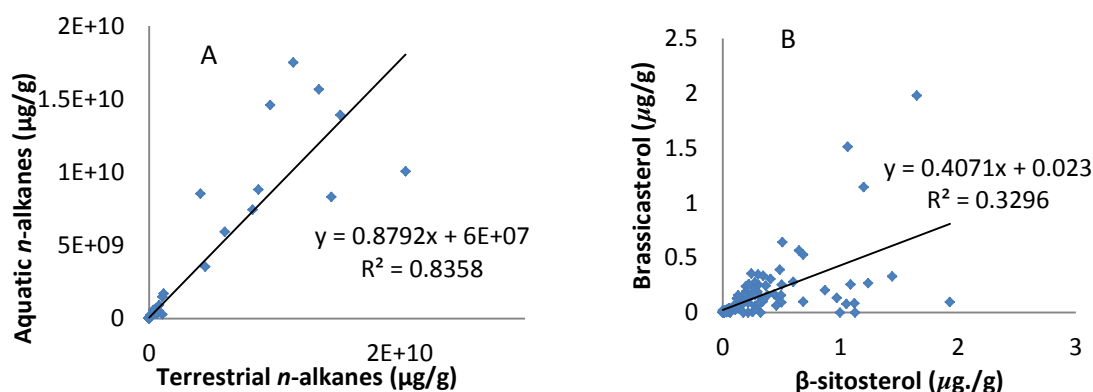


Figure 6.3: Relationship between terrigenous and marine proxies. A) aquatic vs terrigenous *n*-alkanes ($\mu\text{g g}^{-1}$), trendline, relationship equation and r^2 ; B) brassicasterol vs β -sitosterol ($\mu\text{g g}^{-1}$), linear trendline, relationship equation and r^2 .

6.5.2 Main trends during the Pliocene-Pleistocene climate evolution.

TOC MAR is approximately 10 times higher than TON MAR at Site U1417 (Figure 6.1e), yet both TOC and TON MAR records show synchronous patterns of change across the Pliocene and early Pleistocene. The small deviations between these two records explain the changes shown in the TOC/TON ratio. Terrigenous *n*-alkanes are about 35 times more abundant than marine *n*-alkanes (Figure 6.1). The long term increase in marine productivity and terrigenous organic matter revealed by the *n*-alkane records and TOC and TON during the Pliocene-Pleistocene is synchronous with an increase in sedimentation rates, which is also synchronous with an increase in extent of glaciation over Alaska. Figure 6.4 includes TOC, TON, terrigenous and marine *n*-alkane mass accumulation rates to discard the influence of sedimentation rates in our interpretations from these records. The Gulf of Alaska records the highest erosion rates in the world at modern, with annual erosion rates of 100 mm (Hallet *et al.*, 1996). Therefore, it is expected that sedimentation ranges could have a big impact in the ocean. Similarities arise after comparing the TOC, TON, terrigenous and marine *n*-alkanes with “purely terrigenous” proxies such as sedimentation rates, IRD and $C_{37:4}$ (see Chapter 5) (Figure 6.4). We suggest that the similarities between these proxies could be explained by increase in OM preservation due to rapid burial as sedimentation rates increase at Site U1417 during the Pliocene and Pleistocene.

Dinosterol and brassicasterol MAR have a similar variability from the Pliocene to the Pleistocene, with lowest values from 4 to 3.4 Ma and from 3 to 2.8 Ma and the highest values between 3.4 and 3 Ma and from 2.8 to 1.7 Ma. Diatom valve concentrations have the opposite long term variability compared to dinosterol and brassicasterol levels, with highest values around 4 to 3.4 Ma and lower values from 3 to 2.8 Ma, low values from 3.4 to 3 and the valves disappear from 2.8 to 1.7 Ma (Figure 6.4). Alkenone MAR can be used for coccolithophore export production (Prahl and Muehlhausen, 1989). The alkenone MAR record here is significantly different from marine sterol records with the lowest values from 4 to 3.2 Ma, 3.1 to 3.0 Ma and 2.8 to 2.5 Ma and higher MAR values from 3.2 to 3.1 Ma, from 3.0 to 2.8 and from 2.5 to 1.7 Ma (Figure 6.4). Alkenones are around 10 times more abundant in the GOA than brassicasterol and dinosterols and around 4 times more abundant than β -sitosterol records. β -sitosterol MAR variability through the Pliocene and Pleistocene is very similar to the dinosterol and brassicasterol MAR.

Organic matter is present throughout the entire Pliocene and early Pleistocene at Site U1417. However, surprisingly, the sterol records do not show lower values during the Pliocene and higher during the early Pleistocene as shown in the terrigenous and marine *n*-alkanes, bulk TOC and TON and the $\delta^{15}\text{N}$ records outlined above. Dinoflagellate, diatom and coccolithophore blooms occur in late summer, spring, and late summer-early fall in the GOA, respectively (Bringué *et al.*, 2013; Max *et al.*, 2012). With the sterol records we can confirm some productivity in the GOA during the Pliocene and early Pleistocene. Diatom valve preservation is higher during the earlier part of the record (4 to 2.8 Ma), the middle part of the record tends to be characterised by higher alkenone organic matter preservation (3.1 to 2 Ma) and then the sterols show increased abundance/preservation during the latter part of the record (2.1 to 1.9 Ma) (Figure 6.2). At all these times where diatom valves and sterols are present, the $\text{C}_{37:4}$ values are below 5 % (Figure 6.4). This suggests that a decrease in freshwater in the GOA helps silica and OM from sterols preservation through the water column increasing marine productivity export. Alkenones, however, do not show a preference for low $\text{C}_{37:4}$ values. This will be further explored in the following sections.

6.5.3 Changes in terrigenous and marine sourced organic input and productivity in relation to SST and the glacial evolution of the Cordilleran Ice Sheet during the Pliocene and Pleistocene.

The period from 4 to 3.5 Ma is characterised by a warm climate and vegetated landscape. Low sedimentation rates support the interpretation of a small or non-existent Cordilleran Ice Sheet. Freshwater is not present at the core site (low $C_{37:4}$, Figure 6.1g, Figure 6.4h) and so the ocean is likely to be well ventilated with a mixed water column. Relatively high terrestrial OM input from land in relation to marine could also mean a relatively high silica input from the siliceous geology (volcanic and igneous rocks) along the southeast coast of Alaska (USGS). Silica preservation is the highest in our record during the 4 to 3.5 Ma interval (high diatom abundance preserved in the record).

Differential Si and OM preservation at Site U1417 could be explained by silica preservation helped by a well-mixed water column whereas OM is susceptible to degradation in a well ventilated ocean. Low sedimentation rates lead to the sediment-water interface having longer exposure to the OM aggressive oxygenated environment in a well ventilated ocean. Lower TOC (Figure 6.4) also supports the interpretation that OM could have suffered degradation. Whitley *et al.* (2005) also suggested that increase in iron input from the land into the HNLC region of the Gulf of Alaska by ocean circulation would increase Si drawdown. Glacial erosion and terrestrial silica-rich runoff into the ocean could have helped the preservation of diatom valves, as would a rapid burial (Walinsky *et al.*, 2009).

The diatoms are present for most of the 4 to 3.5 Ma period, but the abundance of diatom valves decreased abruptly from 3.5 Ma for the rest of the Pliocene. Calculation of diatom MAR values (Figure 6.4g) suggests that the diatom signal cannot be explained by sediment dilution (Walinsky *et al.*, 2009). Similarly, the increase in sedimentation rates from 4.0 to 2.0 Ma would help in diatom preservation by rapid sediment burial, however, diatom valve concentration drops dramatically from 3.5 to 2.8 Ma to become almost absent. Instead, the abrupt reduction in diatom abundance is likely to be driven by a reduction in preservation. A reduction in preservation could be influenced by global chemistry changes in the deep ocean at 2.8 Ma during the North Hemisphere Glaciation

(Swann *et al.*, 2016; März *et al.*, 2013) at the same time as an increased heat supply to the high latitudes (Haug *et al.*, 2005) which could have helped the growth of the Cordilleran Ice Sheet (increased moisture supply - Chapter 5). Some of these global changes have been attributed to the establishment of the present day halocline in the Pacific, an associated increase of intermediate/deep nutrient storage in the North Pacific and shift of opal deposition from open marine to upwelling environments (März *et al.*, 2013). The series of conditions during the 4 to 3.5 Ma time interval are not repeated in the rest of our Pliocene-early Pleistocene records.

Diatom valves decrease from 3.5 to 2.8 Ma, dinosterol, brassicasterol and alkenone MAR increase, and SSTs decrease slightly again. This period from 3.35 to 3 Ma ends with evidence for the first significant meltwater-sourced freshwater input (increase in $\delta^{13}C_{37:4}$) (Figure 6.1g, Figure 6.4h) and increasing sedimentation rates supporting the hypothesis that the Cordilleran Ice Sheet is developing steadily (see Chapter 5). The nearby landmass is still covered by vegetation that is being eroded and transported to the ocean by mountain glaciers which are growing as part of the Cordilleran Ice Sheet. The reduction in diatom silica preservation in favour of biomarker preservation suggests that diatom blooms still occur, but perhaps a more reductive environment at the sea bed would favour OM preservation. It has also been suggested that the modern halocline across the GOA was established since the NHG (Haug *et al.*, 2005) at 2.8 Ma at Site U1417. Whitley *et al.* (2005) conducted a study in the subarctic gyre in the Gulf of Alaska and observed that the normally rich Si HNL region of the Gulf of Alaska could be depleted in Si due to the northward advection of the California Undercurrent waters during and following El Niño years. The climate of the Pliocene has been suggested to be an El Niño permanent state (Ford *et al.*, 2015) and could support the study of Whitney *et al.* (2005).

In the modern North Pacific, the silica maximum in the GOA is at an intermediate depth of 2000-2500 meters (Talley and Joyce, 1992), half the present day water depth of Site U1417. Coccolithophores have a calcified structure and alkenones are part of their tissue. Low-resolution shipboard analysis shows lower $CaCO_3$ concentrations before 2.5 Ma (up to 1.8 wt (%)) and highest $CaCO_3$ values for the period 2.5 to 1.5 Ma (up to 8% by wt)). The alkenone MAR at Site U1417 indicates

an increase in coccolithophore OM from 2.5 Ma which occurs more or less coherently with the increased carbonate content. Both records provide supporting evidence for changes in marine productivity export increasing from 2.5 Ma and a more favourable OM and CaCO₃ preservation after the NHG.

Before 2.5 Ma, coccolithophore biomarker (alkenones) concentrations seem to show similar variations compared to the diatom valve abundance (Figure 6.4f and g). Alkenones are known to be a more resistant biomarker than sterols and therefore, the alkenone preservation in the sediment record is more effective. Because coccolithophores have a bloom season that follows the diatom and dinoflagellate bloom seasons, alkenone abundance might reflect late autumn rather than spring ocean conditions. Late autumn in the GOA is a more stable season with water column stratification compared to spring, which is the beginning of the melting season. OM preservation could, therefore, reflect reduction conditions at the sediment-water interface due to water column stratification as well as a warmer SST episodes derived from alkenones (Figure 6.4a).

During the oNHG (See Chapter 5), the development of tidewater glaciers is evident from 2.8 Ma to 2.4 Ma, with the delivery of the first IRD peak to the GOA (Figure 6.1g). This suggests a Cordilleran Ice Sheet expansion with clear evidence for a large ice sheet preserved in the marine record (see Chapter 5). Diatom valves become absent from the record and biomarker starts to become the dominant form of organic material preserved in the record, either from sterols or biomarkers in the form of *n*-alkanes and freshwater %C_{37:4}>5%. TOC and TON records show a high variability but overall increase abruptly as sedimentation rates increase abruptly as well, while $\delta^{13}\text{C}$ and $\delta^{15}\text{N}$ do not record a clear trend. Since the Cordilleran glaciation is evident in the GOA and the diatom disappears from Site U1417, the freshwater increase and present IRD thus supports the suggestion of the better preservation of OM during this time.

As stated above TOC and TON show a clear increasing trend similar to the sedimentation rates (Figure 6.4 c and e) through the Plio-Pleistocene whereas $\delta^{13}\text{C}$ and $\delta^{15}\text{N}$ do not follow the same trend (Figure 6.4d). This can be used to

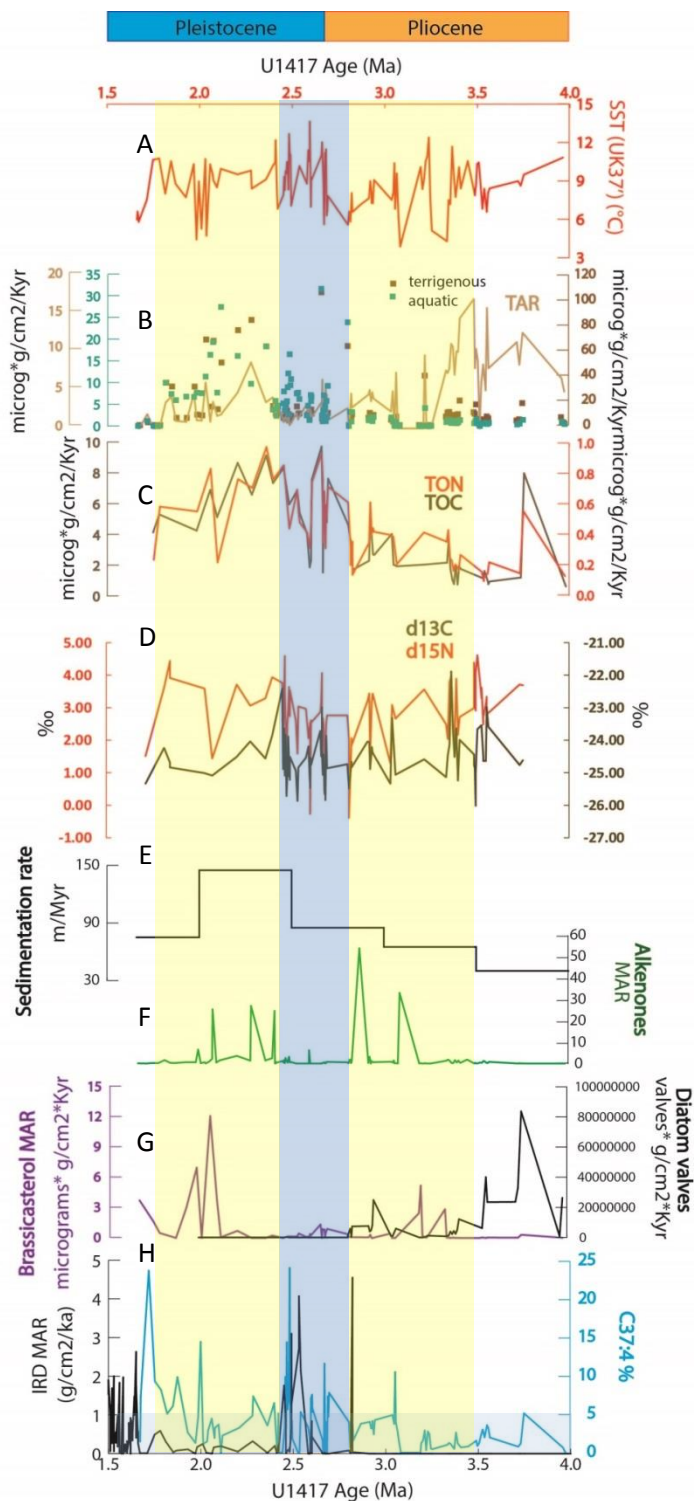


Figure 6.4: Summary figure. A) Sea surface temperature (SST) derived from $U^{K_{37}}$ index (red); B) Terrigenous n-alkanes (brown squares) and aquatic n-alkanes (blue squares) MAR ($\mu\text{g cm}^{-2} \text{kyr}^{-1}$) and terrigenous vs aquatic organic matter (TAR index) (light brown); C) Total organic carbon (TOC) (grey) and total organic nitrogen (TON) (red) MAR ($\mu\text{g cm}^{-2} \text{kyr}^{-1}$); D) $\delta^{13}\text{C}$ (grey) and $\delta^{15}\text{N}$ (red) in ‰; E) Sedimentation rates (m/Myr) (black); F) Alkenone abundance MAR ($\mu\text{g cm}^{-2} \text{kyr}^{-1}$) (green); G) Brassicasterol MAR ($\mu\text{g cm}^{-2} \text{kyr}^{-1}$) (purple)

and diatom MAR (values $\text{cm}^{-2} \text{kyr}^{-1}$) (black) and H) IRD MAR ($\text{g cm}^{-2} \text{Kyr}^{-1}$) (black) and $\text{C}_{37:4}$ % (blue) vs U1417 Age (Ma).

distinguish the terrigenous or marine signal recorded in TOC, TON $\delta^{13}\text{C}$ and $\delta^{15}\text{N}$ when their trends differ from each other. From 4.0 to 3.0 Ma, TOC and TON preservation are low however the heavier $\delta^{13}\text{C}$ and $\delta^{15}\text{N}$ concentrations suggest the terrigenous interpretation of these values. This is supported by our TAR data. From 2.4 to 1.7, there is an increase in TOC and TON preservation due to higher sedimentation rates, however $\delta^{13}\text{C}$ and $\delta^{15}\text{N}$ values suggest an increase in terrigenous source of OM. This time period $\delta^{13}\text{C}$ and $\delta^{15}\text{N}$ interpretation is similar to during the 4.0 to 3.0 Ma interval, with some increases in TAR. The 3.0 to 2.4 Ma however, shows overall lighter $\delta^{13}\text{C}$ and $\delta^{15}\text{N}$ composition and variable TOC and TON. This is discussed further later in this chapter.

It is possible to differentiate two processes taking place: one in the ocean and one originated on land. On land erosion from the Cordilleran Ice Sheet (increase in $\text{C}_{37:4}$ and IRD) increases sedimentation rates at Site U1417 and terrigenous *n*-alkanes, TOC, TON increase synchronously, however, lighter $\delta^{13}\text{C}$ and $\delta^{15}\text{N}$ composition suggest a higher marine productivity role in the ocean. Sterol and alkenone abundances remain low during the 2.8 to 2.4 Ma. Freshwater input ($\% \text{C}_{37:4}$) often increases above 5% and IRD concentration is at the highest of the record. It is likely that the oceanography in the GOA under these conditions was dominated by a warm and stratified water column (see Chapter 5) with limited nutrient availability (low TAR, Figure 6.4b). The depletion of the available surface nutrients delivered from the land during algal production could drive high variability of $\delta^{13}\text{C}$ and $\delta^{15}\text{N}$ from marine productivity preference for lighter $\delta^{13}\text{C}$ and $\delta^{15}\text{N}$ uptake and heavier $\delta^{13}\text{C}$ and $\delta^{15}\text{N}$ signal due to restriction of nutrients. After the NHG and following water column stratification, literature on the North Pacific Ocean suggests the successive advection of the Californian underwater currents into the Gulf of Alaska (Whitney *et al.*, 2005).

From 2.4 to 1.7 Ma, there is a general $\delta^{15}\text{N}$ enriching in the heavier isotope and TOC and TON increase. Lower freshwater for most of this period drives high SST and increase in sterol OM productivity export. Sedimentation rates increase to the

highest levels of the record and *n*-alkane abundances peak as well as sterols due to increase in OM preservation and terrigenous OM input. These records suggest a better mixed water column and increase in nutrient abundance (increase in $\delta^{15}\text{N}$ and TAR) and phytoplankton preferential lighter isotope intake favours the permanently low $\delta^{13}\text{C}$ values. We suggest that the continuous input of terrigenous nutrients into the surface ocean and a rapid OM burial enhanced OM preservation from *n*-alkanes, TON, TOC and sterols. Diatom abundances also respond to punctual nutrient increase and water column mixing at 2.46 and 1.96 Ma.

6.5.4 Isotopic excursions during the early Pleistocene (2.8 to 2.4 Ma).

During variable but overall warmer SST episodes right after the appearance of IRD in the GOA (2.8 to 2.4 Ma), we find increase range of $\%C_{37:4}$ from glacier meltwater and $\delta^{13}\text{C}$ and $\delta^{15}\text{N}$. A shift from lower to higher TOC and TON MAR is synchronous with a general heavier $\delta^{13}\text{C}$ and $\delta^{15}\text{N}$ and overall lower TAR and marine productivity from coccolithophores and sterols in comparison with the rest of the record. The impact of sediment rates on this records can be disregarded as they are stable during most of the period (Figure 6.5e).

The period from 2.8 to 2.4 Ma is characterized by very variable SST but this interval contains the highest SST values from the whole 4 to 1.7 Ma record (Figure 6.5a). The marine *n*-alkane MAR concentrations are similar to terrigenous *n*-alkane MAR values with some intervals where aquatic *n*-alkane MAR are higher than terrigenous *n*-alkane MAR. The TAR drops to relatively low values (<1) through the interval intervals of higher aquatic *n*-alkane MAR (Figure 6.5b). However, during 2.8 to 2.4 Ma with overall lower TAR values, there are peaks in TAR of up to 6. Peaks in TAR are synchronous with 6 to 7 °C variable SST intervals with highlighted in Figure 6.5. The episodes of increase TAR is also reflected in increase in variability of up to 0.5% in TOC and 0.04% in TON, 3 to 4‰ in $\delta^{15}\text{N}$ and around 2‰ in $\delta^{13}\text{C}$. During these high variable proxy intervals, IRD and $C_{37:4}$ also experience variations of up to 4 g cm⁻² kyr⁻¹ and 25%, respectively (Figure 6.5h). Despite the uncomplete sequence during the 2.8 to 2.4 Ma at Site U1417, our data suggest that during a generally stratified ocean due to a glaciated Cordilleran Ice Sheet (e.g. high SST, $C_{37:4}$ and IRD) with limited terrigenous input into the GOA (e.g. low TAR) and low marine productivity (e.g. low aquatic *n*-alkanes, sterols and

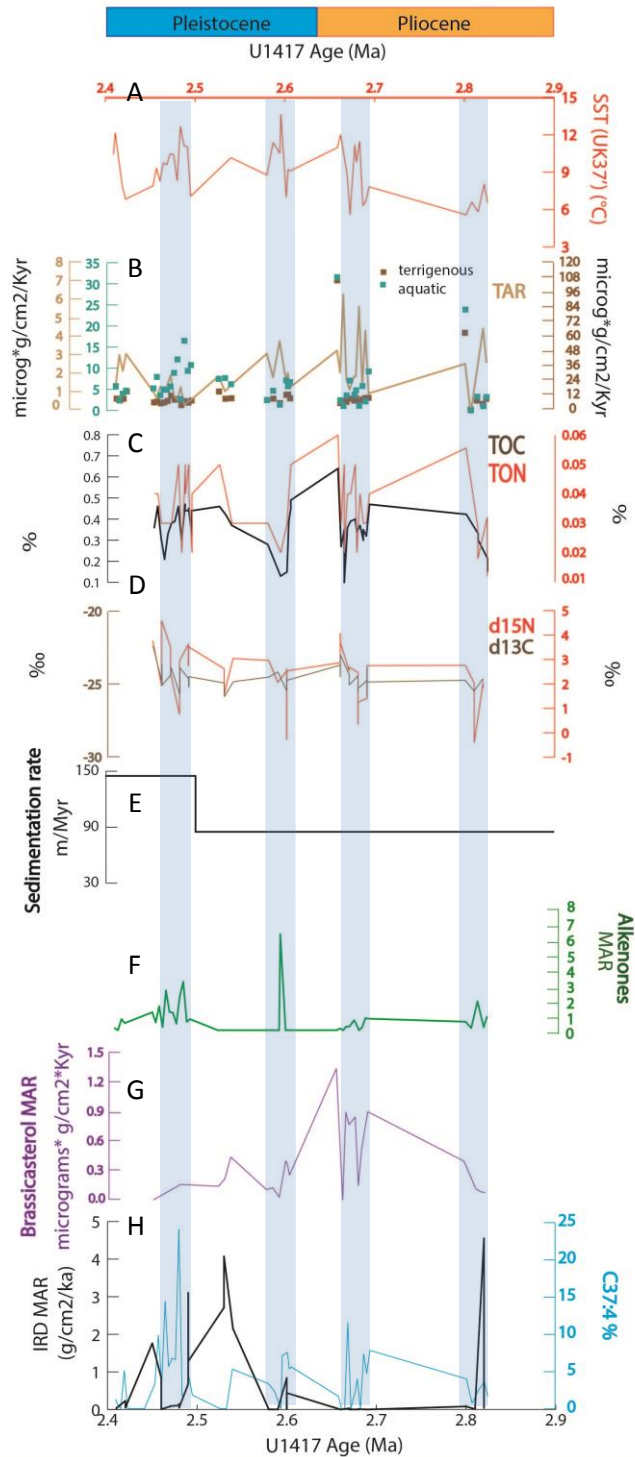


Figure 6.5: Isotopic excursions during the PPT. A) Sea surface temperature (SST) derived from $U^{K_{37}}$ index (red); B) Terrigenous n-alkanes (brown squares) and aquatic n-alkanes (blue squares) MAR ($\mu\text{g cm}^{-2} \text{kyr}^{-1}$) and terrigenous vs aquatic organic matter (TAR index) (light brown); C) Total organic carbon (TOC) (grey) and total organic nitrogen (TON) (red) %; D) $\delta^{13}\text{C}$ (grey) and $\delta^{15}\text{N}$ (red) in ‰; E) Sedimentation rates (m/Myr) (black); F) Alkenone abundance MAR ($\mu\text{g cm}^{-2} \text{kyr}^{-1}$) (green); G) Brassicasterol MAR ($\mu\text{g cm}^{-2} \text{kyr}^{-1}$) (purple) and

diatom MAR (valves cm⁻² kyr⁻¹) (black) and H) IRD MAR (g cm⁻²Kyr⁻¹) (black) and C_{37:4} % (blue) vs U1417 Age (Ma).

alkenone abundance), nutrient availability supply to the GOA (higher TAR) was rapidly used by coccolithopore productivity growth (lighter $\delta^{13}\text{C}$ and $\delta^{15}\text{N}$) until nutrient depletion (higher $\delta^{13}\text{C}$ and $\delta^{15}\text{N}$). The marine productivity blooms during water stratification could have participated in the atmospheric CO₂ drawdown during the NHG, causing lighter $\delta^{13}\text{C}$ and $\delta^{15}\text{N}$ imprint (Raymo *et al.*, 1996). Further studies should focus on confirming these preliminary hypotheses.

6.6 Conclusions

Terrigenous and aquatic n-alkanes, TOC and TON MAR long term trends are similar to sedimentation rates through the Pliocene and Pleistocene. This is interpreted as a dominant OM preservation signal in these records, which are best preserved through sediment rapid burial. Higher TAR and $\delta^{13}\text{C}$ and $\delta^{15}\text{N}$ values show a higher dominance of terrigenous over marine OM signal. Sterols are easily degradable and show higher abundances during increase OM preservation interval. Alkenones are the most resistant OM biomarkers and seem to respond to increases in TAR.

During the Plio-Pleistocene Cordilleran Ice Sheet evolution, there is an overall increase in sedimentation rates and increase in OM preservation, suggested by increases in n-alkane abundance as well as %TOC and %TON. The concentration of brassicasterol, dinosterol, β -sitosterol and alkenone abundance do not show a clear trend during the Pliocene-Pleistocene.

OM preservation is best reflected in sterol abundances whereas alkenones and n-alkanes are indicative of marine and terrestrial OM input into U1417. OM preservation is lowest during 4 to 2.8 Ma, before the glaciation impact in GOA and best during low C_{37:4} after 2.8 Ma after the NHG. The period of 4 to 2.8 Ma suggest a non-stratified and saltier GOA which agrees with previous studies. The period between 2.8 to 1.7 Ma is characterised by water column stratification due to Cordilleran Ice Sheet meltwater (see Chapter 5). The stratification is been suggested (Chapter 5) to be strongest during the 2.8 to 2.4 Ma.

During the variable SST and $C_{37:4}$ from 2.8 Ma to 2.4 Ma, we find increase in variability in TOC, TON, $\delta^{13}C$ and $\delta^{15}N$. Despite the overall low marine productivity, the high variability in TOC, TON, $\delta^{13}C$ and $\delta^{15}N$ together with increase marine than terrigenous OM from *n*-alkanes suggest coccolithophores (alkenone MAR) productivity increases seems to respond to small nutrient input during short events. Coccolithophore blooms could reflect nutrient depletion from lighter to heavier $\delta^{13}C$ and $\delta^{15}N$ and/or atmospheric CO_2 drawdown and lighter isotope biomass intake. However, it could be possible that the water column stratification relaxation would have TOC, TON, $\delta^{13}C$ and $\delta^{15}N$ impacts in marine productivity and increase the occurrence of diatom productivity export. Further studies during this time period are needed in order to increase our understanding of $\delta^{13}C$ and $\delta^{15}N$ imprint and marine production during change in ocean regime in the GOA.

Chapter 7: Late Pleistocene ocean temperature dynamics in the North-east Pacific

7.1 Introduction

The LR04 stack (Lisiecki and Raymo, 2005) is a benthic foraminifera oxygen isotope record which has been proposed to represent global ice volume. During the last 500 Kyr, the LR04 stack curve has a distinctive “saw tooth” shape also noticed by previous studies (i.e. Imbrie *et al.*, 1992) with abrupt warmings and gradual coolings. This saw tooth shape is also recorded in ice core atmospheric CO₂ and CH₄ reconstructions during the last 400 Kyr (Vostok, Antarctica, Petit *et al.*, 1999; Barnola *et al.*, 2003) extending back to 650 ka (EPICA, Siegenthaler *et al.*, 2005). Due to the “saw tooth” timing of the LR04, the climate during this time has been explained as sensitive to eccentricity astronomical configuration, which has 100 kyr and 400 kyr cyclicity. The amplitude of the 100 kyr cycles seen in the climate record are still difficult to explain as the eccentricity forcing is relatively small in comparison to the response. They are arguably forced by a combination of precession cycles and/or obliquity cycles. Climate feedbacks must be involved (i.e. Abe-Ouchi *et al.*, 2013).

The LR04 stack is a record composed of benthic oxygen isotopic data and so it represents the deep ocean characteristics (Lisiecki and Raymo, 2005). SST range is higher than the temperature range in the deep ocean across glacial and interglacial cycles (Lang and Wolff, 2011). This evidences different climate processes acting at different water depths. Furthermore, LR04 is largely based in data from the North Atlantic Ocean (Lisiecki and Raymo, 2005) and therefore, the contribution to global ice volume from regional ice sheets to the Pacific is limited. Most of our explanations of the 100 kyr ice sheet cycles is based on records from the Atlantic Ocean and is dominated by the links between the Atlantic Ocean and the Laurentide and to a lesser extent the Scandian and Eurasian Ice Sheets. The

contribution of the Cordilleran Ice Sheet into the North Pacific ocean characteristics is expected to differ from the LR04 climate records and could greatly contribute to our understanding on under-represented regional environments and their forcing and their role of the North Pacific in the global climate system.

The understanding of North Pacific circulation and teleconnections improves for the Last Glacial Maximum (LGM) and Holocene in comparison to earlier parts of the geological record (e.g. CLIMAP, 1976, 1984). However, there are still some disagreements between different models and between models and proxy data (Otto-Bliesner *et al.*, 2005; Rae *et al.*, 2016) (e.g. proxies recording greater seasonality than predicted by the climatic models, Otto-Bliesner *et al.*, 2005). It is debated when the modern characteristics of ocean temperature dynamics in the subpolar North Pacific appeared, since these were different in the Pliocene and early Pleistocene than present (Chapter 2, Chapter 5 and Chapter 6). Specifically, the subarctic North Pacific shifted at some point from a colder to warmer east than west subarctic Pacific that dominates at modern (Chapter 5). The subarctic Pacific is, together with the Antarctic, a region where the phytoplankton driven carbon sequestration into the ocean (or “biological pump”) is not strong enough to balance the deep ocean CO₂ release into the surface ocean by water mixing, and so there is a net leakage of CO₂ into the atmosphere (Jaccard *et al.*, 2005). CO₂ leak to the atmosphere is reduced with increased water stratification and increased phytoplankton bloom (Francois *et al.*, 1997). Both mechanisms have been proposed to explain a decrease in atmospheric CO₂ during the Last Glacial Maximum (Sarmiento and Toggweiler, 1984; Siegenthaler and Wenk, 1984) and justify the interest in the study of the last 500 kyr in the GOA.

Studying the last 500 Kyr period offers the potential to observe in detail wide time windows with different climate-ice sheet-ocean interactions during glacial and interglacial cycles. In this chapter we study the climate and productivity of the last 500 Kyr from new data from IODP Site U1418 and Site U1417 in the Northeast Pacific (Gulf of Alaska), with emphasis on Site U1418 due to its higher sampling resolution. Site U1418 was drilled with the aim of constraining the timing of glacial

events on the Pacific side of the northwestern Cordilleran Ice Sheet and to investigate the relationship with global ice sheet dynamics (Jaeger *et al.*, 2014). We use marine and terrestrial biomarkers as well as C, N proxies in order to understand the local glacial history of the Cordilleran Ice Sheet over Alaska and northwest Canada and its influence on surface ocean characteristics. A comparison between the northeast and northwest Pacific SST is possible through previously published SST record from OPD 882 (Haug *et al.*, 2005, Martínez-García *et al.*, 2010). This allows the characterisation of the subpolar North Pacific behaviour during the last 500 Kyr. Lower temporal resolution records from Site U1417 (Chapter 3) allows a broad comparison between two points of the Gulf of Alaska to characterize local oceanographic differences, such as temperature and productivity, terrestrial and marine sedimentation changes, even though sites U1417 and U1418 seem to have a different sediment provenance for the last 500 kyr (Gulick *et al.*, 2015).

7.2 Results

7.2.1 Site U1418

U1418 lithostratigraphic Unit I mud has been interpreted as containing gravity flows (Jaeger *et al.*, 2014). However, samples collected for analysis here avoided sections in the core with evidence of gravity flows. Therefore, the samples obtained for this study are suitable for investigating glacial–interglacial palaeoceanographic variability as presented in this chapter.

7.2.1.1 $U^{K_{37}}$ and $U^{K_{37}'}$

$U^{K_{37}}$ values ranges from -0.1 to 0.4, with an average value of 0.1. $U^{K_{37}'}$ values ranges from 0.2 to 0.4, with an average value of 0.3. Long term trends in the $U^{K_{37}}$ and $U^{K_{37}'}$ records are difficult to decipher due to the high variability of the records (Figure 7.1).

7.2.1.2 SST

SST based on the $U^{K_{37}'}$ and using the calibration of Müller *et al.* (1998) at Site U1418 range from 3.9 to 11.6°C, with an average value of 8.0 °C, for the last 500 Kyr (Figure 7.2). The SST from site U1418 shows a warming trend during the last 500

kyr. The LR04 saw tooth shape of glacial-interglacial SST variability is indistinctive during the 500 to 200 ka and easier to recognize during the last 200 kyr, during an increase in sedimentation rates (Figure 7.1).

7.2.1.3 $C_{37:4}$

The % $C_{37:4}$ results for Site U1418 range from 2 to 27.5 % with an average value of 14.5%. All data points from our record show $C_{37:4}$ values above 5%, a value which is associated with subarctic/subpolar water masses in the Nordic Seas (Bendle *et al.*, 2005), with the exception that our most recent sample (Figure 7.2c). From 500 to 200 ka, $C_{37:4}$ values, despite being above 5%, are slightly lower (11.6%) on average than after 200 ka (17.3%). This could be influenced by the higher sample resolution during the last 200 kyr part of the record compared to the 500 to 200 kyr section. However, whilst the low values before and after 200 ka are similar, the peaks in % $C_{37:4}$ are significantly higher after 200 ka compared to before. This is largely responsible for the long term trend of increasing % $C_{37:4}$ during the last 500 kyr at Site U1418.

7.2.1.4 TAR

TAR values at Site U1418 range from 0 to 20, with an average of 1.3 for the last 500 kyr (Figure 7.2d). Higher TAR values suggest more terrestrial origin of the organic matter (OM) and lower TAR values indicate more aquatic sourced OM (Figure 7.2d). Based on the average value of 1.3, considerably higher than average TAR values can be found between 187.9 and 107.8 ka, with the highest value of the record of 20.7 found at 122.6 ka.

Terrigenous *n*-alkane abundance ranges from 0 to $3.7 \mu\text{g g}^{-1}$, with an average value of $0.5 \mu\text{g g}^{-1}$ (Figure 2d). Terrigenous *n*-alkane abundance normalised to TOC ranges from 0 to $8.6 \mu\text{g g}^{-1} \text{TOC}^{-1}$, with an average value of $0.5 \mu\text{g g}^{-1} \text{TOC}^{-1}$ (Chapter 4). Terrigenous *n*-alkane abundance MAR ranges from 0 to $49,100 \mu\text{g cm}^{-2} \text{kyr}^{-1}$ with an average value of $9,300 \mu\text{g g}^{-1}$ (Figure 7.3b).

Aquatic *n*-alkane abundance ranges from 0 to $1.2 \mu\text{g g}^{-1}$, with an average value of $0.3 \mu\text{g g}^{-1}$ (Figure 2d). Aquatic *n*-alkane abundance normalised to TOC ranges from 0 to $2.0 \mu\text{g g}^{-1} \text{TOC}^{-1}$, with an average value of $0.2 \mu\text{g g}^{-1} \text{TOC}^{-1}$ (Chapter 4). Aquatic

n-alkane abundance ranges from 0 to 20575.4 $\mu\text{g cm}^{-2} \text{kyr}^{-1}$ with an average value of 4140.3 $\mu\text{g cm}^{-2} \text{kyr}^{-1}$ (Figure 3b). Terrestrial and aquatic *n*-alkane abundances normalised to MAR similar trends through the 500ka, with the highest peaks concentrated around 180 ka (Figure 7.3b).

7.2.1.5 TOC, TON, $\delta^{13}\text{C}$ and $\delta^{15}\text{N}$

TOC content varies from 0.4 to 0.9 %, with average value of 0.5% (Figure 7.3d). TOC MAR ranges from 15,292.2 to 3,133.2 $\mu\text{g cm}^{-2} \text{kyr}^{-1}$, with an average value of 10,350.4 $\mu\text{g cm}^{-2} \text{kyr}^{-1}$ (Figure 7.3e). Total organic nitrogen values ranges from 0.03 to 0.1 % with an average of 0.05 % (Figure 7.3d). TON MAR ranges from 1,555.1 to 246.6 $\mu\text{g cm}^{-2} \text{kyr}^{-1}$, with an average value of 917.4 $\mu\text{g cm}^{-2} \text{kyr}^{-1}$. $\delta^{13}\text{C}$ values ranges from -25.3 to -20.3 ‰, with an average of -24.1‰ (Figure 7.3f). $\delta^{15}\text{N}$ values from 1.7 ‰ to 6.4 ‰, with an average value of 4.3 ‰ (Figure 7.3f). TOC, TON, $\delta^{13}\text{C}$ and $\delta^{15}\text{N}$ do not show clear long term trends during the last 500 kyr, but there does appear to be an increase in variability in the proxies over the last 200 Kyr (Figure 7.3d and f).

7.2.1.6 Alkenone Concentrations

Alkenone abundances range from 0 to 0.1 $\mu\text{g g}^{-1}$ with an average of 0.017 $\mu\text{g g}^{-1}$ (Figure 7.4e). Alkenone abundances normalised to TOC range from 0 to 0.4 $\mu\text{g g}^{-1} \text{TOC}^{-1}$, with an average of 0.06 $\mu\text{g g}^{-1} \text{TOC}^{-1}$ (Figure 7.4e). Alkenone MAR values range from 0 to 1,685.6 $\mu\text{g cm}^{-2} \text{kyr}^{-1}$, with an average value of 219.6 $\mu\text{g cm}^{-2} \text{kyr}^{-1}$ (Figure 7.4e). The alkenone MAR record shows no long term trend during the last 500 kyr

7.2.1.7 Sterols

β -sitosterol abundance ranges from 0.03 to 1.4 $\mu\text{g g}^{-1}$, with an average of 0.4 $\mu\text{g g}^{-1}$ (Figure 7.4a). β -sitosterol abundances normalized to the TOC ranges from 0.2 to 2 $\mu\text{g g}^{-1} \text{TOC}^{-1}$ (Figure 7.4a). β -sitosterol MAR abundances ranges from 4 to 38,303.7 $\mu\text{g cm}^{-2} \text{kyr}^{-1}$, with an average value of 11,122.0 $\mu\text{g cm}^{-2} \text{kyr}^{-1}$ (Figure 7.4a).

Brassicasterol abundance ranges from 0.01 to 0.8 $\mu\text{g g}^{-1}$, with an average of 0.2 $\mu\text{g g}^{-1}$ (Figure 7.4c). Brassicasterol abundances normalized to the TOC ranges from 0.03 to 0.5 $\mu\text{g g}^{-1} \text{TOC}^{-1}$, with an average value of 0.2 $\mu\text{g g}^{-1} \text{TOC}^{-1}$ (Figure 7.4c).

Brassicasterol MAR abundances ranges from 1.0 to 27,470.5 $\mu\text{g cm}^{-2} \text{kyr}^{-1}$, with an average value of 5,163.7 $\mu\text{g cm}^{-2} \text{kyr}^{-1}$ (Figure 7.4c).

Dinosterol abundance ranges from 0 to 0.9 and an average of 0.14 $\mu\text{g g}^{-1}$ (Figure 7.4b). Dinosterol abundances normalized to the TOC ranges from 0.1 to 0.6 $\mu\text{g g}^{-1} \text{TOC}^{-1}$, with an average value of 0.2 $\mu\text{g g}^{-1} \text{TOC}^{-1}$ (Figure 7.4b). Dinosterol MAR abundances ranges from 0 to 35,737.63 $\mu\text{g cm}^{-2} \text{kyr}^{-1}$, with an average value of 3,799.4 $\mu\text{g cm}^{-2} \text{kyr}^{-1}$ (Figure 7.4b).

Sterols peak during 500 to 200 ka and from around 250 Kyr to the present they diminish (Figure 7.4).

7.2.2 Site U1417

7.2.2.1 SST

SST values at Site U1417 using the calibration of with Müller *et al.* (1998) range from 5.04 to 16.2, with an average of 8.1 °C (Figure 7.6a). Glacial-interglacial cycles are not clearly defined due to the relatively low sampling resolution, but there is significantly greater SST variability than seen in U1418 even though sampling resolution is lower (See chapter 3). From 420 to 280 kyr, SST shows an average variability of 0.4 °C, with a SST average of 8.2 during this time interval (Figure 7.6a).

7.2.2.2 $C_{37:4}$

$C_{37:4}$ values at Site U1417 range from 0 to 23.4%, with an average of 11.2% (Figure 7.6c). $C_{37:4}$ at Site U1417 shows an increasing trend towards during the last 500 kyr.

7.2.2.3 TAR

TAR values range from 0.47 to 3.5, with an average of 1.7 (Figure 7.7c). From this value of 1.7, we have again discriminated between a relative more terrigenous and more aquatic source of the organic matter of our sediments (Figure 7.7C). Before 230 ka, TAR values are below their average value for the 500 kyr (Figure 7.9g) indicating relative increase in marine source of OM than from 230 ka to present, with TAR values increase above average indicating a dominance of terrigenous

material. The period from 232 to 115 Ka contains the highest TAR values of our 500 ka record.

7.2.2.4 TOC, TON, $\delta^{13}\text{C}$ and $\delta^{15}\text{N}$

Total organic carbon at Site U1417 ranges from 0.4 to 1.0%, with an average of 0.5% during the last 500 kyr (Figure 7.7d). Total organic nitrogen ranges from 0.03 to 0.1%, with an average value of 0.05% (Figure 7.7d). $\delta^{13}\text{C}$ ranges from -25.2 to -20.3‰, with an average value of -24.3‰ (Figure 7.7e). $\delta^{15}\text{N}$ ranges from 1.6 to 6.4‰, with an average value of 4‰ (Figure 7.7e).

7.2.2.5 Alkenone Concentrations

Alkenone concentrations range from 0 to 1.0 $\mu\text{g g}^{-1}$, with an average of 0.08 $\mu\text{g g}^{-1}$. Alkenone concentrations normalised to TOC range from 0 to 0.4 $\mu\text{g g}^{-1} \text{TOC}^{-1}$, with an average value of 0.06 $\mu\text{g g}^{-1} \text{TOC}^{-1}$ (Chapter 4). Alkenone MAR concentrations range from 0 to 9.6 $\mu\text{g cm}^{-2} \text{kyr}^{-1}$, with an average value of 1.2 $\mu\text{g cm}^{-2} \text{kyr}^{-1}$.

7.3 Discussion

7.3.1 Site U1418

The glacial-interglacial and marine productivity changes during the last 500 kyr are studied at higher resolution at Site U1418 (closer to land) than the more distal Site U1417. The record covering MIS 6 (the coldest stadial) and MIS 5e (the warmest interstadial in our record) are examined at higher resolution to characterize the different climatic and oceanic characteristics between stadials and interstadials in the Gulf of Alaska region. The period covering the last 200 Kyr has higher sedimentation rates which allowed a higher sample resolution in this study providing a more representative picture of climate variability. By comparing these records with results from ODP 882 in the northwest Pacific surface ocean (Haug *et al.*, 2005), to investigate the development of ocean temperature dynamics and link with the global climate across the subarctic North Pacific Ocean.

7.3.1.1 Glacial-Interglacial variability

As the $\text{U}^{\text{K}_{37}}$ based SST record incorporates the $\text{C}_{37:4}$ together with the $\text{C}_{37:2}$ and $\text{C}_{37:3}$ alkenones. When the % $\text{C}_{37:4}$ is very high (up to 26.5 %), the $\text{U}^{\text{K}_{37}}$ based SST and the

% C_{37:4} follow similar trends. As the C_{37:4} alkenone combines both salinity and temperature signals, the similarity between the U^K₃₇ based SST and the % C_{37:4} suggests that the U^K₃₇ based SST record is also influenced by the % C_{37:4} and incorporates a freshwater signal of the C_{37:4} into the SST record. Therefore, we consider the U^K_{37'} index as a more reliable proxy for SST, but the U^K₃₇ and the % C_{37:4} are used for glacial-interglacial identification (Figure 7.1 and Figure 7.2).

The SST records based on U^K₃₇ and U^K_{37'} derived here show a glacial interglacial pattern with glacial stages generally colder than interglacials (Figure 7.2). The glacial-interglacial cycles identified in SST reconstructions from U1418 in the Gulf of Alaska do not generally show the typical saw-tooth shape of the LR04 benthic record (Figure 7.2). The δ¹⁸O record from *N. pachyderma* (sin) from Site U1418 generated by Dr. Hiro Asahi (pers. comm. ; Figure 7.1), reconstructed with a more refined sedimentation rate record than the shipboard sedimentation rates used in this thesis (Figure 7.1) also does not show the clear glacial-interglacial saw-tooth pattern of the LR04 benthic record.

Glacial-interglacial cycles at Site U1418 are more pronounced in the U^K₃₇ based SST and the % C_{37:4} records than in the U^K_{37'} based SST (Figure 7.1). There is also a reasonable correlation between U^K₃₇ based SST and the % C_{37:4} to the δ¹⁸O record from this site generated by Dr. Hiro Asahi (Figure 7.1). The glacial-interglacial cycle from MIS 7 to MIS 4 based on SST reconstructions from U^K₃₇ and also the %C_{37:4} record shows the typical glacial interglacial saw tooth shape of LR04 stack (Lisiecki and Raymo, 2005) (Figure 7.1 and 7.2). This is possibly due to increased sedimentation rate in U1418 and subsequent higher sample resolution in our record. Comparing our U^K₃₇ and U^K_{37'} with the LR04 stack, it is possible to identify some of the highest and lowest points in the SST record and correlate them with marine isotope stages (MIS). We can identify MIS 10, MIS 8, MIS 7, MIS 6, MIS 5, MIS 4 and MIS 1. The identification of the less pronounced marine isotopic stages (MIS 12, MIS 11, MIS 9, MIS 8, MIS 7, MIS 3, and MIS 2) can only be identified by comparisons with the δ¹⁸O record (Figure 7.1). The U^K₃₇ and U^K_{37'} based SST and the % C_{37:4} records at Site U1418 suggest that during the last 500 kyr glacial-interglacial cycles have a cyclicity of 100 kyr.

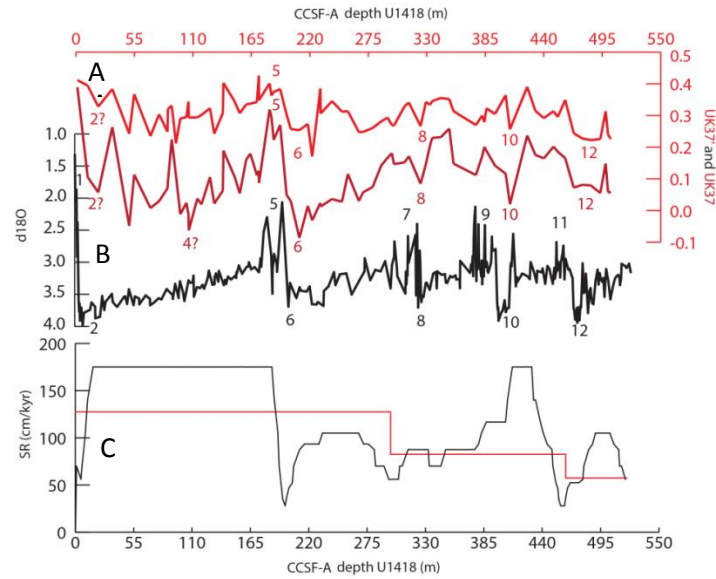


Figure 7.1: Glacial-interglacial changes at Site U1418. (a) UK_{37}' , (b) UK_{37} , (c) planktonic $\delta^{18}O$ (from Dr. Hiro Asahi) and (d) shipboard sedimentation rates used to generate a rough age model for U1418 (red) are compared with more detailed sedimentation rates used to improve the age model of U1418 (black) vs CCSF-A U1418 depth (m) Please note that the y axis for (c) has been inverted.

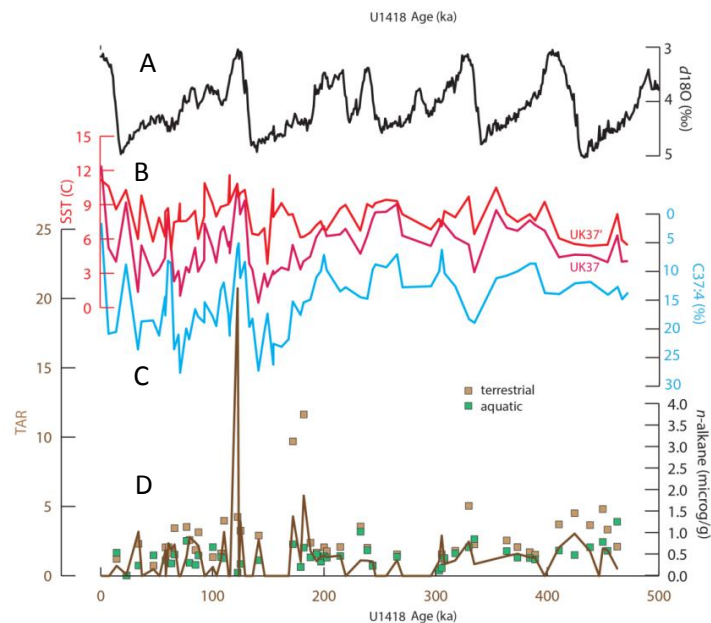


Figure 7.2: Glacial-interglacial cycles and terrigenous and marine OM changes. (a) LR04 benthic stack (Lisiecki and Raymo, 2005) (black), (b) SST based on the UK_{37}' (Müller et al., 1998; red/higher record) and SST based on the UK_{37} (Prah et al., 1988; pink/lower record) indices, (c) % $C_{37:4}$ alkenone, (d) TAR and terrestrial and aquatic n-alkane concentrations in $\mu g g^{-1}$. Please note that the y axis for the (a) and (c) have been inverted.

The $U^{K_{37}}$ record and the $\delta^{18}O$ allow the identification of MIS 1 to MIS 12 (Figure 7.1), with the most intense glacial stages corresponding to higher sedimentation rates at MIS 10, MIS 6 to MIS 2 (Figure 7.1). The increase in sedimentation rates and increase in meltwater flux ($\%C_{37:4}$) recorded periodically in U1418 are likely to be associated with increased erosion rates on land and higher glacier runoff from the Cordilleran Ice Sheet. This, therefore, suggests that the Cordilleran Ice Sheet could have been more extensive during MIS 10 and from MIS 6 to MIS 2. The earlier part of the record (MIS 12 to MIS 6 or 500 to 147 ka) is characterised by a gradual cooling trend and the later part of the record (MIS 6 to MIS 1 or 141 ka to the present) shows a warming trend. The average $U^{K_{37}}$ between 500 and 147 ka is 0.29 and 0.32 between 141 ka and present. $U^{K_{37}}$ average before and after 141 ka are translated into an average SST difference of 0.8 °C using the calibration of Müller *et al.* (1998) (Figure 7.2).

The $U^{K_{37}}$ values are too low (negative) for reliable SST calibration, hence the $U^{K_{37}}$ values are translated into SST. SST (Müller *et al.*, 1998) and $\%C_{37:4}$ at Site U1418 show a gradual long term increasing trend with a 1.7°C warming and a long term increase in $C_{37:4}$ of 8% during the last 500 kyr. $C_{37:4}$ doubles its variability during the last 200 kyr (Figure 7.2). SST (Müller *et al.*, 1998) and $\% C_{37:4}$ maximum variability (Figure 7.1), occurs throughout MIS 6 to MIS 4, with increase in variability of 2°C and double $C_{37:4}$ than during the earlier part of the record (500 to 200 ka). We observe a correlation between colder SST and increase in $C_{37:4}$ and *vice versa*, regardless of the SST calibration used (Figure 7.2). As in previous chapters, we interpret the $C_{37:4}$ as a meltwater indicator. Therefore, meltwater flux to the GOA is higher during glacials than interglacials. $C_{37:4}$ concentrations peak during peak stadials e.g. MIS 10, MIS 6 and MIS 4. This suggests a positive correlation between the intensity/size of the Cordilleran Ice Sheet and glacial runoff during colder climate

7.3.1.2 Terrigenous organic matter

Terrigenous *n*-alkane proxies and β -sitosterol MAR at Site U1418 show similar high variability during 500 to 250 ka and 150 to 0 ka and decrease variability during 250 to 150 ka, with the exception of peaks at 200 kyr (Figure 7.5). In

addition, the temporally shorter TON (%), $\delta^{13}\text{C}$ (‰) and $\delta^{15}\text{N}$ (‰) records do not have a clear trend but a variability that increases around 300 ka, 180, 120 and 50 ka (highlighted in Figure 7.5). The TOC record shows a long term increasing composition and increasing variability during 320 to 50 ka in comparison to earlier and later part of the record. TOC shares similar variability as the TON, $\delta^{13}\text{C}$ (‰) and $\delta^{15}\text{N}$ (‰) during the stated above 4 time intervals.

The increase in terrigenous *n*-alkane MAR is synchronous with the increase in TOC, TON and sedimentation rates (Figure 7.1) due to the intensification of the glacial interglacial cycles in the last 200 kyr (Figure 7.5). The opposite is also true with the decrease in terrigenous *n*-alkane MAR, TOC and TON and with lower sedimentation rates. Ultimately, increased sedimentation rates increase the speed of sediment burial and increases the preservation of OM evidenced in the increase in TOC during the last 200 kyr (Figure 7.3 and 7.5). The TOC, TON, $\delta^{13}\text{C}$ (‰) and $\delta^{15}\text{N}$ (‰) proxies respond abruptly to punctual increases in the TAR and TOC/TON (Figure 7.3) and will be compared with the marine productivity export proxies in the Section 7.3.5 and Section 7.4.1.

As in Chapter 6, we cannot distinguish β -sitosterol terrigenous or marine source. Instead, β -sitosterol reflects changes in the preservation of OM. β -sitosterol MAR and the C and N bulk and isotope excursions in relation with increases in TAR record will be further explored in the next sections.

7.3.1.3 Marine productivity at U1418

Similarly as in Chapter 6, marine and terrigenous *n*-alkane MAR vary synchronously. As an increase in sedimentation rates occurs during an increase in aquatic *n*-alkane MAR into the ocean, the direct relationship between increase in terrigenous and increase in aquatic *n*-alkane MAR raises the question of the land or ocean origin of the aquatic *n*-alkanes. Comparison of aquatic *n*-alkanes with sterols and alkenone MAR would make it possible to identify whether there is a correlation between aquatic *n*-alkanes and marine productivity. Marine MAR productivity export records from dinoflagellates (dinosterol and brassicasterol, see Chapter 2 and Chapter 6) and coccolithophores (alkenones) show similar long term variability throughout the last 500 kyr despite different long term trends

(Figure 7.4 and Figure 7.5). Dinosterol and alkenone MAR do not show a clear long term trend while brassicasterol MAR shows a clear decreasing trend in the last 500 kyr, similarly as β -sitosterol. Regardless of the long term trend disagreements on each of these records, there seems to be a general higher MAR during the 500 to 250 ka and from 150 to present and lower MAR values from 250 to 150 ka (shading in Figure 7.4), similar as identified in the terrigenous OM *n*-alkane MAR.

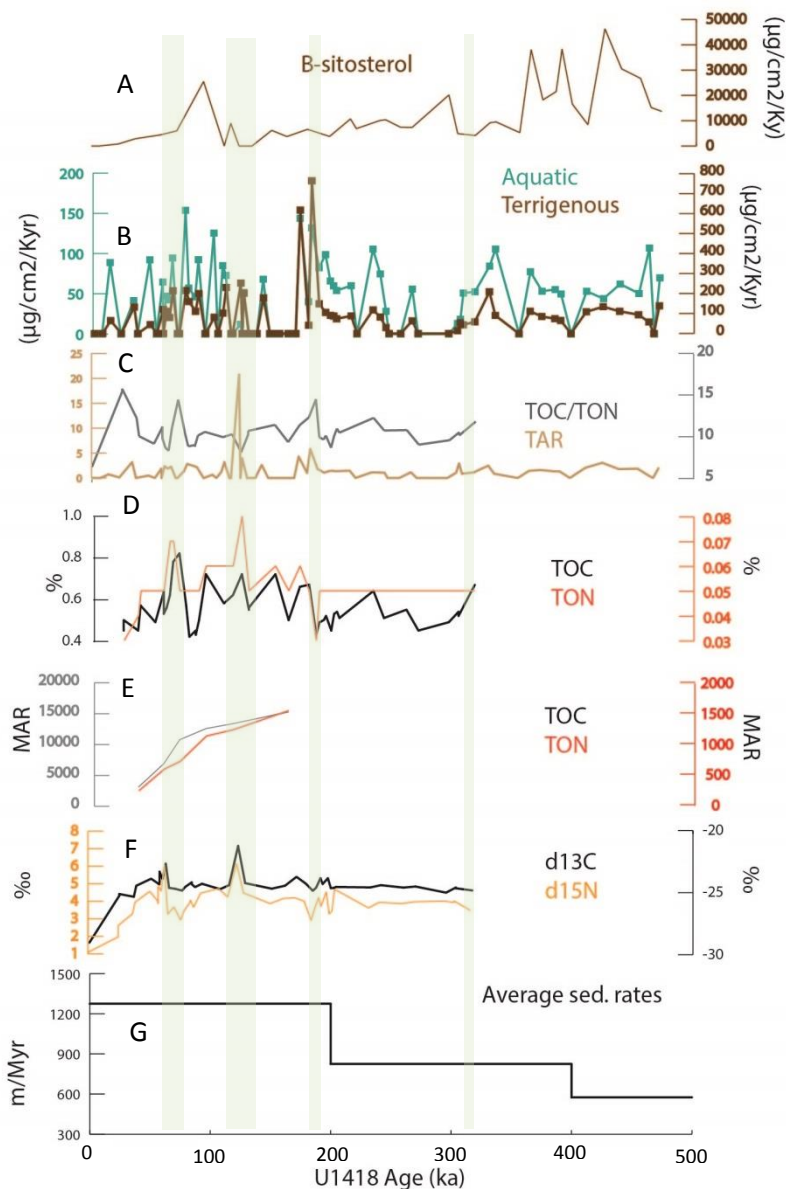


Figure 7.3: Terrigenous and aquatic organic matter source. (A) *B*-sitosterol MAR, (B) aquatic and terrigenous *n*-alkane MAR, (C) TOC/TON and TAR ratios, (D) TOC and TON (%) and (E) TOC and TON MAR, (F) $\delta^{13}\text{C}$ and $\delta^{15}\text{N}$ (‰) and (G) $\delta^{13}\text{C}$ and $\delta^{15}\text{N}$ MAR and (H) average sedimentation rates in m/Myr against U1418 Age (ka).

Increase in sedimentation rates at Site U1418 increase OM preservation in the ocean through rapid burial.

The newly generated sedimentation rate record (Dr. Hiro Asahi, pers. comm. Figure 7.1) coincides with a higher preservation of sterols in the sediment by rapid OM burial during the last 150 kyr. As alkenones are more resistant biomarkers from degradation than sterols and the alkenone MAR signal does not fluctuate according to sedimentation rates.

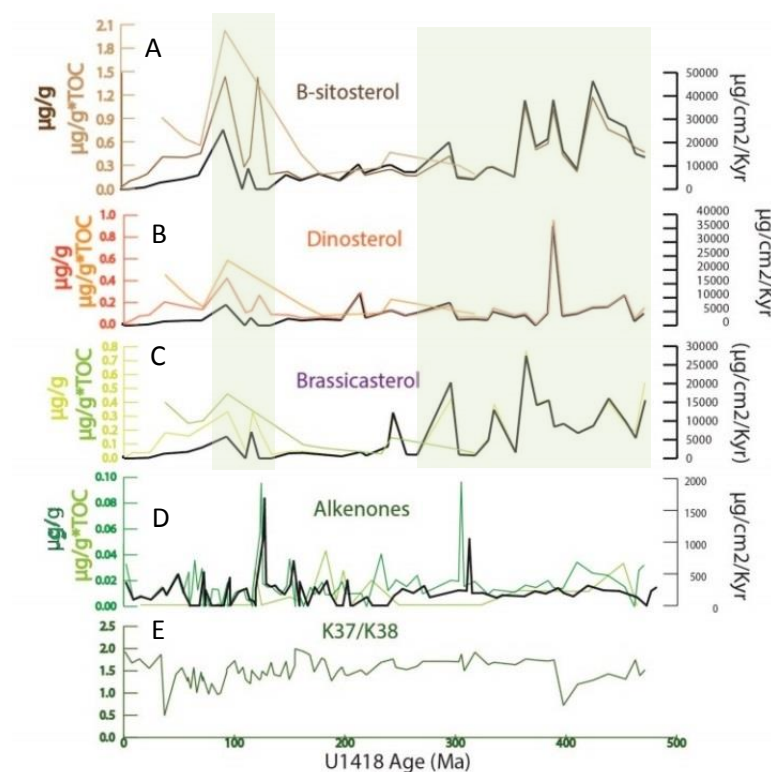


Figure 7.4: Marine productivity export proxies. (A) B-sitosterol in $\mu\text{g g}^{-1}$ (dark brown), $\mu\text{g g}^{-1} \text{TOC}^{-1}$ (light brown) and $\mu\text{g cm}^{-2} \text{kyr}^{-1}$ (black), (B) dinosterol in $\mu\text{g g}^{-1}$ (dark orange), $\mu\text{g g}^{-1} \text{TOC}^{-1}$ (light orange) and $\mu\text{g cm}^{-2} \text{kyr}^{-1}$ (black) (C) brassicasterol in $\mu\text{g g}^{-1}$ (yellow), $\mu\text{g g}^{-1} \text{TOC}^{-1}$ (green) and $\mu\text{g cm}^{-2} \text{kyr}^{-1}$ (black) (D) alkenones in $\mu\text{g g}^{-1}$ (dark green), $\mu\text{g g}^{-1} \text{TOC}^{-1}$ (light green) and $\mu\text{g cm}^{-2} \text{kyr}^{-1}$ (black) and (E) K_{37}/K_{38} alkenone ratio.

Due to changes in sedimentation rates, sterols at Site U1418 have also been adjusted to calculate the sterol mass accumulation rates (MAR) to avoid dilution of the productivity signal by effects of sedimentation rate changes (Figure 7.4, black). By comparing sterol abundances ($\mu\text{g g}^{-1}$) and sterol MAR ($\mu\text{g cm}^{-2} \text{kyr}^{-1}$) at Site

U1418, we observe no changes in sterol abundance with changing in sedimentation rates and therefore, no dilution in the alkenone abundance signal.

Marine productivity based on concentration of sterols increases when sedimentation rates increase from 500 to 300 kyr and from 150 to present (Figure 7.4). Marine productivity from sterols and marine n-alkanes is also high through MIS 12 to MIS 7 together with high β -sitosterol and is low during MIS 6 and increases again from late MIS 5 to the present. However, as terrigenous n-alkane MAR also show high values during the same time intervals it is difficult to interpret the marine or terrestrial origin of the marine n-alkane signal and β -sitosterol records. Similarly, the C/N ratio does not serve as a terrigenous/aquatic organic matter proxy (Walinsky *et al.*, 2009), as the low nitrogen content of the sediment samples were difficult to detect (See chapter 4).

High sedimentation rates and rapid sediment burial are essential for marine productivity export from sterols more than for n-alkanes being the alkenones the most resistant of the OM proxies. Alkenone MAR are present during glacial and interglacials but are highest during low $C_{37:4}$ and high TAR (Figure 7.5). The relationship between alkenone MAR and freshwater and SST proxies will be discussed in the next section.

7.3.1.4 Discussion of the last 500 kyr at Site U1418

During the last 500 kyr, Site U1418 oceanic conditions experience a gradual overall warming and freshening trend towards the present time. SST variability allows the identification of glacial-interglacial cycles, which show more clearly in the last 200 ka due to higher sedimentation rates and sample resolution. The glacial-interglacial cyclicity is best identified in the $\%C_{37:4}$ record (Figure 7.2).

There seems to be a correlation between higher terrigenous and aquatic organic matter from n-alkanes and higher freshwater from $C_{37:4}$ (Figure 7.5). This suggests that terrigenous n-alkanes are transported to Site U1418 by glacier runoff. Our terrigenous n-alkane MAR record shows higher concentrations than aquatic n-alkane MAR throughout the 500 kyr record particularly at MIS 5 and MIS 7 where the highest TAR values are recorded (20.7, 5.8 and 4.3; Figure 7.5). The

synchronous variability between terrigenous and aquatic *n*-alkanes could suggest the terrigenous origin of aquatic *n*-alkanes. It could also suggest the enhanced marine productivity at Site U1418 due to nutrient transport into Site U1418 increasing in situ marine productivity. The terrigenous origin of aquatic *n*-alkanes (could be from a lacustrine, fluvial source or from re-worked marine sediments on land) remain unclear. Instead, we conclude that terrigenous and marine *n*-alkanes, β -sitosterol, dinoflagellate, brassicasterol MAR increase seems to correlate with increases in marine OM input (higher TOC) and to increases in terrigenous OM input from the land to the ocean (Figure 7.3 and 7.4). We interpret *n*-alkane and sterols as indicators of OM preservation.

Maximum terrigenous and marine *n*-alkane values are registered during late MIS 7, before the biggest glaciation in the 500 kyr at MIS 6. Lam *et al.* (2013) observed higher marine productivity during the last deglaciation (14 ka) in the North Pacific. The last sample of our record is dated to 14.1 Kyr and does not represent particularly high aquatic organic matter (Figure 7.5). However, this is true for the deglaciation from MIS 6 through MIS 5e. During peak MIS 6 *n*-alkane are not present in the sediment and coccolithophore blooms occur in a similar intensity as across the 500 ka record (Figure 7.5). During MIS 5e *n*-alkane are highly dominated by terrigenous OM (Figure 7.5). The disappearance of *n*-alkanes from marine samples during MIS 6 could be explained by degradation of *n*-alkanes due to a very stratified water column ($C_{37:4}$ up to 25%). Alkenones are more resistant to degradation than *n*-alkanes and therefore the alkenone-derived records are still quantifiable.

Alkenone MAR do not show a connection to increases in terrigenous OM but seems to vary with $\delta^{13}C$ and $\delta^{15}N$ changes and decrease in $C_{37:4}$. The higher alkenone MAR in comparison with dinosterol and brassicasterol MAR could mean that coccolithophores are the main phytoplankton production in the GOA. The relationship between alkenone MAR and changes in $\delta^{13}C$ and $\delta^{15}N$ not seen between sterols and $\delta^{13}C$ and $\delta^{15}N$ suggest a closer relationship between coccolithophores and climate in the GOA than the records from other marine producers. However, the different long term variability between SST and alkenone

MAR does not suggest that the alkenone and climate linkages are permanent through time but occur at certain times (Section 7.4.1).

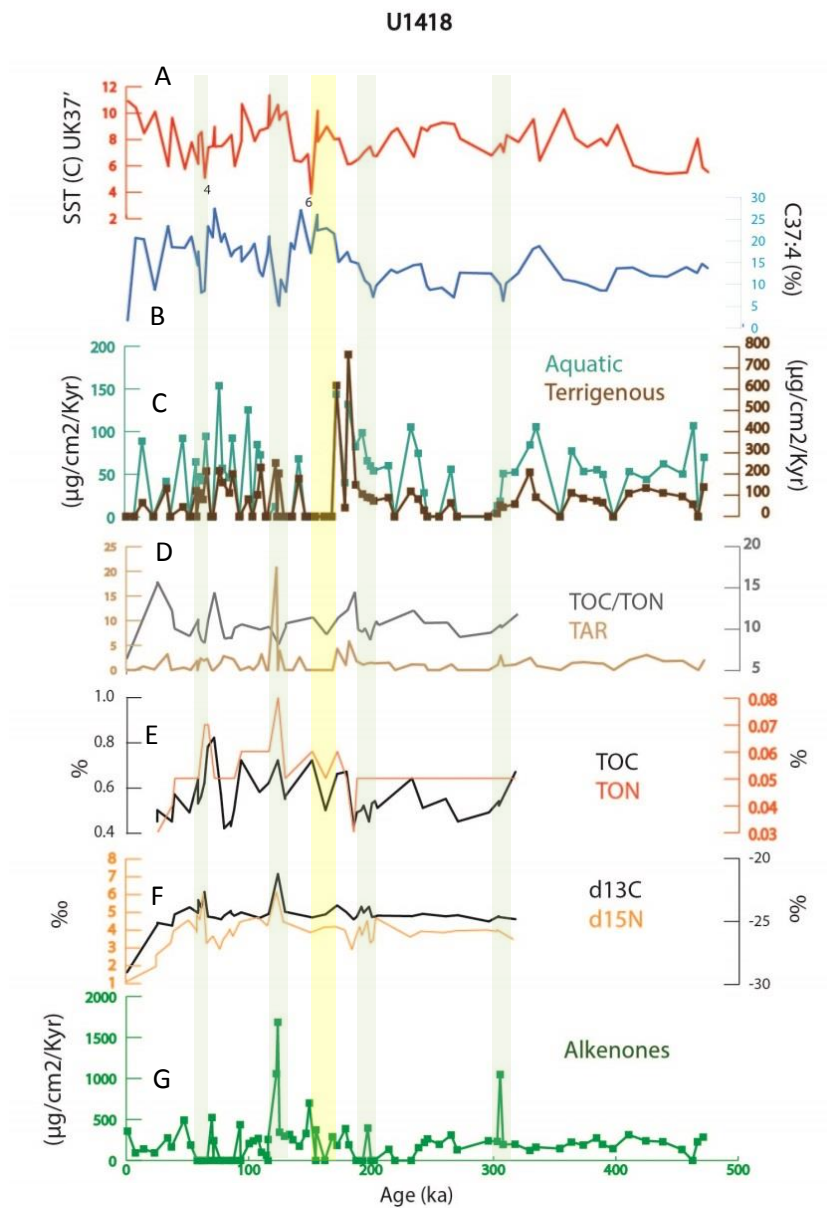


Figure 7.5: Main patterns Site U1418. (A) SST (°C); (B) %C_{37:4}; (C) terrigenous (brown) and aquatic (turquoise) n-alkane MAR; (D) TOC/TON (grey) and TAR (light brown); (E) %TOC (black) and %TON (orange); (F) ‰ δ¹³C (black) and ‰ δ¹⁵N (orange) and (G) alkenone MAR plotted against U1418 age (ka).

7.3.2 Climate of the Gulf of Alaska during the last 500 kyr (Comparison between U1418 and U1417)

SST reconstructions (Müller *et al.*, 1998) from site U1417 and U1418 have similar trends during the last 500 kyr with average SST difference of 0.2 °C, where Site U1418 is generally warmer than U1417 (Figure 7.6). However the difference between U1418 and U1417 SSTs lies within the SST calibration error of 1.5°C of Müller *et al.* (1998). $C_{37:4}$ values have a 3% difference between Site U1417 and U1418, where Site U1418 generally has higher values than U1417 during the last 500 kyr. Other, more detailed, comparisons between core Sites U1418 and U1417 are very difficult due to age model differences. Comparison between the two sites is also difficult due to lower sample recovery at U1417 than U1418 (see chapter 3). However, the % $C_{37:4}$ records from both sites correlate well, with higher freshwater input delivered during glacials (Figure 7.7).

SST variability is similar across the GOA, despite a higher meltwater reaching Site U1418 than Site U1417 due to its proximity to land. The average 3% difference in $C_{37:4}$ between the sites indicating variation in meltwater flux at each site does not have a significant influence on SST (average of 0.2 °C). Glacial meltwater reaches both U1418 and U1417 and both sites record IRD (Ellen Cowan, pers. comm.). This indicates icebergs and meltwater were transported up to 700 km offshore of the west coast of Alaska, as during the early Pleistocene (Chapter 5).

Despite the increase in $C_{37:4}$ at Site U1418 from 500 kyr towards the present, terrigenous *n*-alkane MAR do not show a long term increasing trend, however marine *n*-alkane MAR variability increases (Figure 7.5). This suggests that increases in terrestrial organic matter (and perhaps iron) at Site U1418 is not the major source stimulating coccolithophore productivity. TAR between U1418 and U1417 have similar values (Figure 7.7c), however marine productivity export (as shown by alkenones) is an average of 50 times lower at Site U1417 than U1418 (Figure 7.7f).

The presence of terrigenous OM from *n*-alkanes in U1418 and U1417 suggests that erosion of OM from land was delivered across the GOA, up to 700 km away from land into the ocean (Chapter 4). In terms of modern oceanographic setting, Site

U1417 is in a HNLC region and very sensitive to iron fertilization as a trigger for marine productivity export. Site U1418 is a LNHC region and marine productivity is limited by macronutrients (i.e. nitrate). During the last 500 kyr, alkenone MAR at Site U1418 is up to 100-200 times higher than at Site U1417, however data at Site U1417 is scarce.

Changes in the nutrients (TAR and $\delta^{15}\text{N}$) seem to reflect changes in nutrient utilization ($\delta^{13}\text{C}$ and $\delta^{15}\text{N}$ Figure 7.7c and e). These occur during low glacier meltwater delivery intervals during interglacials (Figure 7.7b). During these episodes coccolithophores respond abruptly to these nutrient conditions concurrent incorporating into their molecule structure heavier $\delta^{13}\text{C}$ and $\delta^{15}\text{N}$. Site U1417 TAR and TOC and TON $\delta^{13}\text{C}$ and $\delta^{15}\text{N}$ concentrations confirm that the ocean nutrient utilization extended in a wide area in the GOA and the two sites U1418 and U1417 shared a common ocean productivity history. The Site U1417 HNLC and Site U1418 LNHC regions are micro and macro-nutrient depleted (see Chapter 2). Both TAR and $\delta^{15}\text{N}$ can serve as nutrient input indicators. TAR can be associated with terrestrial OM input and $\delta^{15}\text{N}$ can be associated with advection of deep nitrogen storage into surface waters. The marine productivity export concentrations during peak interglacials could make evident the linkages between ice-sheet-ocean-marine productivity and nutrient input and test if previous studies from modern GOA (Chapter 2) can be applied for the last 500ka climate-ocean-ice sheet behaviour.

The coastal GOA is a LNHC region where macronutrients such nitrate are limiting marine productivity. Therefore, unlike Site U1417, increases in terrigenous micronutrient (i.e. iron) at Site U1418 do not transfer into increases in marine productivity. Nitrate is a source of $\delta^{15}\text{N}$ and abundant in the deep ocean (Chapter 2). Iron is typically transported by Aeolian dust but in the GOA there are different mechanisms proposed (Chapter 2). Increases in coccolithophores occur during interglacial maxima and glacier runoff minima suggesting a less stratified water column allowing some degree of water mixing in comparison with glacial water stratification. One of the mechanism proposed in the literature (Chapter 2) is the exposure and inundation of rock flour from glacial sediments during ice sheet

retreat and sea level increase as well as deep sediment mixing. Deep ocean nutrient availability in the surface ocean and marine phytoplankton increase during a ventilated ocean could have an impact on CO₂ degassing from the ocean into the atmosphere (Jaccard *et al.*, 2005).

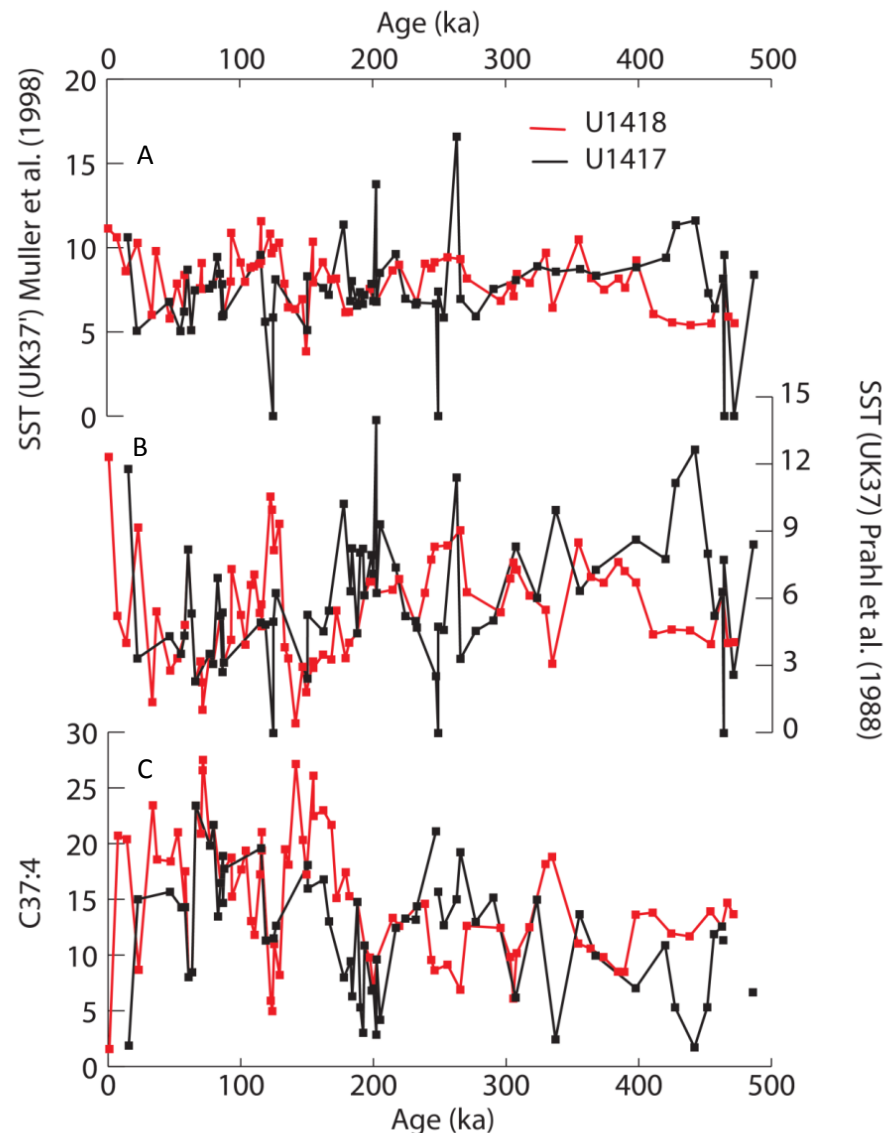


Figure 7.6: Site U1418 and U1417 SST and $C_{37:4}$ comparisons. (A) SST using the calibration from Müller *et al.* (1998) and (B) SST calculated using the calibration of PrahI *et al.* (1988) and (C) $C_{37:4}$ (%) at U1418 (red line) and U1417 (black line).

The non-responsive marine productivity to increases in terrestrial input into the ocean at Site U1418 is consistent with data from the Bering Sea, also influenced by

the Alaskan Coastal Current (Vaughn, 2015), where during glacials MIS 6 and MIS 4, marine productivity decreased synchronously with increased nitrate utilization and increase TAR. They interpreted this to be due to sea ice presence and restricted Alaskan Coastal Current influence, which agrees with our low $C_{37:4}$ concentrations: restrictive glacial meltwater and weaker ACC during MIS 4 and MIS 6.

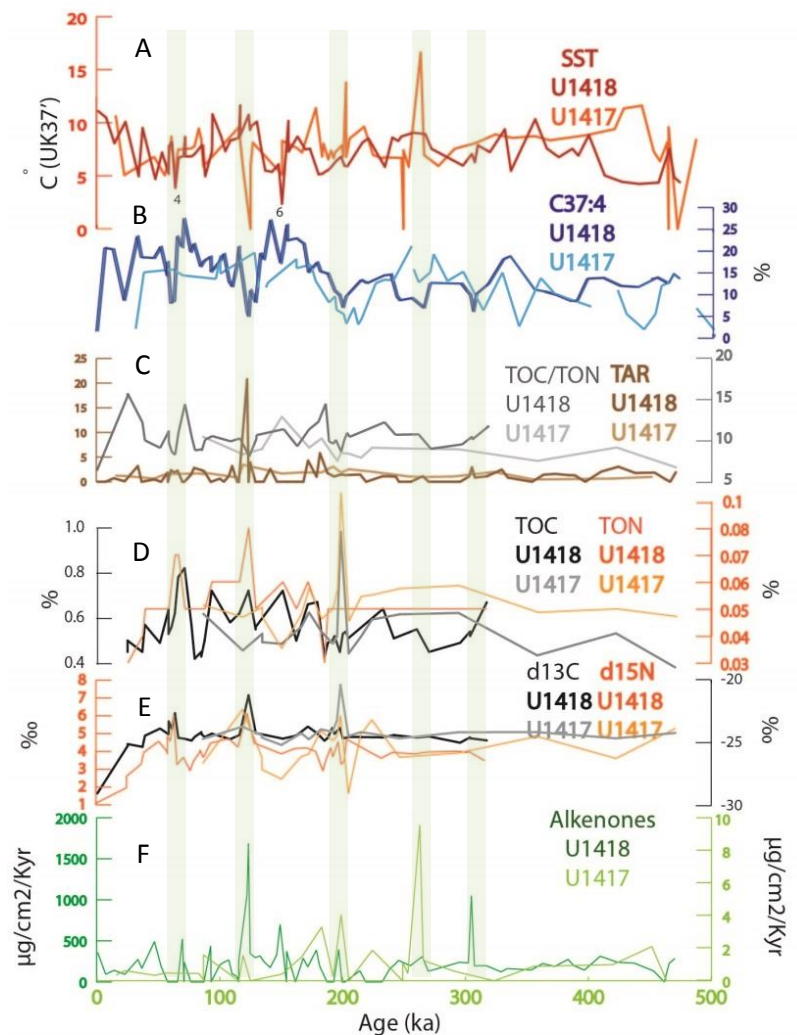


Figure 7.7: Site U1418 and U1417 comparison during the last 500 ka. (A) SST ($^{\circ}\text{C}$); (B) $\%C_{37:4}$; (C) TOC/TON (grey) and TAR (brown); (D) $\%TOC$ (black) and $\%TON$ (orange); (E) $\%_{\text{o}}\delta^{13}\text{C}$ (black) and $\%_{\text{o}}\delta^{15}\text{N}$ (orange) and (F) alkenone MAR plotted against age (ka). Dark colours correspond to Site U1418 data and light colours correspond to Site U1417.

During peak glacials, coccolithophore blooms thrive in an environment of restrictive nutrient input and water mixing. Blooms are restricted to a stratified environment that impacts the $\delta^{13}\text{C}$ and $\delta^{15}\text{N}$ with lighter compositions of the due to biomass preferentially up-taking the lighter isotope, similarly as explained in Chapter 6 during the iNHG. The lowest $\delta^{15}\text{N}$ values in our 500 ka record at Site U1418 coincides with zero alkenone MAR (Figure 7.7f) e.g. at 220 ka (MIS 7).

7.3.2.1 The last 200 Kyr in the GOA: High terrigenous and marine organic matter and isotopic excursions during late MIS 7 to MIS 5

As previously mentioned, the lack of TOC, TON, $\delta^{13}\text{C}$ and $\delta^{15}\text{N}$ data from 500 to 400 ka and a highest sedimentation rate during the last 200 Kyr, the last 200 kyr is a very interesting time interval to explore with our data. The next sections will focus on particularly well defined intervals and high sample resolution records within the last 200 kyr.

7.3.2.1.1 MIS 6

The coldest glacial climate during MIS 6 at Site U1418 is characterised by the highest $\text{C}_{37:4}$ of our 500 kyr record, with lighter isotopic $\delta^{13}\text{C}$ and $\delta^{15}\text{N}$ signatures and higher TOC and TON (Figure 7.5). Terrigenous *n*-alkane transition between the highest values during late MIS 7 to an absence of *n*-alkanes at 150 kyr during the coldest SST during MIS 6. Terrigenous *n*-alkanes increase again during late MIS 5e (Figure 7.5 and Figure 7.7). The climate proxies at Site U1418 during MIS 6 indicate a highly stratified ocean ($\text{C}_{37:4}$ up to 30%) where marine productivity (coccolithophores) can still thrive possibly due to some degree of macro-nutrient availability in coastal GOA. Increases in marine productivity export increases the TOC and TON composition of the marine sediment. Biomass productivity preferentially uptakes lighter isotopes from the surface ocean leading to a high $\delta^{13}\text{C}$ and $\delta^{15}\text{N}$ signature preserved in the sediment record. Similar environmental conditions seem to be replicated during MIS 4. As stated in the introduction of this chapter, marine productivity increases during glacial conditions have been suggested to cause atmospheric CO_2 decrease through carbon sequestration by biomass producing a shift in carbon storage from the atmosphere into the sediments. However, this marine productivity export and carbon sequestration is

suggested to have lower magnitude during glacials than during interglacials (e.g. MIS 5e) it is aided by the water column stratification and reduction of CO₂ degassing effect.

7.3.2.1.2 MIS 5e

After MIS 6 glacial maxima, SST increases (8°C to 10 °C) and TAR increase (up to 20) and lower C_{37:4} (up to 20% decrease) over the transition to MIS 5e marking the start of the deglaciation and Cordilleran Ice Sheet retreat recorded at Site U1418. Peaks in in TOC, TON, ‰ δ¹³C and ‰ δ¹⁵N are synchronous with coccolithophore productivity peaks at Site U1418 (Figure 7.5 and Figure 7.7). Site U1417 alkenone productivity peak at MIS 5e is also synchronous with an increase in δ¹³C and δ¹⁵N signature, although with slightly lower TOC and TON, low C_{37:4} and SST (Figure 7.5 and Figure 7.7).

The ocean conditions at Site U1418 and U1417 during MIS 5e are characterised by water mixing at both core Site U1417 and U1418 during a warm climate and increase the nutrient supply from the deep ocean into the surface and the nutrient OM supply from land to the ocean meeting both nutrient requirements of Site U1418 and U1417 to trigger marine productivity (Figure 7.7). This process seems to be repeated at each interglacial during the last 300 Kyr (if not during the last 500 Kyr, which we can't confirm due to the lack of isotopic data). Water mixing during interglacials and marine productivity associated with it suggests a marine productivity role in contributing to atmospheric CO₂ increase by deep ocean degassing.

During higher ocean ventilation (heavier δ¹³C and δ¹⁵N) during MIS 5e, coccolithophore productivity export increase, aided by increase in nutrient supply (increase in TAR and δ¹⁵N). Coccolithophores could be linked to atmospheric CO₂ changes at limited time intervals within glacial and interglacials and could help in driving the change in climate from cooling by atmospheric CO₂ drawdown during interglacials to warming by atmospheric CO₂ degassing during glacials. This is consistent with the finding of Pacific atmospheric CO₂ reconstructions and is contradictory to present atmosphere-ocean carbon exchange in the North Pacific,

where CO₂ drawdown through surface ocean productivity is not sufficient to cancel ocean degassing into the atmosphere at modern (Jaccard *et al.*, 2005).

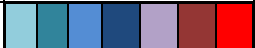
7.3.3 Climate of the subarctic Pacific Ocean during the last 500 kyr.

7.3.3.1 Climate drivers

According to Past Interglacials Working Group of PAGES (2015), MIS 5e, MIS 11c and MIS 9e interglacials are globally the warmest in the 500 Kyr record, with MIS 13a and MIS 7a and MIS 1 being the colder, in that order, in the north Pacific. Based on the highest SST of the interstadials, Site U1418 shows marine isotopic stages that can be arranged from warmer to colder in this order: MIS 5e, MIS 1, MIS 9e, MIS 7e, MIS 11c and MIS 13a (Table 7.1).

Table 7.1: Maximum SST for each interglacial at different cores from the North Pacific Ocean, modified from Past Interglacials Working Group of PAGES (2015) including the data sets of ODP 1020 (Herbert *et al.*, 2016), ODP 1012 (Liu *et al.*, 2005) and ODP 1146 (Herbert *et al.*, 2010). Colour-code from colder to warmer.

Latitude	Longitude	Site	1	5e	7c	7e	9e	11c	13a
58.77	144.49	IODP 1418	10.9	11.3	8.8	9.3	10.3	9.1	8.0
56.95	-147.13	IODP 1417		9.4	13.7	16.2	8.6	8.8	9.4
41.01	-126.43	ODP 1020	11.1	14.1	12.2	11.7	12.8	14.0	10.2
32.28	-118.40	ODP 1012	16.8	19.5	18.9	17.7	19.7	19.1	17.5
19.46	116.27	ODP 1146	26.5	27.3	26.6	26.3	27.3	26.8	26.1

From colder to warmer: 

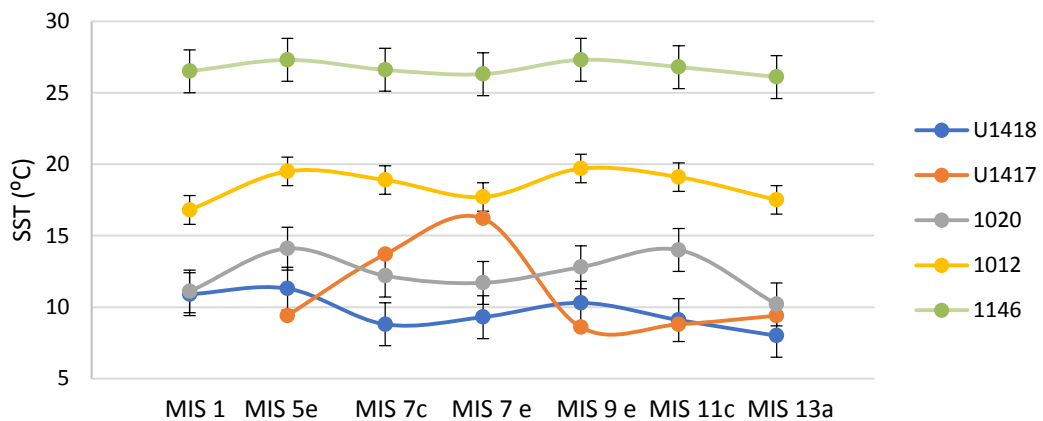


Figure 7.8: Comparison between the SST average values of interglacials represented in Table 7.1, with SST calibration error of 1 °C (Prahl *et al.*, 1988) at ODP 1012 and 1.5 °C

(Müller *et al.*, 1988) at ODP 1146, ODP 1020 and Site U1418. Site U1417 error bars are not included as being less reliable SST data.

The Past Interglacials Working Group of PAGES (2015) created a table to represent the warmer and colder stadials and interstadials during the last 500 kyr, reproduced and modified here (Table 7.1). This table is useful to identify the warmest interglacials but the use of the maximum single data point to determine the warming of an interglacial is not very accurate for SST. Table 7.1 includes the average of the warmest points where the data at Site U1418 and U1417 allow as our SST record is often very variable and the determination of the timing of the sub-stadials can be complicated. At Site U1418, MIS 5e is the warmest stage with an average SST of 11.3 °C, followed by MIS 1, with an average SST of 10.9 °C, MIS 7e with 9.3 °C and MIS 7c 8.8 °C. Average temperatures for MIS 9e, 11c or 13a at Site U1418 with such reliability as they are represented by a single point several degrees warmer than the data points around them. For the interstadials at Site U1417, due to the lower sample resolution of this site compared with Site U1418, there are not enough data points to average the highest SST data points and include a robust SST value in Table 7.1. Despite this, maximum interstadial SST values are included in Table 7.1 for guidance but caution has to be taken when using them to represent the glacial-interglacial history at Site U1417.

The closest site to U1418 is ODP 1020 in the North Pacific Ocean (latitude: 41.01, longitude: -126.43). ODP 1020 show similar trends to U1418 interglacial SSTs. ODP 1012 (latitude 32.28, longitude -118.40) and ODP 1146 (latitude 19.46, longitude 116.27) in the tropical Pacific are slightly different to the SST transition across stages observed in the North Pacific Ocean. Tropical Pacific SST register a relative warmer MIS 9e and colder MIS 11c than the interstadial transitions observed in the North Pacific SST stage evolution (Figure 7.8). Overall, there seem to be pairs of interstadials with similar SST relationships around the North Pacific: MIS 5e and MIS 9e, MIS 1 and MIS 13a, MIS 7c and MIS 11c (Figure 7.8). MIS 7e is slightly different from the other interstadials, intermediate between the coldest MIS 1 and MIS 13a and the warmer MIS 5e and MIS 9e, MIS 7c and MIS 11c (Figure 7.8).

MIS 11c is anomalously warm in ODP 1020 compared to our site U1418. The usual 2°C SST gradient between these two sites became 5°C for this time period (Figure 7.8). MIS 1 was different in the Gulf of Alaska than in the rest of the Pacific Ocean (Figure 7.8). All of the Pacific records in Figure 7.8 show a cooling transition from MIS 5e to MIS 1, most of them show a more dramatic cooling but in the GOA. This suggests that the North Pacific sites located south from the subarctic Pacific cooled since the previous interglacial but the GOA shares similar climate with MIS 5e during MIS 1.

MIS 5e has been considered the warmest interglacial and the closest analogue to the recent climate due to its high atmospheric CO₂. The SST reconstructions from the majority of sites across the North Pacific Ocean presented here (Table 1, Figure 7.8) agree in registering highest SST during MIS 5e over the last 500 kyr (U1418), or share the highest value with MIS 9e (ODP 1146) and MIS 11c (ODP 1020) with the exception of ODP 1012, where MIS 5e is the second warmest interstadial after MIS 9e. The reconstructions from the GOA also support this statement, having a MIS 5e plateau with the highest SST of 11.4 °C (Site U1418) together with a peak in IRD (Site U1417) and freshwater minima due to deglaciation of the Cordilleran Ice Sheet (Site U1418, Figures 7.2 and 7.4).

In Figure 7.9 we represent subarctic SST records (from U1418 and ODP 882) compared with July insolation at 65°N. The SST variability between glacial-interglacial cycles at Site U1418 and ODP 882 shows a reasonable relationship with insolation at 65°N, with more pronounced glacials and interglacials during periods with higher insolation variability through MIS 7 to MIS 4. This relationship between a more intense climate, with high amplitude variability, and an increase in insolation variability suggests that insolation plays a vital role in glacial-interglacial variability in the subarctic Pacific. Insolation variability increases during the MIS 5e warm interglacial alongside increasing Antarctic CO₂ concentrations (Enggleston *et al.*, 2016). It is expected from a higher insolation that the climate would be warmer. However, internal feedback mechanisms have been previously proposed as important driver of glacial-interglacial variability as insolation alone cannot explain the full climate response (Abe-Ouchi *et al.*, 2013).

Carbon cycle and specifically changes in atmospheric CO₂ has been suggested to contribute to the 100 kyr glacial-interglacial cycles (Abe-Ouchi *et al.*, 2013). This chapter results suggest that climate-ocean-marine productivity linkages control atmospheric CO₂ variability that, combined with summer insolation variability are responsible for the glacial-interglacial variability seen in the GOA.

7.3.3.2 *Establishment of modern subarctic Pacific oceanography*

Modern annual sea surface temperature for the GOA is 7 to 9°C (Clayson *et al.*, 2016) and temperatures are warmer towards the east and colder towards the west. However, this longitudinal SST difference across the subarctic Pacific is not clearly identified through most of the SST reconstructions from U1418 and ODP 882 shown in Figure 7.9. SST reconstructions from Site U1418 and U1417 are at different sample resolution and age model resolution so it is difficult to make interpretations of the evolution of SST between these two sites during the last 500 kyr with confidence.

At modern, the SST gradient across the subarctic Pacific shows a pattern of 1 to 2 °C colder west and warmer east during September. This evolves to 3 to 4 °C colder west and warmer east during December (Chapter 2). The September-December annual average SST difference of 1 to 2°C is bigger than the SST calibration error of Müller *et al.* (1998) of 1.5 °C (Chapter 2). Additionally, age model between Site U1418 and ODP 882 can differ and therefore here SSTs are not discussed between glacial and interglacials but across the 500 ka. Despite of this, comparison between Site U1418 and ODP 882 SST reconstructions can help interpreting the timing of the establishment of modern ocean configuration across the subarctic Pacific Ocean but interpretations in this chapter need to be taken cautiously.

It has been suggested that the subtropical North Pacific Ocean was warmer (CLIMAP, 1976) and colder (Lee and Slowey, 1999) during the LGM than the present. MARGO synthesis of LGM SSTs contained only one data point from the GOA (Anan and Hargreaves, 2013; Cauzet *et al.*, 2008) and the contribution of the GOA into the LGM knowledge is very limited. Otto-Bliesner *et al.* (2005) attributes a LGM-PI (pre-industrial) warming anomaly between 0.5 and 1.5°C over the GOA and between 1.5 to 4°C over western subarctic Pacific.

According to CLIMAP (1984), the Gulf of Alaska SST was around 11 °C closer to land and around 9°C further from land during the LGM. Our U1418 two data points that are close to the LGM are 14.17 Kyr and 23.06 Kyr with temperature reconstructions of 8.5 and 10.1 °C, respectively. For U1417, SST reconstructions are made at 15.64 and 22.49 Kyr, with values of 10.5 and 5.0°C, respectively. If we average the limited GOA “LGM” two data values, SST is 9.3°C closer to the land and 7.75 °C further away from the Alaskan Coast. SST reconstructions from U1417 and U1418 of approximate LGM age are around 2°C colder from CLIMAP reconstructions in the GOA. The average values during the LGM based on data points in U1418 and U1417 SST have similar values to the modern SST values. The LGM-modern anomaly based on data from U1418 and U1417 is close to 0. This adds an additional data constraint to the debate between positive or negative LGM SST anomaly in the GOA. This interpretation can be added to the MARGO data coverage of sea surface anomaly for the LGM (MARGO, 2009). However, additional new data from the GOA with better sample resolution and age control is needed to robustly assess the nature of SST changes from the LGM to present.

According to Figure 7.9, modern ocean conditions were established during the LGM (24.3 Kyr), as this is when SST reconstructions from Site U1418 and ODP 882 SST clearly show a 1 to 2°C warmer east than west subarctic Pacific SST. However, MIS 4 is around 1-2 °C warmer in the east than west subarctic Pacific. From MIS 5 until MIS 11 west SST maximum values are around 3°C warmer than SST in the east subarctic Pacific. During MIS 6 and MIS 12 glacial SST values appear similar across the subarctic Pacific.

During most glacial periods, the ocean temperature dynamics across the subarctic Pacific appears to be similar to present, with a warmer northeast than northwest Pacific. The development of ocean temperature dynamics patterns similar to modern conditions during glacial periods seems to be linked with the Cordilleran Ice Sheet expansion and retreat (Figure 7.9). Ocean temperature dynamics during the present interglacial seems to be anomalous in comparison with previous interglacial periods across the subpolar North Pacific, where east subarctic Pacific

is colder than west subarctic Pacific. The present climate across the subarctic Pacific did not show the recovery from previous colder conditions seen in transitions from earlier glacial to interglacial periods (i.e. from glaciations before the LGM). This change in pattern seems to have developed since MIS 4 (71.5 Kyr), where ODP 882 cools dramatically and remains cool with a SST average of 6.8 °C compared to the value of 8°C reconstructed from U1418 (Figure 7.9). The LGM difference across the subarctic Pacific shown in Figure 7.9 does not agree with ocean SST reconstructions from Otto-Bliesner *et al.* (2005), where models show a warmer west than east subarctic Pacific.

During the last 500 kyr, SST across the subarctic Pacific (Site U1418 and ODP 882 comparisons) show 1 to 4°C colder SST in east than west subarctic Pacific during interglacials and 1 to 2°C colder SST in east than west subarctic Pacific during glacials. During 150 ka, a shift to 1°C warmer SST in east than west Pacific during glacials is observable (Figure 7.9). SST comparisons across glacials and interglacials could indicate dramatic changes in ocean temperature dynamics. Still, ODP 882 and U1418 SST share similar patterns and absolute values (Figure 7.9) suggesting a probable connection between the climate at both sites through the extension of the ocean circulation influencing both sites. Modern ocean circulation across the North Pacific is characterised by ACC flowing to the Bering Sea then it is transformed into the Kamchatka current, which returns to the GOA via the North Pacific Current (Chapter 2). The ACC in the GOA is an average of 0.8°C colder than the derivative oceanic currents in the Northwest Pacific. Although 0.8°C is within the error of our SST proxy, it is expected that a site closer to the Cordilleran Ice Sheet would register colder SSTs. The question raises of the origin of this heat in a subpolar climate with glacial influence.

SST conditions during glacials are similar to modern winter SSTs across the subarctic Pacific Ocean (Chapter 2). However, based on modern oceanographic observations, seasonal SST differences across the subarctic Pacific do not record colder east than west Pacific SST as reconstructed during past interglacials, even during lower SST differences across the Pacific during modern summer (Pickart *et al.*, 2009, Chapter 2). However, during decadal time series, negative phases of PDO

show a cooling SST in east and warming in west subarctic Pacific (Chapter 2). Positive phases of the PDO show a similar modern-like ocean configuration with warming east than west subarctic Pacific. Lower latitudinal SST gradient across the Pacific and North Atlantic Oceans suggests lower AMOC strength during MIS 5e (Past Interglacials Working Group of PAGES, 2015). These mechanisms explain similar SSTs in climatic models of Otto-Bliesner *et al.* (2005), during the LGM and mid-Holocene. Site U1418 and ODP 882 data suggest increased longitudinal SST variability across the subarctic Pacific during interglacials than during glacials, which is consistent with negative PDO anomalies (Chapter 2). Therefore, we suggest that over the last 150 kyr, the climate in the North Pacific during glacial cycles was positive PDO-like and during interglacials climate conditions shifted to a more negative PDO-like North Pacific.

Negative PDO is characterised by positive SST anomalies in central North Pacific and negative SST in the east equatorial Pacific. Positive PDO produces the opposite trends. Shifts from positive to negative PDO reverse surface wind stress with an anticyclonic nature during negative PDO and cyclonic nature during positive PDO (Lead and Evans, 2011, Chapter 2). Surface wind during positive PDO phases blows off the south coast of Alaska to the GOA leading to a cooling of GOA surface waters. During a negative PDO phase, in the west subarctic Pacific surface winds have a northwest direction bringing warmer waters in the west than in the east subarctic Pacific. During a positive PDO phase, surface winds blow in a northerly direction off of the coast of California to the GOA bringing warmer waters to the GOA and bringing cold water to the west subarctic Pacific. Shifts between negative and positive PDO can generate SST differences in the GOA of 1°C and to the west subarctic Pacific of up to 1.4 °C.

Tree rings, corals and sedimentology have been used as PDO variability proxies (Mantua and Hare, 2002; Benson *et al.*, 2003; Kirby *et al.*, 2010; Newman *et al.*, 2015) during the Holocene. However, the combination of these proxies has led to a disparity in PDO reconstructions and has put into evidence the complexity of the PDO linkages and dynamics (e.g. Mantua and Hare, 2002). Despite this, prevalence

of warm SST reconstructions has been suggested to show positive PDO phase state during the early Pliocene in the eastern California upwelling regions (Dekens *et al.*,

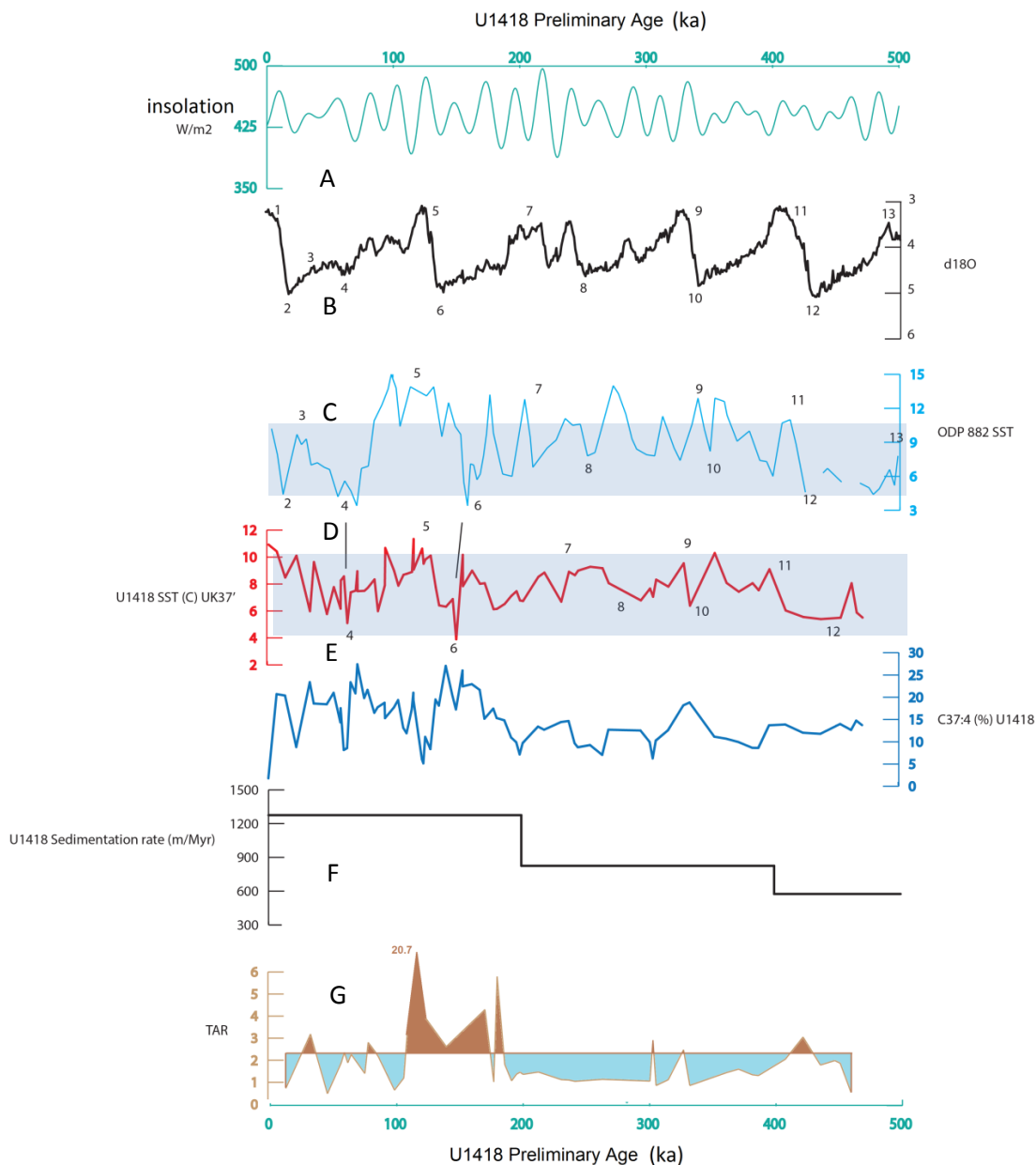


Figure 7.9: July insolation at 65 °N compared to U1418 main patterns. (A) Mid-month extra-terrestrial insolation 65 °N for July reconstruction (Berger and Loutre, 1999)(W/m²), (B) LR04 benthic stack (Lisiecki and Raymo, 2005), (C) U1418 SST from UK₃₇', (D) U1418 C_{37:4}, (E) U1418 shipboard sedimentation rates (m/Myr) and (F) U1418 TAR vs. U1418 preliminary age (ka). Blue shading delimits SST from 4 to 10°C. Numbers on (b) and (c) indicate MIS.

2007). Similarly, we hypothesise North Pacific regional SST anomalies linked with PDO changes during glacial and interglacial cycles during the last 500 kyr.

Higher SST variability at ODP 882 than U1418 between glacials and interglacials is expected due to its location. ODP 882 is located relatively far from the Cordilleran Ice Sheet protecting this region from the cold terrigenous conditions allowing warm surface currents from the south to warm the region. However, it can also be influenced by arctic currents travelling southwards. Lower SST variability in the Northeast Pacific could be related to a greater influence of the Cordilleran Ice Sheet on the Gulf of Alaska oceanography from glacial meltwater flux plus the confined nature of the GOA surrounded by Alaska coast at east and north acting as like a shield from currents reaching the GOA only by west or south.

7.3.3.3 Pacific and Atlantic teleconnections and implications for the climate of the GOA during the last 500 Kyr.

Positive PDO phases are linked with negative NAO and positive AO phases. Negative PDO phases are linked with positive NAO and negative AO phases. Similarly, El Niño is linked to positive PDO phases and La Niña with negative PDO phases (Chapter 2). Stronger atmospheric circulation in the North Pacific (positive PDO) is translated into weaker atmospheric circulation in the North Atlantic (negative NAO) and vice versa. Positive AO extends cold and dry arctic winds to Scandinavian latitudes over Europe but produces weaker wind strength over northern Alaska and the Bering Sea. Negative AO weakens wind strengths over Greenland and increases wind strength over the subarctic Pacific drying and cooling the subarctic Pacific.

Negative PDO and hence, positive NAO then could translate into higher precipitation over the GOA (Chapter 2), which could increase glaciation over mountain ranges of coastal Alaska. Furthermore, positive PDO has been also associated with increase in upwelling in Prince William Sound and an increase in marine productivity (Harwell *et al.*, 2010). As discussed above, GOA data shows increases in marine productivity during glacials over the last 500 kyr. These teleconnections between north Atlantic and North Pacific are decisive to link drier

glacial with wetter interglacial climate which is repeated cyclically. It also explains the anti-phase characteristics between Pacific and Atlantic climate.

7.4 Future climate predictions in GOA based on the past reconstructions

After analysing the climate of the subarctic Pacific Ocean during the last 500 kyr, we observe that the current climate in the subarctic Pacific Ocean, despite being in an interglacial is still in a “glacial-like” state with a positive PDO dominant north Pacific climate since the LGM or even since MIS 4. The predominance of a negative PDO-like climate over the last 500kyr would have driven an increase in glaciation over the last 500yr, as the glacial-interglacial evolution in the GOA shows. This would have converted the GOA into a carbon sink, removing CO₂ from the atmospheric over centuries to millennia.

The glacial-like present climate with an increase in marine phytoplankton productivity will continue to drawdown atmospheric CO₂. This may be partially offsetting anthropogenic atmospheric CO₂ increases. We suggest that natural variability would tend to cool the east and warm the west subarctic Pacific by weakening atmospheric circulation over the Pacific and strengthening atmospheric circulation over the North Atlantic, turning the climate into a negative PDO-like climate. Changes in atmospheric circulation associated with a negative PDO would change precipitation patterns across the Pacific and Atlantic and convert the GOA into a source of CO₂ degassing into the atmosphere.

7.5 Conclusions

Site U1418 glacial-interglacial cycles through the last 500 kyr do not show the typical saw-tooth shape seen in the LR04 benthic stack record. Although the LR04 benthic stack is a global record of ice volume changes, it contains a heavily dominated North Atlantic deep ocean signal. Site U1418 shows marine isotopic stages that can be arranged from warmer to colder in this order: MIS 5e, MIS 1, MIS 9e, MIS 7e, MIS 11c and MIS 13a (Table 1). The most extreme stadials are MIS 6 and MIS 4 based on %C_{37:4} glacial meltwater reconstructions.

Glacials in the GOA are characterised by cooler SST, higher meltwater, lower but still present marine productivity and generally lower terrigenous OM from land than interglacials. These conditions lead to strong ocean stratification in the GOA during glacials and a regional atmospheric CO₂ drawdown to the ocean by phytoplankton productivity. The environment in the GOA during interglacials was characterised by a better ventilated GOA where the CO₂ degassing from the ocean to the atmosphere exceeds the high marine productivity export to the GOA sediments. Regional atmospheric CO₂ and marine productivity uptake or degassing could be a contributor for global atmospheric CO₂ changes during glacial and interglacial time periods.

Site U1418 show a very similar glacial interglacial pattern to ODP Site 882 in the west subarctic Pacific over the last 500 kyr. Other North Pacific records also show similar trends over the last 500 kyr (ODP 1020, ODP 1012 and ODP 1146). This supports a link between ocean circulation in the GOA and the west subarctic Pacific. During glacials and interglacials before 150 ka, the eastern subarctic North Pacific exhibits cooler SST than the west, with an atmospheric and ocean configuration similar to negative PDO phases. Phases in the PDO also have global teleconnections to positive NAO, negative AO and La Niña. The opposite North Pacific east-west SST gradient occurs during glacials during the last 150 ka, similar to present-time positive PDO-like phases, which are linked to negative NAO and positive AO and El Niño. ODP 882 is characterised by higher SST variability through glacial and interglacial cycles compared to U1418. This is likely to be caused by the open ocean in the west compared to the GOA location.

However, for most of the last 500 kyr period, SST reconstructions were an average of 0.8°C colder in the east than west subarctic Pacific (7.9 °C compared to 8.7 °C). The dominance of negative PDO-like climate during much of this period is most likely responsible for the increase in Cordilleran Ice Sheet glaciation over the last 500 kyr.

Site U1418 lies under the influence of the ACC at present and is a LNHC region. It is situated in the North Pacific and presents a warmer annual SST compared to the west (ODP 882). However, present SST across the subarctic Pacific compared to its

climate over the last 500 kyr, presents some similarities during glacials and differences during interglacials. The establishment of modern ocean temperature dynamics in the Northern Pacific is suggested to have started since the LGM and possibly since MIS 4.

From the LGM (or perhaps event MIS 4) the climate regime in the GOA changed from a predominantly negative PDO-like state to a predominantly positive PDO-like state. This study cannot explain how the change occurred due to lack of data. However, future climate can be predicted over the next decades through analogies to the past climate regimes over the North Pacific. The climate in the North Pacific could reverse back to a more negative PDO-like climate in the future, similar to most other interglacials through the last 500 kyr or continue in a more positive PDO-like phase as at present. If the climate in the North Pacific changes back to negative PDO-like phase, the Cordilleran Ice Sheet extent would most likely increase. Ocean temperature dynamics changes in the GOA could also lead to a net increase in carbon supply to the atmosphere through increased CO₂ outgassing and reduced marine phytoplankton productivity CO₂ drawdown. This would contribute to a net increase in atmospheric CO₂ and, hence contribute to the current anthropogenic global warming. This could also have impacts on global circulation patterns due to climate teleconnections. If current climatic pattern in the GOA continues, the Cordilleran Ice Sheet might be reduced even further, with continued atmospheric CO₂ absorption in the ocean in the GOA.

Chapter 8: Conclusions and Future work

8.1 Conclusions

8.1.1. RQ1: What is the magnitude and timing of surface ocean changes during the Pliocene and early Pleistocene, and what impact do they have on ice sheet development in the GOA? *Chapter 5*

The GOA experiences a 10°C SST variability during the Pliocene and Pleistocene similarly to the modern day seasonal SST variability. Maximum and minimum SST values reconstructed for the Pliocene and Pleistocene are 3.9 to 12.4 °C and 4.4 to 13.6 °C, respectively. Pliocene average SST is 8°C and Pleistocene SST average is 8.9°C. There is a marked shift to warmer SST values across the Plio-Pleistocene boundary during 2.8 and 2.69 Ma. This warming took place during the development of the Cordilleran Ice Sheet as part of the global event of the Northern Hemisphere Glaciation. Our records suggest that during the Pliocene, the Cordilleran Ice Sheet was absent or relatively small with the absence of IRD at Site U1417 and $C_{37:4}$ lower than 5% interpreted as limited fresh and cold water input from a riverine source. During this time the increase in terrigenous OM in relation to aquatic OM was very high and synchronous with diatom valve MAR at Site U1417. We hypothesise that siliciclastic acid macronutrient was delivered to Site U1417 possibly by Alaska rivers, increasing diatom productivity. After the first appearance of IRD at 2.8 Ma, the $C_{37:4}$ often exceeds the 5% value and is interpreted as representing development of tidewater glaciers and influx of glacier meltwater to the GOA.

The onset and intensification of glaciation in the St. Elias range of the GOA occurred in two steps. Firstly, at 3 Ma, a decrease in terrestrial/aquatic organic matter is suggestive of increased land ice coverage, and occurs with an increase in $\%C_{37:4}$ that we interpret as an increase in freshwater input into the ocean, likely from glacial meltwater. Secondly, at 2.8 Ma the appearance of IRD suggests the development of tidewater glaciers in the Gulf of Alaska. From 2.8-2.4 Ma, we hypothesise that the intensification of the glaciation in GOA occurred due to the

high efficiency of the ice-ocean-climate coupling where warm sea surface temperatures increased the precipitation as snow over land, which in turn led to increased freshwater delivery from glacier meltwater. Higher snowfall led to a growing Cordilleran Ice Sheet, and bedrock erosion allowed the delivery of IRD into the ocean (and an overall increase in sedimentation rates) during the Pleistocene.

Tropical east and mid latitude east and west Pacific from the literature analysed in this thesis (OPD 846, ODP 1010, ODP 1021, ODP 1208) register a long term cooling trend through the Pliocene and early Pleistocene. This is, however, not the case in the northernmost west and east North Pacific (ODP 882 and Site U1417, respectively). ODP 882 and Site U1417 SST trends through the Pliocene show a cooling trend and warmer SST during the early Pleistocene with no long term trends. Modern northwest Pacific is, however, colder than Northeast Pacific while during the Pliocene and early Pleistocene ODP 882 registered 2 to 4 °C warmer SST than Site U1417. The unusual SST shift during the NHG is most likely linked to changes in the Aleutian Low pressure system and enhanced Alaska gyre oceanography and heat transport to the GOA. The growth of the Cordilleran Ice Sheet during the NHG could be explained by tectonic changes in the GOA, such as the St. Elias range uplift and orographic precipitation associated.

Site U1417 average SST are 1°C colder than the modern annual mean (~7°C). The modern SST range across the subarctic Pacific shows the east 1°C warmer than the west. The east-west North Pacific modern SST relationship establishment will be further discussed in RQ 3.

8.1.2 RQ2: Did productivity change in the GOA during the Pliocene and early Pleistocene, and how does it relate to the timing of climate changes, terrestrial input into the ocean, and circulation changes? *Chapter 6.*

Marine productivity changed during the Pliocene and Pleistocene during different stages. Diatom valves are present and abundant but productivity from sterols and alkenone abundance is low during diatom valve peak intervals from 4 to 2.8 Ma. Our records then suggest that during the 4 to 2.8 Ma period, the GOA had a highly ventilated ocean and the increase in terrigenous OM to the surface ocean triggered

marine productivity from diatoms, however the oxygenated ocean regime prevented OM preservation of sterols. After the onset of the Cordilleran Ice Sheet glaciation, the water column regime became stratified due to an increase in freshwater during the Plio-Pleistocene transition. From 2.8 to 1.7 Ma, diatom valves disappear completely from the record and marine productivity is dominated by alkenone and sterols, in that order. Alkenones are an order of magnitude more abundant than sterol MAR through the Pliocene and early Pleistocene. We suggest that sterols reflect OM preservation rather than marine productivity.

Alkenones are the most responsive biomarker from phytoplankton to track ocean changes in the GOA and respond rapidly to an increase in micronutrients from 2.8 to 1.7 Ma at Site U1417, as well as being a very resistant to degradation. These results agree with the literature in that the GOA is a high nutrient low chlorophyll region (HNLC) and limiting micronutrients such as iron are the trigger for productivity peaks. During periods with greater water stratification (2.7 to 2.4 Ma) due to highest rates in IRD and glacier meltwater input, coccolithophore blooms associated with the increase in terrigenous OM impacted the C and N isotope signal of the OM. This is caused by the preferential uptake of lighter C and N isotopes by the biomass. The stratification of the water column and the preferential lighter C and N intake by phytoplankton might have played a role in decreasing atmospheric CO₂ and perpetuate the glaciation during the early Pleistocene.

8.1.3 RQ3: What is the response of the GOA to the glacial-interglacial cycles of the last 500 kyr? *Chapter 7*

The GOA at Site U1418 registers glacial-interglacial cycles with the approximate cyclicity of 100 Kyr. The intensity of these glacial-interglacial cycles and the abundance of C_{37:4} increase towards the present. In the last 500 Kyr the glacial – interglacial cycles from MIS 12 to MIS 1 can be identified. However, due to higher sedimentation rates at Site U1418, the last 200 Kyr (MIS6 to MIS1) can be investigated at greater resolution. MIS 6 is registered as the coldest glacial stage and MIS 5e is the warmest interglacial. Marine isotopic interstadials can be arranged from warmer to colder as follows: MIS 5e, MIS 1, MIS 9e, MIS 7e, MIS 11c

and MIS 13a. This order is similar to other sites in the North Pacific. Insolation varies similarly to glacial-interglacial intensities at Site U1418.

Marine productivity from coccolithophores in the GOA during the last 500 kyr increased during interglacials at Site U1418. During glacials (e.g. MIS 6), Site U1418 SSTs decreased ($\sim 8^{\circ}\text{C}$ between peak MIS 6 to MIS 5e) and $C_{37:4}$ decreased up to 20% and TAR, TON and $\delta^{15}\text{N}$ are close to the average values during the last 500 kyr. Alkenone MAR show increases in concentrations of up to $700 \mu\text{g cm}^{-2} \text{ kyr}^{-1}$. These records suggest a highly stratified GOA and an increase in Cordilleran Ice Sheet glaciation which stills support marine productivity through continued delivery of nutrients.

During peak interglacials (e.g. MIS 5e) we observe up to 20% lower $C_{37:4}$, up to 1000 times increase in alkenone MAR, 0.02% TON increase, $\sim 3\text{‰}$ increase in $\delta^{13}\text{C}$ and 2‰ increase in $\delta^{15}\text{N}$ (compared with MIS 6). We suggest that during the retreat of the Cordilleran Ice Sheet and decrease in glacier meltwater, the stratified water column during the earlier glacial stage relaxes and nutrients become available in the surface water triggering productivity at Site U1418, a LNHC region and macro-nutrient deprived. Marine productivity blooms could have played a role in atmospheric CO_2 drawdown and contribute to the start of the following glacial stage.

Chapter 7 also discovered an evolution from Chapter 5 Plio-Pleistocene climate. SST range (4 to 11.5°C) and average (8°C) at Site U1418 during the last 500 kyr are comparable with modern SSTs and with average Pliocene SST at Site U1417. Since the late Pleistocene, the GOA registers a 0.6°C cooling at Site U1417, although data for the last 500 kyr at Site U1417 are limited. $C_{37:4}$ abundance is similar between the early and late Pleistocene at Site U1417. During the last 500 kyr TAR range and alkenone MAR are half compared to the Pliocene and late Pleistocene. TOC and TON ranges show increases in TON concentrations and TOC concentrations during the last 500 kyr at Site U1417 as well as heavier $\delta^{13}\text{C}$ and $\delta^{15}\text{N}$ isotopic compositions.

During the last 500 kyr Site U1418 was 0.5°C warmer, 5% higher $C_{37:4}$, double TAR, similar TON and TOC range and $\delta^{13}\text{C}$ although around 1‰ smaller $\delta^{15}\text{N}$ isotope

range than at Site U1417. Alkenone MAR are 200 times higher at U1418 than at U1417.

Following from RQ1, the establishment colder SST values reconstructed from ODP 882 in comparison to the GOA is clear from MIS 4 to MIS 1, and possibly from as early as MIS 6. We attribute this change to an enhanced atmospheric circulation and the North Pacific current warming the GOA through the Alaska Coastal Current, which travels to the Bering Sea and the Kamchatka Current exiting the Bering Sea towards ODP 882.

Appendix

A.1: Alkenone derived SST, %C_{37:4} and alkenone abundances Site U1417

Sample	Depth (m) CCSF-A	Age (ka)	C _{37:4} (%)	U ^K ₃₇	U ^K _{37'}	SST (U ^K _{37'}) Müller <i>et al.</i> , 1998	SST (U ^K _{37'}) Prahll <i>et al.</i> , 1988	K ₃₇ /K ₃₈	Alkenone concentration (µg g ⁻¹ TOC ⁻¹)	Alkenone/weight (µg g ⁻¹)	Alkenone MAR (µg cm ⁻² Kyr ⁻¹)
U1417D 1H-1W 44-48	2.44	15.64	1.88	0.37	0.39	10.61	11.80	2.29	#DIV/0!	0.05	0.36
U1417D 1H-3W 49-53	3.51	22.49	15.01	0.03	0.21	5.06	3.33	1.20	#DIV/0!	0.08	0.63
U1417C 2H-2W 49-53	7.29	46.71	15.67	0.07	0.27	6.78	4.33	1.94	#DIV/0!	0.04	0.34
U1417D 2H-2W 31-35	8.63	55.31	14.28	0.04	0.21	5.04	3.54	1.42	#DIV/0!	0.05	0.47
U1417D 2H-3W 113-117	12.93	82.87	13.47	0.17	0.36	9.45	6.93	1.96	#DIV/0!	0.05	0.45
U1417D 3H-5W 69-73	13.51	86.58	18.89	0.01	0.24	5.91	2.73	1.47	0.01	0.15	0.08
U1417D 2H-5W 69-73	13.51	86.58	14.68	0.11	0.30	7.84	5.38	1.71	#DIV/0!	0.01	1.60
U1417C 3H-2W 86-90	18.00	115.33	19.59	0.09	0.36	9.57	4.94	1.90	#DIV/0!	0.00	0.00
U1417C-3H-4W 21-25	18.55	118.85	11.31	0.09	0.23	5.60	4.85	1.60	0.29	0.13	1.57
U1417A 2H-6	19.48	124.82	#DIV/0!	#DIV/0!	#DIV/0!	#DIV/0!	#DIV/0!	#DIV/0!	#DIV/0!	#DIV/0!	0.00
U1417A 2H-6	19.48	124.82	11.50	0.09	0.24	5.85	4.97	2.55	#DIV/0!	0.00	0.00

Sample	Depth (m) CCSF-A	Age (ka)	C _{37:4} (%)	U ^K ₃₇	U ^K _{37'}	SST (U ^K _{37'}) Müller <i>et al.</i> , 1998	SST (U ^K _{37'}) Prahl <i>et al.</i> , 1988	K ₃₇ /K ₃₈	Alkenone concentration (µg g ⁻¹ TOC ⁻¹)	Alkenone/weight (µg g ⁻¹)	Alkenone MAR (µg cm ⁻² Kyr ⁻¹)
U1417D-3H3-38	21.03	126.66	12.63	0.15	0.31	8.12	6.26			0.01	
U1417D 3H-5W 25-29	23.49	150.49	18.08	-0.01	0.21	5.11	2.43	1.61	0.07	0.03	0.41
U1417D-3H6-38	24.99	150.52	15.97	0.11	0.32	8.30	5.28			0.02	
U1417C-4H3-35	26.98	162.51	16.79	0.08	0.30	7.61	4.54			0.02	
U1417C 4H-2W 92-94	26.00	166.58	13.02	0.11	0.28	7.20	5.47	1.11	#DIV/0!	0.11	1.47
U1417C-4H4-142	29.51	177.75	7.99	0.31	0.42	11.37	10.24			0.01	
U1417C 4H-4W 44-48	28.54	182.86	9.44	0.15	0.27	6.83	6.33	1.24	0.44	0.24	3.30
U1417D-4H2-76	30.54	183.99	6.29	0.23	0.31	8.02	8.26			0.17	
U1417D-4H3-28	31.56	190.14	5.30	0.22	0.29	7.36	8.07			1.01	
U1417D 4H-2W 22-26	30.00	192.25	3.02	0.23	0.26	6.66	8.24	1.97	0.04	0.02	0.27
U1417D 4H-2W 122-126	31.00	198.66	6.82	0.21	0.30	7.85	7.96	1.08	0.28	0.27	4.06
U1417D-4H4-78	33.56	202.19	2.86	0.46	0.50	13.77	13.99			0.03	
U1417D 4H-3W 72-76	32.00	205.07	4.19	0.27	0.32	8.50	9.33	1.66	0.00	0.00	0.00
U1417C-5H3-93	36.01	216.93	12.45	0.19	0.36	9.62	7.40			0.02	
U1417C 5H-2W 140-144	34.98	224.14	13.28	0.10	0.27	6.97	5.22	1.06	0.20	0.12	1.88
U1417C-5H5-42	38.50	231.93	13.17	0.10	0.26	6.62	5.00			0.02	
U1417D-5H4-17	41.03	247.17	21.10	0.00	0.26	6.68	2.54			0.02	

Sample	Depth (m) CCSF-A	Age (ka)	C _{37:4} (%)	U ^K ₃₇	U ^K _{37'}	SST (U ^K _{37'}) Müller <i>et al.</i> , 1998	SST (U ^K _{37'}) Prahll <i>et al.</i> , 1988	K ₃₇ /K ₃₈	Alkenone concentration (µg g ⁻¹ TOC ⁻¹)	Alkenone/weight (µg g ⁻¹) #DIV/0!	Alkenone MAR (µg cm ⁻² Kyr ⁻¹)
U1417A 4H-5	38.83	248.83	#DIV/0!	#DIV/0!	#DIV/0!	#DIV/0!	#DIV/0!	#DIV/0!	0.00	#DIV/0!	0.00
U1417A 4H-5	38.83	248.83	15.68	0.09	0.29	7.40	4.75	1.94	#DIV/0!	0.07	1.11
U1417C 5H-4W 93-97	39.49	253.04	12.67	0.08	0.24	5.85	4.61	1.65	#DIV/0!	0.03	0.46
U1417D 46X-2	41.00	262.72	15.00	0.35	0.59	16.59	11.42	0.91	#DIV/0!	0.48	9.57
U1417C 5H-5W 138-142	41.44	265.54	19.23	0.03	0.27	6.96	3.32	2.08	#DIV/0!	0.06	1.25
U1417C-6H3-16	46.00	277.09	12.97	0.08	0.24	5.92	4.57			0.11	
U1417D 5H-5W 97-101	45.31	290.34	15.16	0.10	0.29	7.55	5.03	2.28	#DIV/0!	0.03	0.60
U1417D-6H3-128	50.99	307.17	6.18	0.23	0.31	8.07	8.34			0.03	
U1417C 6H-4W 117-121	50.45	323.25	14.97	0.14	0.34	8.90	6.03	1.84	#DIV/0!	0.00	0.00
U1417C-7H2-145	55.98	337.24	2.43	0.29	0.33	8.58	9.97			0.05	
U1417D 6H-5W 77-81	55.46	355.38	13.66	0.15	0.33	8.73	6.35	1.96	0.12	0.05	0.89
U1417C-7H6-46	60.99	367.42	9.96	0.19	0.32	8.34	7.30			0.02	
U1417D-7H3-116	66.01	397.67	7.03	0.24	0.34	8.84	8.64			0.01	
U1417D 7H-2W 20-24	65.53	419.92	10.88	0.21	0.35	9.40	7.78	1.97	0.11	0.06	1.00
U1417C-8H3-99	71.06	427.38	5.30	0.34	0.42	11.34	11.18			0.01	
U1417C-8H5-48	73.55	442.01	1.72	0.40	0.43	11.61	12.67			0.01	
U1417A 9H-3W	70.48	451.63	5.31	0.22	0.28	7.30	8.01	2.13	0.34	0.13	2.11

Sample	Depth (m) CCSF-A	Age (ka)	C _{37:4} (%)	U ^K ₃₇	U ^K _{37'}	SST (U ^K _{37'}) Müller <i>et al.</i> , 1998	SST (U ^K _{37'}) PrahI <i>et al.</i> , 1988	K ₃₇ /K ₃₈	Alkenone concentration (µg g ⁻¹ TOC ⁻¹)	Alkenone/weight (µg g ⁻¹)	Alkenone MAR (µg cm ⁻² Kyr ⁻¹)
12-16											
U1417C-8H7-46	76.05	456.69	11.88	0.11	0.25	6.38	5.24			0.03	
U1417A 9H-3	72.36	463.67	#DIV/0!	#DIV/0!	#DIV/0!	#DIV/0!	#DIV/0!	#DIV/0!	#DIV/0!	#DIV/0!	0.00
U1417A 9H-3	72.36	463.67	11.34	0.21	0.36	9.57	7.74	2.90	#DIV/0!	0.00	0.00
U1417D-9H2-46	78.48	470.96		0.00	#DIV/0!	0.00	2.60			0.00	
U1417D-9H4-2	81.04	486.00	6.66	0.23	0.32	8.40	8.43			0.02	

Sample	Depth (m) CCSF-A	Age (Ma)	C _{37:4} (%)	U ^K ₃₇	U ^K _{37'}	SST (U ^K _{37'}) Müller <i>et al.</i> , 1998	SST (U ^K _{37'}) PrahI <i>et al.</i> , 1988	K ₃₇ /K ₃₈	Alkenone concentration (µg g ⁻¹ TOC ⁻¹)	Alkenone/weight (µg g ⁻¹)	Alkenone MAR (µg cm ⁻² Kyr ⁻¹)
U1417A 16H-3	147.75	0.96	#DIV/0!	#DIV/0!	#DIV/0!	#DIV/0!	#DIV/0!	#DIV/0!	#DIV/0!	0.00	0.00
U1417A 16H-3	147.75	0.96	7.80	0.32	0.43	11.78	10.62	2.65	#DIV/0!	0.16	2.99
U1417A 19H-3	179.11	1.30	#DIV/0!	#DIV/0!	#DIV/0!	#DIV/0!	#DIV/0!	#DIV/0!			
U1417B 20H-2W 83-87	196.31	1.50	7.61	0.13	0.22	5.42	5.85	2.25	#DIV/0!	0.01	0.06
U1417B	196.61	1.50	3.96	0.16	0.21	5.00	6.63	2.20	#DIV/0!	0.01	0.11

Sample	Depth (m) CCSF-A	Age (Ma)	C _{37:4} (%)	U ₃₇ ^K	U ₃₇ ^{K'}	SST (U ₃₇ ^{K'}) Müller <i>et al.</i> , 1998	SST (U ₃₇ ^{K'}) PrahI <i>et al.</i> , 1988	K ₃₇ /K ₃₈	Alkenone concentration (µg g ⁻¹ TOC ₁)	Alkenone/weight (µg g ⁻¹)	Alkenone MAR (µg cm ⁻² Kyr ⁻¹)
20H-2W 113-117 U1417B	196.91	1.50	4.78	0.15	0.21	4.95	6.34	2.24	#DIV/0!	0.02	0.19
20H-2W 142-146 U1417B	197.21	1.51	2.33	0.19	0.22	5.24	7.31	2.67	#DIV/0!	0.01	0.15
20H-3W 23-27 U1417B	197.53	1.51	1.83	0.17	0.19	4.33	6.73	2.61	#DIV/0!	0.02	0.22
20H-3W 55-59 U1417B	197.81	1.51	0.95	0.19	0.20	4.78	7.36	3.04	#DIV/0!	0.02	0.20
20H-3W 83-87 U1417B	198.11	1.52	1.72	0.15	0.17	3.79	6.32	1.86	#DIV/0!	0.01	0.14
20H-3W 113-117 U1417B	198.41	1.52	3.50	0.09	0.13	2.65	4.90	1.83	#DIV/0!	0.01	0.16
20H-4W 143-147 U1417B	198.70	1.52	1.39	0.15	0.17	3.69	6.34	2.05	#DIV/0!	0.02	0.25
20H-4W 22-26 U1417B	199.00	1.53	1.94	0.14	0.16	3.56	6.07	2.14	#DIV/0!	0.03	0.31

Sample	Depth (m) CCSF-A	Age (Ma)	C _{37:4} (%)	U ₃₇ ^K	U ₃₇ ^{K'}	SST (U ₃₇ ^{K'}) Müller <i>et al.</i> , 1998	SST (U ₃₇ ^{K'}) PrahI <i>et al.</i> , 1988	K ₃₇ /K ₃₈	Alkenone concentration (µg g ⁻¹ TOC ₁)	Alkenone/weight (µg g ⁻¹)	Alkenone MAR (µg cm ⁻² Kyr ⁻¹)
52-56 U1417B 20H-4w 82-86	199.30	1.53	1.53	0.10	0.12	2.26	5.14	2.12	#DIV/0!	0.02	0.21
U1417B 20H-4W 119-123	199.65	1.53	3.57	0.09	0.13	2.53	4.78	2.11	#DIV/0!	0.01	0.11
U1417B 20H-4w 142-146	199.90	1.53	4.50	0.17	0.22	5.41	6.79	2.03	#DIV/0!	0.01	0.07
U1417B 20H-5W 22-26	200.20	1.54	4.13	0.14	0.19	4.40	6.10	2.19	#DIV/0!	0.01	0.08
U1417B 20H-5W 52-56	200.50	1.54	3.04	0.13	0.17	3.78	5.93	2.48	#DIV/0!	0.01	0.13
U1417B 20H-5w 82-86	200.80	1.54	2.18	0.10	0.13	2.47	5.13	1.98	#DIV/0!	0.02	0.21
U1417B 20H-5w 116-120	201.14	1.55	1.90	0.20	0.22	5.32	7.51	2.38	#DIV/0!	0.02	0.18
U1417B 20H-5W	201.40	1.55	3.80	0.11	0.16	3.46	5.46	2.14	#DIV/0!	0.00	0.04

Sample	Depth (m) CCSF-A	Age (Ma)	C _{37:4} (%)	U ₃₇ ^K	U ₃₇ ^{K'}	SST (U ₃₇ ^{K'}) Müller <i>et al.</i> , 1998	SST (U ₃₇ ^{K'}) PrahI <i>et al.</i> , 1988	K ₃₇ /K ₃₈	Alkenone concentration (µg g ⁻¹ TOC ₁)	Alkenone/weight (µg g ⁻¹)	Alkenone MAR (µg cm ⁻² Kyr ⁻¹)
142-146											
U1417B 20H-6W 24-28	201.72	1.55	4.14	0.18	0.23	5.62	7.07	2.58	#DIV/0!	0.00	0.06
U1417B 20H-6W 54-58	202.02	1.56	1.42	0.22	0.24	5.97	8.19	2.97	#DIV/0!	0.01	0.16
U1417B 20H-6W 84-88	202.32	1.56	0.98	0.20	0.21	4.98	7.51	2.88	#DIV/0!	0.02	0.20
U1417B 20H-6w 114-118	202.62	1.56	0.83	0.21	0.22	5.43	7.92	2.27	#DIV/0!	0.02	0.29
U1417B 20H-7W 12-16	202.90	1.57	0.85	0.20	0.21	4.95	7.53	2.01	#DIV/0!	0.02	0.21
U1417D 24H2W 9- 13	203.21	1.57	2.02	0.16	0.19	4.29	6.64	2.06	#DIV/0!	0.01	0.06
U1417D 24H-2W 39-43	203.51	1.57	7.97	0.15	0.25	6.31	6.41	2.21	#DIV/0!	0.01	0.10
U1417D 24H-2W	203.81	1.57	23.23	-0.04	0.25	6.23	1.58	0.74	0.05	0.02	0.15

Sample	Depth (m) CCSF-A	Age (Ma)	C _{37:4} (%)	U ₃₇ ^K	U ₃₇ ^{K'}	SST (U ₃₇ ^{K'}) Müller <i>et al.</i> , 1998	SST (U ₃₇ ^{K'}) PrahI <i>et al.</i> , 1988	K ₃₇ /K ₃₈	Alkenone concentration (µg g ⁻¹ TOC ₁)	Alkenone/weight (µg g ⁻¹)	Alkenone MAR (µg cm ⁻² Kyr ⁻¹)
69-73											
U1417D 24H-2W 99-103	204.11	1.58	4.32	0.17	0.22	5.30	6.76	1.89	#DIV/0!	0.01	0.12
U1417D 24H-2W 130-134	204.41	1.58	1.63	0.16	0.18	4.06	6.57	1.84	#DIV/0!	0.02	0.22
U1417D 24H-3W 9- 13	204.71	1.58	0.40	0.23	0.24	5.93	8.47	2.21	#DIV/0!	0.06	0.57
U1417C 21H-4W 2- 6	205.03	1.59	4.60	0.15	0.21	4.91	6.37	2.32	#DIV/0!	0.01	0.08
U1417C 21H-4W 28-32	205.30	1.59	2.89	0.18	0.21	5.15	7.07	2.11	#DIV/0!	0.01	0.15
U1417C 21H-4W 62-66	205.60	1.59	1.74	0.22	0.24	5.89	8.02	1.70	#DIV/0!	0.03	0.28
U1417D 21H-4W 88-92	205.90	1.60	2.58	0.19	0.22	5.40	7.36	1.97	#DIV/0!	0.01	0.09
U1417C 21H-4W	206.20	1.60	4.21	0.18	0.23	5.72	7.12	1.73	#DIV/0!	0.01	0.06

Sample	Depth (m) CCSF-A	Age (Ma)	C _{37:4} (%)	U ^K ₃₇	U ^K _{37'}	SST (U ^K _{37'}) Müller <i>et al.</i> , 1998	SST (U ^K _{37'}) PrahI <i>et al.</i> , 1988	K ₃₇ /K ₃₈	Alkenone concentration (µg g ⁻¹ TOC ₁)	Alkenone/weight (µg g ⁻¹)	Alkenone MAR (µg cm ⁻² Kyr ⁻¹)
118-122 U1417D											
25H-1W 54-58 U1417D	206.50	1.60	1.97	0.23	0.25	6.32	8.30	2.58	#DIV/0!	0.01	0.14
25H-1W 84-88 U1417D	206.80	1.61	2.56	0.18	0.21	5.01	7.06	2.08	#DIV/0!	0.02	0.17
25H-1W 114-118 U1417D	207.10	1.61	6.01	0.22	0.29	7.59	8.02	2.54	#DIV/0!	0.01	0.14
25H-1W 144-148 U1417D	207.40	1.61	1.47	0.16	0.18	4.19	6.72	2.02	#DIV/0!	0.03	0.26
25H-2W 25-29 U1417D	207.71	1.62	5.79	0.17	0.24	6.02	6.87	2.44	#DIV/0!	0.01	0.11
25H-2W 55-59 U1417D	208.01	1.62	3.52	0.22	0.26	6.67	8.09	1.93	#DIV/0!	0.01	0.09
25H-2W 85-89 U1417D	208.31	1.62	1.03	0.25	0.26	6.59	8.82	2.62	#DIV/0!	0.01	0.13
25H-2W	208.61	1.62	6.36	0.20	0.28	7.22	7.62	2.15	#DIV/0!	0.01	0.07

Sample	Depth (m) CCSF-A	Age (Ma)	C _{37:4} (%)	U ₃₇ ^K	U ₃₇ ^{K'}	SST (U ₃₇ ^{K'}) Müller <i>et al.</i> , 1998	SST (U ₃₇ ^{K'}) PrahI <i>et al.</i> , 1988	K ₃₇ /K ₃₈	Alkenone concentration (µg g ⁻¹ TOC ₁)	Alkenone/weight (µg g ⁻¹)	Alkenone MAR (µg cm ⁻² Kyr ⁻¹)
118-122 U1417D											
25H-2W 145-149 U1417D	208.91	1.63	8.26	0.25	0.36	9.68	8.87	2.54	#DIV/0!	0.02	0.20
25H-3W 26-30 U1417D	209.22	1.63	5.40	0.24	0.31	7.94	8.49	1.46	0.26	0.12	1.24
25H-3W 51-55 U1417B	209.47	1.63	16.64	0.13	0.36	9.60	5.96	2.61	#DIV/0!	0.01	0.08
22H-3W 1-4 U1417C	209.82	1.64	10.46	0.18	0.32	8.28	7.08	1.77	#DIV/0!	0.01	0.09
21H-3 U1417B	210.00	1.64	#DIV/0!	0.00	#DIV/0!		2.60	#DIV/0!			
22H-3W 18-21 U1417B	210.08	1.64	9.60	0.27	0.40	10.89	9.32	1.65	#DIV/0!	0.00	0.03
22H-3W 59-63 U1417B	210.40	1.64	3.83	0.26	0.31	7.98	9.03	2.35	#DIV/0!	0.01	0.10
22H-3W 93-95	210.70	1.65	10.61	0.17	0.31	8.17	6.95	2.07	#DIV/0!	0.01	0.05

Sample	Depth (m) CCSF-A	Age (Ma)	C _{37:4} (%)	U ₃₇ ^K	U ₃₇ ^{K'}	SST (U ₃₇ ^{K'}) Müller <i>et al.</i> , 1998	SST (U ₃₇ ^{K'}) PrahI <i>et al.</i> , 1988	K ₃₇ /K ₃₈	Alkenone concentration (µg g ⁻¹ TOC ₁)	Alkenone/weight (µg g ⁻¹)	Alkenone MAR (µg cm ⁻² Kyr ⁻¹)
U1417B 22H-4W 15-19	211.00	1.65	2.83	0.25	0.28	7.25	8.77	2.35	#DIV/0!	0.01	0.07
U1417B 22H-4W 45-46	211.30	1.65	8.52	0.25	0.37	9.84	8.90	2.87	#DIV/0!	0.00	0.04
U1417D 26H-1W 34-38	211.60	1.66	1.70	0.35	0.37	9.96	11.34	2.44	#DIV/0!	0.02	0.17
U1417D 26H-1W 64-68	211.90	1.66	0.99	0.33	0.34	8.92	10.73	2.28	#DIV/0!	0.02	0.22
U1417D 26H-1W 90-94	212.20	1.66	3.57	0.20	0.24	5.98	7.53	2.24	#DIV/0!	0.02	0.19
U1417D 26H-1W 124-128	212.50	1.66	4.70	0.20	0.26	6.61	7.67	2.07	#DIV/0!	0.01	0.10
U1417D 26H-2W 5-9	212.81	1.67	1.45	0.23	0.25	6.33	8.47	1.86	#DIV/0!	0.02	0.25
U1417D 26H-2W 35-39	213.11	1.67	7.33	0.15	0.24	5.81	6.23	1.95	#DIV/0!	0.01	0.08

Sample	Depth (m) CCSF-A	Age (Ma)	C _{37:4} (%)	U ₃₇ ^K	U ₃₇ ^{K'}	SST (U ₃₇ ^{K'}) Müller <i>et al.</i> , 1998	SST (U ₃₇ ^{K'}) PrahI <i>et al.</i> , 1988	K ₃₇ /K ₃₈	Alkenone concentration (µg g ⁻¹ TOC ₁)	Alkenone/weight (µg g ⁻¹)	Alkenone MAR (µg cm ⁻² Kyr ⁻¹)
U1417D 27H-1W 87-91	217.35	1.71	23.76	-0.02	0.29	7.51	2.22	1.74	0.00	0.00	0.00
U1417D 28H-1W 31-35	220.62	1.75	9.30	0.27	0.40	10.65	9.24	2.14	#DIV/0!	0.02	0.19
U1417D 29H-1W 106-110	223.83	1.78	8.19	0.28	0.40	10.76	9.71	2.20	#DIV/0!	0.02	0.20
U1417D 29H-CCW 15-19	227.06	1.81	5.07	0.24	0.31	8.02	8.65	1.66	0.36	0.16	1.55
U1417D 30H-2W 63-67	230.10	1.85	6.07	0.31	0.39	10.54	10.28	1.47	0.09	0.03	0.27
U1417D 30H-CCW 5-9	232.47	1.87	9.86	0.20	0.33	8.77	7.65	1.43	#DIV/0!	0.02	0.20
U1417D 31H-1W 39-43	237.90	1.93	2.63	0.26	0.30	7.72	9.22	1.55	#DIV/0!	0.06	0.56
U1417D 32H-1W 23-27	242.00	1.97	1.27	0.37	0.38	10.30	11.76	1.35	#DIV/0!	0.07	0.61

Sample	Depth (m) CCSF-A	Age (Ma)	C _{37:4} (%)	U ₃₇ ^K	U ₃₇ ^{K'}	SST (U ₃₇ ^{K'}) Müller <i>et al.</i> , 1998	SST (U ₃₇ ^{K'}) PrahI <i>et al.</i> , 1988	K ₃₇ /K ₃₈	Alkenone concentration (µg g ⁻¹ TOC ₁)	Alkenone/weight (µg g ⁻¹)	Alkenone MAR (µg cm ⁻² Kyr ⁻¹)
U1417D 32H-2W 17-21	243.44	1.98	4.68	0.13	0.19	4.44	5.97	1.63	#DIV/0!	0.05	0.58
U1417D 32H-2	244.70	2.00	14.46	0.15	0.34	8.96	6.25	2.87	#DIV/0!	0.60	6.44
U1417D 32H-CCW 13-17	246.64	2.01	1.14	0.20	0.22	5.28	7.71	1.84	#DIV/0!	0.01	0.14
U1417D 34H 2W 55-59	249.95	2.03	1.47	0.38	0.40	10.71	12.02	1.94	0.11	0.03	0.56
U1417C 25H-3	250.82	2.04	2.91	0.17	0.20	4.73	6.73	1.62	#DIV/0!	0.00	0.00
U1417D 35H-1W 18-22	253.90	2.06	4.44	0.32	0.38	10.30	10.66	2.44	#DIV/0!	0.04	0.94
U1417D 35H-2W 102-106	256.24	2.07	1.94	0.33	0.36	9.44	10.83	1.37	0.47	0.11	2.16
U1417D 35H-2	256.65	2.07	3.25	0.30	0.34	9.06	10.08	1.93	#DIV/0!	1.25	25.22
U1417D 36H-1W 59-63	259.72	2.09	3.67	0.28	0.32	8.50	9.50	2.75	#DIV/0!	0.02	0.46

Sample	Depth (m) CCSF-A	Age (Ma)	C _{37:4} (%)	U ₃₇ ^K	U ₃₇ ^{K'}	SST (U ₃₇ ^{K'}) Müller <i>et al.</i> , 1998	SST (U ₃₇ ^{K'}) PrahI <i>et al.</i> , 1988	K ₃₇ /K ₃₈	Alkenone concentration (µg g ⁻¹ TOC ₁)	Alkenone/weight (µg g ⁻¹)	Alkenone MAR (µg cm ⁻² Kyr ⁻¹)
U1417D 35H-2	261.70	2.11	#DIV/0!	#DIV/0!	#DIV/0!		#DIV/0!	#DIV/0!			
U1417D 36H-3W 84-88	262.97	2.11	2.24	0.34	0.37	9.95	11.14	1.55	#DIV/0!	0.07	1.50
U1417D 39X-1W 19- 23	277.07	2.20	3.24	0.31	0.36	9.52	10.45	1.83	0.44	0.17	3.53
U1417D 40X-2W 37- 41	288.45	2.28	4.82	0.30	0.37	9.81	10.15	1.45	0.22	0.07	1.32
U1417D 40X-2	289.05	2.28	7.36	0.22	0.32	8.40	8.20	2.10	#DIV/0!	1.38	26.84
U1417D 41X-4W 35- 39	301.13	2.36	3.55	0.30	0.35	9.12	10.03	2.51	0.16	0.07	1.38
U1417D 42X-1W 94- 98	306.88	2.40	6.47	0.29	0.38	10.19	9.88	1.61	0.37	0.13	2.47
U1417D 42X-2	308.91	2.41	1.25	0.37	0.39	10.45	11.89	1.84	#DIV/0!	1.29	24.47
U1417D 42X-3W 23- 27	309.21	2.41	0.58	0.44	0.45	12.18	13.54	1.23	#DIV/0!	0.01	0.13

Sample	Depth (m) CCSF-A	Age (Ma)	C _{37:4} (%)	U ₃₇ ^K	U ₃₇ ^{K'}	SST (U ₃₇ ^{K'}) Müller <i>et al.</i> , 1998	SST (U ₃₇ ^{K'}) Prah <i>et al.</i> , 1988	K ₃₇ /K ₃₈	Alkenone concentration (µg g ⁻¹ TOC ₁)	Alkenone/weight (µg g ⁻¹)	Alkenone MAR (µg cm ⁻² Kyr ⁻¹)
U1417D 42X-3W 83-87	309.81	2.41	0.00	0.38	0.38	10.05	11.99	0.80	#DIV/0!	0.00	0.00
U1417D 42X-4W 26-30	310.42	2.42	5.10	0.24	0.31	7.93	8.57	1.60	#DIV/0!	0.04	0.71
U1417D 42X-CCW 23-27	310.99	2.42	0.00	0.27	0.27	6.84	9.34	#DIV/0!	#DIV/0!	0.02	0.45
U1417D 42X-2	313.96	2.44	#DIV/0!	#DIV/0!	#DIV/0!		#DIV/0!	#DIV/0!			
U1417D 43X-1W 10-14	315.78	2.45	3.33	0.26	0.31	7.91	9.14	1.42	0.15	0.05	1.15
U1417D 43X-1W 70-74	316.38	2.46	9.88	0.22	0.35	9.33	8.06	2.03	0.05	0.02	0.50
U1417D 43X-1W 127-131	316.98	2.46	3.24	0.27	0.32	8.29	9.47	1.56	0.24	0.07	1.53
U1417D 43X-2W 55-59	317.58	2.46	14.42	0.17	0.37	9.76	6.83	0.94	0.05	0.01	0.21
U1417D 43X-2W	318.17	2.47	5.63	0.28	0.36	9.59	9.69	1.61	0.37	0.12	2.53

Sample	Depth (m) CCSF-A	Age (Ma)	C _{37:4} (%)	U ₃₇ ^K	U ₃₇ ^{K'}	SST (U ₃₇ ^{K'}) Müller <i>et al.</i> , 1998	SST (U ₃₇ ^{K'}) PrahI <i>et al.</i> , 1988	K ₃₇ /K ₃₈	Alkenone concentration (µg g ⁻¹ TOC ₁)	Alkenone/weight (µg g ⁻¹)	Alkenone MAR (µg cm ⁻² Kyr ⁻¹)
114-118 U1417D											
43X-3W 27-31 U1417D	318.78	2.47	6.74	0.30	0.39	10.49	10.01	1.49	0.16	0.06	1.16
43W-3W 87-91 U1417D	319.38	2.48	6.60	0.30	0.39	10.41	10.00	1.49	0.15	0.06	1.12
43X-4W 10-14 U1417D	319.98	2.48	24.10	0.00	0.32	8.33	2.62	1.04	0.05	0.02	0.42
43X-4W 63-67 U1417D	320.55	2.48	1.65	0.44	0.46	12.67	13.55	1.41	0.39	0.11	2.12
43X-4W 125-129 U1417D	321.17	2.49	2.33	0.38	0.41	11.16	12.09	1.34	0.36	0.17	3.10
43X-5W 34-38 U1417D	321.78	2.49	4.20	0.35	0.41	11.03	11.32	1.88	0.06	0.03	0.54
43X-CCW 41-45 U1417D	322.34	2.49	1.81	0.25	0.28	7.07	8.96	1.22	0.11	0.04	0.71
44X-1W 18-	325.39	2.53	#DIV/0!	#DIV/0!	#DIV/0!		#DIV/0!	#DIV/0!	0.00	0.00	0.00

Sample	Depth (m) CCSF-A	Age (Ma)	C _{37:4} (%)	U ₃₇ ^K	U ₃₇ ^{K'}	SST (U ₃₇ ^{K'}) Müller <i>et al.</i> , 1998	SST (U ₃₇ ^{K'}) PrahI <i>et al.</i> , 1988	K ₃₇ /K ₃₈	Alkenone concentration (µg g ⁻¹ TOC ₁)	Alkenone/weight (µg g ⁻¹)	Alkenone MAR (µg cm ⁻² Kyr ⁻¹)
23											
U1417D 44X-1W 70-74	326.00	2.53	#DIV/0!	#DIV/0!	#DIV/0!		#DIV/0!	#DIV/0!	0.00	0.00	0.00
U1417D 44X-1W 104-108	326.57	2.54	5.30	0.31	0.38	10.17	10.26	1.61	0.00	0.00	0.00
U1417D 45X-1W 9-13	329.98	2.58	3.36	0.29	0.33	8.79	9.83	2.39	0.00	0.00	0.00
U1417D 45X-1W 60-64	330.57	2.59	2.33	0.39	0.42	11.39	12.27	2.17	#DIV/0!	0.00	0.00
U1417D 45X-1W 123-127	331.20	2.59	0.00	0.39	0.39	10.54	12.40	1.34	0.00	0.00	0.00
U1417D 45X-1	331.31	2.59	7.08	0.39	0.49	13.64	12.31	3.28	#DIV/0!	0.53	6.13
U1417D 45X-2W 46-50	331.81	2.60	7.56	0.18	0.27	6.99	7.06	1.59	0.00	0.00	0.00
U1417D 45X-2W 62-66	331.98	2.60	5.34	0.28	0.35	9.23	9.52	1.43	0.00	0.00	0.00

Sample	Depth (m) CCSF-A	Age (Ma)	C _{37:4} (%)	U ₃₇ ^K	U ₃₇ ^{K'}	SST (U ₃₇ ^{K'}) Müller <i>et al.</i> , 1998	SST (U ₃₇ ^{K'}) PrahI <i>et al.</i> , 1988	K ₃₇ /K ₃₈	Alkenone concentration (µg g ⁻¹ TOC ₁)	Alkenone/weight (µg g ⁻¹)	Alkenone MAR (µg cm ⁻² Kyr ⁻¹)
U1417D 45X-2W 70-74	332.17	2.60	5.60	0.27	0.34	9.11	9.33	1.30	0.00	0.00	0.00
U1417D 46X-1W 0-4	336.66	2.66	1.66	0.38	0.41	10.99	12.18	1.14	0.00	0.00	0.00
U1417D 46X-1W 31-35	336.96	2.66	0.00	0.44	0.44	12.02	13.61	1.70	0.04	0.01	0.12
U1417D 46X-1W 60-64	337.26	2.66	#DIV/0!	#DIV/0!	#DIV/0!		#DIV/0!	#DIV/0!	0.00	0.00	0.00
U1417D 46X-1W 96-100	337.56	2.67	11.61	0.18	0.34	8.97	7.21	1.90	0.05	0.02	0.23
U1417D 46X-1W 119-123	337.86	2.67	0.00	0.23	0.23	5.62	8.34	1.79	0.05	0.02	0.24
U1417D 46X-3W 1-5	338.30	2.68	2.57	0.38	0.41	11.19	12.03	1.59	0.12	0.05	0.64
U1417D 46X-3W 21-25	338.46	2.68	4.01	0.31	0.37	9.82	10.43	1.98	0.10	0.04	0.45
U1417D 46X-3W 46-50	338.76	2.68	0.00	0.42	0.42	11.47	13.16	1.34	0.00	0.00	0.00

Sample	Depth (m) CCSF-A	Age (Ma)	C _{37:4} (%)	U ₃₇ ^K	U ₃₇ ^{K'}	SST (U ₃₇ ^{K'}) Müller <i>et al.</i> , 1998	SST (U ₃₇ ^{K'}) PrahI <i>et al.</i> , 1988	K ₃₇ /K ₃₈	Alkenone concentration (µg g ⁻¹ TOC ₁)	Alkenone/weight (µg g ⁻¹)	Alkenone MAR (µg cm ⁻² Kyr ⁻¹)
U1417D 46X-3W 80-84	339.07	2.69	7.33	0.16	0.25	6.32	6.62	1.59	0.05	0.01	0.19
U1417D 46X-3W 106-110	339.36	2.69	4.69	0.21	0.26	6.69	7.74	1.76	0.19	0.06	0.76
U1417D 46X-3W 138-142	339.66	2.69	7.82	0.20	0.30	7.83	7.62	1.30	0.12	0.06	0.74
U1417D 47X-1W 17-21	348.85	2.80	3.99	0.18	0.23	5.58	7.08	2.20	0.15	0.06	0.54
U1417D 47X-2W 6-10	349.38	2.81	0.71	0.25	0.26	6.61	8.93	2.06	#DIV/0!	0.02	0.14
U1417D 47X-2W 63-69	349.98	2.81	2.43	0.21	0.24	5.83	7.76	2.59	0.63	0.21	1.84
U1417D 47X-3W 29-33	350.56	2.82	3.67	0.26	0.31	8.05	9.14	1.63	#DIV/0!	0.02	0.20
U1417D 47X-3W 59-63	350.87	2.82	1.62	0.24	0.26	6.57	8.61	2.55	0.46	0.10	0.85

Sample	Depth (m) CCSF-A	Age (Ma)	C _{37:4} (%)	U ₃₇ ^K	U ₃₇ ^{K'}	SST (U ₃₇ ^{K'}) Müller <i>et al.</i> , 1998	SST (U ₃₇ ^{K'}) PrahI <i>et al.</i> , 1988	K ₃₇ /K ₃₈	Alkenone concentration (µg g ⁻¹ TOC ₁)	Alkenone/weight (µg g ⁻¹)	Alkenone MAR (µg cm ⁻² Kyr ⁻¹)
U1417D 47X-1	354.35	2.87	3.77	0.23	0.28	7.12	8.37	3.21	#DIV/0!	6.12	53.68
U1417D 48X-1W 29-33	358.47	2.91	4.02	0.24	0.30	7.65	8.71	2.29	0.15	0.03	0.28
U1417D 48X-1W 69-73	359.07	2.92	3.18	0.30	0.34	8.98	10.05	1.32	0.65	0.33	3.11
U1417D 48X-1	359.61	2.93	3.16	0.27	0.31	8.06	9.31	1.69	#DIV/0!	0.00	0.00
U1417D 48X-2W 0-4	359.69	2.93	4.13	0.23	0.28	7.28	8.38	1.70	0.42	0.13	1.28
U1417D 48X-2W 63-68	360.27	2.94	2.42	0.25	0.28	7.26	8.92	2.38	0.33	0.08	0.72
U1417D 48X-2W 106-110	360.79	2.94	4.26	0.29	0.34	9.08	9.76	1.53	0.28	0.06	0.60
U1417D 49X-1W 35-39	368.17	3.04	4.92	0.23	0.29	7.52	8.32	1.33	0.27	0.11	0.81
U1417D 49X-1W 69-73	368.77	3.05	3.76	0.26	0.31	8.11	9.16	1.36	0.33	0.07	0.50

Sample	Depth (m) CCSF-A	Age (Ma)	C _{37:4} (%)	U ₃₇ ^K	U ₃₇ ^{K'}	SST (U ₃₇ ^{K'}) Müller <i>et al.</i> , 1998	SST (U ₃₇ ^{K'}) Prahl <i>et al.</i> , 1988	K ₃₇ /K ₃₈	Alkenone concentration (µg g ⁻¹ TOC ₁)	Alkenone/weight (µg g ⁻¹)	Alkenone MAR (µg cm ⁻² Kyr ⁻¹)
U1417D 49X-1	369.12	3.05	10.53	0.24	0.39	10.39	8.62	1.13	#DIV/0!	0.20	1.39
U1417D 49X-2W 17-21	369.37	3.06	3.99	0.22	0.27	6.84	8.07	1.69	#DIV/0!	0.01	0.10
U1417D 49X-2W 79-83	369.97	3.06	2.79	0.32	0.36	9.59	10.66	1.40	0.10	0.02	0.15
U1417D 49X-2W 134-138	370.56	3.07	1.28	0.23	0.25	6.18	8.40	2.44	#DIV/0!	0.00	0.00
U1417D 49X-3W 49-53	371.16	3.08	0.00	0.17	0.17	3.89	6.91	1.68	#DIV/0!	4.62	32.91
U1417D 50X-1W 27-31	378.05	3.19	#VALUE! !	#VALUE! !	#DIV/0! !		#VALUE! !	#VALUE! !	#DIV/0!	0.00	0.00
U1417D 50X-1W 55-59	378.33	3.19	1.23	0.36	0.38	10.08	11.59	1.13	#DIV/0!	0.02	0.20
U141D 50X-1W 116-120	378.96	3.20	1.63	0.30	0.32	8.38	10.07	1.06	#DIV/0!	0.00	0.00
U1417D 50X-2W 44-	379.56	3.21	2.89	0.31	0.35	9.19	10.31	1.10	#DIV/0!	0.00	0.00

Sample	Depth (m) CCSF-A	Age (Ma)	C _{37:4} (%)	U ₃₇ ^K	U ₃₇ ^{K'}	SST (U ₃₇ ^{K'}) Müller <i>et al.</i> , 1998	SST (U ₃₇ ^{K'}) PrahI <i>et al.</i> , 1988	K ₃₇ /K ₃₈	Alkenone concentration (µg g ⁻¹ TOC ₁)	Alkenone/weight (µg g ⁻¹)	Alkenone MAR (µg cm ⁻² Kyr ⁻¹)
48											
U1417D 50X-2W 93-97	380.08	3.22	0.35	0.39	0.39	10.54	12.28	1.83	0.06	0.01	0.09
U1417D 50X-3W 6-10	380.66	3.23	2.76	0.37	0.40	10.92	11.74	1.79	#DIV/0!	0.00	0.00
U1417D 50X-3W 54-58	381.19	3.24	2.41	0.42	0.45	12.39	13.05	2.29	#DIV/0!	0.00	0.00
U1417D 50X-3W 102-106	381.72	3.25	0.54	0.29	0.29	7.56	9.76	1.74	#DIV/0!	0.00	0.00
U1417D 50X-4W 51-55	382.27	3.25	0.46	0.21	0.21	5.12	7.79	1.71	#DIV/0!	0.00	0.03
U1417D 51X-1W 9-13	387.57	3.34	1.03	0.17	0.19	4.29	6.94	1.59	0.80	0.18	1.28
U1417D 51X-1W 65-69	388.13	3.34	1.29	0.27	0.29	7.50	9.47	1.40	0.68	0.25	1.81
U1417D 51X-1W	388.72	3.35	1.13	0.27	0.28	7.19	9.27	1.40	0.67	0.18	1.28

Sample	Depth (m) CCSF-A	Age (Ma)	C _{37:4} (%)	U ₃₇ ^K	U ₃₇ ^{K'}	SST (U ₃₇ ^{K'}) Müller <i>et al.</i> , 1998	SST (U ₃₇ ^{K'}) PrahI <i>et al.</i> , 1988	K ₃₇ /K ₃₈	Alkenone concentration (µg g ⁻¹ TOC ₁)	Alkenone/weight (µg g ⁻¹)	Alkenone MAR (µg cm ⁻² Kyr ⁻¹)
124-128 U1417D											
51X-2W 40-44 U1417D	389.38	3.36	0.80	0.42	0.43	11.68	13.05	1.38	0.22	0.04	0.26
51X-3W 11-15 U1417D	390.00	3.37	0.51	0.35	0.35	9.40	11.29	1.55	0.18	0.02	0.15
51X-3W 103-107 U1417D	390.59	3.38	2.62	0.27	0.30	7.75	9.24	1.49	0.72	0.25	1.54
51X-4W 11-15 U1417D	391.24	3.39	1.21	0.32	0.34	8.91	10.65	1.97	0.54	0.07	0.44
51X-4W 68-72 U1417D	391.81	3.40	0.90	0.36	0.38	10.07	11.70	1.33	0.64	0.22	1.36
51X-4W 128-132 U1417D	392.41	3.41	0.69	0.31	0.32	8.42	10.42	2.11	0.14	0.04	0.26
51X-2 U1417D	394.87	3.45	0.81	0.38	0.39	10.56	12.13	2.03	#DIV/0!	0.30	1.80
52X-1W 19-23 U1417D	397.37	3.49	1.46	0.29	0.30	7.89	9.73	2.11	0.00	0.00	0.00

Sample	Depth (m) CCSF-A	Age (Ma)	C _{37:4} (%)	U ₃₇ ^K	U ₃₇ ^{K'}	SST (U ₃₇ ^{K'}) Müller <i>et al.</i> , 1998	SST (U ₃₇ ^{K'}) PrahI <i>et al.</i> , 1988	K ₃₇ /K ₃₈	Alkenone concentration (µg g ⁻¹ TOC ₁)	Alkenone/weight (µg g ⁻¹)	Alkenone MAR (µg cm ⁻² Kyr ⁻¹)
U1417D 52X-1W 59-63	397.77	3.49	1.58	0.31	0.33	8.74	10.38	1.46	0.18	0.04	0.31
U1417D 52X-1W 97-101	398.15	3.50	0.88	0.37	0.38	10.32	11.91	1.31	0.00	0.00	0.00
U1417D 52X-1W 134-138	398.57	3.51	1.24	0.37	0.39	10.45	11.89	1.61	0.13	0.03	0.15
U1417D 52X-2W 33-37	398.98	3.52	2.28	0.30	0.33	8.54	9.99	1.48	#DIV/0!	0.12	0.42
U1417D 52X-2W 69-73	399.34	3.53	3.02	0.23	0.27	6.84	8.38	1.67	0.37	0.08	0.30
U1417D 52X-2W 109-113	399.74	3.54	2.01	0.29	0.32	8.39	9.96	1.19	1.13	0.34	1.23
U1417D 52X-3W 40-44	400.28	3.55	3.59	0.22	0.26	6.59	8.01	1.65	0.46	0.11	0.41
U1417D 52X-3W 69-73	400.57	3.56	3.22	0.27	0.31	8.09	9.31	1.76	0.32	0.04	0.16

Sample	Depth (m) CCSF-A	Age (Ma)	C _{37:4} (%)	U ₃₇ ^K	U ₃₇ ^{K'}	SST (U ₃₇ ^{K'}) Müller <i>et al.</i> , 1998	SST (U ₃₇ ^{K'}) PrahI <i>et al.</i> , 1988	K ₃₇ /K ₃₈	Alkenone concentration ($\mu\text{g g}^{-1}\text{TOC}^{-1}$)	Alkenone/weight ($\mu\text{g g}^{-1}$)	Alkenone MAR ($\mu\text{g cm}^{-2}\text{Kyr}^{-1}$)
U1417D 52X-3W 102-106	400.90	3.57	1.98	0.30	0.32	8.43	10.00	1.49	1.18	0.19	0.74
U1417D 53X-1W 19- 23	407.04	3.72	0.79	0.33	0.34	8.99	10.85	1.24	#DIV/0!	0.00	0.00
U1417D 53X-1W 60- 65	407.60	3.73	1.18	0.31	0.33	8.63	10.43	0.91	0.08	0.02	0.07
U1417D 53X-2W 41- 45	408.30	3.75	5.13	0.29	0.36	9.50	9.79	0.64	0.00	0.00	0.00
U1417D 54X-1W 16- 20	416.74	3.96	0.68	0.39	0.40	10.83	12.39	1.09	#DIV/0!	0.00	0.00
U1417D 54X-1W 76- 80	417.34	3.98	#VALUE! !	#VALUE! !	#DIV/0! !	#DIV/0! !	#VALUE! !	#VALUE! !	#DIV/0! !	0.00	0.00
U1417D 54X-2W 36- 40	418.42	4.00	#VALUE! !	#VALUE! !	#DIV/0! !	#DIV/0! !	#VALUE! !	#VALUE! !	#DIV/0! !	0.00	0.00
U1417D 54X-3W 10- 14	419.04	4.02	#VALUE! !	#VALUE! !	#DIV/0! !	#DIV/0! !	#VALUE! !	#VALUE! !	#DIV/0! !	0.00	0.00

Sample	Depth (m) CCSF-A	Age (Ma)	C _{37:4} (%)	U ₃₇ ^K	U ₃₇ ^{K'}	SST (U ₃₇ ^{K'}) Müller <i>et al.</i> , 1998	SST (U ₃₇ ^{K'}) PrahI <i>et al.</i> , 1988	K ₃₇ /K ₃₈	Alkenone concentration (µg g ⁻¹ TOC ₁)	Alkenone/weight (µg g ⁻¹)	Alkenone MAR (µg cm ⁻² Kyr ⁻¹)
U1417D 54X-3W 59-63	419.63	4.03	2.13	0.27	0.30	7.79	9.43	1.40	0.00	0.00	0.00
U1417D 54X-3W 119-123	420.23	4.05	2.38	0.23	0.26	6.62	8.41	1.90	0.41	0.18	0.78
U1417D 54X-4W 29-33	420.81	4.06	3.74	0.24	0.29	7.51	8.68	1.38	0.19	0.06	0.25
U1417D 54X-4W 70-74	421.38	4.08	1.39	0.27	0.29	7.52	9.46	1.46	0.41	0.18	0.86
U1417D 54X-2	425.52	4.18	2.63	0.24	0.27	6.81	8.49	2.74	0.54	0.25	1.21
U1417E 10R-2	432.50	4.36	4.12	0.26	0.32	8.30	9.19	2.36	#DIV/0!	6.15	31.66
U1417D 57X-1	446.64	4.69	4.73	0.37	0.43	11.83	11.77	1.64	#DIV/0!	0.75	3.93
U1417E 7R-2	449.62	4.75	2.34	0.29	0.32	8.41	9.87	2.58	#DIV/0!	0.00	0.00
U1417E 8R-3	456.24	4.92	0.52	0.37	0.38	10.24	11.96	1.43	#DIV/0!	0.49	2.32
U1417D 59X-2	464.56	5.07	25.14	0.25	0.66	18.79	8.75	0.93	#DIV/0!	0.00	0.00

Sample	Depth (m) CCSF-A	Age (Ma)	C _{37:4} (%)	U ^K ₃₇	U ^K _{37'}	SST (U ^K _{37'}) Müller <i>et al.</i> , 1998	SST (U ^K _{37'}) PrahI <i>et al.</i> , 1988	K ₃₇ /K ₃₈	Alkenone concentration (µg g ⁻¹ TOC ₁)	Alkenone/weight (µg g ⁻¹)	Alkenone MAR (µg cm ⁻² Kyr ⁻¹)
U1417E 9R-2	464.59	5.07	33.23	0.09	0.64	17.93	4.90	0.49	#DIV/0!	0.00	0.00
U1417E 9R-2	464.59	5.07	#DIV/0!	#DIV/0!	#DIV/0!	#DIV/0!	#DIV/0!	#DIV/0!	#DIV/0!	0.76	3.28
U1417E 10R-2	474.29	5.25	7.81	0.31	0.42	11.44	10.36	1.40	#DIV/0!	0.03	0.21
U1417E 13R-1	501.91	5.75	1.21	0.28	0.29	7.50	9.50	1.92	#DIV/0!	0.00	0.00
U1417E 13R-1	501.91	5.75	2.35	0.27	0.30	7.89	9.45	1.91	#DIV/0!	0.26	2.31
U1417E 14R-1	510.28	5.90	6.93	0.26	0.35	9.30	9.03	2.48	#DIV/0!	0.11	0.92
U1417E 14R-1	516.32	6.01	4.54	0.23	0.29	7.54	8.46	2.90	#DIV/0!	0.52	8.82
U1417E 15R-4	525.73	6.09	10.38	0.16	0.29	7.56	6.58	1.06	#DIV/0!	0.00	0.00
U1417E 15R-4	525.73	6.09	14.70	0.15	0.35	9.15	6.30	0.84	#DIV/0!	0.03	0.88
U1417E 20R-1	527.50	6.11	1.19	0.46	0.47	13.03	14.01	2.61	#DIV/0!	0.78	11.49
U1417E 20R-1	569.79	6.49	4.37	0.51	0.58	16.15	15.30	1.37	#DIV/0!	0.27	3.89
U1417E 24R-1	608.08	6.89	2.98	0.37	0.41	11.02	11.74	1.38	#DIV/0!	0.00	0.00

Sample	Depth (m) CCSF-A	Age (Ma)	C _{37:4} (%)	U ₃₇ ^K	U ₃₇ ^{K'}	SST (U ₃₇ ^{K'}) Müller <i>et al.</i> , 1998	SST (U ₃₇ ^K) PrahI <i>et al.</i> , 1988	K ₃₇ /K ₃₈	Alkenone concentration (µg g ⁻¹ TOC ⁻¹)	Alkenone/weight (µg g ⁻¹)	Alkenone MAR (µg cm ⁻² Kyr ⁻¹)
U1417E 26R-1	635.35	7.28	1.29	0.49	0.51	14.20	14.93	2.44	#DIV/0!	0.17	1.71
U1417E 29R-5	668.65	9.04	#DIV/0!	#DIV/0!	#DIV/0!	#DIV/0!	#DIV/0!	#DIV/0!	#DIV/0!	4.77	4.77
U1417E 32R-2	694.75	12.99	0.00	0.43	0.43	11.72	13.37	#DIV/0!	#DIV/0!	0.35	0.12
U1417E 37R-1	733.68	20.04	2.42	0.57	0.61	17.23	16.94	6.82	#DIV/0!	0.92	0.61

A.2: Alkenone derived SST, %C_{37:4} and alkenone abundances Site U1418

Sample	Depth (m) CCSF-A	Age (ka)	C _{37:4} (%)	U ₃₇ ^K	U ₃₇ ^{K'}	SST (U ₃₇ ^{K'}) Müller <i>et al.</i> , 1998	SST (U ₃₇ ^K) PrahI <i>et al.</i> , 1988	K ₃₇ /K ₃₈	Alkenone concentration (µg g ⁻¹ TOC ⁻¹)	Alkenone/weight (µg g ⁻¹)	Alkenone MAR (µg cm ⁻² ky ⁻¹)
U1418B 1H-1 145-150	1.43	0.97	1.57	0.39	0.41	11.14	12.34	1.93	0.000	0.03	358.51
U1418B 2H-1W	11.09	7.46	20.72	0.11	0.39	10.62	5.24	1.68	0.000	0.01	93.22

Sample	Depth (m) CCSF-A	Age (ka)	C _{37:4} (%)	U ^K ₃₇	U ^K _{37'}	SST (U ^K _{37'}) Müller <i>et al.</i> , 1998	SST (U ^K ₃₇) PrahI <i>et al.</i> , 1988	K ₃₇ /K ₃₈	Alkenone concentration (µg g ⁻¹ TOC ⁻¹)	Alkenone/weight (µg g ⁻¹)	Alkenone MAR (µg cm ⁻² ky ⁻¹)
145-150											
U1418A 3H-2 145-150	21.05	14.17	20.40	0.06	0.33	8.60	4.03	1.77	0.000	0.01	141.85
U1418A 4H-4 145-150	34.26	23.07	8.67	0.26	0.38	10.28	9.18	1.56	0.000	0.01	93.52
U1418D 6H-3W 44-46	50.16	33.77	23.44	- 0.05	0.24	6.01	1.38	1.87	0.000	0.02	274.59
U1418A 6H-3 145-150	54.84	36.92	18.58	0.11	0.37	9.80	5.43	0.50	0.020	0.01	165.29
U1418D 8H-2W 144-146	70.14	47.22	18.41	0.01	0.24	5.79	2.79	1.42	0.000	0.03	491.87
U1418D 9H-2W 43-45	78.24	52.67	21.02	0.03	0.30	7.87	3.34	1.57	0.000	0.01	188.49
U1418A 9H-3W	86.17	58.01	14.30	0.07	0.25	6.20	4.35	1.26	0.000	13.34	0.00

Sample	Depth (m) CCSF-A	Age (ka)	C _{37:4} (%)	U ^K ₃₇	U ^K _{37'}	SST (U ^K _{37'}) Müller <i>et al.</i> , 1998	SST (U ^K ₃₇) Prahl <i>et al.</i> , 1988	K ₃₇ /K ₃₈	Alkenone concentration (µg g ⁻¹ TOC ⁻¹)	Alkenone/weight (µg g ⁻¹)	Alkenone MAR (µg cm ⁻² ky ⁻¹)
112-114											
U1418A 9H-3W 145-150	86.49	58.22	17.51	0.09	0.32	8.38	4.83	1.36	0.000	0.00	0.00
U1418E 2H-2W 64- 66	90.13	60.67	8.02	0.22	0.33	8.69	8.20	1.10	0.018	0.01	0.00
U1418E 2H-5W 14- 16	94.13	63.37	8.46	0.11	0.21	5.10	5.34	1.57	0.057	0.04	0.01
U1418A 10H-5W 120-122	98.19	66.10	23.41	- 0.01	0.29	7.47	2.31	1.01	0.016	0.01	0.00
U1418D 11H-4W 129-131	103.93	69.96	20.89	0.02	0.29	7.59	3.20	1.47	0.000	0.03	524.11
U1418A 11H-3 145- 150	105.90	71.29	26.58	- 0.01	0.34	9.09	2.27	1.27	0.000	0.00	0.00
U1418D 11H-6W	106.18	71.48	27.51	-	0.29	7.55	1.04	1.38	0.000	0.01	242.74

Sample	Depth (m) CCSF-A	Age (ka)	C _{37:4} (%)	U ₃₇ ^K	U ₃₇ ^{K'}	SST (U ₃₇ ^K) Müller <i>et al.</i> , 1998	SST (U ₃₇ ^K) Prahl <i>et al.</i> , 1988	K ₃₇ /K ₃₈	Alkenone concentration (µg g ⁻¹ TOC ⁻¹)	Alkenone/weight (µg g ⁻¹)	Alkenone MAR (µg cm ⁻² ky ⁻¹)
54-56				0.06							
U1418E 5H-2W 117-119	114.21	76.89	19.82	0.04	0.29	7.58	3.54	0.98	0.000	0.00	0.00
U1418E 5H-5W 61- 63	118.12	79.52	21.68	0.02	0.30	7.81	3.09	1.21	0.032	0.01	0.00
U1418E 6H-3W 4-6	126.12	84.90	16.46	0.11	0.32	8.46	5.23	0.97	0.029	0.01	0.00
U1418E 6H-5W 104-106	130.12	87.59	17.75	0.02	0.24	6.01	3.15	1.00	0.000	0.00	0.00
U1418D 14H-5W 105-107	138.19	93.03	18.75	0.06	0.31	7.99	4.16	1.46	0.000	0.02	436.54
U1418A 14H-2 145- 150	138.71	93.37	15.25	0.19	0.40	10.88	7.33	1.55	0.000	0.00	0.00
U1418A 16H-2 145- 150	149.20	100.44	17.68	0.11	0.34	9.12	5.28	1.73	0.000	0.01	206.97

Sample	Depth (m) CCSF-A	Age (ka)	C _{37:4} (%)	U ₃₇ ^K	U ₃₇ ^{K'}	SST (U ₃₇ ^K)	SST (U ₃₇ ^K)	K ₃₇ /K ₃₈	Alkenone concentration (µg g ⁻¹ TOC ⁻¹)	Alkenone/weight (µg g ⁻¹)	Alkenone
						Müller <i>et al.</i> , 1998	Prahl <i>et al.</i> , 1988				MAR (µg cm ⁻² ky ⁻¹)
U1418D 16H-2W 113-115	154.12	103.75	19.37	0.05	0.31	7.97	3.95	1.44	0.000	0.01	239.27
U1418C 22H-4W 24-26	160.18	107.83	13.05	0.16	0.33	8.82	6.62	1.58	0.023	0.01	267.97
U1418D 17H-1W 94-96	164.10	110.47	11.81	0.18	0.34	8.89	7.09	1.30	0.000	0.01	99.87
U1418D 17H-5W 140-142	170.21	114.58	17.24	0.11	0.34	9.03	5.37	1.21	0.000	0.00	63.85
U1418A 20H-2 145- 150	172.08	115.84	21.03	0.13	0.43	11.57	5.75	1.52	0.000	0.00	0.00
U1418C 23H-3W 84-86	172.16	115.89	19.39	0.09	0.35	9.22	4.77	1.50	0.000	0.01	256.45
U1418C 24H-2W 124-126	182.16	122.63	5.90	0.32	0.40	10.83	10.57	1.30	0.000	0.06	1058.29

Sample	Depth (m) CCSF-A	Age (ka)	C _{37:4} (%)	U ₃₇ ^K	U ₃₇ ^{K'}	SST (U ₃₇ ^K)	SST (U ₃₇ ^K)	K ₃₇ /K ₃₈	Alkenone concentration (µg g ⁻¹ TOC ⁻¹)	Alkenone/weight (µg g ⁻¹)	Alkenone
						Müller <i>et al.</i> , 1998	Prahl <i>et al.</i> , 1988				MAR (µg cm ⁻² ky ⁻¹)
U1418C 24H-3W 146-148	183.88	123.78	4.97	0.30	0.36	9.67	9.98	1.32	0.132	0.10	1685.60
U1418C 24H-5W 59-61	186.01	125.22	10.99	0.22	0.37	10.00	8.17	1.49	0.000	0.02	344.66
U1418C 25H-1W 124-126	192.11	129.32	8.21	0.27	0.38	10.29	9.35	1.39	0.027	0.02	297.04
U1418C 25H-5W 124-126	198.11	133.36	19.49	0.05	0.30	7.86	3.83	1.69	0.000	0.02	316.73
U1418D 20H-4W 134-146	202.11	136.06	18.11	0.03	0.26	6.46	3.34	1.42	0.000	0.01	253.64
U1418D 21H-2W 62-64	210.18	141.49	27.14	- 0.09	0.25	6.35	0.43	1.38	0.000	0.01	174.74
U1418C 27H-3W 134-136	218.13	146.84	20.33	0.01	0.27	6.94	2.96	1.71	0.000	0.02	328.96

Sample	Depth (m) CCSF-A	Age (ka)	C _{37:4} (%)	U ₃₇ ^K	U ₃₇ ^{K'}	SST (U ₃₇ ^K)	SST (U ₃₇ ^K)	K ₃₇ /K ₃₈	Alkenone concentration (µg g ⁻¹ TOC ⁻¹)	Alkenone/weight (µg g ⁻¹)	Alkenone
						Müller <i>et al.</i> , 1998	Prahl <i>et al.</i> , 1988				MAR (µg cm ⁻² ky ⁻¹)
U1418D 22H-2W 50-52	222.21	149.59	17.23	- 0.03	0.17	3.84	1.83	1.31	0.000	0.04	699.47
U1418A 30H-1W 145-150	229.93	154.78	26.09	0.02	0.39	10.35	3.20	1.62	0.000	0.00	0.00
U1418C 28H-5W 64-66	230.11	154.90	22.47	0.01	0.31	7.94	2.91	2.00	0.000	0.02	373.59
U1418A 32H-1 115- 130	240.89	162.16	22.99	0.04	0.35	9.13	3.50	1.94	0.000	0.00	0.00
U1418C 30H-3W 124-126	250.17	168.41	21.68	0.03	0.31	8.12	3.29	1.86	0.000	0.01	289.04
U1418D 25H-4W 84-86	255.76	172.17	15.12	0.11	0.31	8.17	5.47	1.48	0.014	0.01	184.43
U1418D 26H-3W 114-116	266.11	179.14	17.43	0.03	0.25	6.16	3.35	1.79	0.028	0.02	388.02

Sample	Depth (m) CCSF-A	Age (ka)	C _{37:4} (%)	U ₃₇ ^K	U ₃₇ ^{K'}	SST (U ₃₇ ^K)	SST (U ₃₇ ^K)	K ₃₇ /K ₃₈	Alkenone concentration (µg g ⁻¹ TOC ⁻¹)	Alkenone/weight (µg g ⁻¹)	Alkenone
						Müller <i>et al.</i> , 1998	Prahl <i>et al.</i> , 1988				MAR (µg cm ⁻² ky ⁻¹)
U1418D 26H-6W 64-66	270.12	181.84	15.28	0.06	0.25	6.19	4.04	1.75	0.000	0.01	191.85
U1418D 28H-2W 81-83	279.11	187.89	14.77	0.07	0.26	6.56	4.46	1.27	0.017	0.01	0.00
U1418D 30H-1W 94-96	287.14	193.30	10.86	0.14	0.28	7.19	6.16	1.48	0.026	0.01	0.00
U1418D 31H-2W 97-99	293.16	197.35	9.78	0.17	0.29	7.55	6.77	1.59	0.042	0.02	395.70
U1418D 32H-2W 21-23	297.14	200.05	7.00	0.18	0.27	6.84	7.12	1.42	0.020	0.01	0.00
U1418D 32H-3W 74-76	299.14	202.47	9.61	0.15	0.27	6.79	6.26	1.40	0.018	0.01	0.00
U1418D 34X-1W 4- 6	309.13	214.58	13.34	0.15	0.33	8.65	6.40	1.52	0.020	0.01	136.11

Sample	Depth (m) CCSF-A	Age (ka)	C _{37:4} (%)	U ₃₇ ^K	U ₃₇ ^{K'}	SST (U ₃₇ ^K)	SST (U ₃₇ ^K)	K ₃₇ /K ₃₈	Alkenone concentration (µg g ⁻¹ TOC ⁻¹)	Alkenone/weight (µg g ⁻¹)	Alkenone
						Müller <i>et al.</i> , 1998	Prahl <i>et al.</i> , 1988				MAR (µg cm ⁻² ky ⁻¹)
U1418D 34X-3W 104-106	313.13	219.43	12.62	0.17	0.34	8.99	6.88	1.41	0.000	0.00	0.00
U1418D 35H-4W 84-86	324.14	232.78	14.37	0.08	0.27	6.74	4.71	1.69	0.064	0.04	0.00
U1418D 36X-1W 57-60	329.13	238.82	14.60	0.15	0.34	9.05	6.26	1.73	0.000	0.01	157.41
U1418D 36X-4W 59-61	333.06	243.59	9.56	0.21	0.33	8.78	7.76	1.77	0.033	0.02	219.75
U1418F 5R-3W 94- 96	335.14	246.11	8.64	0.23	0.35	9.14	8.33	1.58	0.000	0.02	263.34
U1418F 6R-2W 74- 76	343.13	255.79	9.14	0.23	0.36	9.43	8.39	1.53	0.000	0.02	197.39
U1418F 7R-1W 51- 53	351.10	265.45	6.89	0.26	0.35	9.32	9.06	1.60	0.000	0.02	310.27

Sample	Depth (m) CCSF-A	Age (ka)	C _{37:4} (%)	U ^K ₃₇	U ^K _{37'}	SST (U ^K _{37'}) Müller <i>et al.</i> , 1998	SST (U ^K ₃₇) Prahl <i>et al.</i> , 1988	K ₃₇ /K ₃₈	Alkenone concentration (µg g ⁻¹ TOC ⁻¹)	Alkenone/weight (µg g ⁻¹)	Alkenone MAR (µg cm ⁻² ky ⁻¹)
U1418F 7R-4W 4-6	355.13	270.34	12.62	0.15	0.31	8.17	6.30	1.71	0.022	0.01	130.80
U1418F 9R-5W 14-16	376.13	295.79	12.44	0.11	0.27	6.84	5.39	1.71	0.041	0.02	239.61
U1418F 10R-2W 88-90	382.14	303.08	9.83	0.17	0.30	7.76	6.90	1.70	0.036	0.02	232.64
U1418F 10R-3W 132-135	384.11	305.47	6.10	0.20	0.28	7.12	7.62	1.87	0.000	0.10	1048.01
U1418F 10R-5W 44-46	386.13	307.92	10.17	0.19	0.32	8.44	7.30	1.50	0.000	0.02	196.14
U1418F 11R-4W 21-23	394.10	317.58	12.50	0.14	0.30	7.90	6.14	1.92	0.029	0.02	198.86
U1418F 12R-4W 54-56	404.13	329.73	18.16	0.12	0.36	9.70	5.51	1.64	0.000	0.01	122.79
U1418F 12R-7W 40-	408.20	334.67	18.81	0.02	0.26	6.43	3.10	1.69	0.000	0.01	163.25

Sample	Depth (m) CCSF-A	Age (ka)	C _{37:4} (%)	U ₃₇ ^K	U ₃₇ ^{K'}	SST (U ₃₇ ^K) Müller <i>et al.</i> , 1998	SST (U ₃₇ ^K) PrahI <i>et al.</i> , 1988	K ₃₇ /K ₃₈	Alkenone concentration (µg g ⁻¹ TOC ⁻¹)	Alkenone/weight (µg g ⁻¹)	Alkenone MAR (µg cm ⁻² ky ⁻¹)
42											
U1418F 14R-4W 140-150	424.39	354.29	11.04	0.24	0.39	10.49	8.52	1.64	0.000	0.01	145.77
U1418F 15R-3W 94- 96	432.13	363.67	10.58	0.18	0.31	8.19	6.98	1.77	0.000	0.02	225.02
U1418F 16R-2W 70- 73	440.11	373.35	9.83	0.16	0.29	7.51	6.72	1.74	0.000	0.01	188.84
U1418F 17R-2W 4-6	449.13	384.28	8.51	0.20	0.31	8.17	7.64	1.72	0.000	0.02	274.75
U1418F 17R-4W 102-104	453.13	389.13	8.49	0.19	0.30	7.62	7.24	1.75	0.000	0.01	197.72
U1418F 18R-2W 135-150	460.14	397.62	13.63	0.17	0.35	9.24	6.73	0.72	0.000	0.01	144.36
U1418F 19R-1W 113-115	468.12	410.47	13.81	0.07	0.24	6.06	4.41	1.20	0.000	0.03	313.78

Sample	Depth (m) CCSF-A	Age (ka)	C _{37:4} (%)	U ₃₇ ^K	U ₃₇ ^{K'}	SST (U ₃₇ ^K)	SST (U ₃₇ ^K)	K ₃₇ /K ₃₈	Alkenone concentration (µg g ⁻¹ TOC ⁻¹)	Alkenone/weight (µg g ⁻¹)	Alkenone
						Müller <i>et al.</i> , 1998	Prahl <i>et al.</i> , 1988				MAR (µg cm ⁻² ky ⁻¹)
U1418F 19R-7W 20-22	476.19	424.50	11.94	0.08	0.23	5.56	4.63	1.29	0.000	0.03	239.83
U1418F 20R-5W 141-143	484.13	438.31	11.68	0.08	0.22	5.40	4.59	1.43	0.000	0.02	229.28
U1418F 21R-5W 74-76	493.13	453.97	13.92	0.05	0.23	5.50	3.97	1.31	0.000	0.02	134.36
U1418F 22R-1W 104-106	498.13	462.66	12.56	0.15	0.31	8.16	6.31	1.75	0.000	0.00	0.00
U1418F 22R-3W 137-50	500.46	466.71	14.70	0.06	0.24	5.91	4.02	1.39	0.000	0.03	228.42
U1418F 22R-5W 104-106	503.13	471.36	13.67	0.06	0.23	5.52	4.06	1.52	0.000	0.03	285.94

A.3: N-alkane derived data Site U1417

Sample	Depth (m) CCSF-A	Age (Ma)	Aquatic ($\mu\text{g g}^{-1}$)	Terrestrial ($\mu\text{g g}^{-1}$)	Aquatic ($\mu\text{g g}^{-1}\text{TOC}^{-1}$)	Terrestrial ($\mu\text{g g}^{-1}\text{TOC}^{-1}$)	Aquatic ($\mu\text{g cm}^{-2}\text{Kyr}^{-1}$)	Terrestrial ($\mu\text{g cm}^{-2}\text{Kyr}^{-1}$)	TAR	CPI (1)
U1417D 1H-1W 44-48	2.44	0.02	0.23	0.30	0.00	0.00	1.79	2.27	1.27	1.12
U1417D 1H-3W 49-53	3.51	0.02	0.77	0.93	0.00	0.00	6.33	7.68	1.21	1.53
U1417C 2H-2W 49-53	7.29	0.05	0.49	0.32	0.00	0.00	4.30	2.83	0.66	0.95
U1417D 2H-2W 31-35	8.63	0.06	0.71	1.10	0.00	0.00	6.65	10.21	1.54	1.56
U1417D 2H-3W 113-117	12.93	0.08	0.27	0.47	0.00	0.00	2.63	4.60	1.75	1.19
U1417D 2H-5W 69-73	13.51	0.09	0.43	0.66	0.00	0.00	4.43	6.89	1.55	1.65
U1417D 3H-5W 69-73	13.51	0.09	0.69	1.32	1.11	2.13	7.55	14.44	1.91	1.46
U1417C 3H-2W 86-90	18.00	0.12	0.43	0.37	0.00	0.00	4.92	4.26	0.87	1.10
U1417C-3H-4W 21-25	18.55	0.12	0.25	0.88	0.55	1.93	2.98	10.54	3.54	1.44
U1417D 3H-5W 25-29	23.49	0.15	0.53	0.90	1.09	1.86	6.85	11.70	1.71	1.49
U1417C 4H-2W 92-94	26.00	0.17	0.42	0.81	0.74	1.44	5.63	10.94	1.94	1.54
U1417C 4H-4W 44-48	28.54	0.18	0.38	0.73	0.70	1.36	5.27	10.25	1.95	1.39
U1417D 4H-2W 22-26	30.00	0.19	0.37	1.18	0.77	2.44	5.41	17.11	3.16	1.35
U1417D 4H-2W 122-126	31.00	0.20	0.39	0.74	0.40	0.76	5.82	11.11	1.91	1.43
U1417D 4H-3W 72-76	32.00	0.21	0.30	0.79	0.69	1.79	4.68	12.16	2.60	1.40
U1417C 5H-2W 140-144	34.98	0.22	0.53	1.10	0.89	1.85	8.34	17.44	2.09	1.58
U1417C 5H-4W 93-97	39.49	0.25	0.27	0.30	0.00	0.00	4.88	5.43	1.11	1.11

Sample	Depth (m) CCSF-A	Age (Ma)	Aquatic ($\mu\text{g g}^{-1}$)	Terrestrial ($\mu\text{g g}^{-1}$)	Aquatic ($\mu\text{g g}^{-1}\text{TOC}^{-1}$)	Terrestrial ($\mu\text{g g}^{-1}\text{TOC}^{-1}$)	Aquatic ($\mu\text{g cm}^{-2}\text{Kyr}^{-1}$)	Terrestrial ($\mu\text{g cm}^{-2}\text{Kyr}^{-1}$)	TAR	CPI (1)
U1417C 5H-5W 138-142	41.44	0.27	0.36	0.36	0.00	0.00	6.97	6.90	0.99	0.91
U1417D 5H-5W 97-101	45.31	0.29	0.46	0.51	0.00	0.00	8.72	9.59	1.10	1.10
U1417C 6H-4W 117-121	50.45	0.32	0.33	0.67	0.00	0.00	5.97	12.16	2.04	1.11
U1417D 6H-5W 77-81	55.46	0.36	0.35	0.17	0.00	0.00	6.12	2.94	0.48	0.29
U1417D 7H-2W 20-24	65.53	0.42	0.51	0.34	0.00	0.00	8.78	5.82	0.66	1.14
U1417A 9H-3W 12-16	70.48	0.45	0.26	0.26	0.00	0.00	4.23	4.31	1.02	1.08
U1417B 20H-2W 83-87	196.31	1.50	1.20	1.20	0.00	0.00	12.93	12.92	1.00	1.57
U1417B 20H-2W 113-117	196.61	1.50	0.40	0.58	0.00	0.00	4.30	6.26	1.46	1.53
U1417B 20H-2W 142-146	196.91	1.50	0.00	0.00	0.00	0.00	0.00	0.00	0.00	0.00
U1417B 20H-3W 23-27	197.21	1.51	0.00	0.00	0.00	0.00	0.00	0.00	1.73	1.62
U1417B 20H-3W 55-59	197.53	1.51	0.00	0.00	0.00	0.00	0.00	0.00	0.00	0.00
U1417B 20H-3W 83-87	197.81	1.51	0.00	0.00	0.00	0.00	0.00	0.00	2.67	1.40
U1417B 20H-3W 113-117	198.11	1.52	0.00	0.00	0.00	0.00	0.00	0.00	0.00	0.00
U1417B 20H-3W 143-147	198.41	1.52	0.00	0.00	0.00	0.00	0.00	0.00	0.00	0.00
U1417B 20H-4W 22-26	198.70	1.52	0.24	0.68	0.00	0.00	2.70	7.66	2.84	1.55
U1417B 20H-4W 52-56	199.00	1.53	0.46	0.50	0.00	0.00	5.15	5.57	1.08	1.70
U1417B 20H-4w 82-86	199.30	1.53	0.00	0.00	0.00	0.00	0.00	0.00	0.00	0.00
U1417B 20H-4W 119-123	199.65	1.53	1.06	0.90	0.00	0.00	12.05	10.19	0.85	2.14
U1417B 20H-4w 142-146	199.90	1.53	0.00	0.00	0.00	0.00	0.00	0.00	0.00	0.00
U1417B 20H-5W 22-26	200.20	1.54	0.92	0.87	0.00	0.00	10.45	9.88	0.95	1.58
U1417B 20H-5W 52-56	200.50	1.54	0.95	0.74	0.00	0.00	10.87	8.50	0.78	1.30
U1417B 20H-5w 82-86	200.80	1.54	0.00	0.00	0.00	0.00	0.00	0.00	0.00	0.00

Sample	Depth (m) CCSF-A	Age (Ma)	Aquatic ($\mu\text{g g}^{-1}$)	Terrestrial ($\mu\text{g g}^{-1}$)	Aquatic ($\mu\text{g g}^{-1}\text{TOC}^{-1}$)	Terrestrial ($\mu\text{g g}^{-1}\text{TOC}^{-1}$)	Aquatic ($\mu\text{g cm}^{-2}\text{Kyr}^{-1}$)	Terrestrial ($\mu\text{g cm}^{-2}\text{Kyr}^{-1}$)	TAR	CPI (1)
U1417B 20H-5w 116-120	201.14	1.55	0.00	0.00	0.00	0.00	0.00	0.00	0.00	0.00
U1417B 20H-5W 142-146	201.40	1.55	0.75	0.77	0.00	0.00	8.65	8.93	1.03	1.52
U1417B 20H-6W 24-28	201.72	1.55	0.75	0.59	0.00	0.00	8.73	6.91	0.79	1.54
U1417B 20H-6W 54-58	202.02	1.56	0.50	0.74	0.00	0.00	5.84	8.64	1.48	1.52
U1417B 20H-6W 84-88	202.32	1.56	0.30	0.43	0.00	0.00	3.51	5.03	1.43	1.54
U1417B 20H-6w 114-118	202.62	1.56	0.00	0.00	0.00	0.00	0.00	0.00	0.00	0.00
U1417B 20H-7W 12-16	202.90	1.57	0.26	0.49	0.00	0.00	2.53	4.79	1.89	1.51
U1417D 24H2W 9-13	203.21	1.57	0.00	0.00	0.00	0.00	0.00	0.00	0.00	0.00
U1417D 24H-2W 39-43	203.51	1.57	0.00	0.00	0.00	0.00	0.00	0.00	0.00	0.00
U1417D 24H-2W 69-73	203.81	1.57	0.00	0.00	0.00	0.00	0.00	0.00	0.00	0.00
U1417D 24H-2W 99-103	204.11	1.58	0.00	0.00	0.00	0.00	0.00	0.00	0.00	0.00
U1417D 24H-2W 130-134	204.41	1.58	0.00	0.00	0.00	0.00	0.00	0.00	0.00	0.00
U1417D 24H-3W 9-13	204.71	1.58	0.00	0.00	0.00	0.00	0.00	0.00	0.00	0.00
U1417C 21H-4W 2-6	205.03	1.59	0.00	0.00	0.00	0.00	0.00	0.00	0.00	0.00
U1417C 21H-4W 28-32	205.30	1.59	0.00	0.00	0.00	0.00	0.00	0.00	0.00	0.00
U1417C 21H-4W 62-66	205.60	1.59	0.00	0.00	0.00	0.00	0.00	0.00	0.00	0.00
U1417D 21H-4W 88-92	205.90	1.60	0.00	0.00	0.00	0.00	0.00	0.00	0.00	0.00
U1417C 21H-4W 118-122	206.20	1.60	0.00	0.00	0.00	0.00	0.00	0.00	0.00	0.00
U1417D 25H-1W 54-58	206.50	1.60	0.00	0.00	0.00	0.00	0.00	0.00	0.00	0.00
U1417D 25H-1W 84-88	206.80	1.61	0.00	0.00	0.00	0.00	0.00	0.00	0.00	0.00
U1417D 25H-1W 114-118	207.10	1.61	0.00	0.00	0.00	0.00	0.00	0.00	0.00	0.00
U1417D 25H-1W 144-148	207.40	1.61	0.00	0.00	0.00	0.00	0.00	0.00	0.00	0.00

Sample	Depth (m) CCSF-A	Age (Ma)	Aquatic ($\mu\text{g g}^{-1}$)	Terrestrial ($\mu\text{g g}^{-1}$)	Aquatic ($\mu\text{g g}^{-1}\text{TOC}^{-1}$)	Terrestrial ($\mu\text{g g}^{-1}\text{TOC}^{-1}$)	Aquatic ($\mu\text{g cm}^{-2}\text{Kyr}^{-1}$)	Terrestrial ($\mu\text{g cm}^{-2}\text{Kyr}^{-1}$)	TAR	CPI (1)
U1417D 25H-2W 25-29	207.71	1.62	0.00	0.00	0.00	0.00	0.00	0.00	0.00	0.00
U1417D 25H-2W 55-59	208.01	1.62	0.00	0.00	0.00	0.00	0.00	0.00	0.00	0.00
U1417D 25H-2W 85-89	208.31	1.62	0.00	0.00	0.00	0.00	0.00	0.00	0.00	0.00
U1417D 25H-2W 118-122	208.61	1.62	0.00	0.00	0.00	0.00	0.00	0.00	0.00	0.00
U1417D 25H-2W 145-149	208.91	1.63	0.00	0.00	0.00	0.00	0.00	0.00	0.00	0.00
U1417D 25H-3W 26-30	209.22	1.63	1.19	3.07	2.64	6.78	12.49	32.13	2.57	2.12
U1417D 25H-3W 51-55	209.47	1.63	0.00	0.00	0.00	0.00	0.00	0.00	0.00	0.00
U1417B 22H-3W 1-4	209.82	1.64	0.00	0.00	0.00	0.00	0.00	0.00	0.00	0.00
U1417B 22H-3W 18-21	210.08	1.64	0.69	0.70	0.00	0.00	7.00	7.08	1.01	2.12
U1417B 22H-3W 59-63	210.40	1.64	0.44	0.62	0.00	0.00	4.43	6.19	1.40	1.72
U1417B 22H-3W 93-95	210.70	1.65	0.00	0.00	0.00	0.00	0.00	0.00	0.00	0.00
U1417B 22H-4W 15-19	211.00	1.65	0.25	0.57	0.00	0.00	2.42	5.50	2.28	1.45
U1417B 22H-4W 45-46	211.30	1.65	0.65	0.77	0.00	0.00	6.18	7.25	1.17	1.20
U1417D 26H-1W 34-38	211.60	1.66	0.00	0.00	0.00	0.00	0.00	0.00	0.00	0.00
U1417D 26H-1W 64-68	211.90	1.66	0.00	0.00	0.00	0.00	0.00	0.00	0.00	0.00
U1417D 26H-1W 90-94	212.20	1.66	#DIV/0!	0.00	0.00	0.00	#DIV/0!	0.00	0.00	0.00
U1417D 26H-1W 124-128	212.50	1.66	0.00	0.00	0.00	0.00	0.00	0.00	0.00	0.00
U1417D 26H-2W 5-9	212.81	1.67	#DIV/0!	0.00	0.00	0.00	#DIV/0!	0.00	0.00	0.00
U1417D 26H-2W 35-39	213.11	1.67	#DIV/0!	0.00	0.00	0.00	#DIV/0!	0.00	0.00	0.00
U1417D 27H-1W 87-91	217.35	1.71	0.11	0.20	0.00	0.00	1.14	2.13	1.87	1.38
U1417D 28H-1W 31-35	220.62	1.75	0.00	0.00	0.00	0.00	0.00	0.00	0.00	0.00
U1417D 29H-1W 106-110	223.83	1.78	0.00	0.00	0.00	0.00	0.00	0.00	0.00	0.00

Sample	Depth (m) CCSF-A	Age (Ma)	Aquatic ($\mu\text{g g}^{-1}$)	Terrestrial ($\mu\text{g g}^{-1}$)	Aquatic ($\mu\text{g g}^{-1}\text{TOC}^{-1}$)	Terrestrial ($\mu\text{g g}^{-1}\text{TOC}^{-1}$)	Aquatic ($\mu\text{g cm}^{-2}\text{Kyr}^{-1}$)	Terrestrial ($\mu\text{g cm}^{-2}\text{Kyr}^{-1}$)	TAR	CPI (1)
U1417D 29H-CCW 15-19	227.06	1.81	1.00	3.41	0.00	0.00	9.93	33.84	3.41	2.39
U1417D 30H-2W 63-67	230.10	1.85	0.80	3.36	0.00	0.00	7.35	30.74	4.18	1.87
U1417D 30H-CCW 5-9	232.47	1.87	0.65	0.63	0.00	0.00	5.93	5.79	0.98	1.58
U1417D 31H-1W 39-43	237.90	1.93	0.74	0.63	0.00	0.00	6.75	5.78	0.86	1.64
U1417D 32H-1W 23-27	242.00	1.97	0.73	3.36	0.00	0.00	6.67	30.66	4.59	1.94
U1417D 32H-2W 17-21	243.44	1.98	0.72	0.77	0.00	0.00	7.66	8.26	1.08	1.60
U1417D 32H-CCW 13-17	246.64	2.01	0.40	0.40	0.00	0.00	7.54	7.71	1.02	1.52
U1417D 34H 2W 55-59	249.95	2.03	0.65	3.91	0.00	0.00	11.37	68.33	6.01	2.09
U1417D 35H-1W 18-22	253.90	2.06	0.77	0.69	0.00	0.00	16.38	14.68	0.90	1.58
U1417D 35H-2W 102-106	256.24	2.07	0.96	3.34	0.00	0.00	19.31	67.28	3.48	2.37
U1417D 36H-1W 59-63	259.72	2.09	0.37	0.61	0.00	0.00	7.68	12.61	1.64	1.51
U1417D 36H-3W 84-88	262.97	2.11	1.27	2.32	0.00	0.00	27.42	49.94	1.82	1.67
U1417D 39X-1W 19-23	277.07	2.20	0.76	3.55	2.02	9.49	16.13	75.83	4.70	2.57
U1417D 40X-2W 37-41	288.45	2.28	0.50	4.31	0.00	0.00	9.70	83.98	8.66	2.84
U1417D 41X-4W 35-39	301.13	2.36	0.91	3.11	2.17	7.45	18.32	62.86	3.43	1.96
U1417D 42X-1W 94-98	306.88	2.40	0.20	0.81	0.55	2.26	3.76	15.32	4.08	1.46
U1417D 42X-3W 23-27	309.21	2.41	0.29	0.45	0.00	0.00	5.76	8.99	1.56	1.44
U1417D 42X-3W 83-87	309.81	2.41	0.12	0.37	0.00	0.00	2.38	7.44	3.12	1.32
U1417D 42X-4W 26-30	310.42	2.42	0.20	0.45	0.00	0.00	3.97	8.99	2.27	1.80
U1417D 42X-CCW 23-27	310.99	2.42	0.23	0.73	0.00	0.00	4.68	14.88	3.18	1.68
U1417D 43X-1W 10-14	315.78	2.45	0.25	0.28	0.68	0.76	5.21	5.85	1.12	1.50
U1417D 43X-1W 70-74	316.38	2.46	0.38	0.31	0.00	0.00	7.95	6.57	0.83	1.40

Sample	Depth (m) CCSF-A	Age (Ma)	Aquatic ($\mu\text{g g}^{-1}$)	Terrestrial ($\mu\text{g g}^{-1}$)	Aquatic ($\mu\text{g g}^{-1}\text{TOC}^{-1}$)	Terrestrial ($\mu\text{g g}^{-1}\text{TOC}^{-1}$)	Aquatic ($\mu\text{g cm}^{-2}\text{Kyr}^{-1}$)	Terrestrial ($\mu\text{g cm}^{-2}\text{Kyr}^{-1}$)	TAR	CPI (1)
U1417D 43X-1W 127-131	316.98	2.46	0.17	0.24	0.00	0.00	3.61	5.15	1.43	1.53
U1417D 43X-2W 55-59	317.58	2.46	0.24	0.29	0.00	0.00	4.96	5.88	1.19	1.37
U1417D 43X-2W 114-118	318.17	2.47	0.24	0.35	0.00	0.00	4.88	7.11	1.46	1.83
U1417D 43X-3W 27-31	318.78	2.47	0.29	0.59	0.00	0.00	5.68	11.44	2.01	1.58
U1417D 43W-3W 87-91	319.38	2.48	0.46	0.42	0.00	0.00	8.90	8.07	0.91	1.57
U1417D 43X-4W 10-14	319.98	2.48	0.65	0.47	0.00	0.00	12.10	8.70	0.72	1.65
U1417D 43X-4W 63-67	320.55	2.48	0.14	0.20	0.48	0.67	2.66	3.67	1.38	2.11
U1417D 43X-4W 125-129	321.17	2.49	0.89	0.37	0.00	0.00	16.51	6.88	0.42	1.47
U1417D 43X-5W 34-38	321.78	2.49	0.49	0.30	0.00	0.00	9.35	5.70	0.61	1.66
U1417D 43X-CCW 41-45	322.34	2.49	0.55	0.38	0.00	0.00	10.77	7.42	0.69	1.94
U1417D 44X-1W 18-23	325.39	2.53	0.63	1.25	1.36	2.71	7.47	14.82	1.98	1.63
U1417D 44X-1W 70-74	326.00	2.53	0.65	0.75	1.54	1.79	7.66	8.87	1.16	1.55
U1417D 44X-1W 104-108	326.57	2.54	0.52	0.79	1.43	2.14	6.20	9.29	1.50	1.62
U1417D 45X-1W 9-13	329.98	2.58	0.21	0.68	0.76	2.42	2.45	7.83	3.19	1.48
U1417D 45X-1W 60-64	330.57	2.59	0.41	0.78	0.00	0.00	4.66	8.93	1.92	1.38
U1417D 45X-1W 123-127	331.20	2.59	0.12	0.46	0.92	3.55	1.37	5.30	3.87	1.25
U1417D 45X-2W 46-50	331.81	2.60	0.57	0.97	3.88	6.60	7.11	12.10	1.70	1.55
U1417D 45X-2W 62-66	331.98	2.60	0.46	0.99	1.18	2.54	5.72	12.36	2.16	1.91
U1417D 45X-2W 70-74	332.17	2.60	0.54	0.74	1.20	1.64	6.72	9.17	1.36	1.76
U1417D 46X-1W 0-4	336.66	2.66	2.58	8.67	4.06	13.63	31.58	106.14	3.36	1.96
U1417D 46X-1W 31-35	336.96	2.66	0.20	0.43	0.00	0.00	2.42	5.27	2.18	1.39
U1417D 46X-1W 60-64	337.26	2.66	0.09	0.56	0.25	1.60	1.07	6.81	6.38	1.19

Sample	Depth (m) CCSF-A	Age (Ma)	Aquatic ($\mu\text{g g}^{-1}$)	Terrestrial ($\mu\text{g g}^{-1}$)	Aquatic ($\mu\text{g g}^{-1}\text{TOC}^{-1}$)	Terrestrial ($\mu\text{g g}^{-1}\text{TOC}^{-1}$)	Aquatic ($\mu\text{g cm}^{-2}\text{Kyr}^{-1}$)	Terrestrial ($\mu\text{g cm}^{-2}\text{Kyr}^{-1}$)	TAR	CPI (1)
U1417D 46X-1W 96-100	337.56	2.67	0.29	0.52	0.81	1.45	3.57	6.35	1.78	1.61
U1417D 46X-1W 119-123	337.86	2.67	0.58	0.73	1.47	1.86	7.05	8.93	1.27	1.38
U1417D 46X-3W 1-5	338.30	2.68	0.29	0.57	0.00	0.00	3.75	7.35	1.96	1.72
U1417D 46X-3W 21-25	338.46	2.68	0.37	0.73	1.10	2.16	4.78	9.41	1.97	1.70
U1417D 46X-3W 46-50	338.76	2.68	0.09	0.49	0.23	1.33	1.10	6.30	5.73	1.23
U1417D 46X-3W 80-84	339.07	2.69	0.45	0.64	1.51	2.15	5.77	8.23	1.43	1.26
U1417D 46X-3W 106-110	339.36	2.69	0.17	0.74	0.00	0.00	2.14	9.48	4.43	1.53
U1417D 46X-3W 138-142	339.66	2.69	0.72	0.75	1.51	1.58	9.23	9.68	1.05	1.63
U1417D 47X-1W 17-21	348.85	2.80	2.72	7.20	6.44	17.02	23.88	63.12	2.64	1.53
U1417D 47X-2W 6-10	349.38	2.81	0.00	0.00	0.00	0.00	0.00	0.00	0.00	0.00
U1417D 47X-2W 63-69	349.98	2.81	0.37	0.85	1.12	2.57	3.24	7.45	2.30	1.40
U1417D 47X-3W 29-33	350.56	2.82	0.12	0.52	0.00	0.00	1.01	4.59	4.55	1.51
U1417D 47X-3W 59-63	350.87	2.82	0.36	0.99	1.70	4.65	3.18	8.70	2.74	1.26
U1417D 48X-1W 29-33	358.47	2.91	0.14	0.60	0.71	3.15	1.30	5.74	4.43	1.26
U1417D 48X-1W 69-73	359.07	2.92	0.20	1.01	0.40	2.02	1.93	9.70	5.04	1.54
U1417D 48X-2W 0-4	359.69	2.93	0.20	0.72	0.64	2.28	1.94	6.93	3.57	1.52
U1417D 48X-2W 63-68	360.27	2.94	0.11	0.54	0.51	2.39	1.10	5.17	4.72	1.24
U1417D 48X-2W 106-110	360.79	2.94	0.21	0.84	0.96	3.78	2.05	8.04	3.93	1.30
U1417D 49X-1W 35-39	368.17	3.04	0.28	0.61	0.66	1.46	1.97	4.35	2.21	1.57
U1417D 49X-1W 69-73	368.77	3.05	0.14	0.66	0.65	3.14	0.97	4.69	4.85	1.26
U1417D 49X-2W 17-21	369.37	3.06	0.00	0.00	0.00	0.00	0.00	0.00	0.00	0.00
U1417D 49X-2W 79-83	369.97	3.06	0.13	0.95	0.65	4.76	0.92	6.74	7.31	1.21

Sample	Depth (m) CCSF-A	Age (Ma)	Aquatic ($\mu\text{g g}^{-1}$)	Terrestrial ($\mu\text{g g}^{-1}$)	Aquatic ($\mu\text{g g}^{-1}\text{TOC}^{-1}$)	Terrestrial ($\mu\text{g g}^{-1}\text{TOC}^{-1}$)	Aquatic ($\mu\text{g cm}^{-2}\text{Kyr}^{-1}$)	Terrestrial ($\mu\text{g cm}^{-2}\text{Kyr}^{-1}$)	TAR	CPI (1)
U1417D 49X-2W 134-138	370.56	3.07	0.00	0.00	0.00	0.00	0.00	0.00	0.00	0.00
U1417D 49X-3W 49-53	371.16	3.08	0.00	0.00	0.00	0.00	0.00	0.00	0.00	0.00
U1417D 50X-1W 27-31	378.05	3.19	0.00	0.00	0.00	0.00	0.00	0.00	0.00	0.00
U1417D 50X-1W 55-59	378.33	3.19	0.00	0.00	0.00	0.00	0.00	0.00	0.00	0.00
U141D 50X-1W 116-120	378.96	3.20	0.00	0.00	0.00	0.00	0.00	0.00	0.00	0.00
U1417D 50X-2W 44-48	379.56	3.21	0.00	0.00	0.00	0.00	0.00	0.00	0.00	0.00
U1417D 50X-2W 93-97	380.08	3.22	0.48	4.56	0.00	0.00	4.12	39.48	9.59	2.40
U1417D 50X-3W 6-10	380.66	3.23	0.00	0.00	0.00	0.00	0.00	0.00	0.00	0.00
U1417D 50X-3W 54-58	381.19	3.24	0.00	0.00	0.00	0.00	0.00	0.00	0.00	0.00
U1417D 50X-3W 102-106	381.72	3.25	0.00	0.00	0.00	0.00	0.00	0.00	0.00	0.00
U1417D 50X-4W 51-55	382.27	3.25	0.00	0.00	0.00	0.00	0.00	0.00	0.00	0.00
U1417D 51X-1W 9-13	387.57	3.34	0.12	0.93	0.55	4.22	0.88	6.71	7.60	1.25
U1417D 51X-1W 65-69	388.13	3.34	0.19	1.39	0.52	3.76	1.38	10.01	7.27	1.30
U1417D 51X-1W 124-128	388.72	3.35	0.19	1.46	0.70	5.44	1.34	10.50	7.82	1.30
U1417D 51X-2W 40-44	389.38	3.36	0.11	1.24	0.57	6.32	0.66	7.35	11.10	1.20
U1417D 51X-3W 11-15	390.00	3.37	0.11	1.21	0.82	8.77	0.69	7.37	10.71	1.19
U1417D 51X-3W 103-107	390.59	3.38	0.19	1.34	0.54	3.81	1.16	8.17	7.06	1.46
U1417D 51X-4W 11-15	391.24	3.39	0.10	0.96	0.75	7.54	0.60	6.07	10.09	1.20
U1417D 51X-4W 68-72	391.81	3.40	0.14	1.38	0.41	4.09	0.86	8.67	10.05	1.40
U1417D 51X-4W 128-132	392.41	3.41	0.21	3.10	0.71	10.19	1.35	19.56	14.45	1.22
U1417D 52X-1W 19-23	397.37	3.49	0.07	1.19	0.00	0.00	0.60	10.22	16.97	1.17
U1417D 52X-1W 59-63	397.77	3.49	0.13	1.03	0.00	0.00	1.12	8.86	7.92	1.30

Sample	Depth (m) CCSF-A	Age (Ma)	Aquatic ($\mu\text{g g}^{-1}$)	Terrestrial ($\mu\text{g g}^{-1}$)	Aquatic ($\mu\text{g g}^{-1}\text{TOC}^{-1}$)	Terrestrial ($\mu\text{g g}^{-1}\text{TOC}^{-1}$)	Aquatic ($\mu\text{g cm}^{-2}\text{Kyr}^{-1}$)	Terrestrial ($\mu\text{g cm}^{-2}\text{Kyr}^{-1}$)	TAR	CPI (1)
U1417D 52X-1W 97-101	398.15	3.50	0.18	1.92	0.00	0.00	1.58	16.45	10.42	1.22
U1417D 52X-1W 134-138	398.57	3.51	0.11	0.99	0.00	0.00	0.58	5.21	8.93	1.19
U1417D 52X-2W 33-37	398.98	3.52	0.00	0.00	0.00	0.00	0.00	0.00	0.00	0.00
U1417D 52X-2W 69-73	399.34	3.53	0.15	0.91	0.70	4.24	0.55	3.31	6.03	1.27
U1417D 52X-2W 109-113	399.74	3.54	0.15	1.26	0.54	4.53	0.55	4.58	8.37	1.63
U1417D 52X-3W 40-44	400.28	3.55	0.18	0.89	0.00	0.00	0.69	3.43	5.00	1.42
U1417D 52X-3W 69-73	400.57	3.56	0.11	1.79	0.75	11.81	0.44	6.89	15.79	1.23
U1417D 52X-3W 102-106	400.90	3.57	0.18	1.41	1.09	8.57	0.69	5.43	7.89	1.38
U1417D 53X-1W 19-23	407.04	3.72	0.09	0.98	0.00	0.00	0.32	3.57	11.31	1.23
U1417D 53X-1W 60-65	407.60	3.73	0.15	1.26	0.68	5.69	0.55	4.58	8.37	1.34
U1417D 53X-2W 41-45	408.30	3.75	0.29	3.58	0.26	3.24	1.40	17.54	12.54	1.57
U1417D 54X-1W 16-20	416.74	3.96	0.26	1.74	0.00	0.00	0.95	6.22	6.58	1.24
U1417D 54X-1W 76-80	417.34	3.98	0.12	0.57	0.00	0.00	0.42	2.04	4.85	1.34
U1417D 54X-2W 36-40	418.42	4.00	0.09	0.90	0.00	0.00	0.41	4.02	9.78	1.24
U1417D 54X-3W 10-14	419.04	4.02	0.11	1.09	0.00	0.00	0.47	4.64	9.98	1.19
U1417D 54X-3W 59-63	419.63	4.03	0.20	1.09	0.00	0.00	0.85	4.65	5.44	1.54
U1417D 54X-3W 119-123	420.23	4.05	0.26	1.17	0.00	0.00	1.12	5.01	4.49	1.35
U1417D 54X-4W 29-33	420.81	4.06	0.26	1.79	0.00	0.00	1.23	8.61	7.02	1.39
U1417D 54X-4W 70-74	421.38	4.08	0.24	3.17	0.00	0.00	1.13	15.21	13.43	1.32
U1417E 9R-2	464.59	5.07	0.08	0.80	0.00	0.00	0.36	3.45	9.71	1.18
U1417E 10R-2	474.29	5.25	0.29	0.90	0.00	0.00	2.11	6.51	3.08	2.21
U1417E 13R-1	501.91	5.75	0.41	0.75	0.00	0.00	3.72	6.82	1.83	2.00

Sample	Depth (m) CCSF-A	Age (Ma)	Aquatic ($\mu\text{g g}^{-1}$)	Terrestrial ($\mu\text{g g}^{-1}$)	Aquatic ($\mu\text{g g}^{-1}\text{TOC}^{-1}$)	Terrestrial ($\mu\text{g g}^{-1}\text{TOC}^{-1}$)	Aquatic ($\mu\text{g cm}^{-2}\text{Kyr}^{-1}$)	Terrestrial ($\mu\text{g cm}^{-2}\text{Kyr}^{-1}$)	TAR	CPI (1)
U1417E 14R-1	510.28	5.90	0.47	1.07	0.00	0.00	3.95	9.03	2.29	2.28
U1417E 15R-4	525.73	6.09	0.08	0.50	0.00	0.00	2.14	13.74	6.40	1.32
U1417E 20R-1	569.79	6.49	0.48	1.19	0.00	0.00	7.03	17.44	2.48	2.81

A.4: N-alkane derived proxies Site U1418

Sample	U1418 Age (Kyr)	Depth (m) CCSF-A	Aquatic ($\mu\text{g g}^{-1}$)	Terrestrial ($\mu\text{g g}^{-1}$)	Aquatic Only ($\mu\text{g g}^{-1}\text{TOC}^{-1}$)	Terrestrial only ($\mu\text{g g}^{-1}\text{TOC}^{-1}$)	Aquatic MAR	Terrestrial MAR	TAR	CPI (1)
U1418B 1H-1 145-150	0.97	1.43	0.00	0.00	#DIV/0!	#DIV/0!	0.00	0.00	0.00	0.00
U1418B 2H-1W 145-150	7.46	11.09	0.00	0.00	#DIV/0!	#DIV/0!	0.00	0.00	0.00	0.00
U1418A 3H-2 145-150	14.17	21.05	0.53	0.38	#DIV/0!	#DIV/0!	88.79	64.48	0.73	1.65
U1418A 4H-4 145-150	23.07	34.26	0.00	0.00	#DIV/0!	#DIV/0!	0.00	0.00	0.10	1.70
U1418D 6H-3W 44-46	33.77	50.16	0.23	0.74	#DIV/0!	#DIV/0!	41.61	132.50	3.18	0.95
U1418A 6H-3 145-150	36.92	54.84	0.00	0.00	0.00	0.00	0.00	0.00	0.00	0.00
U1418D 8H-2W 144-146	47.22	70.14	0.47	0.23	#DIV/0!	#DIV/0!	92.19	44.64	0.48	1.83
U1418D 9H-2W 43-45	52.67	78.24	0.00	0.00	#DIV/0!	#DIV/0!	0.00	0.00	0.00	0.00
U1418A 9H-3W 112-114	58.01	86.17	0.35	0.65	0.56	1.04	64.58	120.40	1.86	1.43
U1418A 9H-3W 145-150	58.22	86.49	0.00	0.00	0.00	0.00	0.00	0.00	0.00	0.00
U1418E 2H-2W 64-66	60.67	90.13	0.28	0.66	0.50	1.18	47.15	110.90	2.35	1.42
U1418E 2H-5W 14-16	63.37	94.13	0.28	0.53	0.45	0.84	42.57	80.13	1.88	1.58
U1418A 10H-5W 120-122	66.10	98.19	0.49	1.10	0.62	1.41	94.45	213.83	2.26	2.31

Sample	U1418 Age (Kyr)	Depth (m) CCSF-A	Aquatic ($\mu\text{g g}^{-1}$)	Terrestrial ($\mu\text{g g}^{-1}$)	Aquatic Only ($\mu\text{g g}^{-1}$ TOC ⁻¹)	Terrestrial only ($\mu\text{g g}^{-1}$ TOC ⁻¹)	Aquatic MAR	Terrestrial MAR	TAR	CPI (1)
U1418D 11H-4W 129-131	69.96	103.93	0.00	0.00	#DIV/0!	#DIV/0!	0.00	0.00	0.00	0.00
U1418A 11H-3 145-150	71.29	105.90	0.00	0.00	0.00	0.00	0.00	0.00	0.00	0.00
U1418D 11H-6W 54-56	71.48	106.18	0.00	0.00	#DIV/0!	#DIV/0!	0.00	0.00	0.00	0.00
U1418E 5H-2W 117-119	76.89	114.21	0.81	1.13	1.42	1.99	153.69	215.18	1.40	1.43
U1418E 5H-5W 61-63	79.52	118.12	0.29	0.82	0.69	1.94	57.06	160.12	2.81	1.50
U1418E 6H-3W 4-6	84.90	126.12	0.25	0.59	0.55	1.32	46.14	110.83	2.40	1.66
U1418E 6H-5W 104-106	87.59	130.12	0.46	1.00	0.92	1.99	92.35	199.84	2.16	1.39
U1418D 14H-5W 105-107	93.03	138.19	0.00	0.00	0.00	0.00	0.00	0.00	0.00	0.00
U1418A 14H-2 145-150	93.37	138.71	0.00	0.00	#DIV/0!	#DIV/0!	0.00	0.00	0.00	0.00
U1418A 16H-2 145-150	100.44	149.20	0.66	0.43	#DIV/0!	#DIV/0!	125.46	81.25	0.65	1.23
U1418D 16H-2W 113-115	103.75	154.12	0.00	0.00	#DIV/0!	#DIV/0!	0.00	0.00	0.00	0.00
U1418C 22H-4W 24-26	107.83	160.18	0.43	0.51	0.73	0.88	84.94	101.93	1.20	1.53
U1418D 17H-1W 94-96	110.47	164.10	0.40	1.27	#DIV/0!	#DIV/0!	72.78	230.63	3.17	1.33
U1418D 17H-5W 140-142	114.58	170.21	0.00	0.00	#DIV/0!	#DIV/0!	0.00	0.00	0.00	0.00
U1418A 20H-2 145-150	115.84	172.08	0.00	0.00	0.00	0.00	0.00	0.00	0.00	0.00
U1418C 23H-3W 84-86	115.89	172.16	0.00	0.00	#DIV/0!	#DIV/0!	0.00	0.00	0.00	0.00
U1418C 24H-2W 124-126	122.63	182.16	0.07	1.36	#DIV/0!	#DIV/0!	12.16	252.30	20.74	1.24
U1418C 24H-3W 146-148	123.78	183.88	0.00	0.00	0.00	0.00	0.00	0.00	0.00	0.00
U1418C 24H-5W 59-61	125.22	186.01	0.27	1.04	#DIV/0!	#DIV/0!	51.72	201.67	3.90	1.00
U1418C 25H-1W 124-126	129.32	192.11	0.00	0.00	#DIV/0!	#DIV/0!	0.00	0.00	0.00	0.00
U1418C 25H-5W 124-126	133.36	198.11	0.00	0.00	#DIV/0!	#DIV/0!	0.00	0.00	0.00	0.00

Sample	U1418 Age (Kyr)	Depth (m) CCSF-A	Aquatic ($\mu\text{g g}^{-1}$)	Terrestrial ($\mu\text{g g}^{-1}$)	Aquatic Only ($\mu\text{g g}^{-1}$ TOC ⁻¹)	Terrestrial only ($\mu\text{g g}^{-1}$ TOC ⁻¹)	Aquatic MAR	Terrestrial MAR	TAR	CPI (1)
U1418D 20H-4W 134-146	136.06	202.11	0.00	0.00	#DIV/0!	#DIV/0!	0.00	0.00	0.00	0.00
U1418D 21H-2W 62-64	141.49	210.18	0.36	0.93	#DIV/0!	#DIV/0!	68.16	178.17	2.61	1.40
U1418C 27H-3W 134-136	146.84	218.13	0.00	0.00	#DIV/0!	#DIV/0!	0.00	0.00	0.00	0.00
U1418D 22H-2W 50-52	149.59	222.21	0.00	0.00	#DIV/0!	#DIV/0!	0.00	0.00	0.00	0.00
U1418A 30H-1W 145-150	154.78	229.93		0.00	#DIV/0!	#DIV/0!	0.00	0.00	0.00	0.00
U1418C 28H-5W 64-66	154.90	230.11	0.00	0.00	#DIV/0!	#DIV/0!	0.00	0.00	0.00	0.00
U1418A 32H-1 115-130	162.16	240.89	0.00	0.00	0.00	0.00	0.00	0.00	0.00	0.00
U1418C 30H-3W 124-126	168.41	250.17	0.00	0.00	#DIV/0!	#DIV/0!	0.00	0.00	0.00	0.00
U1418D 25H-4W 84-86	172.17	255.76	0.73	3.12	1.11	4.75	143.80	617.65	4.30	1.07
U1418D 26H-3W 114-116	179.14	266.11	0.20	0.20	0.29	0.30	40.27	41.06	1.02	1.70
U1418D 26H-6W 64-66	181.84	270.12	0.65	3.75	1.50	8.68	131.91	764.06	5.79	1.23
U1418D 28H-2W 81-83	187.89	279.11	0.42	0.76	0.86	1.54	82.32	148.58	1.80	1.54
U1418D 30H-1W 94-96	193.30	287.14	0.50	0.53	0.95	1.01	98.77	105.53	1.07	1.58
U1418D 31H-2W 97-99	197.35	293.16	0.32	0.44	0.70	0.97	65.80	90.56	1.38	1.56
U1418D 32H-2W 21-23	200.05	297.14	0.45	0.65	0.84	1.23	59.84	87.28	1.46	1.41
U1418D 32H-3W 74-76	202.47	299.14	0.41	0.56	0.77	1.04	54.10	73.64	1.36	1.58
U1418D 34X-1W 4-6	214.58	309.13	0.45	0.66	0.89	1.30	60.15	88.19	1.47	3.26
U1418D 34X-3W 104-106	219.43	313.13	0.00	0.00	#DIV/0!	#DIV/0!	0.00	0.00	0.00	0.00
U1418D 35x-4W 84-86	232.78	324.14	1.02	1.14	1.59	1.78	105.45	118.15	1.12	1.57
U1418D 36X-1W 57-60	238.82	329.13	0.58	0.64	#DIV/0!	#DIV/0!	74.64	82.17	1.10	1.58
U1418D 36X-4W 59-61	243.59	333.06	0.22	0.23	0.43	0.45	28.34	29.54	1.04	1.89

Sample	U1418 Age (Kyr)	Depth (m) CCSF-A	Aquatic ($\mu\text{g g}^{-1}$)	Terrestrial ($\mu\text{g g}^{-1}$)	Aquatic Only ($\mu\text{g g}^{-1}$ TOC ⁻¹)	Terrestrial only ($\mu\text{g g}^{-1}$ TOC ⁻¹)	Aquatic MAR	Terrestrial MAR	TAR	CPI (1)
U1418F 5R-3W 94-96	246.11	335.14	0.00	0.00	#DIV/0!	#DIV/0!	0.00	0.00	0.00	0.00
U1418F 6R-2W 74-76	255.79	343.13	0.00	0.00	#DIV/0!	#DIV/0!	0.00	0.00	0.00	0.00
U1418F 7R-1W 51-53	265.45	351.10	0.43	0.49	#DIV/0!	#DIV/0!	55.90	63.38	1.13	1.84
U1418F 7R-4W 4-6	270.34	355.13	0.00	0.00	0.00	0.00	0.00	0.00	0.00	0.00
U1418F 9R-5W 14-16	295.79	376.13	0.00	0.00	0.00	0.00	0.00	0.00	0.00	0.00
U1418F 10R-2W 88-90	303.08	382.14	0.11	0.12	0.20	0.22	13.09	13.79	1.05	1.96
U1418F 10R-3W 132-135	305.47	384.11	0.17	0.49	#DIV/0!	#DIV/0!	18.49	53.74	2.91	1.41
U1418F 10R-5W 44-46	307.92	386.13	0.40	0.34	#DIV/0!	#DIV/0!	50.82	43.37	0.85	1.76
U1418F 11R-4W 21-23	317.58	394.10	0.51	0.57	0.77	0.86	52.52	58.56	1.11	1.43
U1418F 12R-4W 54-56	329.73	404.13	0.65	1.62	0.80	1.98	84.43	208.81	2.47	1.26
U1418F 12R-7W 40-42	334.67	408.20	0.85	0.72	1.99	1.70	105.66	90.23	0.85	1.59
U1418F 14R-4W 140-150	354.29	424.39	0.00	0.00	#DIV/0!	#DIV/0!	0.00	0.00	0.00	0.00
U1418F 15R-3W 94-96	363.67	432.13	0.57	0.81	#DIV/0!	#DIV/0!	77.38	111.09	1.44	1.45
U1418F 16R-2W 70-73	373.35	440.11	0.41	0.66	#DIV/0!	#DIV/0!	53.26	85.02	1.60	1.44
U1418F 17R-2W 4-6	384.28	449.13	0.40	0.54	#DIV/0!	#DIV/0!	55.34	74.29	1.34	1.49
U1418F 17R-4W 102-104	389.13	453.13	0.37	0.48	#DIV/0!	#DIV/0!	49.84	65.12	1.31	1.55
U1418F 18R-2W 135-150	397.62	460.14	0.00	0.00	#DIV/0!	#DIV/0!	0.00	0.00	0.00	0.00
U1418F 19R-1W 113-115	410.47	468.12	0.58	1.19	#DIV/0!	#DIV/0!	53.12	108.70	2.05	1.34
U1418F 19R-7W 20-22	424.50	476.19	0.48	1.45	#DIV/0!	#DIV/0!	43.98	134.08	3.05	1.24
U1418F 20R-5W 141-143	438.31	484.13	0.66	1.17	#DIV/0!	#DIV/0!	62.17	110.85	1.78	1.34
U1418F 21R-5W 74-76	453.97	493.13	0.57	1.07	#DIV/0!	#DIV/0!	50.38	93.89	1.86	1.30

Sample	U1418 Age (Kyr)	Depth (m) CCSF-A	Aquatic ($\mu\text{g g}^{-1}$)	Terrestrial ($\mu\text{g g}^{-1}$)	Aquatic Only ($\mu\text{g g}^{-1}$ $^{13}\text{C}^{-1}$)	Terrestrial only ($\mu\text{g g}^{-1}$ $^{13}\text{C}^{-1}$)	Aquatic MAR	Terrestrial MAR	TAR	CPI (1)
U1418F 22R-1W 104-106	462.66	498.13	1.25	0.67	#DIV/0!	#DIV/0!	106.84	57.28	0.54	1.15
U1418F 22R-3W 137-50	466.71	500.46	0.00	0.00	#DIV/0!	#DIV/0!	0.00	0.00	0.00	0.00
U1418F 22R-5W 104-106	471.36	503.13	0.78	1.55	#DIV/0!	#DIV/0!	69.83	138.51	1.98	1.29

A.5: C and N derived data, Site U1417

Sample I.D.	Average CCSF-A	Age (Myr)	d^{15}N	%N	$\text{D}^{13}\text{C} \text{‰}$	%C	N, μg	C, μg	C/N ratio	N/C μg
3H-5W 69-73	13.51	0.09	3.36	0.05	-24.75	0.62	37.70	433.79	11.51	0.09
C 3H-4W 21-25	18.55	0.12	6.39	0.05	-23.74	0.45	33.99	318.48	9.37	0.11
D 3H-3 38	21.03	0.13	3.68	0.05	-24.45	0.53	36.97	370.99	10.03	0.10
D 3H-3 38	21.03	0.13	3.01	0.05	-24.63	0.49	34.00	344.40	10.13	0.10
3H-5W 25-29	23.49	0.15	2.47	0.03	-25.23	0.48	24.26	338.93	13.97	0.07
C 4H-2W 92-94	26.01	0.17	3.73	0.05	-24.27	0.56	35.24	395.31	11.22	0.09
C 4H-3 35	26.98	0.17	3.88	0.06	-24.77	0.62	43.00	438.00	10.19	0.10
C 4H-4W 44-48	28.54	0.18	5.18	0.05	-23.96	0.54	33.64	380.65	11.32	0.09
4H-2W 22-26	30.00	0.19	4.64	0.05	-24.16	0.48	36.96	343.27	9.29	0.11
D 4H-2 76	30.54	0.20	4.87	0.06	-23.25	0.52	42.43	363.63	8.57	0.12
4H-2W 122-126	31.00	0.20	6.03	0.10	-20.35	0.98	72.39	689.78	9.53	0.10
4H-3W 72-76	32.00	0.21	1.66	0.05	-24.51	0.44	32.93	311.17	9.45	0.11
D 4H-4 78	33.56	0.22	4.96	0.06	-24.19	0.52	40.34	361.19	8.95	0.11

Sample I.D.	Average CCSF-A	Age (Myr)	d ¹⁵ N	%N	D ¹³ c ‰	%C	N, µg	C, µg	C/N ratio	N/C µg
C 5H-2W 140-144	34.98	0.22	5.79	0.06	-24.32	0.59	41.13	418.59	10.18	0.10
C 5H-5 42	38.50	0.25	3.70	0.06	-24.70	0.62	42.81	431.90	10.09	0.10
C 6H-3 16	46.00	0.29	3.94	0.06	-24.19	0.62	43.68	435.91	9.98	0.10
C 7H-2 145	55.98	0.36	4.87	0.05	-24.19	0.43	35.38	302.75	8.56	0.12
D 7H-3 116	66.01	0.42	3.63	0.05	-24.69	0.53	36.56	373.00	10.20	0.10
C 8H-5 48	73.55	0.47	5.32	0.05	-24.25	0.38	34.15	265.27	7.77	0.13
D 9H-2 46	78.48	0.50	3.61	0.05	-24.50	0.52	32.79	361.61	11.03	0.09
D 9H-5 105	83.57	0.54	5.30	0.05	-23.94	0.37	31.53	259.67	8.24	0.12
B 9H-6 100	88.58	0.57	3.60	0.05	-24.76	0.52	33.01	364.72	11.05	0.09
D 10H-5 37	93.51	0.60	2.99	0.04	-24.61	0.47	25.52	329.00	12.89	0.08
B 10H-5 62	98.53	0.64	4.19	0.05	-24.25	0.50	36.95	353.10	9.56	0.10
D 11H-4 47	103.51	0.67	3.35	0.06	-25.05	0.61	38.74	427.67	11.04	0.09
D 11H-4 47	103.51	0.67	3.26	0.05	-25.05	0.62	38.10	437.62	11.49	0.09
B 11H-3 130	108.53	0.70	3.33	0.05	-24.80	0.65	38.35	459.93	11.99	0.08
C 12H-2 48	113.46	0.74	4.79	0.06	-24.28	0.48	40.69	334.48	8.22	0.12
D 13H-2 35	118.51	0.77	3.14	0.05	-24.68	0.53	33.87	375.53	11.09	0.09
D 13H-3 84	120.50	0.78	2.92	0.07	-24.96	0.63	45.97	443.71	9.65	0.10
D 13H-4 34	121.50	0.79	3.57	0.06	-24.63	0.62	43.95	430.83	9.80	0.10
D 13H-5 34	123.00	0.80	1.74	0.05	-24.49	0.48	32.79	339.51	10.35	0.10
A 14H-4 68	125.00	0.81	3.63	0.06	-24.46	0.58	41.24	403.94	9.80	0.10
A14H-6 28	127.61	0.83	3.27	0.05	-24.60	0.54	36.44	377.60	10.36	0.10

Sample I.D.	Average CCSF-A	Age (Myr)	d ¹⁵ N	%N	D ¹³ C ‰	%C	N, µg	C, µg	C/N ratio	N/C µg
D 14H-2 66	128.50	0.84	3.56	0.05	-24.51	0.54	38.09	381.53	10.02	0.10
D 14H-2 66	128.50	0.84	3.83	0.06	-24.70	0.56	39.18	391.29	9.99	0.10
D 14H-4 7	130.91	0.85	3.23	0.05	-24.58	0.58	37.88	405.33	10.70	0.09
D 14H-4 127	132.11	0.86	2.55	0.05	-24.81	0.48	36.73	338.80	9.22	0.11
D14H-5 91	133.31	0.87	4.14	0.05	-24.45	0.41	35.47	289.03	8.15	0.12
C 14H-3 21	134.52	0.88	3.16	0.05	-24.66	0.53	36.69	373.10	10.17	0.10
C 14H-3 141	135.72	0.88	3.11	0.05	-24.79	0.50	34.63	352.47	10.18	0.10
C 14H-4 110	136.91	0.89	3.69	0.05	-24.63	0.46	36.80	325.19	8.84	0.11
C 14H-5 81	138.12	0.90	3.56	0.06	-24.58	0.55	39.49	383.97	9.72	0.10
C 14H-5 81	138.12	0.90	3.68	0.06	-24.50	0.54	39.91	378.91	9.49	0.11
C 14H-6 52	139.33	0.91	3.49	0.05	-24.80	0.50	32.84	348.13	10.60	0.09
C 14H-6 52	139.33	0.91	3.49	0.05	-24.85	0.48	33.43	339.63	10.16	0.10
D 15H-3 61	140.51	0.92	2.66	0.04	-24.63	0.44	27.14	308.16	11.36	0.09
D 15H-3 131	141.21	0.92	4.71	0.05	-24.25	0.38	33.85	267.58	7.90	0.13
D 15H-5 91	143.81	0.94	3.88	0.05	-24.53	0.48	37.94	335.74	8.85	0.11
D 15H-6 62	145.02	0.95	3.20	0.05	-24.63	0.48	33.50	336.17	10.03	0.10
C 15H-3 134	146.21	0.95	3.41	0.05	-25.04	0.50	35.58	348.05	9.78	0.10
C 15H-4 105	147.42	0.96	4.46	0.05	-24.34	0.28	33.13	195.27	5.89	0.17
C 15H-5 75	148.62	0.97	3.65	0.05	-24.63	0.53	36.87	373.75	10.14	0.10
C 15H-6 45	149.82	0.98	3.31	0.05	-24.56	0.48	35.95	338.06	9.40	0.11
D 16H-2 101	151.01	0.99	3.07	0.06	-24.26	0.58	39.53	404.19	10.22	0.10

Sample I.D.	Average CCSF-A	Age (Myr)	d ¹⁵ N	%N	D ¹³ C ‰	%C	N, µg	C, µg	C/N ratio	N/C µg
D 16H-3 63	152.23	0.99	3.41	0.05	-24.86	0.50	35.25	352.84	10.01	0.10
D 16H-4 42	153.42	1.00	3.06	0.05	-25.15	0.58	36.91	406.71	11.02	0.09
D 16H-5 11	154.61	1.02	3.07	0.05	-24.90	0.47	32.80	327.58	9.99	0.10
D 16H-5 130	155.80	1.03	3.35	0.05	-24.62	0.56	37.31	395.16	10.59	0.09
D 16H-5 130	155.80	1.03	3.67	0.05	-24.73	0.54	37.40	377.89	10.10	0.10
C 16H-4 3	157.04	1.04	3.30	0.05	-24.98	0.46	33.73	326.82	9.69	0.10
C 16H-4 140	158.41	1.06	4.55	0.05	-23.92	0.53	37.19	374.38	10.07	0.10
C 16H-5 91	159.42	1.07	3.34	0.05	-25.05	0.46	36.58	319.64	8.74	0.11
C 16H-5 91	159.42	1.07	3.25	0.05	-25.00	0.47	36.07	331.60	9.19	0.11
C 16H-6 62	160.63	1.09	3.36	0.05	-24.92	0.52	37.83	362.90	9.59	0.10
D 17H-2 116	161.82	1.10	4.20	0.05	-24.62	0.41	33.55	290.90	8.67	0.12
D 17H-3 83	162.99	1.11	2.96	0.05	-24.73	0.52	37.03	364.79	9.85	0.10
D 17H-3 83	162.99	1.11	3.16	0.05	-24.61	0.49	38.01	344.17	9.05	0.11
D 17H-4 56	164.22	1.13	4.29	0.05	-24.44	0.41	36.84	287.07	7.79	0.13
D 17H-5 27	165.43	1.14	3.47	0.05	-25.01	0.51	37.47	359.95	9.61	0.10
C 17H-2 13	166.61	1.15	4.05	0.05	-24.75	0.47	33.70	326.40	9.69	0.10
C 17H-2 133	167.81	1.17	3.27	0.05	-24.91	0.46	33.34	325.79	9.77	0.10
C 17H-3 102	169.00	1.18	4.51	0.05	-24.29	0.29	33.41	204.80	6.13	0.16
C 17H-4 73	170.21	1.20	4.14	0.05	-23.21	0.38	32.24	268.72	8.33	0.12
C 17H-4 73	170.21	1.20	3.78	0.04	-23.32	0.38	31.25	268.89	8.61	0.12
C 17H-5 44	171.42	1.21	4.17	0.05	-24.42	0.44	33.15	306.27	9.24	0.11

Sample I.D.	Average CCSF-A	Age (Myr)	d ¹⁵ N	%N	D ¹³ C ‰	%C	N, µg	C, µg	C/N ratio	N/C µg
D 18H-3 48	172.63	1.22	5.58	0.04	-24.15	0.29	31.54	204.64	6.49	0.15
D 18H-4 23	173.82	1.24	2.92	0.05	-25.10	0.47	38.52	334.77	8.69	0.12
D 18H-4 143	175.02	1.25	3.42	0.05	-24.81	0.52	37.32	363.78	9.75	0.10
D 18H-5 113	176.22	1.27	3.10	0.05	-25.00	0.46	34.13	324.29	9.50	0.11
C 18H-3 80	178.92	1.30	3.72	0.05	-25.18	0.42	36.18	292.88	8.09	0.12
B 18H-3 69	181.94	1.33	3.30	0.05	-24.39	0.41	33.67	289.53	8.60	0.12
B 18H-5 65	184.87	1.37	3.34	0.05	-24.92	0.50	37.46	354.17	9.46	0.11
C 19H-2 87	187.92	1.40	3.99	0.04	-24.62	0.27	30.36	188.54	6.21	0.16
B 19H-3 126	190.91	1.44	2.70	0.05	-25.25	0.46	37.59	322.11	8.57	0.12
C 20H-4 15	193.91	1.47	4.24	0.04	-24.27	0.27	26.18	189.57	7.24	0.14
D 24H-2W 69-73	203.81	1.57	3.77	0.04	-24.60	0.30	30.21	208.03	6.89	0.15
D 25H-3W 26-30	209.22	1.63	3.54	0.05	-24.41	0.45	34.96	319.19	9.13	0.11
D 27H-1W 87-91	217.35	1.71	1.51	0.02	-25.35	0.35	13.71	244.17	17.81	0.06
D 29H-CCW 15-19	227.06	1.81	3.60	0.05	-24.25	0.43	33.06	301.31	9.11	0.11
D 30H-2W 63-67	230.10	1.85	4.45	0.04	-24.70	0.34	31.32	241.68	7.72	0.13
D 30H-2W 63-67	230.10	1.85	3.90	0.04	-24.85	0.34	29.91	237.04	7.93	0.13
D 34H-2W 55-59	249.95	2.03	3.59	0.04	-25.01	0.30	25.48	211.40	8.30	0.12
D 35H-2W 102-106	256.24	2.07	1.45	0.01	-25.08	0.23	6.73	161.05	23.91	0.04
D 39X-1W 19-23	277.07	2.20	3.72	0.03	-24.51	0.37	23.28	264.17	11.35	0.09
D 40X-2W 37-41	288.45	2.28	3.06	0.03	-24.03	0.31	23.39	218.59	9.34	0.11
D 41X-4W 35-39	301.13	2.36	3.30	0.04	-24.56	0.42	31.25	293.28	9.38	0.11

Sample I.D.	Average CCSF-A	Age (Myr)	d ¹⁵ N	%N	D ¹³ C ‰	%C	N, µg	C, µg	C/N ratio	N/C µg
D 42X-1W 94-98	306.88	2.40	3.93	0.04	-23.86	0.36	25.96	250.12	9.64	0.10
D 43X-1W 10-14	315.78	2.45	3.77	0.04	-24.86	0.36	26.20	255.50	9.75	0.10
43X-1W 70-74	316.38	2.46	1.92	0.04	-24.90	0.46	28.93	321.77	11.12	0.09
D 43X-1W 127-131	316.98	2.46	3.22	0.03	-23.64	0.31	24.00	214.98	8.96	0.11
D 43X-2W 55-59	317.58	2.46	4.59	0.03	-25.09	0.21	21.27	150.17	7.06	0.14
D 43X-2W 114-118	318.17	2.47	3.50	0.03	-24.38	0.33	21.59	235.94	10.93	0.09
D 43X-3W 27-31	318.78	2.47	2.42	0.03	-23.84	0.38	22.71	270.67	11.92	0.08
43X-3W 87-91	319.38	2.48	0.75	0.04	-25.72	0.39	26.06	273.13	10.48	0.10
D 43X-4W 10-14	319.98	2.48	2.49	0.05	-25.06	0.46	33.63	325.70	9.69	0.10
D 43X-4W 63-67	320.55	2.48	2.94	0.02	-23.89	0.30	15.34	208.77	13.61	0.07
D 43X-4W 125-129	321.17	2.49	3.63	0.05	-24.65	0.47	32.21	329.93	10.24	0.10
D 43X-4W 125-129	321.17	2.49	3.25	0.04	-24.81	0.44	28.51	314.15	11.02	0.09
43X-5W 34-38	321.78	2.49	2.78	0.05	-25.12	0.44	34.39	314.37	9.14	0.11
43X-5W 34-38	321.78	2.49	3.06	0.04	-24.55	0.45	30.17	317.41	10.52	0.10
D 43X-CCW 41-45	322.34	2.49	2.74	0.02	-25.22	0.33	10.59	229.97	21.73	0.05
D 43X-CCW 41-45	322.34	2.49	3.52	0.04	-24.50	0.44	31.19	309.56	9.93	0.10
44X-1W 18-23	325.39	2.53	2.62	0.05	-24.94	0.46	33.10	326.62	9.87	0.10
44X-1W 70-74	326.00	2.53	1.58	0.04	-25.87	0.42	25.70	294.07	11.44	0.09
44X-1W 104-108	326.57	2.54	3.04	0.03	-24.85	0.37	22.69	257.08	11.33	0.09
45X-1W 9-13	329.98	2.58	2.96	0.03	-24.53	0.28	20.10	197.82	9.84	0.10
45X-1W 123-127	331.20	2.59	2.06	0.02	-24.18	0.13	15.16	91.27	6.02	0.17

Sample I.D.	Average CCSF-A	Age (Myr)	d ¹⁵ N	%N	D ¹³ C ‰	%C	N, µg	C, µg	C/N ratio	N/C µg
45X-2W 46-50	331.81	2.60	2.53	0.03	-25.48	0.15	21.26	103.55	4.87	0.21
45X-2W 62-66	331.98	2.60	-0.27	0.04	-24.54	0.39	26.34	277.28	10.53	0.09
45X-2W 70-74	332.17	2.60	2.62	0.05	-24.60	0.45	31.64	311.62	9.85	0.10
45X-2W 70-74	332.17	2.60	2.53	0.05	-24.76	0.49	33.63	344.72	10.25	0.10
46X-1W 0-4	336.66	2.66	2.87	0.06	-23.71	0.64	43.13	449.62	10.42	0.10
46XX-1W 31-35	336.96	2.66	3.15	0.03	-24.49	0.27	23.31	188.16	8.07	0.12
D 45X-1W 60-64	337.26	2.66	4.07	0.05	-24.52	0.35	34.85	245.20	7.04	0.14
46X-1W 60-64	337.26	2.66	3.70	0.02	-22.99	0.10	15.82	69.65	4.40	0.23
46X-1W 96-100	337.56	2.67	2.53	0.04	-24.35	0.36	27.85	251.78	9.04	0.11
46X-1W 119-123	337.86	2.67	2.69	0.04	-25.07	0.39	31.29	275.23	8.80	0.11
46X-3W 1-5	338.30	2.68	2.46	0.05	-24.45	0.40	32.14	284.31	8.85	0.11
46X-3W 21-25	338.46	2.68	0.33	0.02	-25.61	0.34	13.39	237.99	17.77	0.06
46X-3W 46-50	338.76	2.68	1.25	0.04	-25.31	0.37	25.78	258.51	10.03	0.10
46X-3W 80-84	339.07	2.69	1.41	0.03	-24.77	0.30	23.87	207.90	8.71	0.11
46X-3W 80-84	339.07	2.69	1.84	0.03	-25.84	0.35	22.57	243.85	10.81	0.09
46X-3W 106-110	339.36	2.69	2.52	0.03	-23.88	0.32	19.98	222.72	11.14	0.09
D 46X-3W 138-142	339.66	2.69	2.75	0.04	-24.87	0.47	30.99	331.54	10.70	0.09
47X-1W 17-21	348.85	2.80	2.76	0.06	-24.75	0.42	39.20	298.11	7.60	0.13
47X-2W 63-69	349.98	2.81	2.03	0.03	-25.48	0.33	20.02	232.75	11.62	0.09
47X-2W 63-69	349.98	2.81	-0.40	0.02	-25.50	0.30	12.63	211.89	16.77	0.06
47X-3W 59-63	350.87	2.82	2.05	0.03	-24.66	0.21	22.42	149.47	6.67	0.15

Sample I.D.	Average CCSF-A	Age (Myr)	d ¹⁵ N	%N	D ¹³ C ‰	%C	N, µg	C, µg	C/N ratio	N/C µg
47X-3W 59-63	350.87	2.82	1.82	0.01	-24.83	0.15	8.44	107.96	12.79	0.08
48X-1W 29-33	358.47	2.91	3.21	0.03	-24.04	0.19	20.11	134.11	6.67	0.15
48X-1W 69-73	359.07	2.92	3.43	0.05	-24.06	0.50	35.68	351.56	9.85	0.10
48X-2W 0-4	359.69	2.93	1.53	0.03	-24.89	0.32	23.58	224.91	9.54	0.10
48X-2W 63-68	360.27	2.94	3.19	0.04	-24.21	0.23	25.90	158.80	6.13	0.16
48X-2W 106-110	360.79	2.94	3.43	0.03	-24.40	0.22	24.67	157.43	6.38	0.16
49X-1W 35-39	368.17	3.04	1.28	0.04	-25.35	0.42	28.76	294.51	10.24	0.10
49X-1W 69-73	368.77	3.05	3.07	0.04	-23.31	0.21	27.98	148.30	5.30	0.19
49X-2W 79-83	369.97	3.06	2.67	0.02	-25.06	0.20	14.69	139.80	9.51	0.11
D 50X-2W 93-97	380.08	3.22	3.55	0.04	-24.58	0.17	24.61	121.45	4.93	0.20
51X-1W 9-13	387.57	3.34	2.49	0.04	-25.14	0.22	25.23	155.47	6.16	0.16
51X-1W 65-69	388.13	3.34	2.03	0.04	-24.46	0.37	30.66	259.61	8.47	0.12
51X-1W 124-128	388.72	3.35	3.78	0.04	-24.14	0.27	25.87	187.76	7.26	0.14
D 51X-2W 40-44	389.38	3.36	3.96	0.04	-21.88	0.20	29.41	137.75	4.68	0.21
51X-3W 11-15	390.00	3.37	2.50	0.03	-23.66	0.14	20.00	96.54	4.83	0.21
51X-3W 103-107	390.59	3.38	2.01	0.04	-24.53	0.35	25.40	247.04	9.73	0.10
51X-4W 11-15	391.24	3.39	3.88	0.03	-23.63	0.13	23.17	90.61	3.91	0.26
51X-4W 68-72	391.81	3.40	2.15	0.03	-25.24	0.34	19.97	237.09	11.87	0.08
51X-4W 128-132	392.41	3.41	2.70	0.05	-23.99	0.30	32.51	214.29	6.59	0.15
52X-1W 19-23	397.37	3.49	3.00	0.05	-24.44	0.53	36.73	375.03	10.21	0.10
D 53X-1W 19-23	397.37	3.49	3.54	0.03	-24.56	0.16	22.54	112.85	5.01	0.20

Sample I.D.	Average CCSF-A	Age (Myr)	d ¹⁵ N	%N	D ¹³ C ‰	%C	N, µg	C, µg	C/N ratio	N/C µg
D 53X-1W 19-23	397.37	3.49	4.39	0.03	-24.78	0.15	19.64	102.96	5.24	0.19
D 52X-1W 59-63	397.77	3.49	3.29	0.04	-24.86	0.21	28.11	144.75	5.15	0.19
D 52X-1W 97-101	398.15	3.50	2.91	0.02	-26.03	0.20	12.42	143.13	11.52	0.09
D 52X-1W 97-101	398.15	3.50	4.05	0.03	-25.02	0.23	22.48	165.36	7.36	0.14
D 52X-1W 134-138	398.57	3.51	4.60	0.04	-23.67	0.22	30.31	153.82	5.07	0.20
52X-2W 69-73	399.34	3.53	3.30	0.03	-23.55	0.22	19.83	151.58	7.64	0.13
52X-2W 69-73	399.34	3.53	3.60	0.03	-23.58	0.22	18.92	156.44	8.27	0.12
52X-2W 109-113	399.74	3.54	2.48	0.02	-24.53	0.28	12.05	195.76	16.25	0.06
52X-2W 109-113	399.74	3.54	2.70	0.02	-24.65	0.30	14.80	211.14	14.26	0.07
D 52X-3W 40-44	400.28	3.55	3.11	0.03	-24.65	0.23	21.22	164.82	7.77	0.13
52X-3W 69-73	400.57	3.56	3.33	0.02	-23.13	0.15	17.48	106.75	6.11	0.16
52X-3W 69-73	400.57	3.56	2.83	0.03	-23.00	0.13	17.86	93.27	5.22	0.19
52X-3W 102-106	400.90	3.57	2.82	0.04	-23.60	0.16	26.64	115.77	4.35	0.23
D 53X-1W 60-65	407.60	3.73	3.72	0.03	-24.76	0.22	18.58	155.19	8.35	0.12
D 53X-2W 41-45	408.30	3.75	3.68	0.08	-24.62	1.10	53.84	777.90	14.45	0.07
D 54X-3W 10-14	419.04	4.02	2.59	0.02	-24.22	0.12	16.32	81.62	5.00	0.20
D 54X-3W 59-63	419.63	4.03	3.23	0.04	-24.56	0.45	26.22	313.96	11.98	0.08
D 54X-3W 119-123	420.23	4.05	2.80	0.03	-25.68	0.32	24.09	221.77	9.21	0.11
D 54X-4W 29-33	420.81	4.06	1.00	0.02	-25.39	0.43	15.77	305.83	19.40	0.05
54X-4W 70-74	421.38	4.08	3.01	0.05	-24.32	0.47	36.23	329.78	9.10	0.11

A.6: C and N derived data, Site U1418

Sample	Average CCSF-A	Preliminary age (Myr)	d ¹⁵ N	%N	d ¹³ C	%C	N, µg	C, µg	C/N ratio	N/C µg
A 4H-6 121-126	37.02	0.02	1.96	0.03	-25.24	0.45	19.74	313.23	15.87	0.06
A 4H-6 121-126	37.02	0.02	2.61	0.03	-25.11	0.50	21.79	353.21	16.21	0.06
A 6H-3 145-150	54.84	0.04	3.29	0.04	-25.33	0.45	24.86	315.82	12.70	0.08
A 6H-5 145-150	57.84	0.04	3.94	0.05	-24.44	0.57	37.77	398.03	10.54	0.09
A 8H-3 145-150	76.11	0.05	4.57	0.05	-23.88	0.49	35.55	342.49	9.63	0.10
A 9H-3W 112-114	86.16	0.06	4.00	0.05	-24.33	0.63	38.15	441.11	11.56	0.09
A 9H-3W 112-114	86.49	0.06	3.85	0.05	-24.11	0.64	38.44	450.23	11.71	0.09
A 9H-3 145-150	86.49	0.06	4.87	0.05	-23.31	0.53	35.68	368.16	10.32	0.10
E 2H-2W 64-66	90.12	0.06	4.58	0.06	-23.89	0.56	42.82	392.10	9.16	0.11
E 2H-5W 14-16	94.13	0.06	6.05	0.07	-22.67	0.62	49.84	438.35	8.80	0.11
A 10H-5W 120-122	98.18	0.07	3.26	0.07	-24.61	0.78	47.60	547.64	11.51	0.09
A 11H-3 145-150	105.90	0.07	3.67	0.05	-24.69	0.82	38.62	575.92	14.91	0.07
E 5H-2W 117-119	114.20	0.08	2.93	0.05	-24.83	0.57	36.49	397.01	10.88	0.09
E 5H-5W 61-63	118.11	0.08	3.44	0.05	-24.54	0.42	31.80	296.61	9.33	0.11
E 6H-3W 4-6	126.11	0.08	3.97	0.05	-24.17	0.45	33.23	314.71	9.47	0.11
E 6H-3W 4-6	126.11	0.08	4.08	0.05	-24.32	0.43	32.76	304.23	9.29	0.11
E 6H-5W 104-106	130.11	0.09	3.65	0.05	-24.55	0.50	33.42	354.71	10.61	0.09
A 14H-2 140-150	138.71	0.09	4.46	0.06	-24.28	0.72	45.51	503.02	11.05	0.09
A 18H-2 140-150	160.91	0.11	4.73	0.06	-24.72	0.58	39.15	408.14	10.43	0.10
A 20H-2 140-150	172.08	0.12	4.25	0.06	-24.40	0.62	40.39	435.29	10.78	0.09

Sample	Average CCSF-A	Preliminary age (Myr)	d ¹⁵ N	%N	d ¹³ C	%C	N, µg	C, µg	C/N ratio	N/C µg
A 22H-2 140-150	183.13	0.12	6.14	0.08	-21.24	0.72	59.15	509.62	8.62	0.12
A 24H-1 140-150	191.80	0.13	4.44	0.05	-24.23	0.55	35.72	383.62	10.74	0.09
A 24H-1 140-150	191.80	0.13	4.47	0.05	-24.23	0.56	35.45	395.99	11.17	0.09
D 22H-3 135-145	224.56	0.15	3.87	0.06	-24.68	0.72	42.41	504.42	11.89	0.08
A 32H-1 115-130	240.89	0.16	4.16	0.05	-24.44	0.50	35.54	349.45	9.83	0.10
D 25H-3 140-150	254.93	0.17	4.20	0.06	-23.72	0.66	38.78	459.64	11.85	0.08
D 26H-3 140-150	266.38	0.18	4.00	0.05	-24.27	0.67	36.52	467.01	12.79	0.08
D 27H-2 140-150	274.99	0.19	2.90	0.03	-24.85	0.43	20.37	304.86	14.97	0.07
D 28H-2 81-83	279.10	0.19	3.56	0.05	-24.60	0.49	33.17	345.12	10.40	0.10
D 29H-2 140-150	284.39	0.19	4.22	0.05	-23.84	0.50	34.54	350.19	10.14	0.10
D 30H-1W 94-96	287.13	0.19	3.69	0.05	-24.30	0.52	34.56	366.74	10.61	0.09
D 31H-2 140-150	293.59	0.20	4.55	0.05	-23.84	0.45	34.82	318.90	9.16	0.11
D 32H-2W 21-23	297.13	0.20	3.28	0.05	-24.64	0.53	35.47	373.47	10.53	0.09
D 32H-3W 74-76	299.13	0.20	3.45	0.05	-24.62	0.54	32.98	377.66	11.45	0.09
D 33X-1 140-150	300.79	0.20	4.69	0.05	-24.54	0.51	32.61	357.42	10.96	0.09
D 35H-4W 84-86	324.13	0.23	3.62	0.05	-24.58	0.64	35.03	445.81	12.73	0.08
D 36X-2 138-148	331.37	0.24	3.94	0.05	-24.40	0.51	31.99	358.80	11.22	0.09
F 6R-4 140-150	346.79	0.26	3.87	0.05	-24.59	0.55	34.24	385.75	11.27	0.09
F 7R-3 141-150	355.00	0.27	3.97	0.05	-24.51	0.45	33.08	315.04	9.52	0.10
F 9R-4 139-150	375.88	0.30	4.01	0.05	-25.00	0.49	34.24	344.34	10.06	0.10
F 10R-2 138-150	382.57	0.30	3.93	0.05	-24.59	0.54	34.33	377.87	11.01	0.09

Sample	Average CCSF-A	Preliminary age (Myr)	d ¹⁵ N	%N	d ¹³ C	%C	N, µg	C, µg	C/N ratio	N/C µg
F 10R-2 138-150	382.57	0.30	4.02	0.05	-24.65	0.52	34.44	366.15	10.63	0.09
F 11R-3 138-150	393.77	0.32	3.48	0.05	-24.82	0.67	38.35	471.49	12.29	0.08

A.7: Sterol derived data, Site U1417

Sample	Depth Average CCSF-A (m)	Preliminary Age (Myr)	Brassicasterol (µg g ⁻¹)	β-sitosterol (µg g ⁻¹)	Dinosterol (µg g ⁻¹)	Brassicasterol (µg g ⁻¹ TOC ⁻¹)	β-sitosterol (µg g ⁻¹ TOC ⁻¹)	Dinosterol (µg g ⁻¹ TOC ⁻¹)	Brassicasterol Biomarker MAR (µg cm ⁻² Kyr ⁻¹)	β-sitosterol Biomarker MAR (µg cm ⁻² Kyr ⁻¹)	Dinosterol Biomarker MAR (µg cm ⁻² Kyr ⁻¹)
U1417D 1H-3W 49-53	3.510	0.022	0.020	0.524	0.000	#DIV/0!	#DIV/0!	#DIV/0!	0.161	4.316	0.000
U1417C 2H-2W 49-53	7.289	0.047	0.072	0.104	0.000	#DIV/0!	#DIV/0!	#DIV/0!	0.634	0.914	0.000
U1417D 2H-2W 31-35	8.632	0.055	0.023	0.142	0.102	#DIV/0!	#DIV/0!	#DIV/0!	0.218	1.322	0.952
U1417D 2H-3W 113-117	12.932	0.083	0.254	0.304	0.024	#DIV/0!	#DIV/0!	#DIV/0!	2.507	2.994	0.233
U1417D 3H-	13.512	0.087	0.032	0.177	0.152	0.052	0.286	0.245	0.352	1.938	1.658

Sample	Depth Average CCSF-A (m)	Preliminary Age (Myr)	Brassicasterol ($\mu\text{g g}^{-1}$)	β -sitosterol ($\mu\text{g g}^{-1}$)	Dinosterol ($\mu\text{g g}^{-1}$)	Brassicasterol ($\mu\text{g g}^{-1}$ TOC $^{-1}$)	β -sitosterol ($\mu\text{g g}^{-1}$ TOC $^{-1}$)	Dinosterol ($\mu\text{g g}^{-1}$ TOC $^{-1}$)	Brassicasterol Biomarker MAR ($\mu\text{g cm}^{-2}$ Kyr $^{-1}$)	β -sitosterol Biomarker MAR ($\mu\text{g cm}^{-2}$ Kyr $^{-1}$)	Dinosterol Biomarker MAR ($\mu\text{g cm}^{-2}$ Kyr $^{-1}$)
5W 69-73											
U1417C 3H-2W 86-90	17.998	0.115	0.257	1.085	0.202	#DIV/0!	#DIV/0!	#DIV/0!	2.955	12.454	2.313
U1417C-3H-4W 21-25	18.548	0.119	0.000	7.299	0.000	0.000	16.062	0.000	0.000	87.693	0.000
U1417D 3H-5W 25-29	23.486	0.150	0.000	0.257	0.027	0.000	0.531	0.055	0.000	3.347	0.346
U1417C 4H-2W 92-94	25.997	0.167	0.064	0.179	0.043	0.113	0.318	0.076	0.859	2.412	0.578
U1417C 4H-4W 44-48	28.537	0.183	0.013	0.163	0.000	0.024	0.302	0.000	0.178	2.274	0.000
U1417D 4H-2W 22-26	30.003	0.192	0.010	0.141	0.006	0.020	0.290	0.013	0.138	2.032	0.090
U1417D 4H-2W 122-126	31.003	0.199	0.042	0.304	0.043	0.043	0.309	0.044	0.624	4.539	0.647
U1417D 4H-3W 72-76	32.003	0.205	0.005	0.074	0.000	0.012	0.168	0.000	0.084	1.141	0.000
U1417C 5H-2W 140-144	34.980	0.224	0.000	0.000	0.000	0.000	0.000	0.000	0.000	0.000	0.000
U1417C 5H-4W 93-97	39.490	0.253	0.009	0.022	0.011	0.015	0.035	0.018	0.162	0.395	0.205
U1417C 5H-5W 138-142	41.440	0.266	0.267	1.236	0.000	#DIV/0!	#DIV/0!	#DIV/0!	5.183	23.970	0.000
U1417D 5H-	45.311	0.290	0.190	0.295	0.029	0.305	0.475	0.046	3.577	5.560	0.542

Sample	Depth Average CCSF-A (m)	Preliminary Age (Myr)	Brassicasterol ($\mu\text{g g}^{-1}$)	β -sitosterol ($\mu\text{g g}^{-1}$)	Dinosterol ($\mu\text{g g}^{-1}$)	Brassicasterol ($\mu\text{g g}^{-1}$ TOC $^{-1}$)	β -sitosterol ($\mu\text{g g}^{-1}$ TOC $^{-1}$)	Dinosterol ($\mu\text{g g}^{-1}$ TOC $^{-1}$)	Brassicasterol Biomarker MAR ($\mu\text{g cm}^{-2}$ Kyr $^{-1}$)	β -sitosterol Biomarker MAR ($\mu\text{g cm}^{-2}$ Kyr $^{-1}$)	Dinosterol Biomarker MAR ($\mu\text{g cm}^{-2}$ Kyr $^{-1}$)
5W 97-101											
U1417C 6H-4W 117-121	50.447	0.323	#DIV/0!	#DIV/0!	#DIV/0!	#DIV/0!	#DIV/0!	#DIV/0!			#DIV/0!
U1417D 6H-5W 77-81	55.460	0.355	0.253	0.501	0.054	0.476	0.943	0.102	4.471	8.859	0.963
U1417D 7H-2W 20-24	65.533	0.420	0.237	0.254	0.025	#DIV/0!	#DIV/0!	#DIV/0!	4.056	4.339	0.430
U1417B 20H-3W 55-59	197.527	1.510	0.000	0.000	0.041	#DIV/0!	#DIV/0!	#DIV/0!	0.000	0.000	0.453
U1417B 20H-3W 113-117	198.107	1.516	0.026	0.106	0.029	#DIV/0!	#DIV/0!	#DIV/0!	0.291	1.176	0.318
U1417B 20H-4w 82-86	200.797	1.544	0.357	0.243	0.079	#DIV/0!	#DIV/0!	#DIV/0!	4.026	2.745	0.892
U1417B 20H-6w 114-118	202.617	1.563	0.006	0.054	0.005	#DIV/0!	#DIV/0!	#DIV/0!	0.073	0.630	0.057
U1417C 21H-4W 2-6	205.031	1.587	0.077	1.051	0.000	#DIV/0!	#DIV/0!	#DIV/0!	0.817	11.166	0.000
U1417D 25H-1W 144-148	207.402	1.612	0.012	0.029	0.025	0.027	0.064	0.055	0.129	0.304	0.259

Sample	Depth Average CCSF-A (m)	Preliminary Age (Myr)	Brassicasterol ($\mu\text{g g}^{-1}$)	β -sitosterol ($\mu\text{g g}^{-1}$)	Dinosterol ($\mu\text{g g}^{-1}$)	Brassicasterol ($\mu\text{g g}^{-1}$ TOC $^{-1}$)	β -sitosterol ($\mu\text{g g}^{-1}$ TOC $^{-1}$)	Dinosterol ($\mu\text{g g}^{-1}$ TOC $^{-1}$)	Brassicasterol Biomarker MAR ($\mu\text{g cm}^{-2}$ Kyr $^{-1}$)	β -sitosterol Biomarker MAR ($\mu\text{g cm}^{-2}$ Kyr $^{-1}$)	Dinosterol Biomarker MAR ($\mu\text{g cm}^{-2}$ Kyr $^{-1}$)
U1417D 25H-3W 51-55	209.47 2	1.633	0.390	0.486	0.191	#DIV/0!	#DIV/0!	#DIV/0!	4.087	5.089	1.996
U1417B 22H-3W 93-95	210.70 1	1.646	0.335	0.344	0.160	#DIV/0!	#DIV/0!	#DIV/0!	3.283	3.375	1.574
U1417D 26H-2W 35-39	213.11 1	1.671	0.305	0.406	0.148	#DIV/0!	#DIV/0!	#DIV/0!	3.253	4.324	1.582
U1417D 28H-1W 31-35	220.61 6	1.748	0.136	0.173	0.094	#DIV/0!	#DIV/0!	#DIV/0!	1.397	1.786	0.969
U1417D 29H-1W 106-110	223.82 8	1.781	0.040	0.091	0.037	#DIV/0!	#DIV/0!	#DIV/0!	0.426	0.971	0.399
U1417D 30H-CCW 5-9	232.47 1	1.870	0.245	0.366	0.154	#DIV/0!	#DIV/0!	#DIV/0!	2.243	3.344	1.409
U1417D 31H-1W 39-43	237.89 8	1.926	0.281	0.600	0.429	#DIV/0!	#DIV/0!	#DIV/0!	2.564	5.470	3.917
U1417D 32H-2W 17-21	243.44 1	1.983	0.567	0.648	0.212	#DIV/0!	#DIV/0!	#DIV/0!	6.053	6.918	2.268

Sample	Depth Average CCSF-A (m)	Preliminary Age (Myr)	Brassicasterol ($\mu\text{g g}^{-1}$)	β -sitosterol ($\mu\text{g g}^{-1}$)	Dinosterol ($\mu\text{g g}^{-1}$)	Brassicasterol ($\mu\text{g g}^{-1}$ TOC $^{-1}$)	β -sitosterol ($\mu\text{g g}^{-1}$ TOC $^{-1}$)	Dinosterol ($\mu\text{g g}^{-1}$ TOC $^{-1}$)	Brassicasterol Biomarker MAR ($\mu\text{g cm}^{-2}$ Kyr $^{-1}$)	β -sitosterol Biomarker MAR ($\mu\text{g cm}^{-2}$ Kyr $^{-1}$)	Dinosterol Biomarker MAR ($\mu\text{g cm}^{-2}$ Kyr $^{-1}$)
U1417D 32H-CCW 13-17	246.641	2.010	0.058	0.137	0.051	#DIV/0!	#DIV/0!	#DIV/0!	1.100	2.616	0.974
U1417D 35H-1W 18-22	253.904	2.056	0.529	0.683	0.330	#DIV/0!	#DIV/0!	#DIV/0!	11.185	14.460	6.984
U1417D 36H-1W 59-63	259.724	2.093	0.166	0.440	0.196	#DIV/0!	#DIV/0!	#DIV/0!	3.425	9.088	4.043
U1417D 36H-3W 84-88	262.974	2.114	0.003	0.019	0.074	0.008	0.051	0.197	0.064	0.414	1.584
U1417D 39X-1W 19-23	277.070	2.204	0.030	0.026	0.060	#DIV/0!	#DIV/0!	#DIV/0!	0.651	0.547	1.276
U1417D 40X-2	289.050	2.281	0.000	0.322	0.070	0.000	0.773	0.169	0.000	6.279	1.371
U1417D 41X-4W 35-39	301.130	2.358	0.000	0.115	0.082	0.000	0.322	0.229	0.000	2.323	1.654
U1417D 42X-1W 94-98	306.880	2.395	0.011	0.006	0.009	0.031	0.015	0.024	0.217	0.107	0.163
U1417D 43X-1W 10-	315.780	2.452	0.000	0.008	0.020	0.000	0.027	0.068	0.000	0.166	0.427

Sample	Depth Average CCSF- A (m)	Prelimi- nary Age (Myr)	Brassic- asterol ($\mu\text{g g}^{-1}$)	β - sitoste- rol ($\mu\text{g g}^{-1}$)	Dinost- erol ($\mu\text{g g}^{-1}$)	Brassic- sterol ($\mu\text{g g}^{-1}$ TOC ⁻¹)	β - sitoster- ol ($\mu\text{g g}^{-1}$ TOC ⁻¹)	Dinoster- ol ($\mu\text{g g}^{-1}$ TOC ⁻¹)	Brassicasterol Biomarker MAR ($\mu\text{g cm}^{-2}$ Kyr ⁻¹)	β -sitosterol Biomarker MAR ($\mu\text{g cm}^{-2}$ Kyr ⁻¹)	Dinosterol Biomarker MAR ($\mu\text{g cm}^{-2}$ Kyr ⁻¹)
14 U1417D 43X-2W 55- 59	317.58 0	2.464	0.002	0.000	0.007	0.004	0.000	0.014	0.038	0.000	0.134
U1417D 43X-4W 63- 67	320.55 0	2.483	0.008	0.005	0.019	0.019	0.012	0.046	0.145	0.094	0.357
U1417D 44X-1W 18- 23	325.39 0	2.525	0.009	0.191	0.009	0.026	0.520	0.024	0.111	2.254	0.105
U1417D 44X-1W 70- 74	326.00 0	2.532	0.015	0.163	0.008	0.052	0.577	0.030	0.172	1.925	0.100
U1417D 44X-1W 104-108	326.57 0	2.539	0.030	0.141	0.000	#DIV/0!	#DIV/0!	#DIV/0!	0.350	1.663	0.000
U1417D 45X-1W 9- 13	329.98 0	2.579	0.007	0.009	0.006	0.056	0.068	0.049	0.083	0.102	0.073
U1417D 45X-1W 60- 64	330.57 0	2.586	0.009	0.006	0.005	0.059	0.044	0.031	0.100	0.074	0.052
U1417D 45X-1W	331.20 0	2.593	0.002	0.000	0.000	0.005	0.000	0.000	0.021	0.000	0.000

Sample	Depth Average CCSF-A (m)	Preliminary Age (Myr)	Brassicasterol ($\mu\text{g g}^{-1}$)	β -sitosterol ($\mu\text{g g}^{-1}$)	Dinosterol ($\mu\text{g g}^{-1}$)	Brassicasterol ($\mu\text{g g}^{-1}$ TOC $^{-1}$)	β -sitosterol ($\mu\text{g g}^{-1}$ TOC $^{-1}$)	Dinosterol ($\mu\text{g g}^{-1}$ TOC $^{-1}$)	Brassicasterol Biomarker MAR ($\mu\text{g cm}^{-2}$ Kyr $^{-1}$)	β -sitosterol Biomarker MAR ($\mu\text{g cm}^{-2}$ Kyr $^{-1}$)	Dinosterol Biomarker MAR ($\mu\text{g cm}^{-2}$ Kyr $^{-1}$)
123-127											
U1417D 45X-2W 46-50	331.810	2.601	0.026	0.010	0.014	0.057	0.023	0.030	0.318	0.130	0.170
U1417D 45X-2W 62-66	331.980	2.603	0.024	0.017	0.016	0.037	0.026	0.025	0.294	0.209	0.197
U1417D 45X-2W 70-74	332.170	2.605	0.016	0.188	0.014	0.046	0.540	0.040	0.201	2.346	0.174
U1417D 46X-1W 0-4	336.655	2.658	0.088	0.175	0.074	0.245	0.488	0.206	1.075	2.144	0.905
U1417D 46X-1W 31-35	336.955	2.661	0.016	0.062	0.005	0.041	0.158	0.014	0.197	0.761	0.065
U1417D 46X-1W 60-64	337.255	2.665	0.000	0.079	0.000	0.000	0.234	0.000	0.000	0.968	0.000
U1417D 46X-1W 96-100	337.555	2.668	0.059	0.180	0.057	0.159	0.491	0.155	0.718	2.209	0.695
U1417D 46X-1W 119-123	337.855	2.672	0.050	0.207	0.006	0.169	0.697	0.019	0.615	2.532	0.070

Sample	Depth Average CCSF-A (m)	Preliminary Age (Myr)	Brassicasterol ($\mu\text{g g}^{-1}$)	β -sitosterol ($\mu\text{g g}^{-1}$)	Dinosterol ($\mu\text{g g}^{-1}$)	Brassicasterol ($\mu\text{g g}^{-1}$ TOC $^{-1}$)	β -sitosterol ($\mu\text{g g}^{-1}$ TOC $^{-1}$)	Dinosterol ($\mu\text{g g}^{-1}$ TOC $^{-1}$)	Brassicasterol Biomarker MAR ($\mu\text{g cm}^{-2}$ Kyr $^{-1}$)	β -sitosterol Biomarker MAR ($\mu\text{g cm}^{-2}$ Kyr $^{-1}$)	Dinosterol Biomarker MAR ($\mu\text{g cm}^{-2}$ Kyr $^{-1}$)
U1417D 46X-3W 1-5	338.295	2.677	0.068	0.130	0.092	0.145	0.274	0.194	0.883	1.673	1.184
U1417D 46X-3W 21-25	338.455	2.679	0.052	0.285	0.065	0.124	0.675	0.153	0.677	3.680	0.835
U1417D 46X-3W 46-50	338.755	2.682	0.009	0.035	0.000	0.027	0.106	0.000	0.116	0.452	0.000
U1417D 46X-3W 80-84	339.065	2.686	0.032	0.146	0.006	#DIV/0!	#DIV/0!	#DIV/0!	0.415	1.882	0.071
U1417D 46X-3W 106-110	339.355	2.689	0.113	0.351	0.061	0.528	1.647	0.287	1.454	4.535	0.789
U1417D 46X-3W 138-142	339.655	2.693	0.056	0.462	0.060	0.293	2.419	0.316	0.722	5.959	0.779
U1417D 47X-1W 17-21	348.850	2.801	0.036	0.107	0.022	0.072	0.213	0.044	0.316	0.941	0.194
U1417D 47X-2W 63-69	349.980	2.814	0.010	0.061	0.009	0.032	0.193	0.027	0.089	0.539	0.076
U1417D 47X-3W 29-	350.560	2.821	0.007	0.034	0.002	0.032	0.151	0.009	0.063	0.300	0.017

Sample	Depth Average CCSF-A (m)	Preliminary Age (Myr)	Brassicasterol ($\mu\text{g g}^{-1}$)	β -sitosterol ($\mu\text{g g}^{-1}$)	Dinosterol ($\mu\text{g g}^{-1}$)	Brassicasterol ($\mu\text{g g}^{-1}$ TOC $^{-1}$)	β -sitosterol ($\mu\text{g g}^{-1}$ TOC $^{-1}$)	Dinosterol ($\mu\text{g g}^{-1}$ TOC $^{-1}$)	Brassicasterol Biomarker MAR ($\mu\text{g cm}^{-2}$ Kyr $^{-1}$)	β -sitosterol Biomarker MAR ($\mu\text{g cm}^{-2}$ Kyr $^{-1}$)	Dinosterol Biomarker MAR ($\mu\text{g cm}^{-2}$ Kyr $^{-1}$)
33											
U1417D 47X-3W 59-63	350.870	2.825	0.007	0.000	0.009	0.031	0.000	0.041	0.060	0.000	0.081
U1417D 48X-1W 29-33	358.470	2.914	0.005	0.005	0.008	0.012	0.012	0.019	0.048	0.049	0.077
U1417D 48X-1W 69-73	359.070	2.921	0.007	0.085	0.042	0.033	0.407	0.199	0.066	0.816	0.399
U1417D 48X-2W 0-4	359.690	2.929	0.027	0.048	0.022	0.136	0.243	0.113	0.258	0.463	0.215
U1417D 48X-2W 63-68	360.270	2.935	0.000	0.000	0.000	#DIV/0!	#DIV/0!	#DIV/0!	0.000	0.000	0.000
U1417D 48X-2W 106-110	360.790	2.942	0.000	0.015	0.015	#DIV/0!	#DIV/0!	#DIV/0!	0.000	0.143	0.144
U1417D 49X-1W 35-39	368.170	3.037	0.045	0.091	0.024	#DIV/0!	#DIV/0!	#DIV/0!	0.321	0.649	0.170
U1417D 49X-1W 69-73	368.770	3.046	0.000	0.000	0.647	#DIV/0!	#DIV/0!	#DIV/0!	0.000	0.000	4.606

Sample	Depth Average CCSF-A (m)	Preliminary Age (Myr)	Brassicasterol ($\mu\text{g g}^{-1}$)	β -sitosterol ($\mu\text{g g}^{-1}$)	Dinosterol ($\mu\text{g g}^{-1}$)	Brassicasterol ($\mu\text{g g}^{-1}$ TOC $^{-1}$)	β -sitosterol ($\mu\text{g g}^{-1}$ TOC $^{-1}$)	Dinosterol ($\mu\text{g g}^{-1}$ TOC $^{-1}$)	Brassicasterol Biomarker MAR ($\mu\text{g cm}^{-2}$ Kyr $^{-1}$)	β -sitosterol Biomarker MAR ($\mu\text{g cm}^{-2}$ Kyr $^{-1}$)	Dinosterol Biomarker MAR ($\mu\text{g cm}^{-2}$ Kyr $^{-1}$)
U1417D 49X-2W 79-83	369.970	3.065	0.000	0.142	0.000	#DIV/0!	#DIV/0!	#DIV/0!	0.000	1.010	0.000
U1417D 50X-1W 55-59	378.330	3.193	0.156	0.379	0.066	0.708	1.715	0.299	1.815	4.396	0.766
U141D 50X-1W 116-120	378.960	3.203	0.331	1.440	0.000	0.895	3.899	0.000	3.837	16.720	0.000
U1417D 50X-2W 44-48	379.560	3.212	0.019	0.000	0.090	0.071	0.000	0.336	0.164	0.000	0.779
U1417D 50X-3W 6-10	380.660	3.229	0.004	0.000	0.003	0.021	0.000	0.017	0.024	0.000	0.019
U1417D 50X-3W 54-58	381.190	3.237	0.008	0.000	0.000	0.059	0.000	0.000	0.046	0.000	0.000
U1417D 51X-1W 9-13	387.570	3.336	0.292	1.947	0.070	0.834	5.555	0.200	2.108	14.034	0.505
U1417D 51X-1W 65-69	388.130	3.344	0.005	0.000	0.000	0.037	0.000	0.000	0.034	0.000	0.000
U1417D 51X-1W	388.720	3.353	0.004	0.074	0.010	0.011	0.219	0.029	0.025	0.530	0.071

Sample	Depth Average CCSF-A (m)	Preliminary Age (Myr)	Brassicasterol ($\mu\text{g g}^{-1}$)	β -sitosterol ($\mu\text{g g}^{-1}$)	Dinosterol ($\mu\text{g g}^{-1}$)	Brassicasterol ($\mu\text{g g}^{-1}$ TOC $^{-1}$)	β -sitosterol ($\mu\text{g g}^{-1}$ TOC $^{-1}$)	Dinosterol ($\mu\text{g g}^{-1}$ TOC $^{-1}$)	Brassicasterol Biomarker MAR ($\mu\text{g cm}^{-2}$ Kyr $^{-1}$)	β -sitosterol Biomarker MAR ($\mu\text{g cm}^{-2}$ Kyr $^{-1}$)	Dinosterol Biomarker MAR ($\mu\text{g cm}^{-2}$ Kyr $^{-1}$)
124-128 U1417D 51X-2W 40-44	389.380	3.363	0.000	0.000	0.000	0.000	0.000	0.000	0.000	0.000	0.000
U1417D 51X-3W 11-15	390.000	3.373	0.003	0.086	0.006	0.013	0.399	0.027	0.017	0.525	0.036
U1417D 51X-3W 103-107	390.590	3.382	0.005	0.009	0.000	0.018	0.034	0.000	0.030	0.057	0.000
U1417D 51X-4W 11-15	391.240	3.392	0.000	0.118	0.005	0.000	0.774	0.035	0.000	0.742	0.033
U1417D 51X-4W 68-72	391.810	3.401	0.002	0.014	0.004	0.013	0.085	0.022	0.014	0.088	0.023
U1417D 51X-4W 128-132	392.410	3.410	0.000	0.101	0.006	#DIV/0!	#DIV/0!	#DIV/0!	0.000	0.636	0.037
U1417D 52X-2W 69-73	399.340	3.527	0.000	0.006	0.003	0.000	0.026	0.013	0.000	0.020	0.010
U1417D 52X-2W	399.740	3.537	0.008	0.089	0.000	0.008	0.080	0.000	0.030	0.322	0.000

Sample	Depth Average CCSF-A (m)	Preliminary Age (Myr)	Brassicasterol ($\mu\text{g g}^{-1}$)	β -sitosterol ($\mu\text{g g}^{-1}$)	Dinosterol ($\mu\text{g g}^{-1}$)	Brassicasterol ($\mu\text{g g}^{-1}$ TOC $^{-1}$)	β -sitosterol ($\mu\text{g g}^{-1}$ TOC $^{-1}$)	Dinosterol ($\mu\text{g g}^{-1}$ TOC $^{-1}$)	Brassicasterol Biomarker MAR ($\mu\text{g cm}^{-2}$ Kyr $^{-1}$)	β -sitosterol Biomarker MAR ($\mu\text{g cm}^{-2}$ Kyr $^{-1}$)	Dinosterol Biomarker MAR ($\mu\text{g cm}^{-2}$ Kyr $^{-1}$)
109-113											
U1417D 52X-3W 69-73	400.570	3.558	0.000	0.105	0.000	#DIV/0!	#DIV/0!	#DIV/0!	0.000	0.404	0.000
U1417D 52X-3W 102-106	400.900	3.566	0.006	0.007	0.006	#DIV/0!	#DIV/0!	#DIV/0!	0.024	0.025	0.022
U1417D 53X-1W 19-23	407.040	3.720	0.005	0.000	0.000	#DIV/0!	#DIV/0!	#DIV/0!	0.019	0.000	0.000
U1417D 53X-1W 60-65	407.600	3.734	0.005	0.006	0.008	#DIV/0!	#DIV/0!	#DIV/0!	0.017	0.021	0.029
U1417D 53X-2W 41-45	408.300	3.751	0.044	0.191	0.163	#DIV/0!	#DIV/0!	#DIV/0!	0.215	0.937	0.799
U1417D 54X-1W 16-20	416.740	3.962	0.003	0.008	0.004	#DIV/0!	#DIV/0!	#DIV/0!	0.010	0.029	0.015
U1417D 54X-1W 76-80	417.340	3.977	0.003	0.004	0.004	#DIV/0!	#DIV/0!	#DIV/0!	0.010	0.015	0.015
U1417E 10R-2	432.500	4.356	0.000	1.125	0.000	#DIV/0!	#DIV/0!	#DIV/0!	0.000	5.931	0.000

Sample	Depth Average CCSF- A (m)	Prelimi- nary Age (Myr)	Brassic- asterol ($\mu\text{g g}^{-1}$)	β - sitoste- rol ($\mu\text{g g}^{-1}$)	Dinost- erol ($\mu\text{g g}^{-1}$)	Brassic- terol ($\mu\text{g g}^{-1}$ TOC ⁻¹)	β - sitoster- ol ($\mu\text{g g}^{-1}$ TOC ⁻¹)	Dinoster- ol ($\mu\text{g g}^{-1}$ TOC ⁻¹)	Brassicasterol Biomarker MAR ($\mu\text{g cm}^{-2} \text{Kyr}^{-1}$)	β -sitosterol Biomarker MAR ($\mu\text{g cm}^{-2}$ Kyr ⁻¹)	Dinosterol Biomarker MAR ($\mu\text{g cm}^{-2} \text{Kyr}^{-1}$)
U1417D 57X-1	446.64 0	4.686	0.002	0.030	0.006	#DIV/0!	#DIV/0!	#DIV/0!	0.011	0.160	0.032
U1417E 8R- 3	456.23 5	4.918	0.100	0.342	0.109	#DIV/0!	#DIV/0!	#DIV/0!	0.407	1.386	0.441
U1417D 59X-2	464.56 0	5.069	0.000	0.216	0.000	#DIV/0!	#DIV/0!	#DIV/0!	0.000	0.889	0.000
U1417E 9R- 2	464.58 5	5.070	0.095	1.931	0.000				0.408	8.305	0.000
U1417E 13R-1	501.90 5	5.748	0.083	0.307	0.063				0.755	2.774	0.574
U1417E 14R-1	516.32 0	6.005	0.158	0.497	0.101				1.334	4.198	0.849
U1417E 15R-4	525.72 5	6.091	0.000	0.174	0.000				0.000	4.819	0.000
U1417E 20R-1	527.50 0	6.107	0.203	0.868	0.131				2.971	12.724	1.924
U1417E 24R-1	608.07 5	6.893	0.098	0.685	0.000				1.453	10.117	0.000

A.8: Sterol derived data, Site U1418

Sample	Depth (m) CCSF-A	Preliminary Age(yr)	Brassicasterol ($\mu\text{g g}^{-1}$)	β -sitosterol ($\mu\text{g g}^{-1}$)	Dinosterol ($\mu\text{g g}^{-1}$)	Brassicasterol ($\mu\text{g g}^{-1} \text{TOC}^{-1}$)	β -sitosterol ($\mu\text{g g}^{-1} \text{TOC}^{-1}$)	Dinosterol ($\mu\text{g g}^{-1} \text{TOC}^{-1}$)	Brassicasterol MAR ($\mu\text{g cm}^{-2} \text{Kyr}^{-1}$)	β -sitosterol MAR ($\mu\text{g cm}^{-2} \text{Kyr}^{-1}$)	Dinosterol MAR ($\mu\text{g cm}^{-2} \text{Kyr}^{-1}$)
U1418B 1H-1 145-150	1.434	965.332	0.008	0.031	0.010	0.000	0.000	0.000	0.985	3.968	1.304
U1418B 2H-1W 145-150	11.08 6	7462.807	0.039	0.099	0.040	0.000	0.000	0.000	49.565	125.848	51.610
U1418A 3H-2 145-150	21.04 5	14166.94 7	0.036	0.129	0.077	0.000	0.000	0.000	92.783	337.882	200.229
U1418A 4H-4 145-150	34.26 4	23065.29 8	0.040	0.187	0.087	0.000	0.000	0.000	168.84 0	795.129	371.922
U1418A 6H-3 145-150	54.84 3	36918.88 3	0.182	0.410	0.206	0.403	0.908	0.457	1261.5 42	2845.210	1431.632
U1418A 9H-3W 112-114	86.16 8	58006.05 9	0.158	0.402	0.160	0.250	0.638	0.254	1727.8 40	4403.796	1751.118
U1418A 11H-3 145-150	105.8 96	71286.43 6	0.221	0.455	0.136	0.270	0.555	0.166	2914.2 16	5991.812	1795.048
U1418A 14H-2 145-150	138.7 08	93374.62 1	0.332	1.449	0.423	0.464	2.023	0.591	5842.2 46	25480.58 8	7448.107
U1418D 17H- 1W 94-96	164.0 96	110465.1 63	0.038	0.279	0.108	0.000	0.000	0.000	750.63 7	5470.105	2123.798
U1418A 20H-2 145-150	172.0 82	115841.1 31	0.328	0.413	0.128	0.000	0.000	0.000	7109.1 50	8945.496	2781.517
U1418C 24H- 2W 124-126	182.1 60	122625.3 79	0.190	1.440	0.268	0.000	0.000	0.000	4544.0 57	34410.46 1	6399.855

Sample	Depth (m) CCSF- A	Prelimina ry Age(yr)	Brassic asterol ($\mu\text{g g}^{-1}$)	β - sitoster ol ($\mu\text{g g}^{-1}$)	Dinoster ol ($\mu\text{g g}^{-1}$)	Brassic asreol ($\mu\text{g g}^{-1}$ TOC $^{-1}$)	β - sitosterol ($\mu\text{g g}^{-1}$ TOC $^{-1}$)	Dinosterol ($\mu\text{g g}^{-1}$ TOC $^{-1}$)	Brassic asterol MAR ($\mu\text{g cm}^{-2}$ Kyr $^{-1}$)	β -sitosterol MAR(μg cm $^{-2}$ Kyr $^{-1}$)	Dinosterol MAR (μg cm $^{-2}$ Kyr $^{-1}$)
U1418C 25H- 5W 124-126	198.1 09	133361.8 31	0.023	0.184	0.091	0.000	0.000	0.000	608.34 8	4809.920	2382.952
U1418D 22H- 2W 50-52	222.2 10	149585.9 98	0.048	0.217	0.086	0.095	0.436	0.173	1351.7 51	6167.706	2444.307
U1418A 32H-1 115-130	240.8 87	162158.8 69	0.048	0.122	0.057	0.072	0.183	0.086	1468.0 49	3734.160	1759.493
U1418D 26H- 3W 114-116	266.1 14	179141.0 30	0.030	0.195	0.067	0.000	0.000	0.000	1031.9 90	6584.644	2257.229
U1418D 31H- 2W 97-99	293.1 60	197347.6 94	0.014	0.100	0.051	0.000	0.000	0.000	544.81 9	3774.984	1911.171
U1418D 34X- 1W 4-6	309.1 30	214581.8 18	0.044	0.271	0.292	0.000	0.000	0.000	1117.2 08	6927.208	7462.332
U1418D 34X- 3W 104-106	313.1 30	219430.3 03	0.019	0.172	0.070	0.030	0.269	0.109	487.34 6	4432.949	1800.896
U1418D 36X- 1W 57-60	329.1 30	238824.2 42	0.076	0.239	0.120	0.147	0.466	0.235	2063.1 36	6518.261	3281.907
U1418D 36X- 4W 59-61	333.0 60	243587.8 79	0.289	0.245	0.127	0.000	0.000	0.000	7940.9 76	6717.691	3477.490
U1418F 6R-2W 74-76	343.1 30	255793.9 39	0.024	0.170	0.082	0.000	0.000	0.000	663.17 5	4794.557	2310.817
U1418F 7R-1W 51-53	351.1 00	265454.5 45	0.022	0.164	0.099	0.000	0.000	0.000	630.04 0	4744.374	2882.827
U1418F 9R-5W 14-16	376.1 30	295793.9 39	0.423	0.420	0.171	0.000	0.000	0.000	13150. 662	13058.80 4	5325.592

Sample	Depth (m) CCSF-A	Preliminary Age(yr)	Brassicasterol ($\mu\text{g g}^{-1}$)	β -sitosterol ($\mu\text{g g}^{-1}$)	Dinosterol ($\mu\text{g g}^{-1}$)	Brassicasterol ($\mu\text{g g}^{-1}$ TOC $^{-1}$)	β -sitosterol ($\mu\text{g g}^{-1}$ TOC $^{-1}$)	Dinosterol ($\mu\text{g g}^{-1}$ TOC $^{-1}$)	Brassicasterol MAR ($\mu\text{g cm}^{-2}$ Kyr $^{-1}$)	β -sitosterol MAR ($\mu\text{g cm}^{-2}$ Kyr $^{-1}$)	Dinosterol MAR ($\mu\text{g cm}^{-2}$ Kyr $^{-1}$)
U1418F 10R-2W 88-90	382.1 40	303078.7 88	0.031	0.155	0.065	0.060	0.297	0.124	984.82 6	4877.149	2039.456
U1418F 11R-4W 21-23	394.1 00	317575.7 58	0.024	0.128	0.069	0.035	0.190	0.103	766.65 4	4155.946	2256.288
U1418F 12R-4W 54-56	404.1 30	329733.3 33	0.145	0.275	0.057	0.000	0.000	0.000	4839.5 26	9191.667	1905.007
U1418F 12R-7W 40-42	408.2 00	334666.6 67	0.387	0.284	0.148	0.000	0.000	0.000	13004. 248	9524.897	4978.488
U1418F 14R-4W 140-150	424.3 90	354290.9 09	0.045	0.151	0.082	0.000	0.000	0.000	1579.3 11	5268.756	2873.168
U1418F 15R-3W 94-96	432.1 30	363672.7 27	0.771	1.069	0.104	0.000	0.000	0.000	27470. 547	38101.36 5	3716.316
U1418F 16R-2W 70-73	440.1 10	373345.4 55	0.392	0.503	0.000	0.000	0.000	0.000	14198. 526	18214.01 3	0.000
U1418F 17R-2W 4-6	449.1 30	384278.7 88	0.420	0.582	0.118	0.000	0.000	0.000	15516. 443	21521.14 6	4362.607
U1418F 17R-4W 102-104	453.1 30	389127.2 73	0.225	1.021	0.953	0.000	0.000	0.000	8452.8 83	38303.68 7	35737.633
U1418F 18R-2W 135-150	460.1 40	397624.2 42	0.245	0.438	0.088	0.000	0.000	0.000	9269.7 93	16566.11	3343.531

Sample	Depth (m) CCSF-A	Preliminary Age(yr)	Brassicasterol ($\mu\text{g g}^{-1}$)	β -sitosterol ($\mu\text{g g}^{-1}$)	Dinosterol ($\mu\text{g g}^{-1}$)	Brassicasterol ($\mu\text{g g}^{-1} \text{TOC}^{-1}$)	β -sitosterol ($\mu\text{g g}^{-1} \text{TOC}^{-1}$)	Dinosterol ($\mu\text{g g}^{-1} \text{TOC}^{-1}$)	Brassicasterol MAR ($\mu\text{g cm}^{-2} \text{Kyr}^{-1}$)	β -sitosterol MAR ($\mu\text{g cm}^{-2} \text{Kyr}^{-1}$)	Dinosterol MAR ($\mu\text{g cm}^{-2} \text{Kyr}^{-1}$)
										7	
U1418F 19R-1W 113-115	468.1 20	410469.5 65	0.175	0.217	0.107	0.000	0.000	0.000	4729.9 22	5865.471	2891.033
U1418F 19R-7W 20-22	476.1 90	424504.3 48	0.223	1.182	0.162	0.000	0.000	0.000	6085.0 01	32309.85 0	4434.610
U1418F 20R-5W 141-143	484.1 30	438313.0 43	0.404	0.767	0.167	0.000	0.000	0.000	11189. 473	21252.06 0	4622.657
U1418F 21R-5W 74-76	493.1 30	453965.2 17	0.240	0.659	0.268	0.000	0.000	0.000	6783.5 13	18628.44 9	7582.882
U1418F 22R-1W 104-106	498.1 31	462662.6 09	0.190	0.533	0.051	0.000	0.000	0.000	5431.8 93	15219.68 9	1451.968
U1418F 22R-5W 104-106	503.1 30	471356.5 22	0.538	0.473	0.150	0.000	0.000	0.000	15560. 314	13682.54 4	4328.462

List of References

Abe-Ouchi, A., Saito, F., Kawamura, K., Raymo, M. E., Okuno, J., Takahashi, K., and Blatter, H., 2013, *Insolation-driven 100.000 year glacial cycles and hysteresis of ice-sheet volume*, Nature 500, 190-193.

Addison, J. A., Finney, B. P., Dean, W. E., Davies, M. H., Mix, A. C., Stoner, J. S. and Jaeger, J. M., 2012, *Productivity and sedimentary $d^{15}N$ variability for the last 17,000 years along the northern Gulf of Alaska continental slope*, Paleoceanography, Vol 27, PA 1206.

Alaska Channel, 2017, <http://www.alaska.org/advice/shortest-day-in-alaska>, last day accessed 17/03/2017.

Anklin, M., J. Schwander, B. Stauffer, J. Tschumi, A. Fuchs, J. M. Barnola, and D. Raynaud, 1997, *CO₂ record between 40 and 8 kyr B.P. from the Greenland Ice Core Project ice core*, J. Geophys. Res., 102, 26 539–26 546.

Annan, J.D. and Hargreaves, J.C., 2013, *A new global reconstruction of temperature changes at the Last Glacial Maximum*, Clim. Past, 9, 367-376.

Bachem, Paul E., Risebrobakken, Bjørg, De Schepper, Stijn and McClymont, Erin L., 2017, *Highly variable Pliocene sea surface conditions in the Norwegian Sea*, Climate of the Past, 13:1153-1168.

Bachem, P.E., Risebrobakken, B. and McClymont, E.L., 2016, *Sea surface temperature variability in the Norwegian Sea during the late Pliocene linked to subpolar gyre strength and radiative forcing*, Earth and Planetary Science Letters, 446:113-122.

Bailey, I., Foster, G.L., Wilson, P.A., Jovane, L., Storey, C.D., Trueman, C.N., Becker, J., 2012, *The flux and provenance of ice-rafted debris in the earliest Pleistocene sub-polar North Atlantic Ocean comparable to that of the Last Glacial maximum*, EPSL 341e344, 222e233. <http://dx.doi.org/10.1016/j.epsl.2012.05.034>.

Bailey, I., Hole, G. M., Foster, G. L., Wilson, P. A., Storey, C. D., Trueman, C. N. and Raymo, M. E., 2013, *An alternative suggestion for the Pliocene onset of major*

northern hemisphere glaciation based on the geochemical provenance of North Atlantic Ocean ice-rafted debris, *Quat. Sci. Rev.*, 75, 181–194.

Ballantyne, A.P., Greenwood, D.R., Sinninghe Damste, J.S., Csank, A.Z., Eberle, J.J., Rybczynski, N., 2010, *Significantly warmer Arctic surface temperatures during the Pliocene indicated by multiple independent proxies*, *Geology* 38, 603–606.

Barnola, J.-M., D. Raynaud, C. Lorius, and N.I. Barkov, 2003, *Historical CO₂ record from the Vostok ice core*, *Trends: A Compendium of Data on Global Change*. Carbon Dioxide Information Analysis Center, Oak Ridge National Laboratory, U.S. Department of Energy, Oak Ridge, Tenn., U.S.A.

Barron, J.A., 1996, *Diatom constraints on the position of the Antarctic Polar Front in the middle part of the Pliocene*, *Marine Micropaleontology* 27 (1–4), 195–213.

Barron, J.A., Anderson, L., 2010, *Enhanced Late Holocene ENSO/PDO expression along the margins of the eastern North Pacific*, *Quaternary International*, doi:10.1016/j.quaint.2010.02.026.

Bartoli, G., Sarnthein, M., Weinelt, M., Erlenkeuser, H., Garbe-Schönberg, C-D., Lea, D. W., 2005, *Final closure of Panama and the onset of northern hemisphere glaciation*, *Earth and Planetary Science Letters*, 237, 33-44, doi:10.1016/j.epsl.2005.06.020.

Beerling DJ, Royer DL., 2011, *Convergent Cenozoic CO₂ history*. *Nat. Geosci.* 4, 418–420, doi:10.1038/ngeo1186.

Belt, S.T., Massé, G., Rowland, S.J., Poulin, M., Michel, C., LeBlanc, B., 2007, *A novel chemical fossil of palaeo sea ice: IP₂₅*, *Organic Geochemistry* 38, 16–27.

Belt, S.T. and Müller, J., 2013, *The Arctic sea ice biomarker IP₂₅: a review of current understanding, recommendations for future research and applications in palaeo sea ice reconstructions*, *Quaternary Science Reviews*, <http://dx.doi.org/10.1016/j.quascirev.2012.12.001>.

Bendle, J. A. and Rosell-Melé, A., 2004, *Distributions of U^K₃₇ and U^K_{37'} in the surface waters and sediments of the Nordic Seas: implications for paleoceanography*,

Geochemistry, Geophysics, Geosystems 5, Q11013-Q11013, doi:10.1029/2004GC000741.

Bendle, J. A. P., A. Rosell-Melé, N. J. Cox, and I. Shennan, 2009, *Alkenones, alkenoates, and organic matter in coastal environments of NW Scotland: Assessment of potential application for sea level reconstruction*, *Geochem. Geophys. Geosyst.*, 10, Q12003, doi:10.1029/2009GC002603.

Bendle, J. A.; Rosell-Melé, A., Ziveri, P., 2005, *Variability of unusual distributions of alkenones in the surface waters of the Nordic seas*, *Paleoceanography*, 20(2), PA2001, doi:10.1029/2004PA001025.

Benson, L., Linsley, B., Smoot, J., Mensing, S., Lund, S., Scott, S. and Andre, S.-W., 2003, *Influence of the Pacific Decadal Oscillation on the climate of the Sierra Nevada, California and Nevada*, *USGS Staff - Published Research*, 782.

<http://digitalcommons.unl.edu/usgsstaffpub/782>

Berger, A. and Loutre, M.-F., 1999, *Parameters of the Earths orbit for the last 5 Million years in 1 kyr resolution*, PANGAEA, <https://doi.org/10.1594/PANGAEA.56040>, Supplement to: Berger, A. and Loutre, M.-F., 1991, *Insolation values for the climate of the last 10 million of years*. *Quaternary Science Reviews*, 10(4), 297-317, [https://doi.org/10.1016/0277-3791\(91\)90033-Q](https://doi.org/10.1016/0277-3791(91)90033-Q).

Bischof, J. A., and Darby, D. A., 1997, *Mid to Late Pleistocene ice drift in the western Arctic Ocean: Evidence for a different circulation in the past*, *Science*, 277, 74 – 78.

Bohaty, S.M., Harwood, D.M., 1998. *Southern Ocean Pliocene paleotemperature variation from high-resolution silicoflagellate biostratigraphy*, *Mar. Micropaleontol.* 33, 241–272.

Bonham, S. G., Haywood, A. M., Lunt, D. J., Collins, M., and Salzmann, U., 2009, *El Niño-Southern Oscillation, Pliocene climate and equifinality*, *Philos.Trans.R.Soc.A*, 367, 127–156, doi:10.1098/rsta.2008.0212.

Boon, J.J., Rijpstra, W.I.C., de Lange, F., de Leeuw, J.W., Yoshioka, M., Shimizu, Y., 1979, *Black Sea sterol – a molecular fossil for dinoflagellate blooms*, *Nature* 277, 125–127.

Bourbonniere, R.A., Meyers, P.A., 1996, *Sedimentary geolipid records of historical changes in the watersheds and productivities of Lakes Ontario and Erie*, *Limnology and Oceanography* 41, 352–359.

Boyd, P.W and Ellwood, M.J., 2010, *The biogeochemical cycle of iron in the ocean*, *Nature Geoscience*, 675-682.

Brassell, S.C., 1993. *Applications of biomarkers for delineating marine paleoclimatic fluctuations during the Pleistocene*, Engel, M.H., Macko, S.A. (Eds.), *Organic Geochemistry: Principles and Applications*. Plenum Press, New York, pp. 699–738.

Brassell, S. C., and Eglinton, G., 1983a, *The potential of organic geochemical compounds as sedimentary indicators of upwelling*, *Coastal Upwelling, Its Sediment Record*, Part A (E. Suess and J. Thiede, eds.), Plenum Press, New York, pp. 545-571.

Brassell, S. C., and Eglinton, G., 1983b, *Steroids and triterpenoids in deep sea sediments as environmental and diagenetic indicators*, *Advances in Organic Geochemistry 1981*, (M. Bjorøy et al., eds.) Wiley, Chichester, England, pp. 684-697.

Brassell, S. C., and Eglinton, G., 1986, *Molecular geochemical indicators in sediments*, *Marine Organic Geochemistry* (M. Sohn, ed.), ACS Symposium Series No. 305, American Chemical Society, Washington, D.C., pp. 10-32.

Bray, R. R. and Evans, E. D., 1961, *Distribution of n-paraffins as a clue to recognition of source beds*, *Geochimica et Cosmochimica Acta*, 22, 2-15.

Bringham-Grette, J., Melles, M., Minyuk, P., Andreev, A., Tarasov, P., Deconto, R., Koenig, S., Nowaczyk, N., Wennrich, V., Rosén, P., Haltia, E., Cook, t., Gebhardt, C., Meyer-Jacob, C., Snyder, J., Herzschuh, U., 2013, *Pliocene warmth, polar amplification, and stepped pleistocene cooling recorded in NE Arctic Russia*, *Science*, 340(6139), 1421-1427, <https://doi.org/10.1126/science.1233137>

Bringué, M., Pospelova, V., Pak, D., 2013, *Seasonal production of organic-walled dinoflagellate cysts in an upwelling system: A sediment trap study from the Santa Barbara Basin, California*, Mar. Micropaleontol. 100, 34–51.

Brodeur, R. D. and Ware D. M., 1995, *Interdecadal variability in distribution and catch rates of epipelagic nekton in the Northeast Pacific Ocean*, Beamish RJ (ed), *Climate Change and Northern Fish Populations*. Canadian Special Publication of Fisheries & Aquatic Sciences 121:329–356.

Broecker, W. S., and G. M. Henderson, 1998, *The sequence of events surrounding Termination II and their implications for the cause of glacial-interglacial CO₂ changes*, *Paleoceanography*, 13, 352–364.

Brown, C. W., and Yoder, J. A., 1994, *Coccolithophorid blooms in the global ocean*, J. Geophys. Res., 99, 7467 – 7482.

Brunelle, B. G., Sigman, D. M., Cook, M. S., Keigwin, L. D., Haug, G. H., Plessen, B., Schettler, G. and Jaccard, S. L., 2007, *Evidence from diatom-bound nitrogen isotopes from subarctic Pacific stratification during the last ice age and link to North Pacific denitrification changes*, *Paleoceanography*, vol 22, PA1215.

Bullard, J. E., Baddock, M., Bradwell, T., Crusius, J., Darlington, E., Gaiero, D., Gassó, S., Gisladottir, G., Hodgkins, R., McCulloch, R., Mckenna-Neuman, C., Mockford, T., Stewart, H. and Thorsteinsson, T., 2016, *High latitude dust in the Earth system*, Rev. Geophys., 54, 447–485, doi:10.1002/2016RG000518.

Burcke, L. H., Mortlock, R. and Rudolph, S., 1996, *No evidence for extreme, long term warming in early Pliocene sediments of the Southern Ocean*, *Marine Micropaleontology* 27, 215-226.

Candy, I. and McClymont, E.L., 2013, *Interglacial intensity in the North Atlantic over the last 800,000 years: investigating the complexity of the mid-Brunhes Event (MBE)*, *Journal of Quaternary Science*, 28:343-348.

Cane, M. A., and P. Molnar, 2001, *Closing of the Indonesian seaway as a precursor to east African aridification around 3 –4 million years ago*, *Nature*, 411, 157–162.

Castaneda, I.S., Werne, J.P., Johnson, T. C., Powers, L. A., 2011, *Organic geochemical records from Lake Malawi (East Africa) of the last 700 years, part II, biomarker evidence for recent changes in primary productivity*. *Palaeogeogr Paleoclimatol Palaeoecol* 303:140-154.

Cauzet, Gabriel, Wainer, Ilana and Bicego, Marcia, 2008, *Validating NCAR-CCSM last glacial maximum sea surface temperature in the tropical and South Atlantic with proxy-data*, *Palaeogeography, Palaeoclimatology and Palaeoecology*, 267, 153-160.

Chan, P., Halfar, J., Williams, B., Hetzinger, S., Steneck, R., Zack, T. and Jacob, D. E., 2011, *Freshening of the Alaska Coastal Current recorded by coralline algal Ba/Ca ratios*, *Journal of Geophysical Research: Biogeosciences*, 116(1), 1–8. <http://doi.org/10.1029/2010JG001548>

Childress, L. B., 2016, *The Active Margin Carbon Cycle: Influences of Climate and Tectonics in Variable Spatial and Temporal Records*, PhD thesis Northwestern University, Evanston, Illinois.

CIAAW (Commission on Isotopic Abundances and Atomic Weights), 2007-2015, <http://www.ciaaw.org/> last day accessed 1/02/2018.

Clayson, Carol Anne; Brown, Jeremiah; and NOAA CDR Program, 2016, *NOAA Climate Data Record (CDR) of Sea Surface Temperature - WHOI, Version 2*, NOAA National Climatic Data Center, doi:10.7289/V5FB510W [26/05/2017].

CLIMAP, 1976, *The surface of the ice-age earth*: By CLIMAP Project Members *Science* 191, 1131–1137.

CLIMAP, 1984, *The last interglacial ocean*. *Quat. Res.* 21, 123–224, doi:10.1016/0033-5894(84)90098-X.

Conte, M. H., Sicre, M-A., Rühlemann, C., Weber, J. C., Schulte, S., Schulz-Bull, D., Blanz, T., 2006, Global temperature calibration of the alkenone unsaturation index ($U^{k_{37}}$) in surface waters and comparison with surface sediments, *Geochemistry, Geophysics, Geosystems (G3)*, vol. 7, n. 2, Q02005, doi:10.1029/2005GC001054.

Conte M. H., Thompson A., Lesley D., and Harris R. P., 1998a, *Genetic and physiological influences on the alkenone/ alkenoate versus growth temperature relationship in Emiliana huxleyi and Gephyrocapsa oceanica*, *Geochim. Cosmochim. Acta* 62, 51–68.

Cortese, G., Gersonde, R., Hillenbrand, C.-D. and Kuhn, G., 2004, *Opal sedimentation shifts in the World Ocean over the last 15 Myr*, *Earth Planet. Sci. Lett.*, 224, 509 – 527, doi:10.1016/j.epsl.2004.05.035.

Cowan, E.A., Hillenbrand, C.-D., Hassler, L.E., Ake, M.T., 2008, *Coarse-grained terrigenous sediment deposition on continental rise drifts: a record of Plio-Pleistocene glaciation on the Antarctic Peninsula*, *Palaeogeogr. Palaeoclimatol. Palaeoecol.* 265, 275–291.

Cranwell, P. A, 1973, *Chain-length distribution of n-alkanes from lake sediments in relation to post-glacial environmental change*, *Freshwater Biol.* 3:259-265.

Cranwell, P.A., 1981, *Diagenesis of free and bound lipids in terrestrial detritus deposited in a lacustrine sediment*, *Organic Geochemistry* 3 (3), 79 – 89.

Creager, J. S., Scholl, D. W., Boyce, R. E., Echols, R. J., Lee, H. J., Ling, H. Y., Stewart, R. J., Supko, P. R. and Worsley, T. R., 1971, *ODP 18 Site 183 Initial Report Volume*, doi:10.2973/dsdp.proc.19.102.1973.

Crosta, X. and Koc, N., 2007, *Chapter Eight Diatoms: From Micropaleontology to Isotope Geochemistry*, *Developments in Marine Geology*, Volume 1, Pages 327–369, [https://doi.org/10.1016/S1572-5480\(07\)01013-5](https://doi.org/10.1016/S1572-5480(07)01013-5).

Crusius, J., A. W. Schroth, S. Gassó, C. M. Moy, R. C. Levy, and M. Gatica, 2011, *Glacial flour dust storms in the Gulf of Alaska: Hydrologic and meteorological controls and their importance as a source of bioavailable iron*, *Geophys. Res. Lett.*, 38, L06602, doi:10.1029/2010GL046573.

Damsté, J. S. S., Rijpstra, W. I. C. and Reichart, G. J., 2002a, *The influence of oxic degradation on the sedimentary biomarker record II: Evidence from Arabian Sea sediments*, *Geochim. Cosmochim. Acta*, 66, 2737 – 2754.

D'anjou, R. M., Wei, J. H., Castaneda, I.S., Brigham-Grette, J., Petsch, S. T. and Finkelstein, D.B., 2013, *High Latitude environmental chance during MIS 9 and 11: biogeochemical evidence from Lake El'gygytgyn*, Far East Russia, *Clim Past*, 9, 567-581.

Davies, M.H., Mix, A. C., Stoner, J. S., Addison, J. A., Jaeger, J., Finney, B. and Wiest, J., 2010, *The deglacial transition on the southeastern Alaska Margin: Meltwater input, sea level rise, marine productivity, and sedimentary anoxia*, *Paleoceanography*, Vol. 26, PA2223.

De Lange, G. J., Van Os, B., Pruyssers, P. A., Middelburg, J. J., Castradori, D., Van Santvoort, P., Müller, P. J., Eggenkamp, H. and Prahl, F. G., 1994, *Possible Early Diagenetic Alteration of Palaeo Proxies*, Volume 17 pp 225-258, Chapter of the series NATO ASI Series in Rainer Zahn, Thomas F. Pedersen, Michael A. Kaminski, Laurent Labeyrie, 1994, *Carbon Cycling in the Glacial Ocean: Constraints on the Ocean's Role in Global Change*, Quantitative Approaches in Paleoceanography, Volume 17, ISBN: 978-3-642-78739-3 (Print) 978-3-642-78737-9 (Online).

De Schepper, S., Groeneveld, J., Naafs, B. D., Van Renterghem, C., Hennissen, J., Head, M. J., Louwye, S. and Fabian, K., 2013, *Northern Hemisphere Glaciation during the Globally Warm Early Late Pliocene*, *PLOS ONE*, Vol. 8, Issue 12, 1-15.

De Schepper, S., Schreck, M., Beck, K. M., Matthiessen, J., Fahl, K. and Mangerud, G., 2015, *Early Pliocene onset of modern Nordic Seas circulation related to ocean gateway changes*, *Nature Communications*, 6:8659, DOI: 10.1038/ncomms9659.

Dekens, P. S., Ravelo, A. C. and McCarthy, M. D., 2007, *Warm upwelling regions in the Pliocene warm period*, *Paleoceanography and Paleoclimatology*, vol. 22, PA3211, doi:10.1029/2006PA001394.

Di Lorenzo, E., and Coauthors, 2008, *North Pacific Gyre Oscillation links ocean climate and ecosystem change*, *Geophys. Res. Lett.*, 35, L08607, doi:10.1029/2007GL032838.

Di Lorenzo, E., Fiechter, J., Schneider, N., Bracco, A., Miller, A. J., Franks, P. J. S., Bograd, S. J., Moore, A. M., Thomas, A. C., Crawford, W., Peña, A. and Hermann, A. J.,

2009, *Nutrient and salinity decadal variations in the central and eastern North Pacific*, *Geophys. Res. Lett.*, 36, L14601, doi:10.1029/2009GL038261.

Di Lorenzo E., N. Schneider, K. M. Cobb, J. Furtado and M. Alexander, 2011, *ENSO and the North Pacific Gyre Oscillation: an integrated view of Pacific decadal dynamics*, *Geophysical Research Letters*, in revision.

Dodson, J.R., Macphail, M.K., 2004, *Palynological evidence for aridity events and vegetation change during the Middle Pliocene, a warm period in Southwestern Australia*, *Global and Planetary Change* 41 (3–4), 285–307

Dolan, A. M., Haywood, A. M., Hill, D. J., Dowsett, H. J., Hunter, S. J., Lunt, D. J. and Pickering, S. J., 2011, *Sensitivity of Pliocene Ice Sheets to Orbital Forcing*, *Palaeogeography, Palaeoclimatology, Palaeoecology* 309, 98-110.

Dolan, A. M., Haywood, A. M., Hunter, S. J., Tindall, J. C., Dowsett, H. J., Hill, D. J. and Pickering, S. J., 2015, *Modelling the enigmatic Late Pliocene Glacial Event, Marine Isotope Stage M2*, *Global and Planetary Change* 128, 47-60.

Dowsett, H. J., Chandler, M. A., and Robinson, M. M., 2009, *Surface temperatures of the mid-Pliocene North Atlantic Ocean: implications for future climate*, *Philos. T. R. Soc. A*, 367, 69–84.

Dowsett, H., A. Dolan, D. Rowley, R. Mocha, A.M. Forte, J.X. Mitrovica, M. Pound, U. Salzmann, M. Robinson, M. Chandler, K. Foley, and A. Haywood, 2016, *The PRISM4 (mid-Piacenzian) palaeoenvironmental reconstruction*, *Clim. Past*, 12, 1519-1538, doi:10.5194/cp-12-1519-2016.

Dowsett, H. J., Foley K.M., Stoll D.K., Chandler M.A., Sohl L.E., Bentsen M., Otto-Bliesner B.L., Bragg F.J., Chan W.L., Contoux C., Dolan A.M., Haywood A.M., Jonas J.A., Jost A., Kamae Y., Lohmann G., Lunt D.J., Nisancioglu K.H., Abe-Ouchi A., Ramstein G., Riesselman C.R., Robinson M.M., Rosenbloom N.A., Salzmann U., Stepanek C., Strother S.L., Ueda H., Yan Q., Zhang Z., 2013, *Sea surface temperature of the mid-Piacenzian Ocean: A data model comparison*, *Sci. Rep.*, 3.

Dowsett, H.J., Robinson, M.M., Haywood, A.M., Hill, D.J., Dolan, A.M., Stoll, D.K., Chan, W.-L., Abe-Ouchi, A., Chandler, M.A., Rosenbloom, N.A., Otto-Bliesner, B.L., Bragg,

F.J., Lunt, D. J., Foley, K.M., Riesselman, C.R., 2012, *Assessing confidence in Pliocene sea surface temperatures to evaluate predictive models*, *Nat. Clim. Chang.* 2, 365–371.

Dowsett, H.J., Robinson, M.M., Stoll, D.K., Foley, K.M., 2010, *Mid-Piacenzian mean annual sea surface temperature analysis for data-model comparisons*, *Stratigraphy* 7, 189–198.

Dowsett, H., Thompson, R., Barron, J., Cronin, T., Fleming, F., Ishman, S., Poore, R., Willard, D. and Holtz Jr., T., 1994, *Joint investigations of the middle Pliocene climate I: PRISM paleoenvironmental reconstructions*, *Global and Planetary Change* 9, 169–195.

Dugdale, R. C. and Wilkerson, F. P., 2001, *Sources and fates of silicon in the ocean: the role of diatoms in the climate and glacial cycles*, *Scientia Marina* 65, 141–152.

Eggleston, S, Schmitt, J., Bereiter, B., Schneider, R. and Fischer, H., 2016, *Evolution of the stable carbon isotope composition of atmospheric CO₂ over the last glacial cycle*, *Paleoceanography*, 31, <https://doi.org/10.1002/2015PA002874>.

Elderfield, H., Ferretti, P., Greaves, M., Crowhurst, S., McCave, I. N., Hodell, D. and Piotrowski, A. M., 2012, *Evolution of Ocean Temperature and Ice Volume Through the Mid-Pleistocene Climate Transition*, *Science*, 337(6095), 704–709.

Emile-Geay, J., Cane, M. A., Naik, N., Seager, R., Clement, A. C. and van Geen, A., 2003, *Warren revisited: Atmospheric freshwater fluxes and Why is no deep water formed in the North Pacific*, *J. Geophys. Res.*, 108(C6), 3178, doi:10.1029/2001JC001058.

Enkelmann, E., Garver, J. I. and Pavlis, T. L., 2008, *Rapid exhumation of ice-covered rocks of the Chugach-St. Elias orogen, Southeast Alaska*, *Geology*, 36, 915–918, doi:10.1130/G2252A.1.

Enkelmann, E., Koons, P. O., Pavlis, T. L., Hallet, B., Barker, A., Elliott, J., Garver, J. I., Gulick, S. P. S., Headley, R. M., Pavlis, G. L., Ridgway, K. D., Ruppert, N., Van Avendonk, H. J. A., 2015, *Cooperation among tectonic and surface processes in the St. Elias Range, Earth's highest coastal mountains*, *Geophysical Research Letters*, 42 (14): 5838 DOI: 10.1002/2015GL064727.

Enkelmann, E., Zeitler, P.K., Pavlis, T. L., Grver, J.I. and Ridgway, K. D., 2009, *Intense localized rock uplift and erosion in the St. Elias orogeny of Alaska*, *Nature Geoscience*, 1-4.

Evans, W., and Mathis, J. T., 2013, *The Gulf of Alaska coastal ocean as an atmospheric CO₂ sink*, *Continental Shelf Research*, 65(February), 52–63. <http://doi.org/10.1016/j.csr.2013.06.013>.

Expedition 341 Scientists, 2014, *Southern Alaska Margin: interactions of tectonics, climate, and sedimentation*, IODP Prel. Rept., 341. doi:10.2204/iodp.pr.341.2014.

Fedorov, A. V., Burls, N. J., Lawrence, K. T., and Peterson, L. C., 2015, *Tightly linked zonal and meridional sea surface temperature gradients over the past five million years*, *Nat. Geosci.*, 8(12), 975–980.

Fedorov, A. V., Hu, S., Lengaigne, M. and Guilyardi, E., 2014, *The impact of Westerly wind bursts and ocean initial state on the development, and diversity of El Niño events*, *Clim. Dyn.*, doi:10.1007/s00382-014-2126-4.

Fedorov, A. V., Lawrence, K. T., Liu, Z., Dekens, P. S., Ravelo, A. C., and Brierley, C. M., 2013, *Patterns and mechanisms of early Pliocene warmth*, *Nature*, 496, 43–49, doi:10.1038/nature12003.

Feely, R.A., Baker, E.T., Schumacher, J.D., Massoth, G.J. and Landing, W.M., 1979, *Processes affecting the distribution and transport of suspended matter in the northeastern Gulf of Alaska*, *Deep-Sea Research*, 26, pp. 445-464

Ferreira, D., Marshall, J. and Campin, J.-M., 2010, *Localization of deep water formation: Role of atmospheric moisture transport and geometrical constraints on ocean circulation*, *J. Clim.*, 23, 1456–1476.

Finzel, E.S., Trop, J.M., Ridgway, K.D. and Enkelmann, E., 2011, *Upper plate proxies for flat- slab subduction processes in southern Alaska*, *Earth Planet. Sci. Lett.*, 303(3–4):348–360, doi:10.1016/j.epsl.2011.01.014.

Ford, H. L., Ravelo, A. C., Dekens, P. S., LaRiviere, J. P. M. W. Wara, M. W., 2015, *The evolution of the equatorial thermocline and the early Pliocene El Padre mean state*, *Geophysical Research Letters*, 42, doi: 10.1002/2015GL064215.

Francois, R., Altabet, M. A., Yu, E.-F., Sigman, D. M., Bacon, M., Frank, M., Bohrmann, G., Bareille, G. and Labeyrie, L. D., 1997, *Contribution of Southern Ocean surface-water stratification to low atmospheric CO₂ concentrations during the last glacial period*, *Nature*, 389, 929 – 935.

Furtado, J. C., Di Lorenzo, E., Schneider, N. and Bond, N.A., 2011, *North Pacific Decadal Variability and Climate Change in the IPCC AR4 Models*, American Meteorological Society, Vol. 24, 3049-3067.

Galaasen, E. V., Ninnemann, U.S., Irvani, N., Kleiven, H. K., Rosenthal, Y., Kissel, C. and Hodell, D. A., 2014, *Rapid reconstructions in North Atlantic Deep Water during the peak of the last interglacial period*, *Science*, 343, DOI: 10.1126/science.1248667.

Galbraith, E. D., Jaccard, S. L., Pederson, T. F., Sigman, D. M., Haug, G. H., Cook, M., Southon, J. R. and Francois, R., 2007, *Carbon dioxide release from the North Pacific abyss during the last deglaciation*, *Nature Letters*, vol 449.

Galbraith, E. D., M. Kienast, T. F. Pedersen, and S. E. Calvert, 2004, *Glacial-interglacial modulation of the marine nitrogen cycle by high- latitude O₂ supply to the global thermocline*, *Paleoceanography*, 19, PA4007, doi:10.1029/2003PA001000.

Gaskell, S. J. and Eglinton, G., 1974, *Short-term diagenesis of sterols*, *Adv. Org. Geochem., Proc. Int. Meet., 6th, Meeting Date 1973*, 963-76.

Gebhardt, H., Sarnthein, M., Grootes, P.M., Kiefer, T., Kuehn, H., Schmieder, F. and Röhl, U., 2008, *Paleonutrient and productivity records from the subarctic North Pacific for Pleistocene glacial terminations I to V*, *Paleoceanography*, 23:PA4212–PA4232. doi:10.1029/2007PA001513

Goad, L. and Withers, N., 1982, *Identification of 27-nor-(24R)-24-methylcholesta-5,22-dien-3 β -ol and brassicasterol as the major sterols of the marine dinoflagellate *Gymnodinium simplex**, *Lipids*, 17, 853–858, doi:10.1007/bf02534578.

Goni, M. A., Woodworth, M. P., Aceves, H. L., Thunell, R. C., Tappa, E., Black, D., Müller-Karger, F., Astor, Y. and Varela, R., 2004, *Generation, transport, and preservation of the alkenone-based UK₃₇' sea surface temperature index in the water*

column and sediments of the Cariaco Basin (Venezuela), Global Biogeochem. Cycles, 18, GB2001, doi:10.1029/2003GB002132.

Google earth V 7.1.7.2606 (December 2016), Gulf of Alaska, 56° 57' 38.32"N 147° 09'33.41"W, elevation -4191m, eye alt 1795.14 Km, SIO, NOAA, U.S. Navy, NGA, GEBCO, Landsat, IBCAO, 2016 <http://www.earth.google.com> data from IODP drilled holes file <http://www.iodp.org/resources/maps-and-kml-tools>, viewed 6th Dec., 2016.

Grice, K. W. C., Breteler, M. K., Schouten, S. and Grossi, V., 1998, *Effects of zooplankton herbivory on biomarker records*, Paleooceanography, 13, 686–693.

Gu, B., Alexander, V. and Schell, D. M., 1999, *Seasonal and interannual variability of plankton carbon isotope ratios in a subarctic lake*, Freshwater Biology, 42: 417–426. doi:10.1046/j.1365-2427.1999.00472.x.

Gulick, S. P. S., Jaeger, J. M., Mix, A. C., Asahi, H., Bahlburg, H., Belanger, C. L., Berbel, G. B., Childress, L., Cowan, E., Drab, L., Forwick, M., Fukumura, A., Ge, S., Gupta, S., Kiola, A., Konno, S., LeVay, L. J., Marz, C., Matsuzaki, K. M., McClymont, E. L., Moy, C., Muller, J., Nakamura, A., Ojima, T., Ribeiro, F. R., Ridgway, K. D., Romero, O. E., Slagle, A. L., Stoner, J. S., St-Onge, G., Suto, I., Walczak, M. D., Worthington, L. L., Bailey, I., Enkelmann, E., Reece, R. and Swartz, J.M., 2015, *Mid-Pleistocene climate transition drives net mass loss from rapidly uplifting St. Elias Mountains, Alaska*, Proceedings of the National Academy of Sciences of the United States of America, 112(49), 15042–15047. <http://doi.org/10.1073/pnas.1512549112>

Gutjahr, M., Frank, M., Stirling, C. H., Keigwin, L. D. & Halliday, A. N., 2008, *Tracing the Nd isotope evolution of North Atlantic Deep and Intermediate Waters in the western North Atlantic since the Last Glacial Maximum from Blake Ridge sediments*. Earth and Planetary Science Letters 266, 61-77, doi:<http://dx.doi.org/10.1016/j.epsl.2007.10.037>.

Haeussler, P.J. and Plafker, G., 2003, *Earthquakes in Alaska*, US Department of the Interior, US Geological Survey, 95-624 <http://www.infohow.org/wp-content/uploads/2012/11/Earthquakes-in-Alaska.jpg> (date accessed 13/11/2015).

Hallet, B., Hunter, L. and Bogen, J., 1996, *Rates of erosion and sediment evacuation by glaciers: A review of field data and their implications*, *Global Planet. Change*, 12, 213–235.

Han, J. and Calvin, M., 1969, *Hydrocarbon distribution of algae and bacteria, and microbiological activity in sediments*, *Proceedings of the National Academy of Sciences* 64(2) 436-443, DOI: 10.1073/pnas.64.2.436

Hansen, J., Sato, M., Ruedy, R., Lo, K., Lea, D. and Medina-Elizalde, M., 2006, *Global temperature change*, *Proc. Nat. Acad. Sci. USA* 103, 14 288–14 293, doi:10.1073/pnas.0606291103.

Hansen, J., Sato, M., Russell G. and Kharecha, P., 2013, *Climate sensitivity, sea level and atmospheric carbon dioxide*, *Philosophical Transactions of the Royal Society A*, vol 371, issue 2001, DOI: 10.1098/rsta.2012.0294.

Harada, N., Sato, M., Sakamoto, T., 2008, *Freshwater impacts recorded in tetraunsaturated alkenones and alkenone sea surface temperatures from the Okhotsk Sea across millennial-scale cycles*, *Paleoceanography* 23.

Harada, N., Sato, M., Shiraishi, A. and Honda, M.C., 2006, *Characteristics of alkenone distributions in suspended and sinking particles in the northwestern North Pacific*, *Geochim. Cosmochim. Acta*, 70, pp. 2045–2062.

Harwell, M. A. Gentile, J.H., Cummins, K. W., Highsmith, R. C., Hillborn, R., McRoy, P. Parrish, J. and Weingartner, T., 2010, *A Conceptual Model of Natural and Anthropogenic Drivers and Their Influence on the Prince William Sound, Alaska, Ecosystem*, *Human and Ecological Risk Assessment*, 16: 672–726.

Haug, G. H., Ganopolski, A., Sigman, D. M., Rosell-Mele, A., Swann, G. E. A., Tiedemann, R., Jaccard, S. L., Bollmann, J., Maslin, M A, Leng, M. J. and Eglinton, G., 2005, *North Pacific seasonality and the glaciation of North America 2.7 million years ago*, *Nature*, vol 433, 821-825.

Haug, G. H., Sigman, D. M., Tiedemann, R., Pedersen, T. F. and Sarnthein, M., 1999, *Onset of Permanent stratification in the subarctic Pacific Ocean*, *Letters to Nature*, Vol. 401, 779-782.

Haug, G.H. and Tiedemann, R., 1998, *Effect of the formation of the Isthmus of Panama on Atlantic Ocean thermohaline circulation*, *Nature* 393, 673–676.

Hays, J.D., Lozano, J.A., Shackleton, N.J. and Irving, G., 1976, *Reconstruction of the Atlantic and western Indian Ocean sectors of the 18,000 BP Antarctic Ocean*. In: Cline, R.M. and Hays, J.D. (eds), *Investigations of Late Quaternary Paleoceanography and Paleoclimatology*, Geological Society of America Memoirs 145, pp. 337-372.

Haywood, A.M., Dolan, A.M., Pickering, S.J., Dowsett, H.J., McClymont, E.L., Prescott, C.L., Salzmann, U., Hill, D.J., Hunter, S.J., Lunt, D.J., Pope, J.O., Valdes, P.J., 2013a, *On the identification of a Pliocene time slice for data–model comparison*. *Philos. Trans. R. Soc., Math. Phys. Eng. Sci.* 371, 20120515. <http://dx.doi.org/10.1098/rsta.2012.0515>.

Haywood, A.M., Dowsett, H.J., Otto-Bliesner, B., Chandler, M.A., Dolan, A.M., Hill, D.J., Lunt, D.J., Robinson, M.M., Rosenbloom, N., Salzmann, U. and Sohl, L.E., 2010, *Pliocene Model Intercomparison Project (PlioMIP): Experimental design and boundary conditions (Experiment 1)*. *Geosci. Model Dev.*, 3, 227-242, doi:10.5194/gmd-3-227-2010.

Haywood, A. M., Hill, D. J., Dolan, A. M., Otto-Bliesner, B. L., Bragg, F., Chan, W.-L., Chandler, M. A., Contoux, C., Dowsett, H. J., Jost, A., Kamae, Y., Lohmann, G., Lunt, D. J., Abe-Ouchi, A., Pickering, S. J., Ramstein, G., Rosenbloom, N. A., Salzmann, U., Sohl, L., Stepanek, C., Ueda, H., Yan, Q., and Zhang, Z., 2013, *Large-scale features of Pliocene climate: results from the Pliocene Model Intercomparison Project*, *Clim. Past*, 9, 191–209, doi:10.5194/cp-9-191-2013, 2013.

Haywood A.M. and Valdes P.J., 2004, *Modelling Pliocene warmth: contribution of atmosphere, oceans and cryosphere*, *Earth and Planetary Science Letters*, 218, pp.363-377. doi: 10.1016/S0012-821X(03)00685-X.

Herbert, T. D., 2001, *Review of alkenone calibrations (culture, water column and sediments)*, *Geochem. Geophys. Geosyst.*, vol 2, paper number 2000GC000055.

Herbert, T. D., 2003, *Alkenone Paleotemperature Determinations*, *Treatise on Geochemistry*, Elsevier, Volume 6; (ISBN: 0-08-044341-9); pp. 391–432.

Herbert, T.D., Cleaveland Peterson, L., Lawrence, K.T., Liu, Z., 2010, *Tropical ocean temperatures over the past 3.5 million years*, Science 328, 1530, <http://dx.doi.org/10.1126/science.1185435>.

Herbert, T. D., Lawrence, K. T., Tzanova, A., Peterson, L. C., Caballero-Gill, R., Kelly, C. S., 2016, *Late Miocene global cooling and the rise of modern ecosystems*, Nature Geoscience, 9(11), 843-847, <https://doi.org/10.1038/ngeo2813>.

Herman, Y, 1970, *Arctic paleoceanography in late Cenozoic time*, Science, 169:474-477.

Hill, D.J., Csank, A.Z., Dolan, A.M., Lunt, D.J., 2011, *Pliocene climate variability: Northern Annular Mode in models and tree-ring data*, Palaeogeography, Palaeoclimatology, Palaeoecology 309 (1–2), 118–127.

Hill, D. J., Bruhis, N., Calos, S. E., Arendt, A. and Beamer, J., 2015, *Spatial and temporal variability of freshwater discharge into the Gulf of Alaska*, Journal of Geophysical Research:Oceans, vol. 120, issue 2, 634–646,doi:10.1002/2014JC010395.

Hinckley, S., Coyle, K.O., Gibson, G., Hermann, A.J. and Dobbins, E.L., 2009, *A biophysical NPZ model with iron for the Gulf of Alaska: reproducing the differences between an oceanic HNLC ecosystem and a classical northern temperate shelf ecosystem*, Deep-Sea Research II 56 (24), 2520–2536.

Hogan, C., 2013, *Oceans and Seas Gulf of Alaska*, The Encyclopedia of Earth, <http://www.eoearth.org/view/article/153188> (date accessed 13/11/2015).

Hopkinson, C.S. and Vallino, J., 2005, *Efficient export of carbon to the deep ocean through dissolved organic matter*, Nature, 433, 142-145.

Horikawa, K., Martin, E. E., Basak, C., Onodera, J., Seki, O., Sakamoto, T., Ikehara, M., Sakai, S. and Kwamura, K., 2015, *Pliocene cooling enhanced by flow of low-salinity Bering Sea water to the Arctic Ocean*, Nature Communications, 6:7587.

Huang, W. Y., Meinschein, W. G., 1976, *Sterols as source indicators of organic materials in sediments*, Geochimica et Cosmochimica Acta 40, 323–330.

Ikehara, M., Kawamura, K., Ohkouchi, N., Murayama, M., Nakamura, T. and Tira, A., 2000, *Variations of terrestrial input and marine productivity in the Southern Ocean (48°S) during the last two deglaciations*, *Paleoceanography*, 15, 170-180.

Imbrie, J., Berger, A., Boyle, E. A., Clemens, S. C., Duffy, A., Howard, W. R., Kukla, G., Kutzbach, J., Martinson, D. G., McIntyre, A., Mix, A. C., Molino, B., Morley, J. J., Peterson, L. C., Pisias, N. G., Prell, W. L., Raymo, M. E., Shackleton, N. J. and Toggweiler, J. R., 1993, *On the structure and origin of major glaciation cycles 2. The 100,000-year cycle*, *Paleoceanography*, 8, 699–735, doi:10.1029/93PA02751.

Imbrie, J., Boyle, E. A., Clemens, S. C., Duffy, A., Howard, W. R., Kukla, G., Kutzbach, J., Martinson, D. G., McIntyre, A., Mix, A. C., Molino, B., Morley, J. A., Peterson, L. C., Pisias, N. G., Prell, W. L., Raymo, M. E., Shackleton, N. J. and Toggweiler, J. R., 1992, *On the Structure and Origin of Major Glaciation Cycles 1. Linear Responses to Milankovitch Forcing*, *Paleoceanography*, 7(6), 701-738. DOI: 10.1029/92PA02253

Imbrie, J.Z., Imbrie-Moore, A., Lisiecki, L.E., 2011, *A phase-space model for Pleistocene ice volume*. *Earth and Planetary Science Letters* 307, 94–102.

IPCC, 2007, Chapter 6.4.1 *Climate Forcings and Responses Over Glacial-Interglacial Cycles*, *Climate Change 2007: Working Group I: The Physical Science Basis* https://www.ipcc.ch/publications_and_data/ar4/wg1/en/ch6s6-4.html (last accessed 13/11/2015).

Jaccard, S. L., Galbraith, E. D., Sigman, D. M., Haug, G. H., François, R., Pedersen, T. F., Dulski, P. and H. R. Thierstein, 2009, *Subarctic Pacific evidence for a glacial deepening of the oceanic respired carbon pool*, *Earth Planet. Sci. Lett.*, 277, 156–165.

Jaccard, S. L., Haug, G. H., Sigman, D. M., Pedersen, T. F., Thierstein, H. R. and Rohl, U., 2005, *Glacial/interglacial changes in subarctic north pacific stratification*. *Science* 308, 1003–1006.

Jackson, M. G. and Hart, S. R., 2006, *Strontium isotopes in melt inclusions from Samoan basalts: Implications for heterogeneity in the Samoan plume*, *Earth and Planetary Science Letters* 245, 260-277, doi:http://dx.doi.org/10.1016/j.epsl.2006.02.040.

Jaeger, J.M., Gulick, S.P.S., LeVay, L.J., and the Expedition 341 Scientists, 2014. *Southern Alaska Margin*, Proc. IODP, 341: College Station, TX (Integrated Ocean Drilling Program). doi:10.2204/iodp.proc.341.2014

Jaeger, J.M., Gulick, S.P.S., LeVay, L.J., Asahi, H., Bahlburg, H., Belanger, C.L., Berbel, G.B.B., Childress, L.B., Cowan, E.A., Drab, L., Forwick, M., Fukumura, A., Ge, S., Gupta, S.M., Kioka, A., Konno, S., März, C.E., Matsuzaki, K.M., McClymont, E.L., Mix, A.C., Moy, C.M., Müller, J., Nakamura, A., Ojima, T., Ridgway, K.D., Rodrigues Ribeiro, F., Romero, O.E., Slagle, A.L., Stoner, J.S., St-Onge, G., Suto, I., Walczak, M.H., and Worthington, L.L., 2014, *Site U1417*. In Jaeger, J.M., Gulick, S.P.S., LeVay, L.J., and the Expedition 341 Scientists, Proc. IODP, 341: College Station, TX (Integrated Ocean Drilling Program). doi:10.2204/iodp.proc.341.103.2014.

Jaeger, J.M., Gulick, S.P.S., LeVay, L.J., Asahi, H., Bahlburg, H., Belanger, C.L., Berbel, G.B.B., Childress, L.B., Cowan, E.A., Drab, L., Forwick, M., Fukumura, A., Ge, S., Gupta, S.M., Kioka, A., Konno, S., März, C.E., Matsuzaki, K.M., McClymont, E.L., Mix, A.C., Moy, C.M., Müller, J., Nakamura, A., Ojima, T., Ridgway, K.D., Rodrigues Ribeiro, F., Romero, O.E., Slagle, A.L., Stoner, J.S., St-Onge, G., Suto, I., Walczak, M.H., and Worthington, L.L., 2014, *Site U1418*. In Jaeger, J.M., Gulick, S.P.S., LeVay, L.J., and the Expedition 341 Scientists, Proc. IODP, 341: College Station, TX (Integrated Ocean Drilling Program). doi:10.2204/iodp.proc.341.103.2014.

Jaeger, J., Gulick, S., Mix, A., and Petronotis, K., 2011, *Southern Alaska margin: interactions of tectonics, climate, and sedimentation*, IODP Sci. Prosp., 341. doi:10.2204/iodp.sp.341.2011

Jakob, K. A., Wilson, P. A., Bahr, A., Bolton, C.T., Pross, J., Fiebig, J. and Friedrich, O., 2016, *Plio Pleistocene glacial-interglacial productivity changes in the eastern equatorial Pacific upwelling system*, *Paleoceanography*, 31, 453–470, doi:10.1002/2015PA002899.

Jansen, E., Fronval, T., Rack, F., Channell, J.E.T., 2000, *Pliocene–Pleistocene ice rafting history and cyclicity in the Nordic Seas during the last 3.5 Myr*, *Paleoceanography* 15, 709–721. <http://dx.doi.org/10.1029/1999PA000435>.

Jansen, E., Overpeck, J., Briffa, K.R., Duplessy, J.-C., Joos, F., Masson-Delmotte, V., Olago, D., Otto-Bliesner, B., Peltier, W.R., Rahmstorf, S., Ramesh, R., Raynaud, D., Rind, D., Solomina, O., Villalba, R. and Zhang, D., 2007, *Palaeoclimate*. In. Solomon, S., Qin, D., Manning, M., Chen, Z., Marquis, M., Averyt, K.B., Tignor, M. and Miller, H.L., 2007, *Climate Change 2007: The Physical Science Basis*. Contribution of Working Group I to the Fourth Assessment Report of the Intergovernmental Panel on Climate Change, Eds. Cambridge University Press, ISBN 978 0521 88009-1, 433-497.

Jansen, E., Sjöholm, J., 1991, *Reconstruction of glaciation over the past 6 My, from ice-borne deposits in the Norwegian Sea*, Nature 349, 600-603.

Jaschinski, S., Hansen, T. and Sommer, U., 2008, *Effects of acidification in multiple stable isotope analyses*, Limnology and Oceanography: Methods 6, 12-15.

Kamikuri, S-I, Nishi, H. and Motoyama, I., 2007, *Effects of late Neogene climatic cooling on North Pacific radiolarian assemblages and oceanographic conditions*, Palaeogeography, Palaeoclimatology, Palaeoecology, 249(3-4), 370-392.

Kanazawa, A., Yoshioka, M., Teshima, S.-I., 1971, *The occurrence of brassicasterol in the diatoms Cyclotella nana and Nitzschia closterium*, Bull. Jpn. Soc. Sci. Fish. 37, 889-903.

Kandiano, E.S., Bauch, H.A., Müller, A., 2004, *Sea surface temperature variability in the North Atlantic during the last two glacial-interglacial cycles: comparison of faunal, oxygen isotopic, and Mg/Ca derived records*, Palaeogeography, Paleoclimatology, Palaeoecology 204, 145-164.

Karas, C., Nürnberg, D., Tiedemann, R., Garbe-Schönberg, D., 2011a, *Pliocene climate change of the Southwest Pacific and the impact of ocean gateways*, Earth Planet. Sci. Lett. 301, 117-124.

Karas, C., Nürnberg, D., Tiedemann, R., Garbe-Schönberg, D., 2011b, *Pliocene Indonesian Throughflow and Leeuwin Current dynamics: implications for Indian Ocean polar heat flux*, Paleoceanography 26, PA2217.
<http://dx.doi.org/10.1029/2010PA001949>.

Kato, Y., Onodera, J., Suto, I., Teraishi, A. and Takahashi, K., 2016, *Pliocene and Pleistocene paleoceanography in the western subarctic Pacific based on diatom analyses of ODP Leg 145 Hole 884B and IODP Expedition 323 Holes U1341B and U1343E*, Deep-Sea Res. II, vol. 125-126, 29-37.

Keeling, R. F., Piper, S. C., Bollenbacher, A. F. and Walker, S. J., 2009, *Scripps CO₂ program*. In: Jolla, La. (Ed.), Scripps Institution of Oceanography (SIO). University of California, California USA.

Kennedy, P., Kennedy, H. and Papadimitriou, S., 2005, *The effect of acidification on the determination of organic carbon, total nitrogen and their stable isotopic composition in algae and marine sediment*, Rapid Communications in Mass Spectrometry, 19, 1063-1068.

Kent DV and Muttoni G, 2008, *Equatorial convergence of India and Early Cenozoic climate trends*, Proc. Natl Acad. Sci. USA 105, 16 065–16 070. (doi:10.1073/pnas.0805382105)

Kienast, F., Wetterich, S., Kuzmina, S., Schirrmeister, L., Andreev, A.A., Tarasov, P., Nazarova, L., Kossler, A., Frolova, L., and Kunitsky, V.V., 2011, *Paleontological records indicate the occurrence of open woodlands in a dry inland climate at the present-day Arctic coast in western Beringia during the Last Interglacial: Quaternary Science Reviews*, v. 30, , p. 2134–2159, doi: 10.1016/j.quascirev.2010.11.024.

Killops, S. and Killops, V., 2005, *Introduction to Organic Geochemistry*, 2nd ed., 393 pp. Oxford: Blackwell Publishing, Online ISBN: 9781118697214, DOI: 10.1002/9781118697214.

Kim, J-H., Schouten, S., Buscail, R., Ludwig, W., Bonnin, J., Sinninghe Damste, J., S., and Bourrin, F., 2006, *Origin and distribution of terrestrial organic matter in the NW Mediterranean (Gulf of Lions): Exploring the newly developed BIT index*, Geochemistry, Geophysics Geosystems: An electronic Journal of the Earth Sciences, vol. 7, n. 11, 1-20.

Kim, J.-H., Schouten, S., Hopmans, E.C., Donner, B., Sinninghe Damsté, J.S.S., 2008, *Global sediment core-top calibration of the TEX₈₆ paleothermometer in the ocean*, *Geochimica et Cosmochimica Acta* 72, 1154e1173.

Kipphut, G. K., 1990, *Glacial meltwater input to the Alaska Coastal Current: Evidence from oxygen isotope measurements*, *Journal of Geophysical Research*, Volume 95, Issue C4.

Kirby, M.E., Lund, S.P., Patterson, W.P., Anderson, M. A., Bird, B. W., Ivanovici, L., Monarrez, P., Nielsen, S., 2010, *A Holocene record of Pacific Decadal Oscillation (PDO)-related hydrologic variability in Southern California (Lake Elsinore, CA)*, *J Paleolimnol* 44, 819, <https://doi.org/10.1007/s10933-010-9454-0>.

Knudson, K. P. and Ravelo, A. C., 2015, *North Pacific Intermediate Water circulation enhanced by the closure of the Bering Strait*, *Paleoceanography*, 30, 1287–1304.

Kornilova, O. and Rosell-Melé, A., 2003, *Application of microwave-assisted extraction to the analysis of biomarker climate proxies in marine sediments*, *Organic Geochemistry*, 34, 1517–1523.

Krissek, L. A., *Late Cenozoic Ice-Rafting Records From Leg 145 Sites In The North Pacific: Late Miocene Onset, Late Pliocene Intensification and Pliocene-Pleistocene Events*, in Rea D. K. Basov, L. A., Scholl, D. W. and Allan, J.F., 1995 *Proceedings of the Ocean Drilling Scientific Results*, Vol 145.

Kucera, M., 2007, *Planktonic foraminifera as tracers of past oceanic environments*, In Hillaire, M., and de Vernal, A. (Eds.), *Proxies in Late Cenozoic Paleoceanography*. *Dev. Mar. Geol.*, 1:213–262. doi:10.1016/S1572- 5480(07)01011-1

Kuijpers, A., Knutz, P. and Moros, M., 2014, *Ice Rafter Debris (IRD)*, *Encyclopedia of Marine Geosciences*, doi 10.1007/978-94-007-6644-0_182-1.

Kürschner W. M., van der Burgh J., Visscher H. and Dilcher D. L., 1996, *Oak leaves as biosensors of late Neogene and early Pleistocene paleoatmospheric CO₂ concentrations*, *Marine Micropaleontology*, 27,299–312.

Ladd, C., Hunt, Jr. G.L., Mordy, C.W., Salo, S.A. and Stabeno, P.J., 2005, *Marine environment of the eastern and central Aleutian Islands*, Fisheries Oceanography, 14(Suppl. 1), 22-38.

Lagoe, M.B., Eyles, C.H., Eyles, N., and Hale, C., 1993, *Timing of late Cenozoic tidewater glaciation in the far North Pacific*, Geol. Soc. Am. Bull., 105(12):1542–1560. doi:10.1130/0016-7606(1993)105<1542:TOLCTG>2.3.CO;2.

Lam, P. J., Robinson, L. F., Blusztajn, J., Li, C., Cook, M. S., McManus, J. F. and Keigwin, L. D., 2013, *Transient stratification as the cause of the North Pacific productivity spike during the deglaciation*, Nature Geoscience letters, 1-10.

Lang, N., Wolff, E.W., 2011, *Interglacial and glacial variability from the last 800 ka in marine, ice and terrestrial archives*, Climate of the Past 7, 361–380. <http://dx.doi.org/10.5194/cp-5197-5361-5201>.

LaRiviere, J.P., Ravelo, A.C., Grimmings, A., Dekens, P., Ford, H.L., Lyle, M., Wara, M.W., 2012, *Late Miocene decoupling of oceanic warmth and atmospheric carbon dioxide*, Nature 486, 97–100.

Lawrence, K. T., Herbert, T. D., Brown, C. M., Raymo, M. E. and Haywood, A. M., 2009, *High-amplitude variations in North Atlantic sea surface temperature during the early Pliocene warm period*, Paleoceanography, 24, PA2218, <https://doi.org/10.1029/2008PA001669>.

Lawrence, K.T., Liu, Z., Herbert, T.D., 2006, *Evolution of the eastern tropical Pacific through Plio-Pleistocene glaciation*, Science 312, 79–83.

Lawrence, K. T., Sigman, D. M., Herbert, T. D., Riihimaki, C. A., Bolton, C. T., Martinez-Garcia, A., Rosell-Melé, A. and Haug, G. H., 2013, *Time-transgressive North Atlantic productivity changes upon Northern Hemisphere glaciation*, Paleoceanography, 28, 740–751, doi:10.1002/2013PA002546.

Lawrence, K. T., Sosdian, S., Wite, H. E. and Rosenthal, Y., 2010, *North Atlantic climate evolution through the Plio-Pleistocene climate transitions*, Earth and Planetary Science Letters 300, 329-342.

Lead, A. L., and Evans, J.-L., 2011-2016, *Introduction to Tropical Meteorology*, 2nd Edition 1997-2017, COMET/UCAR, University Corporation for Atmospheric Research.

Lee, K. and Slowey, N., 1999, *Cool surface waters of the subtropical north Pacific during the last glacial*, *Nature* 397: 512–514

Leg 145 Scientific Party, 1992, *ODP Leg 145 Scientific Prospectus North Pacific Transect*, Scientific Prospectus n. 45.

Lei, Y., Servais, T. and Feng, Q. and He, W., 2012, *The spatial (nearshore–offshore) distribution of latest Permian phytoplankton from the Yangtze Block, South China*, *Palaeogeography Palaeoclimatology Palaeoecology* 363–364:151–162 DOI10.1016/j.palaeo.2012.09.010.

Lei, Y., Servais, T. and Feng, Q., 2013, *The diversity of the Permian phytoplankton*, *Review of Palaeobotany and Palynology* 198, 145-161, DOI:10.1016/j.revpalbo.2013.03.004.

Leroy, S., Dupont, L., 1994, *Development of vegetation and continental aridity in northwestern Africa during the Late Pliocene: the pollen record of ODP site 658*, *Palaeogeography, Palaeoclimatology, Palaeoecology* 109, 2–4, 295–316.

Levitus, Sydney; Boyer, Tim P.; Garcia, Hernan E.; Locarnini, Ricardo A.; Zweng, Melissa M.; Mishonov, Alexey V.; Reagan, James R.; Antonov, John I.; Baranova, Olga K.; Biddle, Mathew; Hamilton, Melanie; Johnson, Daphne R.; Paver, Christopher R.; Seidov, Dan, 2015, *World Ocean Atlas 2013 (NCEI Accession 0114815)*, Version 3.3. NOAA National Centers for Environmental Information Dataset, doi:10.7289/V5F769GT [26/05/2017].

Lin, M., Wu, D. and Chen, X., 2006, *Changes in Atlantic Thermohaline Circulation under Different Atmospheric CO₂ Scenarios in a Climate Model*, *Journal of China University Geosciences*, Vol. 17, Issue 4, 326-331.

Linkin, M. E., and Nigam, S., 2008, *The North Pacific oscillation– west Pacific teleconnection pattern: Mature-phase structure and winter impacts*, *J. Climate*, 21, 1979–1997.

Lisiecki, L. E. and Raymo, M. E. A., 2005, *Pliocene-Pleistocene stack of 57 globally distributed benthic $\delta^{18}O$ records*, *Paleoceanography* 20, PA1003.

Liu, Z. H., Altabet, M. A. and Herbert, T. D., 2005, *Glacial-interglacial modulation of eastern tropical North Pacific denitrification over the last 1.8-Myr*, *Geophys. Res. Lett.*, 32, L23607, doi:10.1029/2005GL024439.

Liu, Z., Altabet, M. A. and Herbert, T. D., 2008, *Plio-Pleistocene denitrification in the eastern tropical North Pacific: Intensification at 2.1 Ma*, *Geochemistry, Geophysics and Geosystems (G3)*, vol 9, n. 11, 1-14.

Liu, J.P., Zhang, Z., Horton, R.M., Wang, C. and Ren, X., 2007, *Variability of North Pacific sea ice and East Asia-North Pacific winter climate*, *J. Climate*, 20, 1991-2001, doi:10.1175/JCLI4105.1.

Locarnini, R. A., Mishonov, A. V., Antonov, J. I., Boyer, T. P. and Garcia, H. E., 2006, *World Ocean Atlas 2005, Volume 1: Temperature*. S. Levitus, Ed. NOAA Atlas NESDIS 61, U.S. Government Printing Office, Washington, D.C., 182 pp.

Lunt, D. J., Elderfield, H., Pancost, R., Ridgwell, A., Foster, G. L., Haywood, A., Kiehl, J., Sago, N., Shields, C. and Valdes, P., 2013, *Warm climates of the past—a lesson for the future?*, *Philosophical Transactions. Series A, Mathematical, Physical, and Engineering Sciences*, 371, 20130146, DOI: 10.1098/rsta.2013.0146.

Lunt, D. J.; Foster, G. L.; Haywood, A. M.; Stone, E. J., 2008, *Late Pliocene Greenland glaciation controlled by a decline in atmospheric CO₂ levels*, *Nature* 454 (7208), 1102–1105.

Lunt, D. J., Haywood, A. M., Schmidt, G. A., Salzmann, U., Valdes, P. J., Dowsett, H. J. and Loptson, C. A., 2012, *On the causes of the mid-Pliocene warmth and polar amplification*, *Earth and Planetary Science Letters*, 321-322, 128-138.

Lüthi, D., Le Floch, M., Bereiter, B., Blunier, T., Barnola, J-M., Siegenthaler, U., Raynaud, D., Jouzel, J., Fischer, H., Kawamura, K. and Stocker, T. F., 2008, *High-resolution carbon dioxide concentration record 650,000 - 800,000 years before present*, *Nature*, 453, 379-382, <https://doi.org/10.1038/nature06949>

Maier, E., Méheust, M., Abelman, A., Gersonde, R., Chaplign, B., Ren, J., Stein, R., Meyer, H. and Tiedemann, R., 2015, *Deglacial subarctic Pacific surface water hydrography and nutrient dynamics and links to North Atlantic climate variability and atmospheric CO₂*, *Paleoceanography*, 30, 949–968, doi:10.1002/2014PA002763.

Maier-Reimer, E., Mikolajewicz, U. and Crowley, T., 1990, *Ocean general circulation model sensitivity experiment with an open Central American Isthmus*, *Paleoceanography* 5, 349–366.

Mantua, N. J. and Hare, S.R., 2002, *The Pacific Decadal Oscillation*, *Journal of Oceanography*, vol. 58, pp. 35 to 44.

MARGO Project Members, 2009, *Constraints on the magnitude and patterns of ocean cooling at the Last Glacial Maximum*, *Nat. Geosci.*, 2, 127–132.

Marlowe, I.T., Green, J.C., Neal, A.C., Brassell, S.C., Eglinton, G. and Course, P.A., 1984, *Long-chain (n-C₃₇-C₃₉) alkenones in the Prymnesiophyceae. Distribution of alkenones and other lipids and their taxonomic significance*, *British Phycological Journal* 19, 203-216 doi:10.1080/00071618400650221.

Martin, J. H., 1990, *Glacial-interglacial CO₂ change: The iron hypothesis*, *Paleoceanography*, 5, 1-13.

Martin, J. H. and Fitzwater, S. E., 1988, *Iron deficiency limits phytoplankton growth in the north-east Pacific subarctic*, *Nature*, 331, 341-343.

Martin, J. H., Michael Gordon, R. and Fitzwater, S. E., 1991, *Iron limitation?*, *Limnol. Oceanogr.*, 36(8), 1793-1802.

Martínez-Botí, M. A., Foster, G. L. Chalk, T. B., Rohling, E. J., Sexton, P.F., Lunt, D. J., Pancost, R. D., Badger, M. P. S. and Schmidt, D. N., 2015, *Plio-Pleistocene climate sensitivity valuated using high-resolution CO₂ records*, *Nature* Vol 518, issue 7537, 49-54, DOI: [10.1038/nature14145](https://doi.org/10.1038/nature14145).

Martínez-García, A., Rosell-Melé, A., McClymont, E.L., Gersonde, R. & Haug, G., 2010, *Subpolar Link to the Emergence of the Modern Equatorial Pacific Cold Tongue*, *Science*, 328, 1550-1553.

Martrat, B., Grimalt, J. O., Shackleton, N. J., de Abreu, L., Hutterli, M. A. and Stocker, T. F., 2007, *Four Climate Cycles of Recurring Deep and Surface Water Destabilizations on the Iberian Margin*, Science Volume 317, 5837, 502-507.

März, C., Schnetger, B., and Brumsack, H.-J., 2013, *Nutrient leakage from the North Pacific to the Bering Sea (IODP Site U1341) following the onset of Northern Hemispheric Glaciation?*, Paleoclimatology, 28, 68–78, doi:10.1002/palo.20011.

Maslin, M.A., Haug, G.H., Sarnthein, M., Tiedemann, R., 1996, *The progressive intensification of Northern Hemisphere glaciation as seen from the North Pacific*, Geol. Rundsch 85, 452–465.

Mateo, A. M., Serrano, O., Serrano, L. and Muchener, R. H., 2008, *Effects of sample preparation on stable isotope ratios of carbon and nitrogen in marine invertebrates: implications for food web studies using stable isotopes*, Ecosystem Ecology- Method, Oecologia 157, 105-115.

Max, L., Lembke-Jene, L., Riethdorf, J.-R., Tiedemann, R., Nürnberg, D., Kühn, H., Mackensen, A., 2014, *Pulses of enhanced North Pacific Intermediate Water ventilation from the Okhotsk Sea and Bering Sea during the last deglaciation*, Clim. Past 10, 591–605.

Max, L., Riethdorf, J. R., Tiedemann, R., Smirnova, M., LembkeJene, L., Fahl, K., Nürnberg, D., Matul, A., and Mollenhauer, G., 2012, *Sea surface temperature variability and sea-ice extent in the subarctic northwest Pacific during the past 15,000 years*, Paleoclimatology, 27, PA3213, doi:10.1029/2012PA002292.

McClymont, E.L., Elmore, A.C., Kender, S., Leng, M.J., Greaves, M. and Elderfield, H., 2016, *Pliocene-Pleistocene evolution of sea surface and intermediate water temperatures from the southwest Pacific*, Paleoclimatology, 31, 895-913.

McClymont, E.L., Ganeshram, R.S.S., Pichevin, L.E., Talbot, H.M., van Dongen, B.E., Thunell, R.C., Haywood, A.M., Singarayer, J.S.S. and Valdes, P.J., 2012, *Sea-surface temperature records of Termination 1 in the Gulf of California: challenges for seasonal and inter-annual analogues of tropical Pacific climate change*, Paleoclimatology, 2012, 27, PA2202.

McClymont, E., Martínez-García, A. and Rosell-Melé, A., 2007, *Benefits of freeze-drying sediments for the analysis of the total chlorins and alkenone concentrations in marine sediments*, *Organic Geochemistry* 38, 1102-1007.

McClymont, E.L. and Rosell-Melé, A., 2005, *Links between the onset of modern Walker circulation and the mid-Pleistocene climate transition*. *Geology*, 33, 389-392.

McClymont, E.L., Rosell-Melé, A., Giraudeau, J., Pierre, C. and Lloyd, J.M., 2005, *Alkenone and coccolith records of the Mid-Pleistocene in the south-east Atlantic: Implications for the $U^{K_{37}}$ index and south African climate*, *Quaternary Science Reviews*, 24, 1559-1572.

McClymont, E.L., Rosell-Melé, A., Haug, G. and Lloyd, J.M., 2008, *Expansion of subarctic water masses in the North Atlantic and Pacific oceans and implications for mid-Pleistocene ice sheet growth*, *Paleoceanography*, 23, PA4214.

McClymont, E.L., Sostian, S.M., Rosell-Melé, A. and Rosenthal, Y., 2013, *Pleistocene sea-surface temperature evolution: Early cooling, delayed glacial intensification, and implications for the mid-Pleistocene climate transition*, *Earth-Science Reviews*, 123, 173-193.

McDonald, D., Pedersen, T.F., and Crusius, J., 1999, *Multiple late Quaternary episodes of exceptional diatom production in the Gulf of Alaska*, *Deep-Sea Res., Part II*, 46(11-12):2993-3017, doi:10.1016/S0967-0645(99)00091-0.

McManues, J., Berelson, W. M., Klinkhammer, G. P., Johnson, K. S., Coale, K. H., Anderson, R. F., Kumar, N., Burdige, D. J., Hammond, D. E., Brumsack, H. J., McCorkle, D. C. and Rushdi, A., 1998, *Geochemistry of barium in marine sediments: Implications for its use as a paleoproxy*, *Geochim. Cosmochim. Acta* 62 (21/22), 3453-3473.

Meheust, M. Fahl, K. and Stein, R., 2013, *Variability in modern sea surface temperature, sea ice and terrigenous input in the sub-polar North Pacific and Bering Sea: Reconstruction from biomarker data*, *Organic Geochemistry* 57, 54-64.

Melles, M., Brinham-Grette, J., Minyuk, P. S., Nowaczyk, N. R., Wennrich, V., DeConto, R. M., Anderson, P. M., Andreev, A. A., Coletti, A., Cook, T. L., Haltia-Hovi,

E., Kukkonen, M., Lozhkin, A. V., Rosén, P., Tarasov, P., Vogel, H. and Wagner, B., 2012, *2.8 million years of Arctic climate change from Lake El'gygytgyn, NE Russia*, *Science*, v. 337, p. 315–320, doi: 10.1126/science.1222135.

Milankovitch, M., 1941, *Das Ende des julianischen Kalenders und der neue Kalender der orientalischen Kirchen*, *Astronomische Nachrichten*, volume 220, Issue 23, p.379.

Molnar, P., England, P., 1990, *Late Cenozoic uplift of mountain ranges and global climate change: chicken or egg?* *Nature* 346, 29–34.

Molnia, B.F., 2008, *Glaciers of North America -- Glaciers of Alaska*, in Williams, R.S., Jr., and Ferrigno, J.G., eds., *Satellite image atlas of glaciers of the world*: U.S. Geological Survey Professional Paper 1386-K, 525 p.

Montes, C., Cardona, A., Jaramillo, C., Pardo, A., Silva, J.C., Valencia, V., Ayala, C., Perez-Angel, L.C., Rodríguez-Parra, L.A., Ramírez, V., Nino, H., 2015, *Middle Miocene closure of the Central American Seaway*, *Science* 348, 226e229. <http://dx.doi.org/10.1126/science.aaa2815>.

Moore, T.C. Jr., 1993, *The super-productive and super-El Niño oceans*, *Stratigraphic Record of Global Change*, SEPM Meeting Abstr. Program, 54-55.

Mudelsee, M. and Raymo, M. E., 2005, *Slow dynamics of the Northern Hemisphere glaciation*, *Paleoceanography*, vol 20, PA4022.

Müller P. J., Kirst G., Ruhland G., von Storch I., and RosellMelé A., 1998, *Calibration of the alkenone paleotemperature index $U^{K_{37}}$ based on core-tops from the eastern South Atlantic and the global ocean (608 N–608 S)*, *Geochim. Cosmochim. Acta* 62, 1757–1772, doi:10.1016/S0016-7037(98)00097-0.

Müller, J., Wagner, A., Fahl, K., Stein, R., Prange, M. and Lohmann, G., 2011, *Towards quantitative sea ice reconstructions in the northern North Atlantic: A combined biomarker and numerical modelling approach*, *Earth Planet. Sci. Lett.* 306, 137–148.

Naafs, B. D. A., Hefter, J., Acton, G., Haug, G. H., Martínez-García, A., Pancost, R. and Stein, R., 2012, *Strengthening of the North American dust sources during the late*

Pliocene (2.7 Ma), *Earth and Planetary Science Letters* 317-318, 8-19, <http://dx.doi.org/10.1016/j.epsl.2011.11.026>.

Naafs, B. D. A., Hefter, J. and Stein, R., 2013, *Millennial-scale ice rafting events and Hudson Strait Heinrich(-like) events during the late Pliocene and Pleistocene: a review*, *Quat. Sci. Rev.*, 80, pp. 1-28, [10.1016/j.quascirev.2013.08.014](http://dx.doi.org/10.1016/j.quascirev.2013.08.014).

Nasir A, Lukman M, Tuwo A, Hatta M, Tambaru R and Nurfadilah, 2016, *The Use of C/N Ratio in Assessing the Influence of Land-Based Material in Coastal Water of South Sulawesi and Spermonde Archipelago, Indonesia*. *Front. Mar. Sci.* 3:266.[doi:10.3389/fmars.2016.00266](https://doi.org/10.3389/fmars.2016.00266).

Newman, M., Compo, G. P. and Alexander, M. A., 2003, *ENSO-Forced Variability of the Pacific Decadal Oscillation*, *Journal of Climate*, vol. 16, n. 23, 3853-3857.

Newman, M., Alexander, M. A., Ault, T. R., Cobb., M., Deser, C., Di Lorenzo, E., Mantua, N. J., Miller, A. J., Minobe, S., Nakamura, H., Schneider, N., Vimont, D. J., Phillips, A. S., Scott, J. D. and Smith, C. A., 2015, *The Pacific decadal oscillation, revisited*, Submitted to *Bull. Amer. Meteor. Soc.*, March 3 2015, 29 Revision submitted to *J. Climate*, October 28 2015.

Nie, J., Stevens, T., Song, Y., King, J., Zhang, R., Ji, S., Gong, L. and Cares, D., 2014, *Pacific freshening drives Pliocene cooling and Asian monsoon intensification*, *Scientific Reports* 4, n. 5474, 1-8.

Nilsson, J., Langen, P. L., Ferreira, D. and Marshall, J., 2013, *Ocean Basin Geometry and the Salinification of the Atlantic Ocean*, *J. Clim.*, 26, 6163–6184.

Nishioka, J., Ono, T., Saito, H., Sakaoka, K. and Yoshimura, T., 2011, *Oceanic iron supply mechanisms which support the spring diatom bloom in the Oyashio region, western subarctic Pacific*, *Journal of Geophysical Research*, vol. 116, C02021, [doi:10.1029/2010JC006321](https://doi.org/10.1029/2010JC006321).

Ohkouchi N., Eglinton T. I., Keigwin L. D., and Hayes J. M., 2002, *Spatial and temporal offsets between proxy records in a sediment drift*, *Science* 298, 1224–1227.

Ortiz, J. Mix, A. C. Hostetler, S. and Kashgarian. M., 1997, *California Current of the last glacial maximum: Reconstruction at 42 °N based on multiple proxies*, *Paleoceanography* 12.2, 191-205.

Otto-Bliesner, B.L., 1995, *Continental drift, runoff, and weathering feedbacks: Implications from climate model experiments*, *Journal of Geophysical Research*, Volume 100, Issue D6, Pages 11537–11548.

Otto-Bliesner, B., Brandy, E. C., Clauzet, G., Tomas, R., Levis, S. and Kothavala, Z., 2005, *Last Glacial Maximum and Holocene Climate in CCSM3*, *Journal of Climate* vol. 19, 2526-2544.

Otto-Bliesner, B. L., Brandy, E. C., Fasullo, J., JAhn, A., Landrum, L., Stevenson, S., Rosenbloom, N., Mai, A. and Strand, G., 2016, *Climate Variability and Change since 850 CE: An Ensemble Approach with the Community Earth System Model*, *American Meteorological Society*, 97, 735–754, <https://doi.org/10.1175/BAMS-D-14-00233.1>.

Pagani, M., Liu, Z., La Riviere, J. and Ravelo, A. C., 2010, *High Earth-system climate sensitivity determined from Pliocene carbon dioxide concentrations*, *Nature Geoscience*, Vol 3., 27-30.

Pancost, R. D., and Boot, C. S., 2004, *The palaeoclimatic utility of terrestrial biomarkers in marine sediments*, *Mar. Chem.*, 92, 239–261.

Past Interglacials Working Group of PAGES, 2015, *Interglacials of the last 800,000 years*, *Rev. Geophys.*, 54, 162–219, doi:10.1002/2015RG000482.

Pearson, P. N. and Palmer, M. R., 2000, *Atmospheric carbon dioxide concentrations over the past 60 million years*, *Nature*, 406, 695-699, <https://doi.org/10.1038/35021000>.

Perch-Nilsen, K., 1985, *Mesozoic calcareous nannofossils*, In: Bolli, H. H., Saunders, J. B. and Perch-Nielsen, K. *Plankton Stratigraphy*, Vol. 1: 329-427. Cambridge: Cambridge University Press.

Peters, K. R., Walters, C. C. and Moldowan, J. M., 2005, *The Biomarker Guide. Volume 2: Biomarkers and Isotopes in Petroleum Exploration and Earth History*, Second

Edition. (First edition published 1993 by Chevron Texaco.) , Cambridge, New York, Melborne: Cambridge University Press.

Peterson C., 2005, *Nearshore benthic communities*, Mundy P (ed), The Gulf of Alaska, Biology and Oceanography, pp 59–68. Alaska Sea Grant College Program, University of Alaska, Fairbanks, AK, USA.

Peterson, W.T., Schwing, F.B., 2003, *A new climate regime in Northeast Pacific ecosystems*, Geophysical Research Letters 30, 1896.

Petit, J. R., Jouzel, J., Raynaud, D., Barkov, N.I., Barnola, J. M., Basile, I., Bender, M., Chappellaz, J., Davis, M., Delaygue, G., Delmotte, M., Kotlyakov, V. M., Legrand, M., Lopenkov, V. Y., Lorius, C., Pepin, L., Ritz, C., Saltzman, E. and Stievenard, M., 1999, *Climate and atmospheric history of the past 420,000 years from the Vostok ice core*, Antarctica. Nature 399, 429–436.

Petrick, B.F., McClymont, E.L., Marret, F. and van der Meer, M.T.J., 2015, *Changing surface water conditions for the last 500 ka in the Southeast Atlantic: Implications for variable influences of Agulhas leakage and Benguela upwelling*, Paleoceanography, 30, 1153-1167.

Pickart, RS, Macdonald, A. M., Moore, ,G. W. K., Renfrew, I. A., Walsh, J. E. and Kessler, W. S., 2009, *Seasonal evolution of Aleutian low pressure systems: implications for the North Pacific subpolar circulation*. J Phys Oceanogr 39, 1317–1339.

Plafker, G., Moore, J.C., Winkler, G.R., 1994, *Geology of the southern Alaska margin*. In: Plafker, G., Berg, H.C. (Eds.), The Geology of Alaska: Boulder, Colorado, Geological Society of America, Geology of North America, G-1, pp. 389–449.

Powell, R. D., and Molnia, B. F., 1989, *Glacimarine sedimentary processes, facies and morphology of the south-southeast Alaska shelf and fjords*, Mar. Geol., 85, 359–390, doi:10.1016/0025-3227(89)90160-6.

Praetorius, S. K., Mix, A.C., Walczak, M.H., Wolhowe, M.D., Addison, J.A and Prahl, F. G., 2015, *North Pacific deglacial hypoxic events linked to abrupt ocean warming*, Nature volume 527, pages 362–366, doi:10.1038/nature15753.

Prahl, F.G., Collier, R.B., Dymond, J., Lyle, M., and Sparrow, M.A., 1993, *A biomarker perspective on prymnesiophyte productivity in the northeast Pacific Ocean*, Deep-Sea Res. Part A, 40:2061–2076.

Prahl, F. G. and Muehlhausen, L. A., 1989, *Lipid biomarkers as geochemical tools for paleoceanographic study*, In: W. H. Berger, V. S. Smetacek & G. Wefer (Eds), *Productivity of the ocean: Present and past* (pp. 271–289). New York: John Wiley & Sons.

Prahl F. G., Muehlhausen L. A., and Zahnle D. L., 1988, *Further evaluation of long-chain alkenones as indicators of paleoceanographic conditions*, Geochim. Cosmochim. Acta 52, 2303–2310.

Prahl, F. G., Wakeham, S. G., 1987, *Calibration of unsaturation patterns in long-chain ketone compositions for paleotemperature assessment*, Nature 330: 367– 369. doi:10.1038/330367a0

Rabassa, J. and Ponce, J. F., 2013, *The Heinrich and Dansgaard-Oeschger climatic events during Marine Isotopic Stage 3: Searching for appropriate times for human colonization of the Americas*, Quaternary International 299, 94-105.

Rae, J. W. B., Sarnthein, M., Foster, G. L., Ridgwell, A., Grootes, P. M. and Elliott, T., 2014, *Deep water formation in the North Pacific and deglacial CO₂ rise*, Paleoceanography, 29, 645–667, doi:10.1002/2013PA002570.

Ragueneau, O., Treguer, P., Leynaert, A., Anderson, R. F., Brzezinski, M. A., DeMaster, D. J., Dugdale, R. C., Dymond, J., Fisher, G., Francois, R., Heinze, C., Maier-Reimer, E., Martin- Jezequel, V., Nelson, D. M., Queguiner, B., 2000, *A review of the Si cycle in the modern ocean: recent progress and missing gaps in the application of biogenic opal as a paleoproductivity proxy*, Global and Planetary Change 26, 317–365.

Rampen S. W., Abbas B. A., Schouten S., Sinninghe Damste J. S., 2010, *A comprehensive study of sterols in marine diatoms (Bacillariophyta): implications for their use as tracers for diatom productivity*. Limnol. Oceanogr. 55, 91–105. Doi:10.4319/lo.2010.55.1.0091.

Ravelo, A.C., Billups, K., Dekens, P.S., Herbert, T.D., Lawrence, K.T., 2007, *Onto the ice ages: proxy evidence for the onset of Northern Hemisphere glaciation*. In: Williams, M., Haywood, A.M., Gregory, F.J., Schmidt, D.N. (Eds.), *Deep-Time Perspectives on Climate Change: Marrying the Signal from Computer Models and Biological Proxies*. The Micropalaeontological Society, Special Publications. The Geological Society, London, pp. 563–573.

Raymo, M. E., Grant, B., Horowitz, M. and Rau, G. H., 1996, *Mid-Pliocene warmth: stronger greenhouse and stronger conveyor*, *Marine Micropalaeontology* 27, 313-326.

Raymo, M.E., Hearty, P., De Conto, R., O'Leary, M., Dowsett, H.J., Robinson, M. and Mitrovica, J.X., 2009, *PLIOMAX: Pliocene maximum sea level project*, *PAGES News*, v. 17, p. 58-59.

Raymo, M.E., Hodell, D., and Jansen, E., 1992, *Response of deep ocean circulation to initiation of Northern Hemisphere glaciation (3-2 Ma)*, *Paleoceanography*, 7:645-672.

Rea, D.K., Basov, I.A., Janecek, T.R., Palmer-Julson, A., et al., 1993, *Proc. ODP, Init. Repts., 145: College Station, TX (Ocean Drilling Program)*. doi:10.2973/odp.proc.ir.145.1993.

Rea, D. K., Basov, I. A., Krissek, L. A. and the Leg 145 Scientific Party, 1995, *Scientific Results of drilling the North Pacific Transect*, in Rea, D. K., Basov, I. A., Scholl, D. W and Allan, J. F., 1995, *Proceedings of the Ocean Drilling Program, Scientific Results, VOL 145*.

Reece, R. S., Gulick, S. P. S., Horton, B. K., Christeson, G. L. and Worthington, L. L., 2013, *Tectonic and climatic influence of the evolution of the Surveyor Fan and Channel system, Gulf of Alaska*, *Geosphere* 7, 830-844.

Reece, R. S., Gulick, S. P. S., Horton, B. K., Christeson, G. L., and Worthington, L. L., 2011, *Tectonic and climatic influence on the evolution of the Surveyor fan and channel system, Gulf of Alaska*, *Geosphere*, 7(4), 830–844, doi:10.1130/GES00654.1.

Reghellin, D., Coxall, H. K., Dickens, G. R. and Backman, J., 2015, *Carbon and oxygen isotopes of bulk carbonate in sediment deposited beneath the eastern equatorial Pacific over the last 8 million years*, *Paleoceanography*, 30, 1261–1286, doi:10.1002/2015PA002825.

Rieley G., Collier, R. J., Jones D. M. and Eglinton G., 1991, *The biogeochemistry of Ellesmere Lake, U.K. I: source correlation of leaf wax inputs to the sedimentary record*, *Org Geochem* 17, 901-912.

Rieley G., Collier R. J., Jones D. M., Eglinton G., Eakin P. A. and Fallick A. E., 1991, *Sources of sedimentary lipids deduced from stable carbon-isotope analyses of individual compounds*, *Nature* 352, 425–427.

Rind, D. and Chandler, M., 1991, *Increased ocean heat transports and warmer climate*, *J. Geophys. Res.*, 96, 7437-7461.

Risebrobakken, B., Dokken, T., Otterå, O. H., Jansen, E., Gao, Y. and Drange, H., 2007, *Inception of the Northern European ice sheet due to contrasting ocean and insolation forcing*, *Quat. Res.*, 67, 128–135.

Robinson, M. M., 2009, *New quantitative evidence of extreme warmth in the Pliocene Arctic*, *Stratigraphy* 6, 265–275.

Robinson, N., Cranwell, P. A., Eglinton, G., Jaworski, G. H. M., 1987, *Lipids of four species of freshwater dinoflagellates*, *Phytochemistry* 26, 411–421.

Robinson, N., Cranwell, P.A., Finlay, B.J., Eglinton, G., 1984, *Lipids of aquatic organisms as potential contributors to lacustrine sediments*, *Organic Geochemistry* 6, 143–152.

Rodionov, S. N., Bond, N. A. and Overland, J. E., 2007, *The Aleutian Low, storm tracks, and winter climate variability in the Bering Sea*, *Deep Sea Res., Part II*, 54, 2560–2577, doi:10.1016/j.dsr2.2007.08.002.

Ronge, T. A., Tidemann, R., Lamy, F., Köhler, P., Alloway, B.V., De Pol-Holz, R., Pahnke, K., Southon, J. and Wacker, L., 2016, *Radiocarbon constraints on the extent and evolution of the South Pacific glacial carbon pool*, *Nat. Commun.* 7:11487 doi: 10.1038/ncomms11487.

Rosell-Melé, A., 1998, *Interhemispheric appraisal of the value of alkenone indices as temperature and salinity proxies in high-latitude locations*, *Paleoceanography* 13, 694–703.

Rosell-Melé, 2003, *Biomarkers as proxies of climate change in Global Climate Change in the Holocene*, In: Mackay, A., Battarbee, R., Birks, J. and Oldfield, F., Oxon, Global Change in the Holocene, New York, Routledge, 358.

Rosell-Melé, A., Carter, J. F., Parry, A. T. and Eglinton, G., 1995, *Determination of the UK_{37} Index in Geological Samples*, *Analytical Chemistry*, 67, 1283-1289.

Rosell-Melé, A. and McClymont, E.L., 2007, *Biomarkers as palaeoceanographic proxies*. In Hillaire-Marcel, C. and de Vernal, A., *Proxies in Late Cenozoic Paleooceanography*, Amsterdam Oxford: Elsevier. 441-490.

Rosell-Melé A., Prahl F.G., 2013, *Seasonality of UK_{37} temperature estimates as inferred from sediment trap data*", *Quaternary Science Reviews*, vol. 72, p. 128-136.

Royer, T.C., 1981a, *Baroclinic transport in the Gulf of Alaska*, Part I. Seasonal variations of the Alaska Current. *J. Mar. Res.* 39: 239-250.

Royer, T.C, 1982, *Coastal fresh water discharge in the northeastern Pacific*, *J. Geophys. Res.* 87: 2017-2021.

Ryabenko, E., 2013, *Stable Isotope Methods for the Study of the Nitrogen Cycle*, Topics in Oceanography, Prof. Enrico Zambianchi (Ed.), ISBN: 978-953-51-1179-5, InTech, DOI: 10.5772/56105. Available from: <http://www.intechopen.com/books/topics-in-oceanography/stable-isotope-methods-for-the-study-of-the-nitrogen-cycle>

Ryba, S. A., and Burgess, R. M., 2002, *Effects of sample preparation on the measurement of organic carbon, hydrogen, nitrogen, sulfur and oxygen concentrations in marine sediments*, *Chemosphere* 48, 139-147.

Salzmann, U., Williams, M., Haywood, A. M. Johnson, A. I. A, Kender, S. and Zalasiewicz, J., 2011, *Climate and environment of a Pliocene warm world*, *Palaeogeography, Palaeoclimatology, Palaeoecology*, 309, 1-8.

Sanches-Filho, P. J., Luz, L. O., Betemps, G.R., Silva, M. D. R. G. and Cramão, E. B., 2013, *Studies of n-alkanes in the sediments of Colony Z3 (Pelotas-RS-Brazil)*, Braz. J. Aquat. Sci. Technol., 17 (1), 27-33.

Sarmiento, J. L., Gruber, N., Brezinski, M. A., and Dunne, J. P., 2004, *High-latitude controls of thermocline nutrients and low latitude biological productivity*, Nature 427, 56-60.

Sarmiento, J. and Toggweiler, J., 1984, *A new model for the role of the oceans in determining atmospheric pCO₂*, Nature 308, 621-624.

Sarnthein, M., Bartoli, G., Prange, M., Schmittner, A., Schneider, B., Weinelt, M., Andersen, N. and Garbe-Schönberg, D., 2009, *Mid-Pliocene shifts in ocean overturning circulation and the onset of Quaternary-style climates*, Clim. Past 5, 269-283.

Sarnthein, M., Schneider, B. and Grootes, P. M., 2013, *Peak glacial ¹⁴C ventilation ages suggest major draw-down of carbon into the abyssal ocean*. Climate of the Past, 9, 2595-2614.

Schaeffer, R., and Spiegler, D., 1986, *Neogene Kalteinbrüche und Vereisungsphasen im Nordatlantik*, Z. Dtsch. Geol. Ges., 137, 537-552.

Scholl, D. W. and Creager, J. S., 1973, *Geologic synthesis of Leg 19 (DSDP) results; Far North Pacific, and Aleutian Ridge, and Bering Sea*, Texas A & M University, Ocean Drilling Program, College Station, TX, United States, Initial Reports of the Deep Sea Drilling Project, 19 (Kodiak, Alaska to Yokohama, Japan; July-Sept. 1971), 897-913, georefid:1976-018944.

Schroth, A. and Crusius, J., 2008, *USGS Researchers Participate in Research Cruise Studying Iron Biogeochemistry in the Gulf of Alaska*, U.S. Department of the Interior, U. S. Geological Survey, Sound Waves Monthly Newsletter, access: <http://soundwaves.usgs.gov/2008/03/> updated 06 May 2014. Last visited 28-11-2016.

Schubert, C. J. and Calvert, S. E., 2001, *Nitrogen and carbon isotopic composition of marine and terrestrial organic matter in Arctic Ocean sediments: implications for*

nutrient utilization and organic matter composition, Deep-Sea Research I, 48, 789-810.

Schulte, S., Rostek, F., Bard, E., Rullkötter, J., and Marchal, O., 1999, *Variations of oxygen-minimum and primary productivity recorded in sediments of the Arabian Sea*, Earth and Planetary Science Letters, 173, 205–221.

Seki, O., Foster, G. J., Schmidt, D. N., Mackensen, A., Kawamura, K. and Pancost, R. D., 2010, *Alkenone and boron-based Pliocene pCO₂ records*, Earth and Planetary Science Letters 292, 201-211, doi:10.1016/j.epsl.2010.01.037.

Serrano, O., Serrano, L., Mateo, M. A., Colombini, I., Chelazzi, L., Gagnarli, E. and Fallci, M., 2008, *Acid washing effect on elemental and isotopic composition of whole beach arthropods: Implications for food web studies using stable isotopes*, Acta Oecologica 34, 80-96.

Shackleton, N. J., Hall, M. A. and Boersma, A., 1984, *Oxygen and carbon isotope data from Leg 74 foraminifers*. In: Moore, TC Jr; Rabinowitz, PD; et al. (eds.), Initial Reports of the Deep Sea Drilling Project (U.S. Govt. Printing Office), 74, 599-612, doi:10.2973/dsdp.proc.74.115.1984

Shipboard Scientific Party, 1993a, *Introduction to Leg 145: North Pacific Transect*, Chapter 1 in Rea, D.K., Basov, I.A., Janecek, T.R., Palmer-Julson, A., et al., 1993, Proceedings of the Ocean Drilling Program, Initial Reports, Vol 145.

Shipboard Scientific Party, 1993b, *Site 882*, Chapter 4 in Rea, D.K., Basov, I.A., Janecek, T.R., Palmer-Julson, A., et al., 1993, Proceedings of the Ocean Drilling Program, Initial Reports, Vol 145.

Shipboard Scientific Party, 1993h, *Site 887*, Chapter 8 in Rea, D.K., Basov, I.A., Janecek, T.R., Palmer-Julson, A., et al., 1993, Proceedings of the Ocean Drilling Program, Initial Reports, Vol 145.

Siddall, M., Rohling, E.J., Blunier, T. and Spahni, R., 2010, *Patterns of millennial variability over the last 500 Ka*, Clim. Past, 6, 295-303.

Siegenthaler, U. and Wenk, T., 1984, *Rapid atmospheric CO₂ variations and ocean circulation*, Nature 308, 624--626.

Siegenthaler, U., Stocker, T. F., Monnin, E., Lüthi, D., Schwander, J., Stauffer, B., Raynaud, D., Barnola, J.M., Fischer, H., Masson-Delmotte, V. and Jouzel, J., 2005, *Stable carbon cycle-climate relationship during the Late Pleistocene*, *Science*, 25, vol 310, issue 5752, 1313-1317, doi:10.1126/science.1120130.

Sigman, D. M., Jaccard, S. L. and Haug, G. H., 2004, *Polar ocean stratification in a cold climate*, *Nature*, 428, 59–63.

Sikes, E. L., Keigwin, L. D., and Curry, W. B., 1991, *Pliocene paleoceanography: circulation and Oceanographic changes associated with the 2.4 Ma glacial event*, *Paleoceanography*, 6, 245-258.

Sikes, E. L., Nodder, S. D., O'Leary, T. and Volkman, J. K., 2005, *Alkenone temperature records and biomarker flux at the Subtropical Front on the Chatham Rise, SW Pacific Ocean*, *Deep Sea Res., Part I*, 52, 721–748, doi:10.1016/j.dsr.2004.12.003.

Sikes, E. L., and Sicre, M., 2002, *Relationship of the tetra-unsaturated C₃₇ alkenone to salinity and temperature: Implications for paleoproxy applications*, *Geochem. Geophys. Geosyst.*, 3(11), 1063, doi:10.1029/2002GC000345.

Sikes, E. L., Volkman, J. K., Robertson, L. G. and Pichon, J.-J., 1997, *Alkenones and alkenes in surface waters and sediments of the Southern Ocean: implications for paleotemperature estimation in polar regions*, *Geochimica et Cosmochimica Acta* 61, 1495–1505.

Sikes, E. L., and Volkman, J. K., 1993, *Calibration of alkenone unsaturation ratios ($U^{K_{37}}$) for paleotemperature estimation in cold polar waters*, *Geochim. Cosmochim. Acta*, 57, 1883–1889.

Smith, K. L. Jr., Robinson, B. H., Helly, J. J., Kaufmann, R. S., Ruhl, H. A., Shaw, T. J., Twining, B. S. and Vernet, M., 2007, *Free-drifting icebergs: hot spots of chemical and biological enrichment in the Weddell Sea*, *Science* 317, 478–482.

Snoeckx, H., Rea, D. K., Jones, C. E. and Ingram, B. L., 1995, *Eolian and silica deposition in the central North Pacific: Results from Sites 885/886*, in Rea, D.K., Basov, I.A., Scholl, D.W., and Allan, J.F. (Eds.), *Proceedings of the Ocean Drilling Program, Scientific Results*, Vol. 145.

Spencer, E.W., 1965, *Geology: a survey of Earth Science*, Thomas Y. Crowell Company, New York, ISBN B0006BMQU0.

Spies, R. B., 2007, *Long-term Ecological Change in the Northern Gulf of Alaska*, Elsevier, ISBN 978-0-444-52960-2.

St. John, K. and Krissek, L.A., 2002, *The late Miocene to Pleistocene ice-rafting history of southeast Greenland*, *Boreas* 31, 28–35.

Stabeno, P.J., Bond, N.A., Hermann, A.J., Kachel, N.B., Mordy, C.W. and Overland, J.E., 2004, *Meteorology and oceanography of the northern Gulf of Alaska*, *Continental Shelf Research* 24, 859–897. <http://dx.doi.org/10.1016/j.csr.2004.02.007>.

Stanley, S., 2016, *Glacial meltwater features depend on glacier type and location*, *Eos*, 97, doi:10.1029/2016E0048265. Published on 21 March 2016.

State of Alaska, 2001-2017, *Official State of Alaska Vacation and Travel information*, <https://www.travelalaska.com/Planning/Alaska%20Climate/Southwest.aspx>, last accessed 17/03/2017.

Stax, R. and Stein, R., 1995, *Data Report: Organic Carbon and Carbonate Records from Detroit Seamount and Patton Murray Seamount: Results from Sites 882 and 887 (North Pacific Transect)*, Chapter 42, in: Rea, D.K., Basov, I.A., Janecek, T.R., Palmer-Julson, A., et al., 1993, *Proceedings of the Ocean Drilling Program, Initial Reports*, Vol 145.

Stein, R. and McDonald, R. W., 2004, *The Organic Carbon Cycle in the Arctic Ocean*, *Springer-Verlag Berlin Heidelberg*, ISBN 978-3-642-62351-6, DOI:10.1007/978-3642-18912.

Stein, R., Fahl, K., Fütterer, D. K., Galimov, E. M. and Stepanets, O.V., 2003, *Siberian River run-off in the Kara Sea, Volume 6: Characterisation, quantification, variability, and environmental significance*, 1st edition, Amsterdam: Elsevier, ISBN:9780080951423.

Stommel, H., 1961, *Thermohaline convection with two stable regimes of flow*, *Tellus*, 13, 224–230.

Stone, E. J., Capron, E., Lunt, D. J., Payne, A. J., Singarayer, J. S., Valdes, P. J. and Wolff, E. W., 2016, *Impact of meltwater in high latitude early Last Interglacial climate*, *Clim. Past Discuss*, doi:10.5194/cp-2016-11, 2016.

Stroynowski, Z., Ravelo, A. C. and Andreasen, D., 2015, *A Pliocene to recent history of the Bering Sea at Site U1340A*, IODP Expedition 323, *Paleoceanography*, 30, 1641–1656, doi:10.1002/2015PA002866.

Sun, Y.B., Clemens, S.C., Morrill, C., Lin, X.P., Wang, X.L., and An, Z.S., 2012, *Influence of Atlantic meridional overturning circulation on the East Asian winter monsoon*, *Nature Geoscience*, v. 5, p. 46–49, doi:10.1038/ngeo1326.

Swann, G. E. A., Snelling, A. M. and Pike, J., 2016, *Biogeochemical cycling in the Bering Sea over the onset of major Northern Hemisphere Glaciation*, *Paleoceanography*, 31, doi:10.1002/2016PA002978.

Syväranta, J., Hämäläinen, H and Jones, R., 2006, *Within-lake variability in carbon and nitrogen stable isotope signatures*, *Freshwater Biology*, 51: 1090–1102, doi:10.1111/j.1365-2427.2006.01557.x

Takeda, S., 2011, *Iron and phytoplankton growth in the subarctic North Pacific*, *Aqua-BioScience Monogr.*, 4, 41–93.

Talley, L. D., 1993, *Distribution and formation of North Pacific intermediate water*, *Journal of Physical Oceanography* 23, 517--517.

Talley, L. D and Joyce, T. M., 1992, *The Double Silica Maximum in the North Pacific*, *Journal of Geophysical Research*, vol 97, no C4, pages 5465-5480.

Tedesco, M., 2014, *Remote Sensing of the Cryosphere*, The Cryosphere Science Series, John Wiley & Sons Ltd, ISBN:9781118368855, DOI:10.1002/9781118368909.

Teece, M. A., Getliff, J. M., Leftley, J. W., Parkes, R. J. and Maxwell, J. R., 1998, *Microbial degradation of the marine prymnesiophyte *Emiliana huxleyi* under oxic and anoxic conditions as a model for early diagenesis: long chain alkadienes, alkenones and alkyl alkenoates*, *Org. Geochem.* 29, 863–880.

Thiébaud, F., Cremer, M., Debrabant, P., Foulon, J., Nielsen, O. B. and Zimmerman, H., 1989, *Analysis of sedimentary facies, clay mineralogy, and geochemistry of the Neogene-Quaternary sediments in Site 645, Baffin Bay*, Proc. Ocean Drill. Program Sci. Results, 105, 83– 100.

Tiedemann, R, Sarthein, M. and Shackleton, N. J., 1994, *Astronomic timescale for the Pliocene Atlantic $\delta^{18}O$ and dust flux records of Ocean Drilling Program site 659*, Paleoceanography, 9(4), 619-638, <https://doi.org/10.1029/94PA00208>.

Turner J., Hosking, J. S., Bracegirdle, T. J., Marshall, G. J. and Phillips, T., 2015, *Recent changes in Antarctic Sea Ice*, Philosophical Transactions of the Royal Society, 2015 DOI: 10.1098/rsta.2014.0163.

Vafeiadou, A-M., Adão, H., De Troch, M. and Moens, T., 2013, *Sample acidification effects on carbon and nitrogen stable isotope ratios of macrofauna from a *Zostera noltii* bed*, Marine and Freshwater Research, doi.org/10.1071/MF12169.

van Dongen, B. E., Semiletov, I., Weijers, J. W. H. and Gustafsson, Ö., 2008, *Contrasting lipid biomarker composition of terrestrial organic matter exported from across the Eurasian Arctic by the five great Russian Arctic rivers*, Global Biogeochem. Cycles, 22, GB1011, doi:10.1029/2007GB002974.

VanLaningham, S., Pisias, N. G., Duncan, R. A. and Clift, P. D., 2009, *Glacial-interglacial sediment transport to the Meiji Drift, northwest Pacific Ocean: Evidence for timing of Beringian outwashing*, Earth and Planetary Science Letters 277, 64-72.

Vaughn, D.R., 2015, *Marine Isotope Stage (MIS) 5 on the Umnak Plateau, Bering Sea (IODP Site U1339): diatom taxonomy, grain size and isotopic composition of marine sediments as proxies for primary productivity and sea ice extent*, Graduate Theses and Dissertations, Iowa State University 14705.

Volkman, J. K., 1986, *A review of sterol markers for marine and terrigenous organic matter*, Org. Geochem., 9, 83–99, 1986.

Volkman, J.K., 2006, *Lipid markers for marine organic matter*. In: Volkman, J.K. (Ed.), Handbook of Environmental Chemistry, vol. 2. Springer-Verlag, Berlin, Heidelberg, pp. 27–70.

Volkman, J. K., Barrett, S. M., Dunstan, G. A. and Jeffrey, S. W., 1993, *Geochemical significance of the occurrence of dinosterol and other 4-methyl sterols in a marine diatom*. *Org. Geochem.* 20: 7–15.

Volkman, J. K., Eglinton, G., Corner, E. D. S., and Forsberg, T. E. V., 1980a, *Lone chain alkenes and alkenones in the marine coccolithophorid Ekmania huxleyi*, *Phytochemistry* 19, 2619-2622.

Von Huene, R., Kulm, L. D., Duncan, J. R., Ingle, J.C., Kling, S. A., Musich, L. F., Piper, D. J. W., Pratt, R. M., Schrader, Hans-Joachim, Weser, O. and Wise, S. W., 1971a, *Site 178*, DSDP Volume XVIII Table of Contents, doi:10.2973/dsdp.proc.18.1973.

Von Huene, R., Kulm, L. D., Duncan, J. R., Ingle, J.C., Kling, S. A., Musich, L. F., Piper, D. J. W., Pratt, R. M., Schrader, Hans-Joachim, Weser, O. and Wise, S. W., 1971b, *Site 179*, DSDP Volume XVIII Table of Contents, doi:10.2973/dsdp.proc.18.1973.

Von Huene, R., Kulm, L. D., Duncan, J. R., Ingle, J.C., Kling, S. A., Musich, L. F., Piper, D. J. W., Pratt, R. M., Schrader, Hans-Joachim, Weser, O. and Wise, S. W., 1971c, *Site 180*, DSDP Volume XVIII Table of Contents, doi:10.2973/dsdp.proc.18.1973.

Von Huene, R., Kulm, L. D., Duncan, J. R., Ingle, J.C., Kling, S. A., Musich, L. F., Piper, D. J. W., Pratt, R. M., Schrader, Hans-Joachim, Weser, O. and Wise, S. W., 1971d, *Site 181*, DSDP Volume XVIII Table of Contents, doi:10.2973/dsdp.proc.18.1973.

Von Huene, R., Kulm, L. D., Duncan, J. R., Ingle, J.C., Kling, S. A., Musich, L. F., Piper, D. J. W., Pratt, R. M., Schrader, Hans-Joachim, Weser, O. and Wise, S. W., 1971e, *Site 182*, DSDP Volume XVIII Table of Contents doi:10.2973/dsdp.proc.18.1973.

Wakeham, S.G., Peterson, M.L., Hedges, J.I., Lee, C., 2002, *Lipid biomarker fluxes in the Arabian Sea, with a comparison to the equatorial Pacific Ocean*, *Deep-Sea Research. Part 2, Topical Studies in Oceanography* 49 (12), 2265 – 2301.

Walinsky, S.E., Prahl, F.G., Mix, A.C., Finney, B.P., Jaeger, J.M., and Rosen, G.P., 2009, *Distribution and composition of organic matter in surface sediments of coastal southeast Alaska*. *Cont. Shelf Res.*, 29, 13, 1565–1579, doi:10.1016/j.csr.2009.04.006.

Walsh, E. M., Ingalls, A. E. and Keil, R. G., 2008, *Sources and transport of terrestrial organic matter in Vancouver Island fjords and the Vancouver-Washington Margin: a multi proxy approach using $\delta^{13}\text{C}$ (org), lignin phenols, and the ether lipid BIT index*, *Limnol. Oceanogr.* 53, 1054–1063, 10.4319/lo.2008.53.3.1054.

Wara, M. W., Ravelo, A. C., and Delaney, M. L., 2005, *Permanent El Niño-like conditions during the Pliocene warm period*, *Science*, v. 309, p. 758–761, doi: 10.1126/science.1112596.

Watanabe, T., Suzuki, A., Minobe, S., Kawashima, T., Kameo, K., Minoshima, K., Aguilar, Y. M., Wani, R., Kawahata, H., Sowa, K., Nagai, T., Kase, T., 2011, *Permanent El Niño during the Pliocene warm period not supported by coral evidence*, *Nature* 471 (7337), 209–211.

Weingartner, T., 2007. *Chapter 2.2: The physical environment of the Gulf of Alaska*. In: Spies, R.B. (Ed.), *Long-term Ecological Change in the Northern Gulf of Alaska*. Elsevier, Oxford, p. 589.

Weingartner, T, Danielsen, S., Shipton, P and Leech, D, 2016, *GAK 1 Time Series*, access online <http://www.ims.uaf.edu/gak1/>, last date accessed 23/12/2016.

Whitney, F.A., Crawford, D.W. and Yoshimura, T. 2005, *The uptake and export of silicon and nitrogen in HNLC waters of the NE Pacific Ocean*, *Deep Sea Research Part II*, 52, 7-8, 1055-1067.

Wolff, E. W., Shepherd, J. G., Shuckburgh, E. and Watson, A. J., 2015, *Feedbacks on climate in the Earth system: Introduction*, *Philosophical Transactions of the Royal Society A, Mathematical, Physical and Engineering Sciences*, 373, ISSN 1364-503X Online ISSN 1471-2962, DOI 10.1098/rsta.2014.0428.

Wolf-Welling, T. C.W., Cremer, M., O'Connell, S., Winkler, A. and Thiede, J., 1996, *Cenozoic Arctic gateway paleoclimate variability: Indications from changes in coarse-fraction composition*, *Proc. Ocean Drill. Program Sci. Results*, 151, 515– 567.

Xiao, X., Stein, R., Fahl, K., 2013, *Biomarker distributions in surface sediments from the Kara and Laptev Seas (Arctic Ocean): indicators for organic-carbon sources and sea ice coverage*, *Quaternary Science Reviews* 79, 40e52.

Yadav, P., Steinbach, M., Kumar, V., Simon, G., 2016, *Mining Electronic Health Record (EHRs): A Survey*, ACM Trans. Embedd. Comput. Syst. 1, 1, Article 1, 41 pages, DOI: 0000001.0000001.

Yamamoto, M., Kobayashi, D., 2016, *Surface ocean cooling in the subarctic North Pacific during the late Pliocene suggests an atmospheric reorganization prior to extensive North Hemisphere glaciation*, Deep-Sea Research II, <http://dx.doi.org/10.1016/j.dsr2.2015.03.005>.

Yamamoto, M., Shiraiwa, Y. and Inouye, I., 2000, *Physiological responses of lipids in *Emiliana huxleyi* and *Gephyrocapsa oceanica* (Haptophyceae) to growth status and their implications for alkenone paleothermometry*, Org. Geo-chem., 31, 799–811.

Yokoo, Y., Nakano, T., Nishikawa, M. and Quan, H., 2004, *Mineralogical variation of Sr- Nd isotopic and elemental compositions in loess and desert sand from the central Loess Plateau in China as a provenance tracer of wet and dry deposition in the northwestern Pacific*, Chemical Geology 204, 45-62.

Yu, F., Zong, Y., Lloyd, J. M., Huang G., Leng M. J., Kendrick C., Lamb, A. L. and Yim, W. W. S., 2010, *Bulk organic $\delta^{13}C$ and C/N as indicators for sediment sources in the Pearl River delta and estuary, southern China*, Estuarine, Coastal and Shelf Science 87(4), 618-630.

Yu F., Zong Y., Lloyd J. M., Leng, M. J., Switzer, A. D., Yim, W. W. S., 2011, *Mid-Holocene variability of the East Asian monsoon based on bulk organic $\delta^{13}C$ and C/N records from the Pearl River estuary, southern China*, The Holocene, 22, 705-715.

Zachos, J., Pagani, M., Sloan, L., Thomas, E. and Billups, K., 2001a, *Trends, rhythms, and aberrations in global climate 65 Ma to present*, Science, 292(5517), 686–693.

Zahn, R., Pedersen, T. F., Bornhold, B. D., and Mix, A. C., 1991, *Water mass conversion in the glacial subarctic Pacific (54N, 148W): physical constraints and the benthic-planktonic stable isotope record*, Paleoceanography, 6(5), 543–560. doi:10.1029/91PA01327.

Zhang Y., Sintes E., Chen J., Zhang Y., Dai M., Jiao N. and Herndl, G. J., 2009, *Role of mesoscale cyclonic eddies in the distribution and activity of Archaea and Bacteria in*

the South China Sea, Inter. Res. Aquat. Microb. Ecol. 56 65–79, doi:10.3354/ame01324.

Zheng, H.B., Powell, C.M., An, Z.S., Zhou, J. and Dong, G.R., 2000, *Pliocene uplift of the northern Tibetan Plateau*, *Geology* 28, 715–718.

Zohary, T., Erez, J., Gophen, M., Berman-Frank, I. and Stiller, M., 1994, *Seasonality of stable carbon isotopes within the pelagic food web of Lake Kinneret*, *Limnology and Oceanography*, 39: 1030–1043, doi:10.4319/lo.1994.39.5.1030.